Imperial College
London

Imperial College London
Department of Aeronautics

Computational modelling of diffusion magnetic resonance imaging based on cardiac histology

Jan Niklas Rose

Submitted for the degree of Doctor of Philosophy
at Imperial College London, London, UK

Copyright Declaration

The copyright of this thesis rests with the author. Unless otherwise indicated, its contents are licensed under a Creative Commons Attribution 4.0 International Licence (CC BY).

Under this licence, you may copy and redistribute the material in any medium or format for both commercial and non-commercial purposes. You may also create and distribute modified versions of the work. This on the condition that you credit the author.

When reusing or sharing this work, ensure you make the licence terms clear to others by naming the licence and linking to the licence text. Where a work has been adapted, you should indicate that the work has been changed and describe those changes.

Please seek permission from the copyright holder for uses of this work that are not included in this licence or permitted under UK Copyright Law.

Statement of Originality

I hereby declare that I composed this thesis myself. The contributions of my supervisors, Prof. Denis J. Doorly and Dr. Andrew D. Scott, are limited to conceptualisation and guidance as well as review of the final manuscript. All work presented as part of this thesis is my own. Information derived from the published and unpublished works of others has been acknowledged in the text and references are given in the bibliography.

Jan Niklas Rose
London, UK
Summer 2021

Abstract

The exact relationship between changes in myocardial microstructure as a result of heart disease and the signal measured using diffusion tensor cardiovascular magnetic resonance (DT-CMR) is currently not well understood. Computational modelling of diffusion in combination with realistic numerical phantoms offers the unique opportunity to study effects of pathologies or the efficacy of improvements to acquisition protocols in a controlled in-silico environment. In this work, Monte Carlo random walk (MCRW) methods are used to simulate diffusion in a histology-based 3D model of the myocardium. Sensitivity of typical DT-CMR sequences to changes in tissue properties is assessed.

First, myocardial tissue is analysed to identify important geometric features and diffusion parameters. A two-compartment model is considered where intra-cellular compartments with a reduced bulk diffusion coefficient are separated from extra-cellular space by permeable membranes. Secondary structures like groups of cardiomyocyte (sheetlets) must also be included, and different methods are developed to automatically generate realistic histology-based substrates. Next, in-silico simulation of DT-CMR is reviewed and a tool to generate idealised versions of common pulse sequences is discussed. An efficient GPU-based numerical scheme for obtaining a continuum solution to the Bloch–Torrey equations is presented and applied to domains directly extracted from histology images. In order to verify the numerical methods used throughout this work, an analytical solution to the diffusion equation in 1D is described. It relies on spectral analysis of the diffusion operator and requires that all roots of a complex transcendental equation are found. To facilitate a fast and reliable solution, a novel root finding algorithm based on Chebyshev polynomial interpolation is proposed. To simulate realistic 3D geometries MCRW methods are employed. A parallel simulator for both grid-based and surface mesh–based geometries is presented. The presence of permeable membranes requires special treatment. For this, a commonly used transit model is analysed. Finally, the methods above are applied to study the effect of various model and sequence parameters on DT-CMR results. Simulations with impermeable membranes reveal sequence-specific sensitivity to extra-cellular volume fraction and diffusion coefficients. By including membrane permeability, DT-CMR results further approach values expected in vivo.

To Pattareeya

Acknowledgements

The completion of this project would not have been possible without the direct or indirect help of many fantastic people.

First and foremost, I would like to thank my supervisors: Denis Doorly and Andrew Scott. Not only have you helped me every step along the way throughout this Ph.D., you are also the reason I took it on in the first place. Back in 2015 when I was completing my M.Sc. I found great joy working with the both of you, and the almost 5 years that followed have not disappointed me. Denis, you were always able to give me a fresh perspective to problems that I ran into. It was an absolute pleasure to be able to discuss not only work but also other topics of interest with you. I also very much enjoyed branching out into the work on CFD of airways that you let me get involved in. Andrew, I admire your energy and positivity. I could always count on you to read anything I put in front of you and to always provide helpful feedback. Your expertise on everything MRI has helped me get a quick grasp of the vast field that I faced from the start.

I also need to thank several funders of my research. My stipend was paid for by the Department of Aeronautics, which allowed me to carry out this research in the first place. During my Ph.D. I made extensive use of the Imperial College HPC facilities, and I would like to thank the whole RCS team. I was indirectly supported by the British Heart Foundation through two grants, which in large part paid for the high performance workstation I was able to rely on for development as well as for the collection of some of the microscopy images in this work. The NVIDIA corporation kindly provided the P4000 GPU that I used for several projects, including the deep learning–based segmentation and diffusion simulations. I also want to thank the ISMRM and SIAM organisations for the student travel awards that helped me attend several conferences.

During this thesis I made use of countless tools, many of which are free open-source software. I want to express my gratitude to all open-source contributors, who do a great service to many researchers. I also need to acknowledge every StackExchange contributor whose insightful question, answer, or comment I read.

The time spent on the Ph.D. certainly would not have been as bearable without many friends and colleagues. I want to thank Rishabh Gvalani, Paul Mannix, Lee Nissim, and Rob Sullivan for many enjoyable coffee breaks, both in person and virtual. My thanks also go to my desk neighbour Jan Eichstädt for countless coding-related discussions, panic over NVIDIA drivers, and teaching preparations. Lastly, I must acknowledge Qiwei Xiao for many trips to the common room or long chats at your desk.

I am eternally grateful to my loving and patient fiancée. Pattareeya, this thesis would not have been possible without you. Your support and encouragement were more important to me than you might realise. Thanks also to my cats Filo and (more recently) Milo, for attempting to help me type out this thesis when I was not looking.

Last but certainly not least: Vielen lieben Dank an meine Eltern und Großeltern für eure bedingungslose Ermutigung, Liebe, und Unterstützung.

Table of Contents

List of Figures

List of Tables

List of Equations

List of Algorithms

Chapter 1

Introduction

Contents

1.1 Background

The heart is responsible for pumping blood through the vasculature of the body, accomplished by periodic synchronised contraction and relaxation of the cardiac muscle cells (cardiomyocytes). This life-critical function is performed continuously from early gestation, reaching a steady resting rate of 60 to 100 beats per minute in adults. Efficient function of the heart as a pump is dependent on the complex microstructural arrangement of the cardiomyocytes (Arts et al., 2003). An understanding of this microstructure and its function in health and disease will be a powerful tool for discovering new diagnostic and prognostic markers and developing new treatments.

The human cardiovascular system has been studied since ancient times (Aird, 2011). The first accurate drawings of human hearts were performed by Leonardo da Vinci (Sterpetti, 2019), but it was not until 1628 that the concept of cardiology was introduced with William Harvey's ground-breaking book *Exercitatio Anatomica de Motu Cordis et Sanguinis in Animalibus*[*].

Modern cardiology research primarily focuses on prevention and treatment of heart and circulatory disease, or cardiovascular disease (CVD). According to official estimates (British Heart Foundation, 2021) CVD is the number one cause of death worldwide and accounts for 34 % of deaths annually. Advanced medical imaging techniques like diffusion tensor

---

[*] Latin for *Anatomical Exercise on the Motion of the Heart and Blood in Animals.*

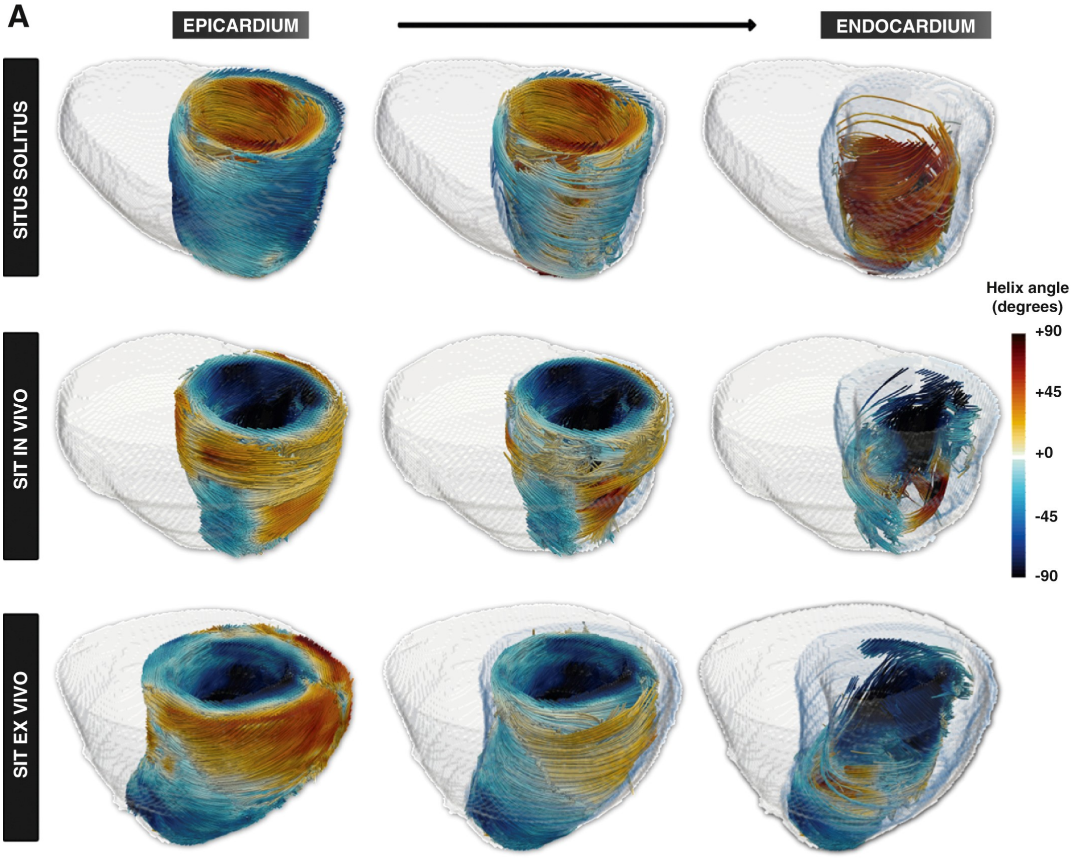

Figure 1.1: Left ventricular cardiomyocyte orientation in a normal (situs solitus, SS) and situs inversus totalis (SIT) subject measured using DT-CMR. The helix angle (HA) varies from a left-handed (negative HA) orientation in the epicardium smoothly through to a right-handed (positive HA) in the endocardium in SS, but transitions between an SS-like arrangement in the apex to a reversal (right-handed in the epicardium to left-handed in the endocardium) in the base in SIT. [*Reproduced with permission from (Khalique et al., 2018), Copyright American College of Cardiology Foundation.*]

cardiovascular magnetic resonance (DT-CMR) are necessary to better understand the structure of both healthy and diseased hearts. For example in recent work with situs inversus subjects Khalique et al. (2018) demonstrated unexpected differences in cardiomyocyte orientation, shown in figure 1.1.

DT-CMR, or diffusion tensor imaging (DTI) as it is more generally known outside the heart, is a non-invasive imaging modality that provides information on microstructural tissue characteristics through macroscopic investigation (Nielles-Vallespin et al., 2020). The technique is based on measuring the restriction and hindrance of the diffusion of water molecules as a result of the microscopic structure of the tissue. In each imaging voxel, which typically has a resolution of millimetres, the apparent diffusion behaviour can be modelled by a 3×3 positive-definite rank-2 diffusion tensor (Basser et al., 1994). It is commonly visualised as an ellipsoid or superquadric glyph (Ennis et al., 2005), whose

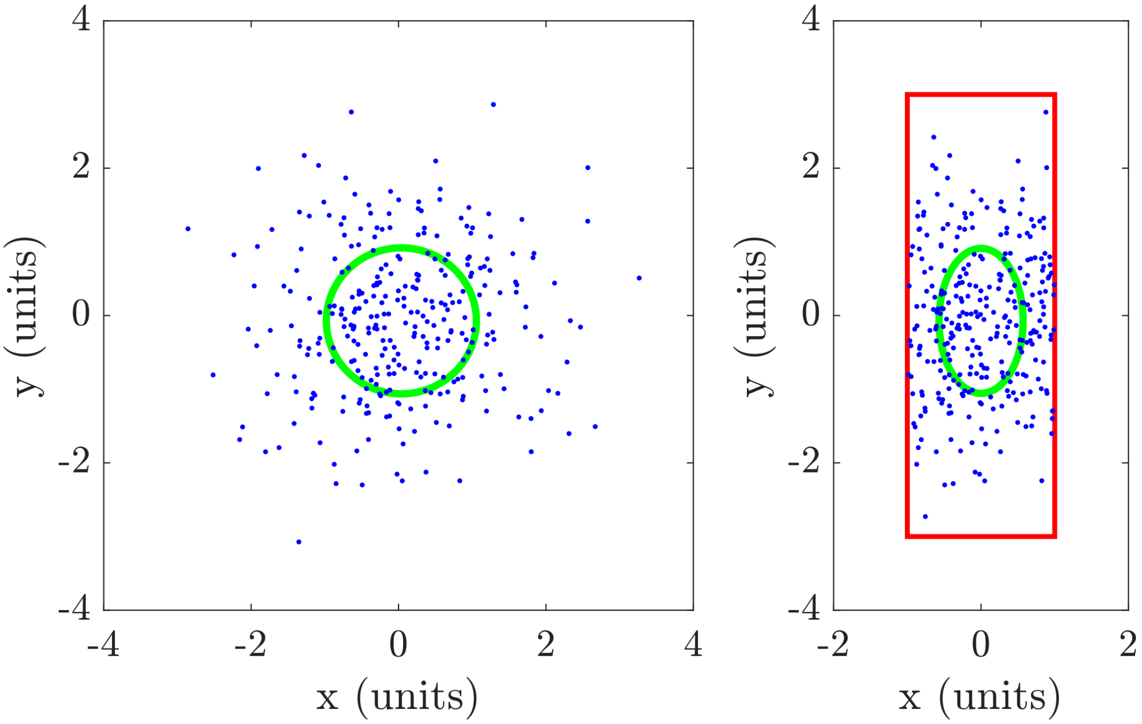

Figure 1.2: Apparent diffusion of an ensemble of random walkers initially located at the origin. All parameters have been non-dimensionalised. In the case of unrestricted diffusion **(Left)**, the mean squared displacement (MSD) can be represented by a circle (green) of unit radius. Next, the walkers are confined by barriers (red) at $x = \pm 1$ and $y = \pm 3$. Their MSD is now significantly reduced in the x-direction and their apparent diffusion is represented by an ellipse **(Right)** whose axes align with those of the rectangular box.

shape, size, and orientation are dependent on the tensor's three orthogonal eigenvectors and corresponding eigenvalues, respectively. Analysis of the diffusion tensor properties provides surrogate measures of the tissue microstructure from the measured data, which is sensitive to changes in factors such as (average) cell size or orientation.

Consider an ensemble of diffusing particles in two dimensions, located initially at the origin. The diffusive behaviour of these particles may be modelled as a Monte Carlo random walk[†] that causes them to spread out randomly as seen in figure 1.2. In the absence of barriers their distribution of positions or net displacement is isotropic, meaning displacement is equally likely in every direction, and the mean square displacement (MSD) is represented by a circle. By confining the walkers to the rectangular shape seen in the figure their diffusion becomes more restricted in the x-direction than in y and this is clearly visible from the MSD taking on an elliptical instead of a circular shape. This two-dimensional example can be trivially extended to 3D, where the circle becomes a sphere, the rectangular box a cuboid, and the ellipse an ellipsoid.

[†] Monte Carlo random walks form an integral part of this work and their details will be explained later in chapter 5.

The above *Gedankenexperiment* is the basis of DTI. In biological tissue the restriction is caused by cell membranes and the MR experiment can be designed to provide a measurable signal loss relating to the mean squared displacement. In the myocardium, the first and second eigenvectors[‡] of the diffusion tensor are aligned with the directions of least restriction to diffusion. For myocardial tissue the first eigenvector has been demonstrated to align with the cardiomyocyte orientation (Scollan et al., 2000), while the angle of the second eigenvector (E2A) corresponds to that of the dominant direction of shear layers separating groups of cardiomyocytes known as sheetlets (Nielles-Vallespin et al., 2017; Smerup et al., 2009).

Current research is focused on investigating further clinical applications of DT-CMR. These include application as potential biomarkers of disease such as tractography for myocardial scar delineation (Mekkaoui et al., 2018), identification of disarray (Ariga et al., 2019), sheetlet dysfunction (Deuster et al., 2016a; Khalique et al., 2020b), and the investigation of novel congenital heart conditions (Khalique et al., 2018). The use of diffusion imaging beyond the diffusion tensor model, which assumes Gaussian diffusion, allows for non-Gaussian models (McClymont et al., 2017), which may provide insights including into multiple populations of microstructural components within a voxel (Sosnovik et al., 2009).

DT-CMR has a limited spatial resolution as a result of its low signal-to-noise ratio. This reduces its usefulness, particularly in patients with a thinned myocardium or where small regions of focal disease are expected. The use of spiral readouts (Gorodezky et al., 2019) aims to improve resolution over the conventional single shot echo-planar imaging (EPI) readout techniques. The need for repeated acquisitions along different diffusion-encoding directions to bolster signal to noise ratio also leads to long scan times. Research is ongoing into addressing these shortcomings via compressed sensing (Teh et al., 2020) and deep learning–based denoising (Phipps et al., 2021). Motion compensated spin-echo approaches as proposed by Welsh et al. (2015) may provide increased imaging efficiency, but are less reliable when acquisitions are performed in diastolic cardiac phases. More advanced approaches, providing both motion compensation and advanced diffusion schemes (b-tensors), are being investigated (Lasič et al., 2020) for in-vivo cardiac imaging.

While geometric features associated with the eigenvectors are qualitatively understood, the more subtle relationship between microstructural changes and the resulting diffusion tensor are not easily quantified. For example, the exact mechanism for abnormal E2A in hypertrophic cardiomyopathy (HCM) patients (Ferreira et al., 2014) is not clear. Other microstructural disruptions common in diseases affecting the myocardium include changes in extra-cellular volume fraction, cellular hypertrophy, and cardiomyocyte disarray. It is not well understood what changes in DT-CMR parameters should be expected as a

---

[‡] The third eigenvector is determined by the cross-product of the first two and thus contains no additional information.

consequence of known pathological changes in myocardial microstructure, and hence the detectability of expected microstructural abnormalities using DT-CMR remains unknown.

Computational modelling offers the unique opportunity to study these effects in a controlled in-silico environment. With carefully designed simulations and appropriate numerical phantoms, the sensitivity of DT-CMR to changes in the underlying microstructure and confounding factors can be investigated deterministically. Lipinski (1990) was the first to carry out Monte Carlo random walk simulations of extra-cellular diffusion in brain tissues and biophysical modelling has gained considerable popularity since then (Jelescu et al., 2020). Despite the potential of such methods, prior works applying computational simulations of diffusion to the myocardium are few (Bates et al., 2017; Wang et al., 2014). Models and simulations developed for other anatomical targets, for example in neuroimaging (Fieremans et al., 2018) and musculoskeletal (Berry et al., 2018) DTI, are not well-suited for translation to the cardiac microstructure due to different microstructural features and morphology, and the acquisition methods and protocols typical used in DT-CMR differ significantly from those used in other disciplines as a result of cardiac motion.

1.2 Hypothesis

The aim of this project is to develop a computational DT-CMR framework that enables the study of changes to the cardiac microstructure and acquisition techniques and their effects on typical measures derived from DT-CMR data. This project will also investigate the feasibility of and need for a high-fidelity microstructural model that includes hitherto neglected features of the tissue. This will pave the road for future studies linking in-vivo DT-CMR parameters to underlying pathological changes on a microscopic scale.

The research hypothesis can thus be formulated as follows:

> *Using a realistic virtual model (acquisition protocol; voxel size; intrinsic tissue morphology and diffusion parameters) as input for Monte Carlo random walk simulations allows for more realistic in-silico estimates of the DT-CMR measures typically found in vivo.*

From this hypothesis, the following three research objectives (**RO**s) are derived:

RO1 Create a virtual geometric model of myocardial microstructure that is based on histology data of real tissue and contains a realistic representation of cardiomyocyte shapes and their distribution and organisation in sheetlets.

RO2 Develop a Monte Carlo random walk simulator to solve for the behaviour of spins undergoing diffusion in arbitrary environments and subject to DT-CMR imaging, and verify its accuracy using numerical and analytical reference solutions.

RO3 Study the sensitivity of DT-CMR measures to the underlying in-vivo tissue model parameters (diffusion coefficient, membrane permeability, morphology of the geometry) for common DT-CMR pulse sequences (spin echo and stimulated echo–based sequences).[§]

1.3 Overview

The thesis is structured as follows:

Chapter 2 starts with a review of myocardial tissue geometry and function, followed by a description of methods to generate a virtual substrate (**RO1**). This includes the collection and labelling of microscopy images of histology and is further extended to automatic synthesis of representative tissue without the requirements for a reference histological image.

The fundamentals of DT-CMR are explained in chapter 3. The process of solving the governing equations (**RO2**) is illustrated through development of a GPU-based algorithm to efficiently obtain continuum solutions of the Bloch–Torrey equations.

Chapter 4 considers diffusion in 1D. Through spectral analysis of the diffusion operator, an analytical solution for permeable layered media is derived that can serve as a reference or ground truth solution to other methods in this work. Additionally, this reduction of the tissue model to lower dimensions offers new insights into the mechanisms of diffusion and membrane permeability.

Chapter 5 discusses diffusion as a Monte Carlo random walk. This simulation technique is commonly used to efficiently model the diffusion of matter in complex environments. However, the treatment of permeability is not well understood. A considerable part of the chapter is dedicated to the analysis of membrane transit models to correctly treat membrane transit.

Finally, chapter 6 addresses the last objective (**RO3**). By combining the techniques developed in chapters 2 to 5 several parameter studies are carried out that vary tissue and sequence parameters.

Conclusions and limitations are summarised and future work is discussed in chapter 7. A list of publications that emerged from this work can be found in appendix A, while an overview of available software and data is given in appendix B. Permissions for reproduction of copyrighted material in this work are attached in appendix C.

[§] These model parameters and pulse sequences are defined later in this work.

Chapter 2

The Myocardium

Contents

2.1 Introduction

The study of diffusion inside the myocardium requires an understanding of the myocardial function and structure at a microscopic level. To perform realistic simulations of diffusion within the myocardial microstructure as done in chapter 6, a substrate (virtual myocardium) needs to be constructed that represents the true tissue to a sufficient degree.

This chapter first provides an overview of the structure, organisation, and function of the myocardium (including parameters such as diffusion coefficient and membrane permeability) in section 2.2. Next, the requirements and considerations for virtual tissue substrates are discussed in section 2.3. Finally, different ways of generating these substrates are described: by analysing and segmenting histology images (section 2.4) and from scratch by synthesis (section 2.5).

2.2 Myocardial tissue

Figure 2.1 illustrates the cross-section of the human heart, cut along the horizontal long axis through the left and right atria and ventricles. Standard nomenclature (Cerqueira

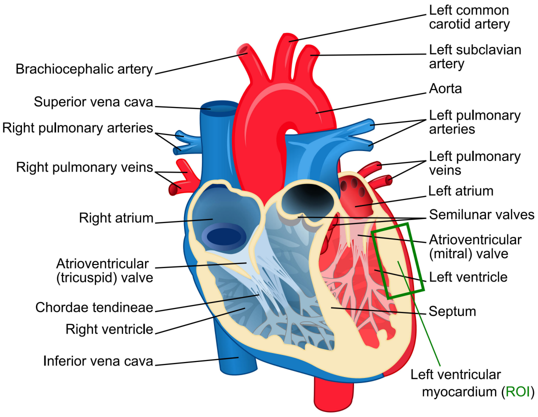

Figure 2.1: Cross-section of a normal human heart showing the atria, ventricles, septum, and myocardial walls. The left ventricular myocardium, designated as region of interest (ROI), is the part of the heart considered in this work. [*Diagram modified from (ZooFari, 2010). This graphic is licensed under the original CC BY-SA 3.0 license terms.*]

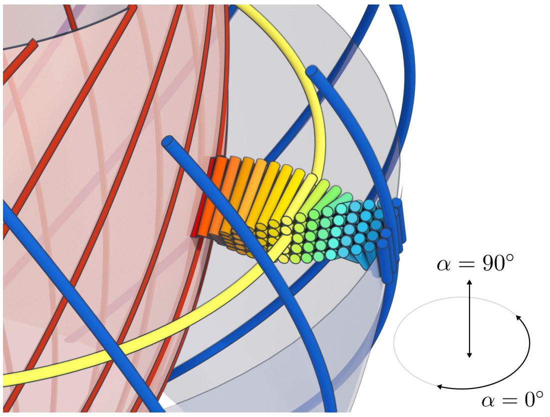

Figure 2.2: Helical orientation of cardiomyocytes varies in the transmural direction, from a −60° left-handed helical angle in the epicardium to +60° in the endocardium. The coordinate frame explains the definition of helix angle (HA). [*Reproduced with permission from (Nielles-Vallespin et al., 2017), modified to include a coordinate frame.*]

et al., 2002) is used. This work is limited to considering the left ventricular myocardium at the mid-ventricular level. While the basal region, apical region, atria, and right ventricle are also of clinical interest, current in-vivo acquisitions are commonly limited to the mid-ventricular region due to additional challenges in applying current imaging methods elsewhere. The left ventricle, which drives oxygenated blood around the body, has the greatest clinical significance (Khalique et al., 2020a). The myocardium (heart muscle tissue) is bounded on the "inside" by the endocardium and on the "outside" by the visceral serous pericardium, also known as epicardium.

As was famously observed by Pettigrew (1864) in his work describing the meticulous dissection and drawing of cardiac muscle tissue, the long axes of the cardiac muscle cells (cardiomyocytes) are arranged in a helical pattern around the ventricle—albeit not in the form of continuous fibres as described in the original work. According to Streeter et al. (1969) the orientation of the cardiomyocyte long axis varies continuously in the transmural direction from an approximately −60° left-handed helical angle (HA, measured relative to the circumferential direction) in the epicardium, smoothly through to a circumferential orientation (HA $= 0°$) in the mesocardium, to a right-handed approximately +60° helical arrangement in the endocardium. A schematic view of this can be seen in figure 2.2. This arrangement is vital to the normal function of the heart. The distribution of fibre orientations is responsible for torsion in the heart as it contracts and expands, and this ensures that cardiomyocytes experience constant force everywhere (Young et al., 2012).

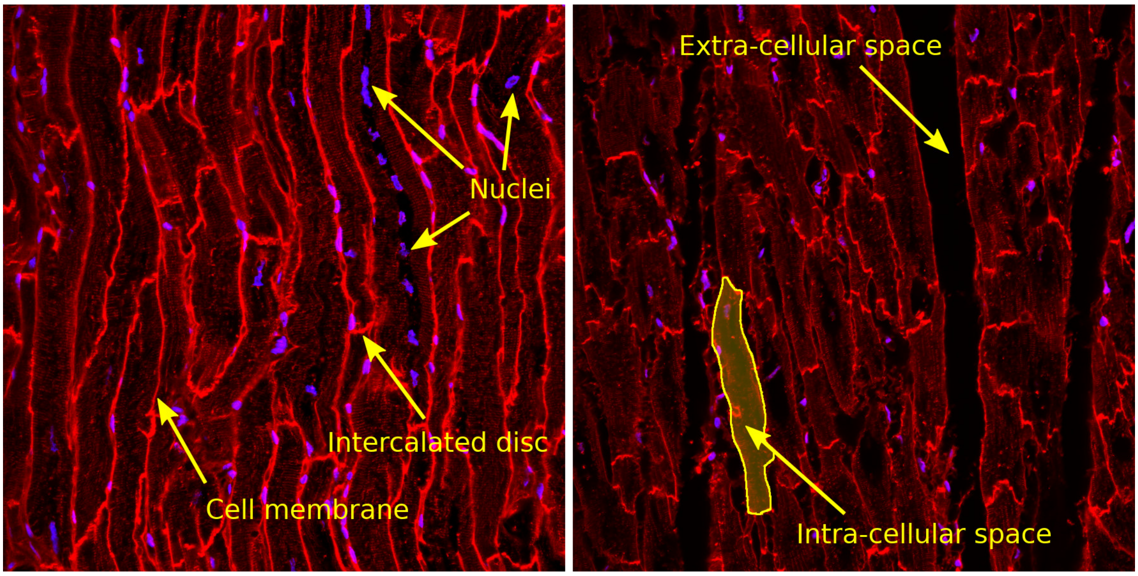

Figure 2.3: 3D confocal microscopy images acquired with fluorescent labelling of the cell membranes (red) and nuclei (blue). Data was obtained from sections of porcine myocardium and the annotations show some key features of myocardial microstructure. [*Tissue and confocal images were kindly provided by P. Sarathchandra and A. Scott.*]

2.2.1 Cardiomyocyte morphology

Cardiomyocytes are the building blocks of the myocardium (Barnett, 2009). These cells contract and relax with local synchrony to enable the heart muscle to pump blood. The three-dimensional network of cardiomyocytes is best observed through confocal microscopy (Price et al., 2014), as is done in figure 2.3.

A more schematic view is given in figure 2.4 (Braunwald et al., 1967). In the figure, (B–D) show sketches of the functional composition of a cardiomyocyte, based on electron micrographs. Actin and myosin filaments provide contractile force along the length of the cell and are arranged into bundles of myofilaments (fibrils). Cardiomyocytes also contain organelles and other sub-structures. Figure 2.4 (A) shows cardiomyocyte branching. One cell may connect to several at the ends, forming a syncytium, with intercalated discs acting as the cells' end caps that separate one from the next. In this work only individual cardiomyocytes are considered and their longitudinal connectivity is ignored, essentially assuming impermeable intercalated discs. While more sophisticated geometries with connected networks of cardiomyocytes are required for fully-realistic simulations, this first-order approximation to the geometry shown in figure 2.4 (A) is deemed sufficient.

With the high spatial resolution of confocal imaging one can observe the size and shape of the myocytes. Human* cardiomyocytes are typically around 120 µm long and 20 µm in diameter (Campbell et al., 1989; Olivetti et al., 1996; Satoh et al., 1996). While an idealised

---

*The cardiomyocytes found in the adult human heart are comparable in size to those of other mammals often used as animal models: pigs, rabbit, rats, sheep (Bensley et al., 2016).

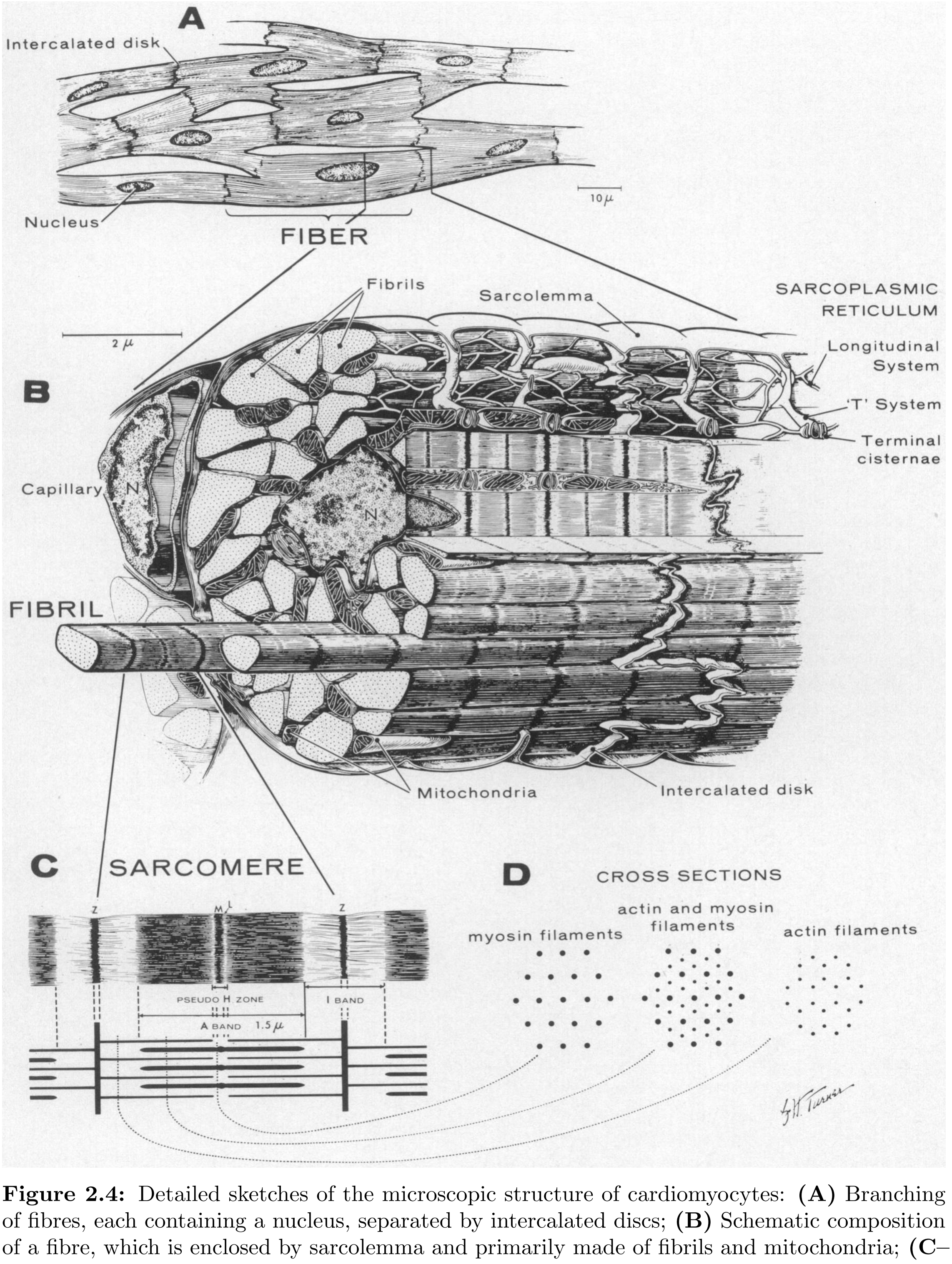

Figure 2.4: Detailed sketches of the microscopic structure of cardiomyocytes: **(A)** Branching of fibres, each containing a nucleus, separated by intercalated discs; **(B)** Schematic composition of a fibre, which is enclosed by sarcolemma and primarily made of fibrils and mitochondria; **(C–D)** Fibrils are made up of sarcomeres that in turn consist of myofilaments. [*Reproduced with permission from (Braunwald et al., 1967), Copyright Massachusetts Medical Society.*]

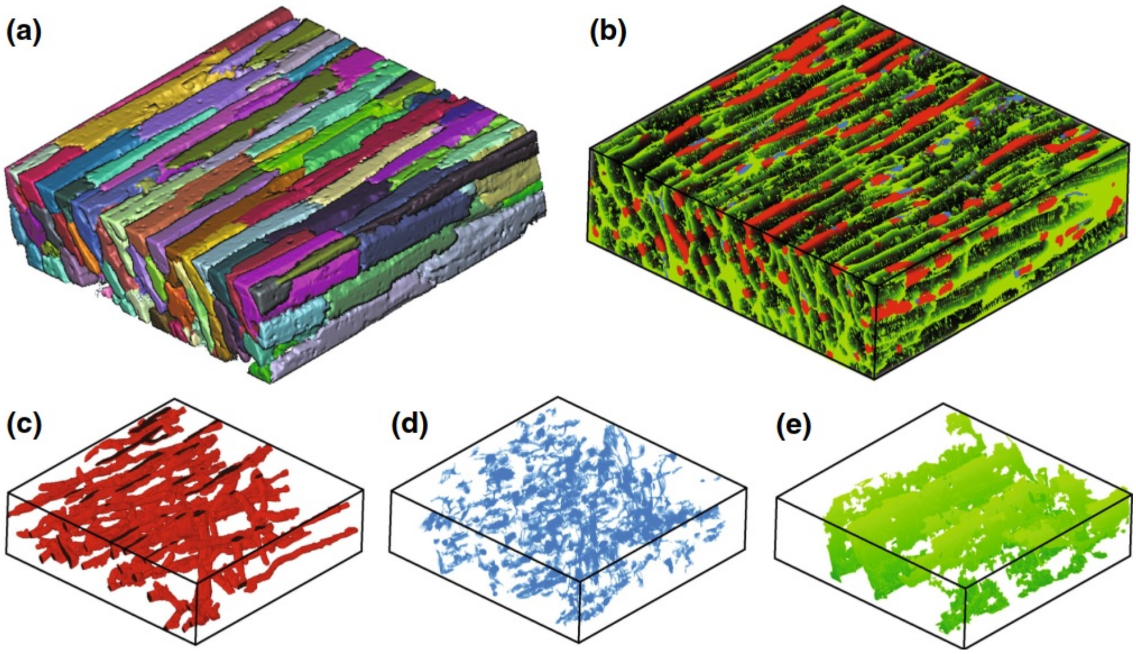

Figure 2.5: Three-dimensional reconstruction of ventricular tissue segmented from a stack of confocal microscopy images: **(a)** Individual cardiomyocytes, in total 124; **(b–d)** Segmentation of ECS (green), vasculature (red), fibroblasts (blue), and myocytes (black); **(e)** extra-cellular laminas perpendicular to the epicardial surface. [*Reproduced with permission from (Seidel et al., 2016), Copyright Springer Nature.*]

cell may be modelled as a simple cylinder, either with circular or square cross-section, their actual shape is more complex (Bensley et al., 2016; Seidel et al., 2016). Recent work by Seidel et al. (2016) on rabbit hearts has produced the segmented microstructure seen in figure 2.5, which shows a broad range of cross-sections. The figure also shows the composition of the extra-cellular space, which serves as a support network for the myocytes.

The contents of the cardiomyocytes are enclosed by the cell membrane or sarcolemma (figure 2.4), which consists of a lipid bilayer containing protein-based channels. The surface of the cell is dotted with T-tubules, which are regions of membrane diving into the cell. Water molecules can diffuse through the lipid bilayer and, like other molecules, can transit through specialised channels. Water passes through a family of channels known as aquaporins (Rutkovskiy et al., 2013).

2.2.2 Mesostructural arrangement

In addition to the organised structure of cardiomyocytes, they themselves aggregate into units known as sheets or sheetlets (Smerup et al., 2009). They are clearly visible in large-scale wide-field microscopy images such as figure 2.6. Sheetlets are typically 8 to 12 cardiomyocytes thick and extend an undetermined distance in the perpendicular

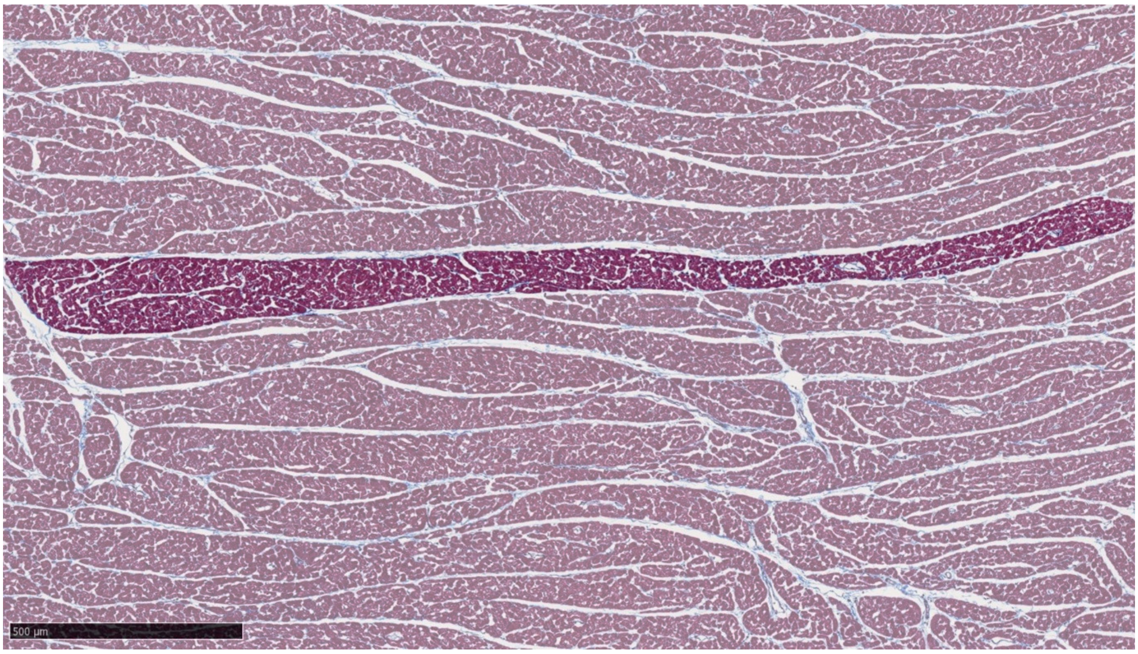

Figure 2.6: Widefield microscopy image showing the organisation of cardiomyocytes in sheetlets. One such sheetlet is fully opaque, while the rest of the image is partially transparent. The porcine histology was prepared with Masson's trichrome which stains cardiomyocytes red and collagen blue and is cut perpendicular to the cardiomyocyte long axis. [*Original histology image kindly provided by S. Nielles-Vallespin as part of the data set from (Nielles-Vallespin et al., 2017).*]

directions. LeGrice et al. (1995a) report a thickness of 4 ± 2 cardiomyocytes, which seems to contradict this observation. However, sheetlet boundaries are difficult to identify in histology images (the source used in this work) as sectioning in preparation for imaging tends to distort the structured arrangement.

As shown in figure 2.7 sheetlets are separated by perimysial connective tissue. These collagen-lined shear layers are filled with extra-cellular fluid, allowing the sheetlets to slip over each other as the heart contracts. This secondary structure is required in order to translate the $\approx 8\,\%$ radial thickening of cardiomyocytes during systole into the $>35\,\%$ radial thickening of the myocardium with longitudinal shortening and torsion (Nielles-Vallespin et al., 2017). Besides this important mechanical function (LeGrice et al., 1995b), the alignment of sheetlets is also integral to the electrical function of the heart (Hooks et al., 2007).

Sheetlets (or rather the shear layers separating them) can be observed through directional information in the plane orthogonal to the primary eigenvector. This is the same plane as the imaging plane in figure 2.6. For that particular image, the preferred (secondary) direction of diffusion is approximately horizontal. This corresponds to the dominant sheetlet orientation. Kung et al. (2011) observed two populations of sheetlet angles through DT-CMR imaging, validated by histological analysis. This "two sheet" model warrants

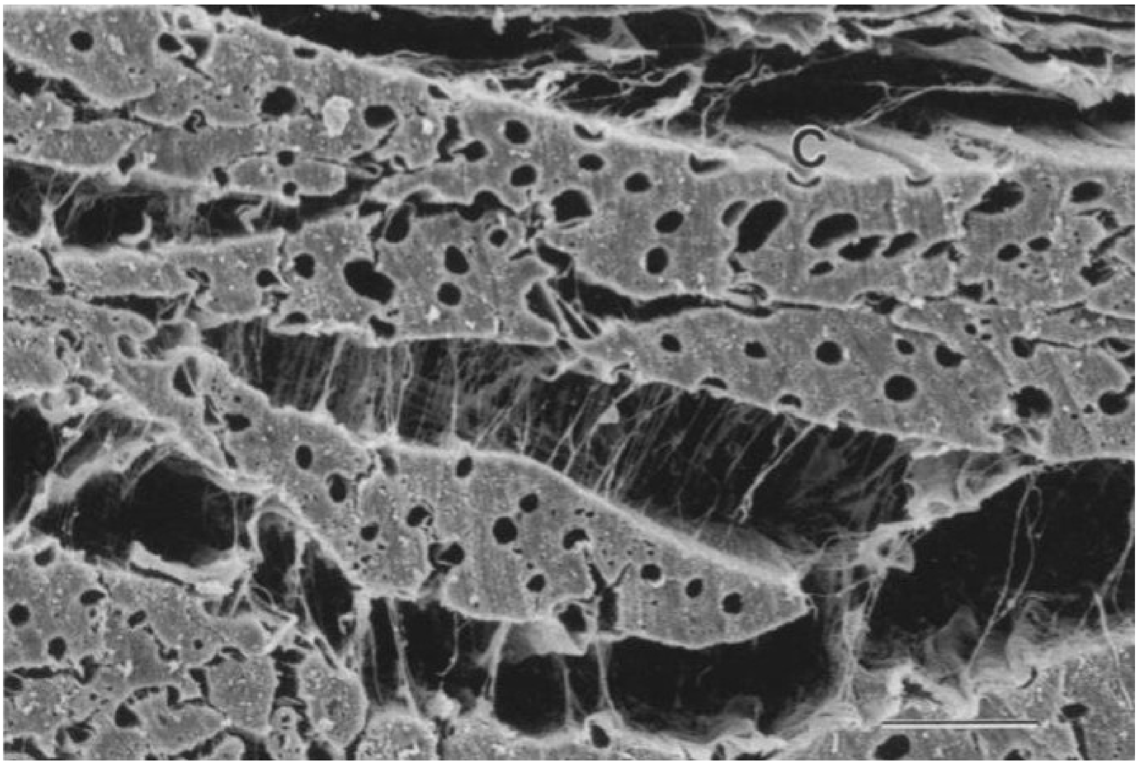

Figure 2.7: Cross-sectional view of myocardial sheetlets as seen from an electron micrograph. The sheetlets are separated by perimysial connective tissue. The scale bar (bottom right) has length 25 µm. [*Reproduced with permission from (LeGrice et al., 1995a), Copyright The American Physiological Society.*]

further investigation.

Current research (Deuster et al., 2016a; Ferreira et al., 2014; Khalique et al., 2018) is particularly interested in detecting changes in sheetlet orientation via the measurement of E2A (orientation of the second eigenvector) through DT-CMR due to the insights that it provides on the alteration of cardiac function on a microstructural scale in health and disease. It is therefore essential to include this sheetlet structure in any model of the myocardium.

2.3 Constructing a virtual model of the myocardium

Up to now the composition and geometry of the myocardium was described. This section takes a more pragmatic approach and considers how a virtual model can approximate the myocardium with sufficient accuracy. The aim of such a virtual model is to serve as an input substrate for the numerical simulations carried out in this work. Focus is placed on substrates constructed directly from histology, as this minimises model error and allows the model substrate to be used for direct validation studies.

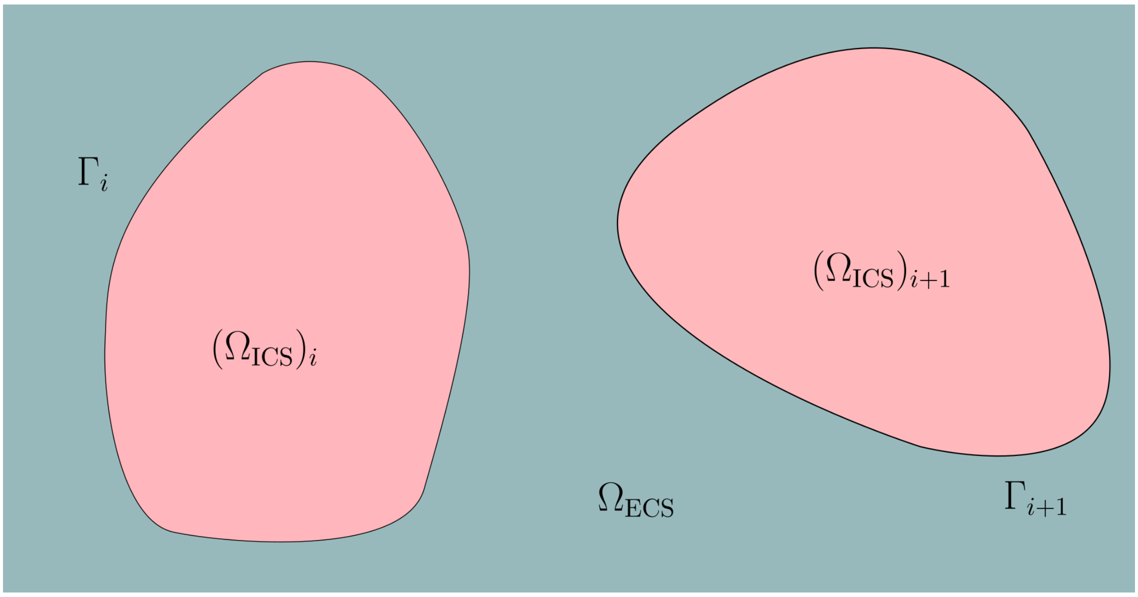

Figure 2.8: Illustration of the bi-compartment model used in this work. Extra-cellular space (ECS) is the contiguous space represented by Ω_{ECS}. Intra-cellular space (ICS) are regions $(\Omega_{\text{ICS}})_i$ embedded in the ECS and separated by membranes Γ_i.

2.3.1 Compartment models

Let us consider two distinct compartment types as is commonly done in studies of biological tissue (Fieremans et al., 2010; Kärger, 1985; Panagiotaki et al., 2012; Snaar et al., 1992; Stanisz, 2003). A schematic is shown in figure 2.8. Intra-cellular space (ICS) consists of distinct regions $(\Omega_{\text{ICS}})_i$ with infinitely thin boundaries Γ_i that separate them from the extra-cellular space (ECS, Ω_{ECS}) that these regions are located in. In this work, all regions of ICS are assumed to be non-overlapping and separated by ECS. For simulation substrates in section 5.4.4 this is in fact *required*.

This two-compartment system is characterised by the shape of the restrictions Γ and the relative volumes of the two domains. The extra-cellular volume fraction (ECV) is formally defined as

$$\rho \equiv \frac{\int_{\Omega_{\text{ECS}}} \mathrm{d}v}{\int_{\Omega_{\text{ICS}} \cup \Omega_{\text{ECS}}} \mathrm{d}v} \,. \tag{2.1}$$

From MRI measurements, C. Nguyen et al. (2015) and Wu et al. (2018) estimated values of ECV to be in the range of 20 to 30 % in healthy hearts.

Recall the cardiomyocyte morphology from section 2.2. For the purposes of modelling the cells, the intra-cellular space is considered to be an isotropic homogenous region. This ignores the intricate details in favour of a more manageable and easier to understand geometry. In addition, the time scales of interest result in diffusion distances much larger than these small structures. The diffusion processes may thus be modelled by a single homogeneous bulk diffusion coefficient D_{ICS}. Due to the presence of these additional nanostructures, the value of D_{ICS} is expected to be less than that of water ($D_{\mathrm{H_2O}}$). This mesoscopic model of a reduced bulk diffusion coefficient accounts for the apparent hindrance experienced in the compartment.

A similar approach is taken for the ECS, which may be interstitial or intravascular tissue. The collagen that surrounds the cells is expected to cause hindrance that reduces the effective bulk diffusion coefficient. Owing to the different levels of sub-microstructural features, the ECS has a lower degree of restriction than ICS. Therefore:

$$D_{\mathrm{ICS}} \leq D_{\mathrm{ECS}} \leq D_{\mathrm{H_2O}} \tag{2.2}$$

The underlying diffusion coefficient for water $D_{\mathrm{H_2O}}$ is only dependent on the viscosity (and thus temperature) of the fluid and is approximately equal to $3\,\mathrm{\mu m^2/ms}$ at body temperature and $2\,\mathrm{\mu m^2/ms}$ at room temperature (Mills, 1973). The other two compartment-specific diffusion coefficients (D_0 is used as a placeholder when the type of compartment is not specified or is otherwise clear from context) need to be estimated. In ex-vivo MR experiments in rat hearts, Seland et al. (2007) observed two distinct apparent diffusivities† at very short diffusion times. Because these times are slower than the expected time needed for water to sense restriction by diffusion, the observed diffusivities can be attributed to the intra- and extra-cellular diffusion coefficients of $D_{\mathrm{ICS}} = 1.2\,\mathrm{\mu m^2/ms}$ and $D_{\mathrm{ECS}} = 3\,\mathrm{\mu m^2/ms}$. Other authors (Garrido et al., 1994; Safford et al., 1978) have found values in the range of 0.5 to $2.5\,\mathrm{\mu m^2/ms}$.

2.3.2 Exchange

Regarding the cell barriers Γ_i, the sarcolemma (recall figure 2.4) is considered to be a homogeneous smooth (no T-tubules) permeable membrane of negligible thickness. Each is characterised by a single permeability value κ (often also denoted as P), which is constant along Γ_i. Throughout this work the assumption is made that all cells have the same value for κ, however this is not strictly necessary.

Membrane permeability has the units of velocity and thus dictates the effective speed at which water (the permeate) can pass through the porous cell membrane. In this work only the kinetics of the steady-state (equilibrium) exchange of H_2O, which is described and quantified by diffusional (as opposed to osmotic) permeability, are considered. The permeability κ is an approximation of

$$\kappa \equiv \lim_{\substack{b\to 0,\\ D_b\to 0}} \left(\frac{D_b}{b}\right), \tag{2.3}$$

in the limit where both the reduced diffusion coefficient D_b inside the membrane and its thickness b approach zero (Powles et al., 1992).

---

† As described later in section 3.2.2, the apparent (observed) diffusivity depends on the imaging parameters, primarily the diffusion time Δ. At short values for Δ, it approaches D_0.

Values for the cell membrane permeability are commonly estimated from the apparent exchange rate (AXR) or mean intra-cellular lifetime τ_{ICS} observed using diffusion MRI (Hills et al., 1989; Lasič et al., 2011). Exchange rates are reported in a range of 6 to 30 Hz (Coelho-Filho et al., 2013; Seland et al., 2007), but have been found as high as 50 Hz for healthy leg muscles of rats (Sobol et al., 1991). For comparison, Landis et al. (1999) reports $\kappa = 0.013\,\mu\mathrm{m/ms}$ for human thigh muscle. An upper limit on the AXR can be placed as that of the well-mixed erythrocytes (red blood cells, RBC). Literature values for τ_{ICS}^{-1} of RBC are reported to be around 100 Hz (Herbst et al., 1989). Most cells have $\kappa > 0.001\,\mu\mathrm{m/ms}$, and this value serves as a lower bound for permeable cells (Fieremans et al., 2010).

The exchange time constant τ_{ex} (its inverse being the exchange rate) is related to the cell membrane permeability (Reginald Waldeck et al., 1995) via

$$\tau_{\mathrm{ex}} = \frac{\rho}{\kappa}\frac{V}{S}\,. \tag{2.4}$$

Here, the claustrophobia ratio V/S is the characteristic length C that relates the size of the compartment Ω_i (its volume $V = \int_{\Omega} \mathrm{d}v$) to that of its membrane Γ_i (its surface area $S = \oint_{\Gamma} \mathrm{d}s$). Note that equation (2.4) is only valid for well-mixed cells, which applies to most cell types (Springer et al., 2014; Strijkers et al., 2009) including cardiomyocytes (Bruvold et al., 2007). In the limit $\kappa \to \infty$ however, one must account for the diffusion time inside the compartment (Meier et al., 2003, eqn. 14). The exchange time is related to the intra-compartmental lifetimes (τ_{ICS} and τ_{ECS}) by volume-weighting with ECV (ρ) through

$$\tau_{\mathrm{ex}} = \rho\tau_{\mathrm{IC}} = (1-\rho)\tau_{\mathrm{EC}}\,. \tag{2.5}$$

In 3D, the claustrophobia ratio is simply the volume to surface area ratio (V/S). For a cylinder with radius R and height H, it is given by

$$C_{\mathrm{3D}} = \frac{V}{S} = \frac{\pi R^2 H}{2\pi RH + 2\pi R^2} = \frac{RH}{2\,(H+R)}\,. \tag{2.6}$$

For lower-dimensional domains, this reduces to a circle with area A and perimeter P in 2D:

$$C_{\mathrm{2D}} = \frac{A}{P} = \frac{\pi R^2}{2\pi R} = \frac{R}{2}\,. \tag{2.7}$$

This is also recovered from C_{3D} in the limit $H \to \infty$.

In a domain with multiple compartments of different sizes the values must be averaged correctly. The mean claustrophobia ratio $\langle C\rangle$ is the mean of each cell's C as per

$$\langle C\rangle = \langle\frac{V}{S}\rangle \neq \frac{\langle V\rangle}{\langle S\rangle}\,. \tag{2.8}$$

2.3.3 Simulation substrates and geometric fidelity

Over the past years, microstructural models used in the literature have become more accurate to represent either certain specific geometric features or simulate larger domains.

In early simulation work by Szafer et al. (1995) the substrate was limited to a regular grid of cuboidal cells. Since then, advances in both simulation hardware and computational methods have made numerical simulations more practical.

In neuroimaging, white matter consists primarily of tightly-packed myelinated axons. These are often modelled numerically through their circular cross-section in 2D and are well-understood by theoretical means (Novikov et al., 2019). However, recent work extended simulations of axons to 3D to investigate the effect of axonal beading (H.-H. Lee et al., 2020a; Lundell et al., 2021). Grey matter on the other hand contains a variety of different cell types that require more accurate 3D modelling (Jelescu et al., 2020). This is the origin of analytical models such as the ball-and-stick model (Behrens et al., 2003) or neurite orientation dispersion and density imaging (NODDI) by H. Zhang et al. (2012). Amongst cells of interest are astrocytic glial cells and some recent work has focused on generating realistic substrates and simulating their signal contributions (Palombo et al., 2019).

Berry et al. (2021, 2018) simulated a single block of muscle tissue and modified the substrate to consider different pathologies. Comparison with idealised cylinders was made and good agreement reported. While musculoskeletal tissue has similar cell sizes and shapes, the distinct myocardial sheetlet structure is not found here. As noted by Stephenson et al. (2016), the two (skeletal and cardiac) musculatures should not be treated as analogous.

While simulations of diffusion by means of Monte Carlo random walk or continuum methods are popular in neuroimaging, there are not many simulation works considering DT-CMR in the literature. Wang et al. (2011) were the first to create a Monte Carlo random walk model of the myocardium, using parallel hexagonal myocytes. This was followed by a model of dispersed circular cylinders (Wang et al., 2012) and a simulation of voxels in a whole heart model at different stages in the cardiac cycle (Wang et al., 2014). Bates et al. (2017) built on this to carry out simulations of cuboidal cells with transmural rotation. Recent work by Moulin et al. (2020b) investigated the sensitivity of diffusion encoding waveforms to ECV by using a simplified grid of circular cylinders as cells. Below describes work to generate a more complex and realistic substrate (Rose et al., 2019c).

2.3.4 From histology images to a realistic substrate

Figure 2.9 illustrates the proposed workflow: A block of tissue (A) is cut and subsequently imaged (B). A representative region is segmented (C) and each cardiomyocyte extruded (D) into a building block (E). The full substrate (F) is then composed of transformed copies of this block. Each of these steps is now described in more detail:

A large set of wide-field microscopy images were obtained from the hearts of 30 kg Yorkshire pigs with ventricular mass of 88 g (Nielles-Vallespin et al., 2017). Prior to excision, the hearts were arrested in a contracted (systolic-like) state using barium chloride. A transmural block of tissue from the mid-myocardium was excised and subsequently fixed.

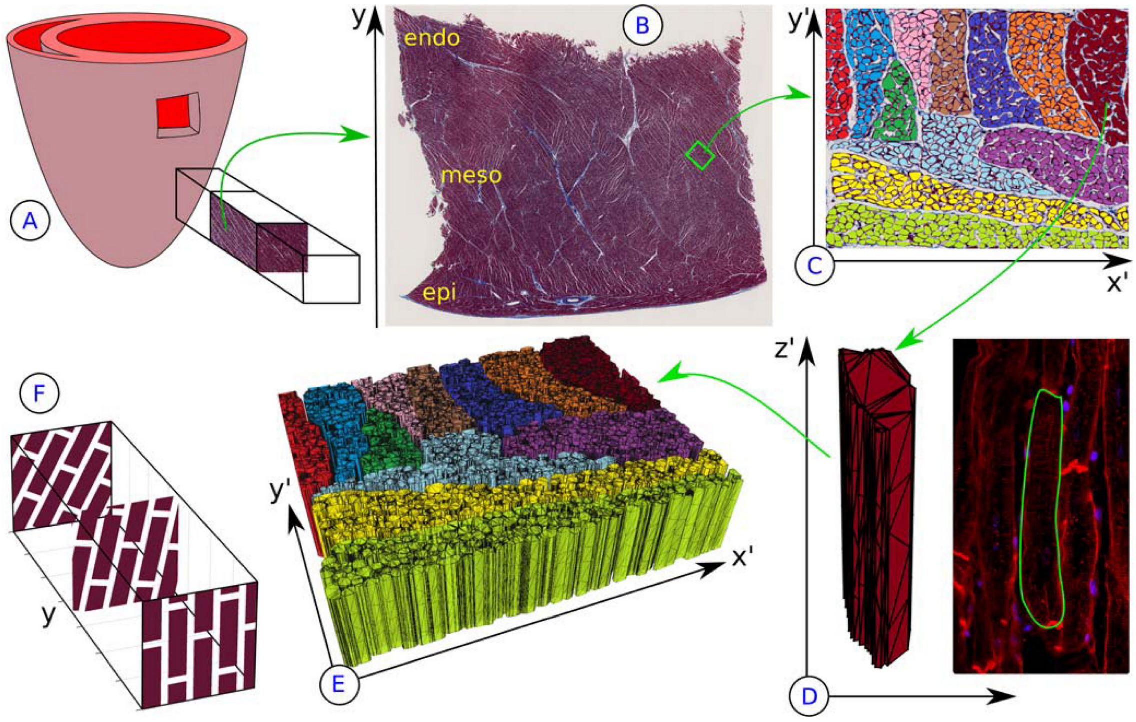

Figure 2.9: Proposed workflow for building a virtual model of myocardial tissue. **(A–B)** A transmural tissue block is cut from the heart and imaged using wide-field microscopy. **(C)** Manual segmentation produces a pixel mask of cardiomyocytes, coloured by sheetlet. **(D–E)** Each myocyte is extruded along the image-normal direction (compare a confocal microscopy image) to form a 3D block. **(F)** This block is repeated and transformed to fill an imaging voxel. Each purple rectangle shows the $x'z'$ plane of the block in (E), with the longer side the x'-axis. Note that the gaps between blocks have been exaggerated. [*Reproduced with permissions from (Rose et al., 2019c).*]

The block was cryosectioned while cutting along the short axis, creating non-contiguous slices of thickness 10 mm spaced approximately 100 mm apart. The tissue was stained with Masson's trichrome, which colours the cardiomyocytes red/purple, collagen blue, and nuclei black. Imaging was done with a magnification of 20× at a resolution of 456 nm/px using a Hamamatsu NanoZoomer slide scanner.

The gold standard for labelling histology images is manual segmentation. This is a time-intensive process—other options are discussed below in section 2.4. A small block of $500 \times 400\,\mu\text{m}^2$ from the mesocardium in a mid-myocardial slice was selected as region of interest (ROI). Through inspection this ROI was chosen as being representative of the surrounding tissue. In total 1182 cardiomyocytes were manually labelled and grouped into 12 sheetlets. The data for this is made available, see appendix B.2.2.

Each segmented cardiomyocyte in the ROI is represented as a polygon. They are extruded by random lengths perpendicular to the imaging plane. These lengths are drawn from a normal distribution with mean $\mu_L = 120\,\mu\text{m}$ and standard deviation σ_L equal to $\pm 5\,\%$ of μ_L. This results in the 3D tissue block seen in figure 2.9 (E). The entire imaging voxel is filled with transformed copies of this block. For a given transmural (y) location, the blocks are stacked like masonry in the z-direction: every other row along x is offset by half a block width (block size in x). Every new row of blocks in y is rotated, with respect to the previous row of blocks, by ≈10 °/mm around the y-axis. This approximates the continuous transmural rotation found in the myocardium (Streeter et al., 1969).

2.3.5 Differences between ex-vivo histology and in-vivo tissue

The labelling method of choice for the histology images was manual segmentation, which remains the gold standard for tissue classification. By overlaying the resulting label on top of the histology image, one can appreciate that the individual cell masks are generally smaller than the tissue. This is due to several factors, including limited microscope resolution and user error (conservative manual edge detection), and could be addressed with additional resources and labour. However, the effect of this is most likely small compared to the more significant differences between in-vivo tissue and ex-vivo histology:

Fixation, which is essential for preparing the tissue for histological analysis, causes tissue shrinkage. As a result, the size of cardiomyocytes seen in the microscopy images is expected to be smaller. However, the exact mechanism of this is unknown. This leads to an unrealistically high extra-cellular volume fraction. Typical values of ECV should be 20 to 30 % as discussed in section 2.3.1. The initial segmentation on the other hand has an ECV in excess of 40 %. In addition to this, sectioning of the tissue blocks may have distorted the extra-cellular and especially the intra-sheetlet space. This could have led to a widening of the shear layers, although the magnitude of this effect is not known at this point.

Here, a method is proposed to correct for the errors resulting from both conservative segmentation and tissue shrinkage. It involves morphing the segmentation mask progressively until a desired ECV is achieved. This also allows for the simulation of pathologies that present with a change in ECV, although this application is not the focus of this present work.

A custom MATLAB code (appendix B.1.1) operates directly on the binary segmentation masks. These images have value 1 (`true`) for ICS and 0 (`false`) for ECS. Each region of 4-connected[‡] pixels is considered to be an individual cardiomyocyte. This allows neighbouring cardiomyocytes to touch diagonally at the corners of pixels. Two types of operations can be performed: morphological thickening and shrinking, executed using the MATLAB routine `bwmorph`. They are described in the following. The thickening operations add additional ICS pixels to the ECS around each existing ICS region until doing so would cause two regions to become 4-connected. It was chosen to keep the sheetlet boundaries fixed in this work, but morphing operations for sheetlets can easily be implemented in the existing

---

[‡] Only touching at their edges, i.e. direct neighbours in pixel coordinates.

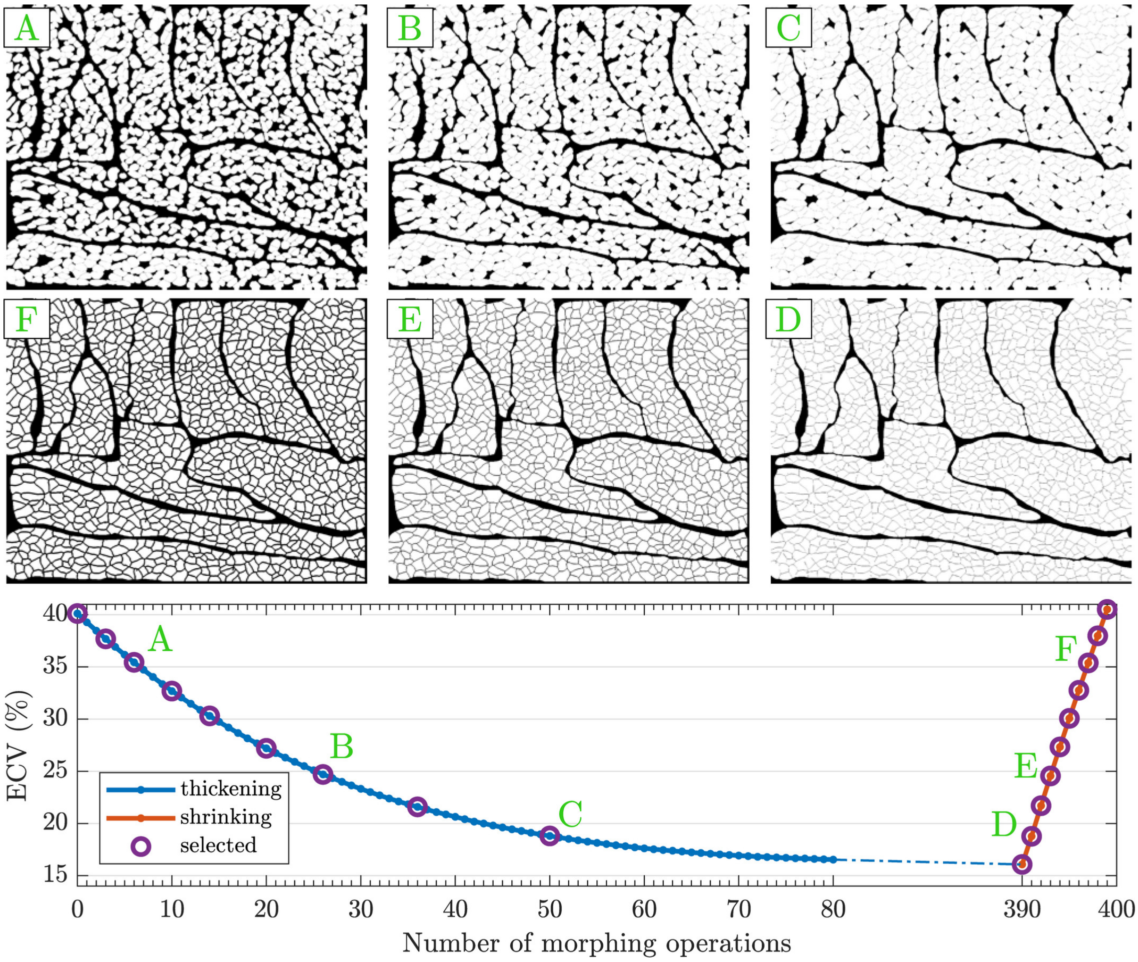

Figure 2.10: Change in extra-cellular volume fraction (ECV) due to morphing of the cardiomyocyte segmentation mask. Starting at an ECV of >40 %, progressive thickening **(A–C)** of the intra-cellular space (ICS) reduces ECV until the minimum is reached after 390 iterations. From here, ECV increases through shrinking of ICS **(D–F)**. Selected points (purple circles) are used as substrates for simulations. [*Reproduced with permission from (Rose et al., 2019c).*]

algorithm. Cardiomyocytes that grow past their assigned sheetlet are truncated to this boundary. The shrinking operations remove pixels from the outside of each ICS region to shrink the region towards a point. This is unlike morphological thinning, which reduces the region to a line, and erosion, which can lead to complete loss of pixels with a sufficient number of iterations. Before each shrinking operation, the image needs to be split into a stack of smaller images around each of these individual regions of pixels (cardiomyocytes).

The resulting change in ECV can be seen in figure 2.10. After starting at a high initial ECV of over 40 %, the thickening operations reduce ECV progressively. After 43 iterations ECV has dropped to below 20 %. Morphing of the image continues until reaching the point of minimum ECV after 390 operations. Here, the gaps between cells are minimal and the shear layers account for almost all of the ECS.

Increasing ECV from this point does not invert the operations performed before. The cardiomyocytes are shrunk using the process described above. It can be observed from figure 2.10 how the ECV increases rapidly. The extra-cellular space is growing uniformly everywhere, which leads to a similar ECV but less realistic extra-cellular space without the characteristic larger and smaller pools of ECS. After 3 iterations the ECV has increased from the minimum of 15.1 % to almost 25 %. It only takes a total of 9 iterations to increase ECV back to 40 %.

All morphed binary images (including an animation of the morphing process) and the corresponding extruded tissue blocks are made available, see appendix B.1.1.

2.4 Segmentation of histology images

Moving from step (B) to (C) in figure 2.9 requires the labelling of the histology image. Previously manual segmentation was used, which is time consuming and becomes unfeasible as the size of the ROI increases to more than a few thousand cells. In this section the focus is on automatic ways to achieve a comparable result. Note that the description of the methods is kept brief since this is preliminary and ongoing work that is not the focus of this thesis. The methods are mentioned here for completeness and to encourage future work, because a successful implementation may allow for histological analysis at a much larger scale and thus more realistic simulation substrates.

2.4.1 Automatic classification with deep learning

Image labelling or classification is traditionally very suitable for machine learning (ML) applications, specifically deep learning (DL). For an in-depth review of the theory behind ML/DL, particularly in the context of (medical) image analysis, the reader is directed to the book by Zhou et al. (2017). Few references to segmentation of myocardial tissue at a cellular level can be found in literature. One attempt was by Nirschl et al. (2017), whose results are encouraging but lack the detailed segmentation of individual cardiomyocytes that are required as a basis for simulation substrates.

The U-Net (Ronneberger et al., 2015) network architecture, a type of convolutional neural network (CNN), was implemented in the TensorFlow framework (Google Inc et al., 2021). The chosen implementation only allows for two classes of objects for segmentation: ICS and ECS. Through iterative testing, the optimal parameter set for training was determined: 4 network layers and 16 features. Two networks were trained, one based on RGB (colour) and one on BW (greyscale) images, and they both used on-the-fly data augmentation to increase the size of the training data set. After inference, a confidence map is produced where values from 0 to 1 indicate the likelihood of a given pixel being ICS. This confidence map is thresholded to a value of 0.95. The individual cardiomyocytes

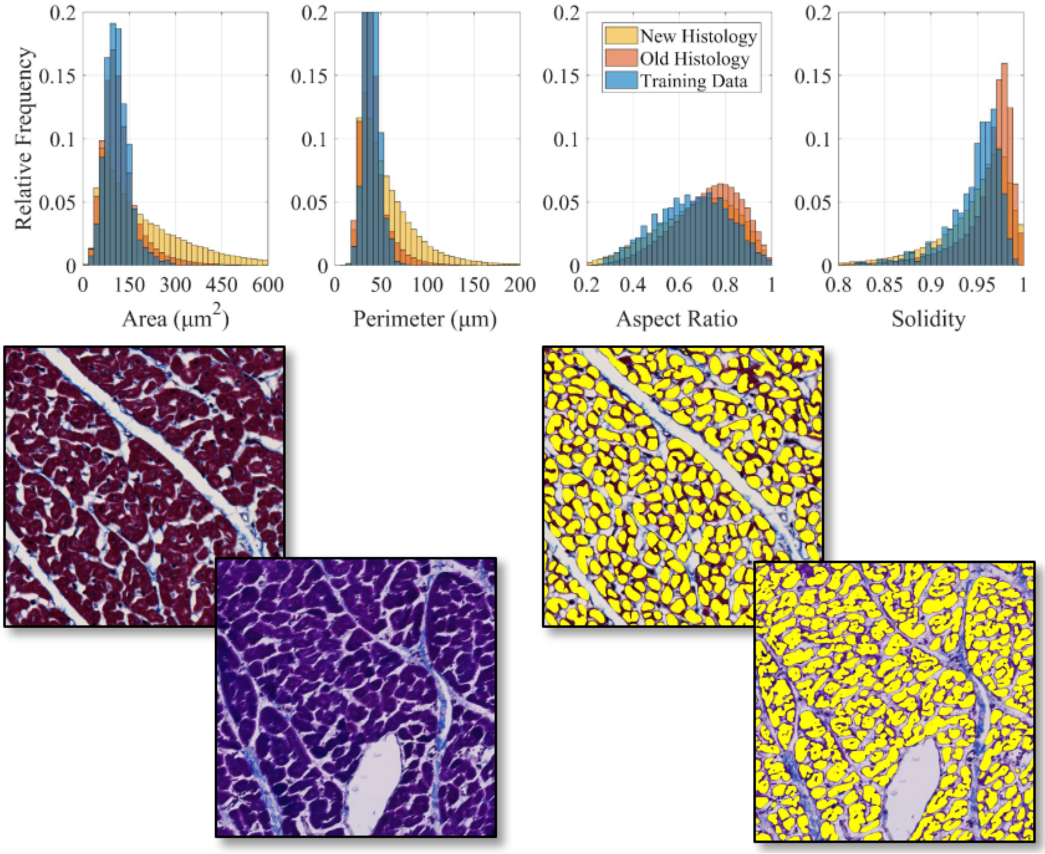

Figure 2.11: Result of automatic segmentation with U-Net. Two populations of histology data were used for inference: The “Old” one stems from the same population as the “Training” data, while the “New” one uses a slightly different staining and imaging protocol. The segmentation masks were processed to extract contiguous regions of ICS (cardiomyocytes), whose size and shape parameters are plotted in the histograms. [*Parts of this figure were presented in (Rose et al., 2018c,f).*]

then need to be extracted via post-processing. Objects that are too small and most likely noise are discarded from the image mask output by U-Net. Furthermore, the image is cleaned by removing any spurious pixels.

The manual segmentation in figure 2.9 (C) serves as training data. The image was tiled into $100 \times 100\,\text{px}^2$ blocks with a $10\,\%$ overlap. For inference, two histology data sets are used: one from the same set as the training data, whose acquisition was described in section 2.3.4; the other set was obtained using a similar protocol at a different site. The unprocessed data set containing raw images and inference results is made available, see appendix B.1.2. The difference between these, primarily in the staining, can be seen in figure 2.11. The figure also shows the inferred segmentation overlaid with the histology. The network performs reasonably well on the original histology data set. It can also be observed from figure 2.11 that the histograms for cardiomyocyte area and perimeter matches well. The trained network does not however transfer to the new histology images. This is due to the strong difference in underlying image and lack of generality of the trained network. The histograms show that the tail of the distribution of areas and perimeters is larger for this new histology data set, which supports the observation that a lot of neighbouring cells are grouped together. Attempts were made to use additional data augmentation techniques such as rotation, shear, scaling, and colour changes in the training data, but at this point the inference only produces a result that is at best as good as a thresholding result.

In their paper, Ronneberger et al. (2015) report good results based on a small training data set for touching cells. However, the major difference is that Ronneberger et al. inserted background pixels between touching objects and implemented a weighted loss function to penalise undesirable merging of neighbouring objects. So far this has only lead to anecdotal success, but future investigation is warranted. The lack of a large high-quality training data set from diverse sources is a big obstacle to successful implementation of a DL method. A promising area for future investigation may be the use of a region-based convolutional neural network (R-CNN) (Fujita et al., 2020). One weakness of U-Net is that it can only identify pixels and assign them to classes, in this case ICS and ECS. R-CNNs have the capability of identifying individual *objects* of a given class, which might help with neighbouring and touching or even overlapping cells.

This work was carried out in collaboration with Wee Zhao Chua Khoo and has been published (Rose et al., 2018c,f); in this joint work, the methods described above are presented. The specific contributions to this thesis were the large-scale inference computations, post-processing of the data, and interpretation of the results.

2.4.2 Labelling through image processing techniques

Due to the unreliable results achieved in section 2.4.1, tools based on classical image processing techniques were also developed. Image segmentation is a common task when processing biological images (Semmlow, 2004). Figure 2.12 presents the workflow of processing steps as a pipeline. Recall that the Masson's trichrome used for the histology images stains collagen (blue), nuclei (black), and ICS (red/purple), while the ECS remains transparent (white). The different colour channels and their intensities contain rich information that can be extracted through thresholding. Regions of interest are the ICS and ECS, but also specifically collagen as a subset of ECS since it serves as a barrier between ICS and ECS, as well as nuclei which are found inside[§] the ICS. The thresholded ICS mask undergoes a series of other operations intended to transform the segmentation into a binary image of individual cardiomyocytes. Dilation serves the purpose of cleaning

---

[§] Some nuclei of other cell types that are not cardiomyocytes exist in ECS, and cardiomyocyte nuclei may have left the confines of the cells as a result of damage from sectioning.

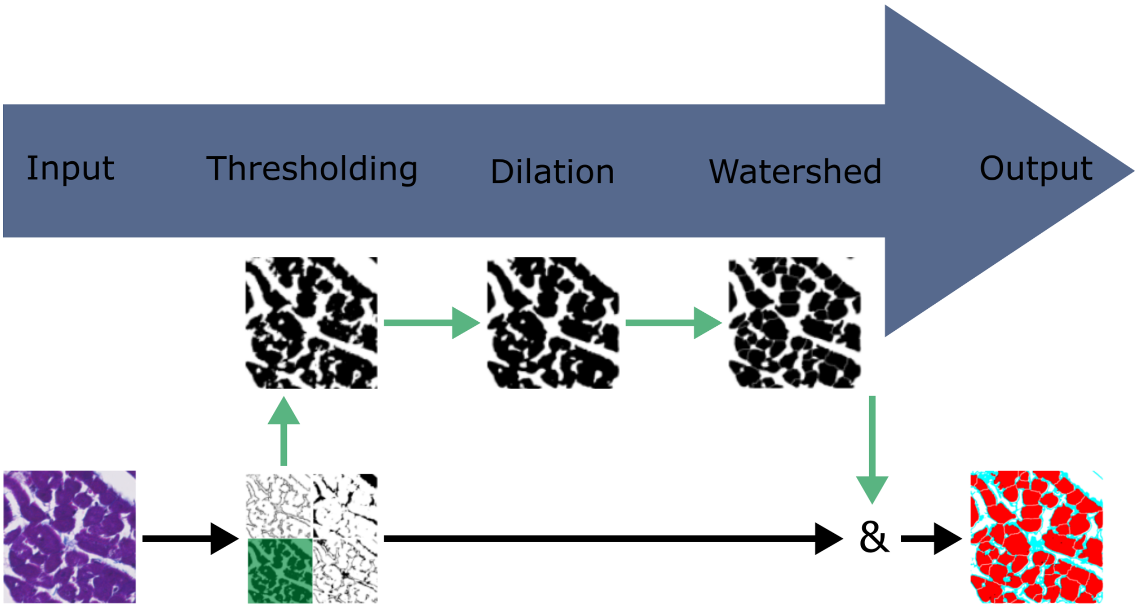

Figure 2.12: Image processing pipeline for segmentation of myocardial tissue features. The input image is first thresholded to obtain four masks based on different combinations of colour channels. This is followed by a dilation step. A watershed algorithm splits large blocks of contiguous pixels. Finally, the different masks are combined to create the segmentation result.

up the noisy thresholding result, while the watershed algorithm attempts to find and enforce cell boundaries based on the shape of the region boundaries.

An example result can be seen in figure 2.13. Overall, the algorithm produces a result consistent with the appearance of the original histology. Further processing may be necessary to convert the output to a suitable format for use in a simulation substrate. For example, holes in myocytes need to be filled and surfaces may require smoothing before extracting the bounding polygons. In the future, the methods presented here may be combined with other techniques. The use of structure tensor analysis has shown promising results for use in edge detection (Khor, 2020; Köthe, 2003).

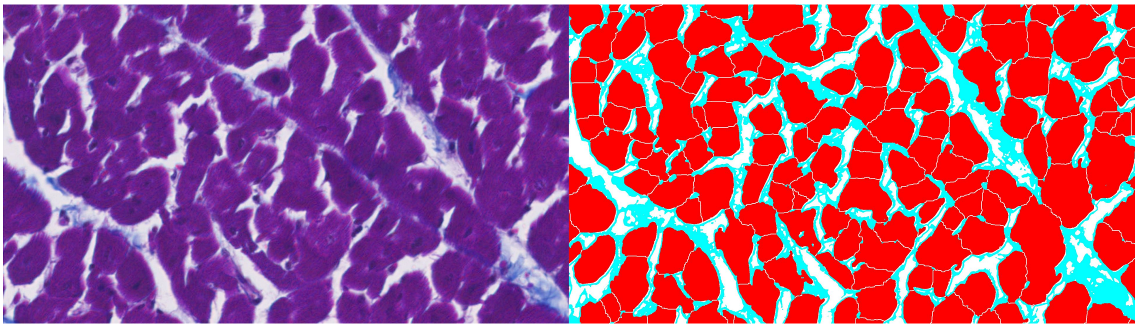

Figure 2.13: Example result of the image processing pipeline, showing the original image **(Left)** and the output masks **(Right)**. Intra-cellular space (ICS) is red, extra-cellular space (ECS) is white, and collagen is cyan (which may be combined with ECS).

This work was carried out in collaboration with Lukasz Sliwinski and has been published (Rose et al., 2019d); in this joint work, the method presented above is applied and the output is directly used as a substrate for numerical simulations of diffusion.

2.5 Synthesising a microstructure

The process described in the previous sections involves constructing a substrate directly from microscopy images, either by manual or automatic segmentation. Using the methods from section 2.3.5, the resulting cardiomyocyte masks can even be modified by means of morphing operations to account for e.g. tissue shrinkage or to simulate underlying pathologies. However, the reliance on a high-quality microscopy image makes this process cumbersome and slow. If one wanted to investigate a large amount of different microstructures in a parameter study, the substrates need to be synthesised.

2.5.1 Drawing inspiration from neuroimaging

The recent rise in popularity of diffusion simulations in the field of neuroimaging has come with advances in the (semi-)automatic generation of models of various brain tissues. To the knowledge of the author, Panagiotaki et al. (2010) were the first to present 3D simulations using high-fidelity meshes, which they constructed directly from segmented tissue samples. This process is very time consuming as it requires acquisition and processing of confocal microscopy images. Mingasson et al. (2017) solved this problem by introducing AxonPacking, a tool for simulating the packing of circles into dense arrangements. This allowed the user to synthesise white matter substrates, which consist primarily of tightly packed axons that are often modelled as being circular in cross-section. Others (R. Callaghan et al., 2020, 2019; Ginsburger et al., 2019) generated three-dimensional numerical phantoms of white matter by “growing” axons in silico. Palombo et al. (2019) have developed a model to generate various types of brain cells in grey matter, including neurons and glia, by relying on the tree-like skeletonised structure of such cellular networks.

2.5.2 A new packing algorithm for cardiac cells

Packing objects densely is a difficult optimisation problem and has many applications. Dense usually means efficient, e.g. filling a cargo container by maximising the number of objects per space, minimising the material used for construction of cell walls in a honeycomb. Industrial applications are usually limited to 2D and/or simplified shapes such as cuboids, which presents a well-defined problem suitable for mathematical analysis (Dyckhoff, 1990). In general, however, packing arbitrary objects is computationally intensive and has no guarantee of convergence. Often the best or only suitable algorithm involves rejection sampling, where objects are placed repeatedly until the space is filled to a sufficient degree.

This relies on a nearly infinite supply of objects of all sizes and shapes because, otherwise, the gaps that randomly appear between objects may not be able to accommodate any of the available shapes in the library.

Section 2.2 has shown that myocardial tissue is well-approximated as being 2.5-D. Cardiomyocytes are almost cylindrical (compare figure 2.5) and they are packed nearly parallel and relatively densely. This simplifies the problem to packing cell cross-sections in 2D and extruding them to build the 3D substrate, as was done in section 2.3.4. To achieve this, a novel method (Rose et al., 2021b) is presented to rigidly pack polygons into a dense arrangement and allow for additional control of the spacing between them. This improves upon the work by Mingasson et al. (2017), which only packed circular discs. While the latter is computationally more efficient, the circular shape that is a good approximation in neuroimaging fails to represent real myocyte shapes which are circular only in the idealised case.

Histology-accurate geometries are achieved by taking a hierarchical approach: Instead of packing the entire ROI with myocytes, the proposed method fills the space with sheetlets, either deterministically/rule-based or through packing, and then packs these sheetlets with myocytes. The irregular pools of ECS within sheetlets are modelled by inclusion of "ghost" cells. These objects are included in the packing simulation but treated as ECS during post-processing. By choosing an appropriate size and shape, some control is possible over how many of these pools will likely occur in the final packing. A minimum spacing between objects is also ensured by assigning a buffer region of width d around their perimeters, which is done by inflating them before the packing simulation. During post-processing the objects are reverted to their original shape.

Polygons are represented as a list of vertices, using the Shapely library (Adair et al., 2021) which provides an extensive set of methods to operate on polygons. At the beginning of the simulation, the N polygons are placed in a lattice centred around the target region. The grid spacing is chosen as a multiple of the largest bounding dimension of any polygon. The grid aspect ratio should match that of the target region to accelerate convergence in the final stages of the packing simulation. Every time step the objects move towards the origin with an attraction velocity $\boldsymbol{u}_{\text{att}}$. If any of them intersect, no attraction takes place for these objects but instead they repel each other with a repulsion velocity $\boldsymbol{u}_{\text{rep}}$. Each object's repulsion direction is the normalised sum of the vectors pointing from their intersected objects' centres to its own centre. This is illustrated in figure 2.14. The implementation details of the algorithm can be found in the source code, see appendix B.1.3.

The code is accelerated through the use of bounding circles. At the start the centre of the polygon $\boldsymbol{x}_0$, defined here as the centre of the axis-aligned bounding box, needs to be determined. The radius of the bounding circle is the maximum Euclidean distance of all vertices to this centre. During the simulation, only this position $\boldsymbol{x}_0$ is updated. The

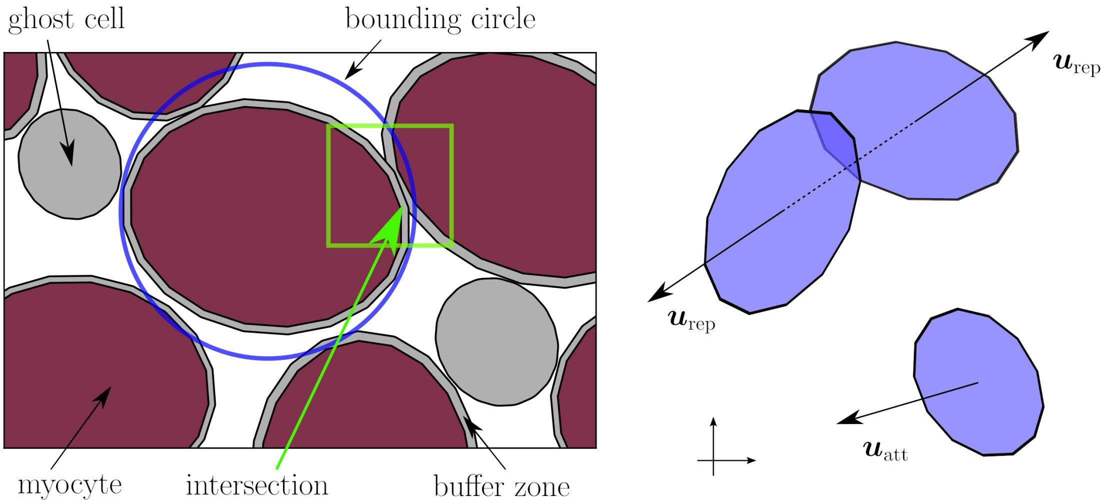

Figure 2.14: Schematic explanation of the packing algorithm. **(Left)** Snapshot of a packing simulation: Purple polygons are cardiomyocytes, the grey regions are the buffer zones, and ghost cells are also coloured grey. Each polygon has a bounding circle around it to quickly identify if any pair of polygons may intersect. **(Right)** All objects converge towards the origin with attraction velocity $\boldsymbol{u}_{\mathrm{att}}$, unless they are intersecting with another object. In that case, they repel each other along the axis connecting their centres with repulsion velocity $\boldsymbol{u}_{\mathrm{rep}}$.

pairwise sums of object radii are pre-computed once and used to determine if two objects (i and j) with centre positions $\boldsymbol{x}_0^i$ and $\boldsymbol{x}_0^j$ are close enough to warrant polygon intersection checking. This computationally inexpensive method is similar to the implementation in AxonPacking (Mingasson et al., 2017), based on the original method by Donev et al. (2005). It allows for an easy and efficient collision rejection check, since it is expected that most polygons will be too far apart to intersect. The problem of rejecting these is now reduced to computing the Euclidean norm between the two centres and comparing it to the sum of (bounding circle) radii.

There is no requirement on the shape or number of vertices for the cells, for example they may be drawn from a library of cell-like shapes such as the ones obtained in section 2.3.4 or section 2.4. For simplicity, one could also generate all of them to be of a similar shape with random parameters, drawn to fit a target distribution. An optional target region (e.g. the sheetlet that is to be packed) is also specified as a polygon.

Packing simulations can vary widely in runtime depending on many factors. Consider N objects with each (or an average of) M vertices. The cost of checking which bounding circles overlap is constant every time step since it relies on the same matrix algebra irrespective of the positions of the circle centres, but scales with $\mathcal{O}(N^2)$. Calculating the intersection between the candidate polygons then scales with $\mathcal{O}(N^2)$ for a fixed cost per pair of polygons. The Shapely library calls methods in GEOS (Davis et al., 2021) internally. A worst case implementation for concave polygons would scale with $\mathcal{O}(M^2)$ as more vertices are used. More efficient techniques are possible, but reference to the original

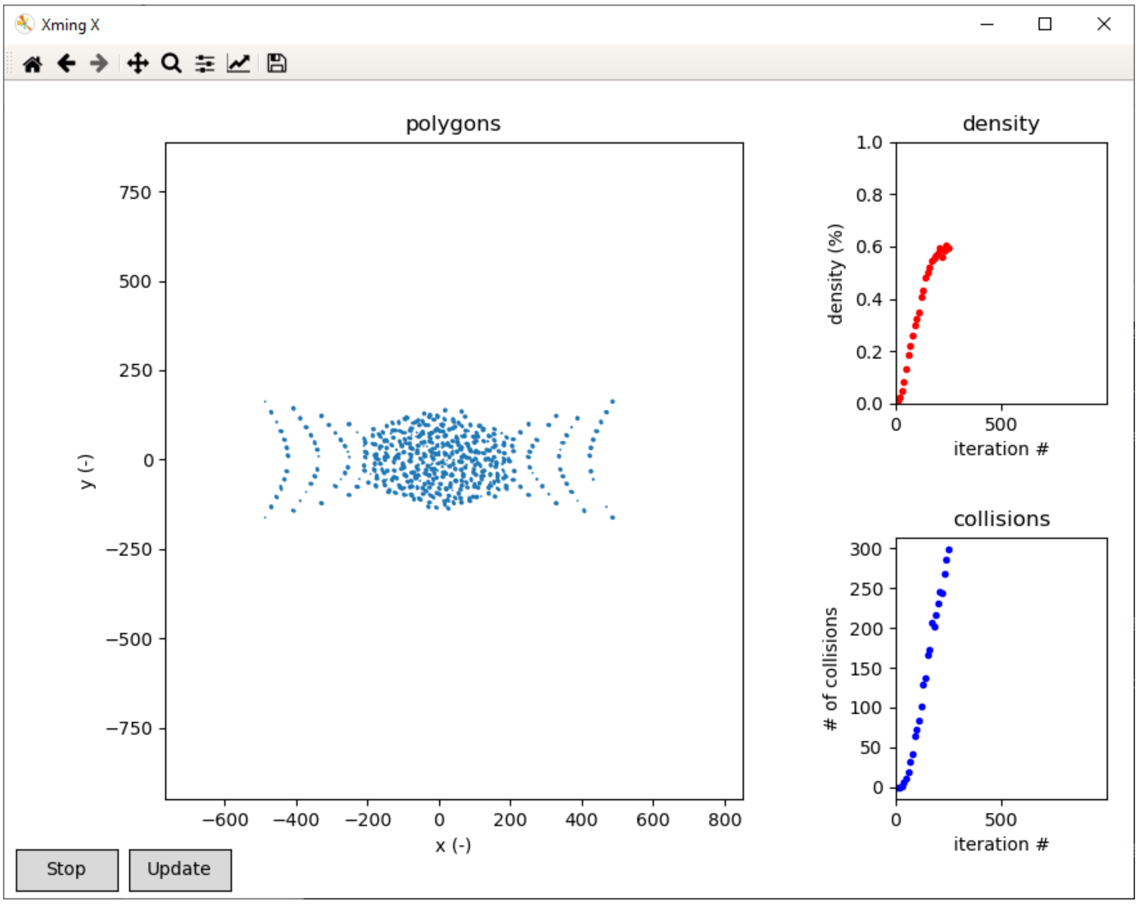

Figure 2.15: Graphical user interface (GUI) for the packing simulation. The figure on the left directly plots the polygons at their positions throughout the simulation. On the right side, two plots show the changing cell density (ECV) in the target region and the number of collisions recorded during a time step. The "Stop" control buttons allow manual termination if a desirable state is achieved. Because plotting significantly slows down the simulation, updates can be limited to occur every n time steps, which can be overridden with the "Update" button.

underlying source code would be needed to determine whether any such techniques have been implemented.

The state of convergence of the simulation can be assessed based on two metrics: the density in the target region and the number of collisions. As more cells aggregate near the origin, the density will increase and eventually reach a plateau. Note that this may not correspond to the desired (corresponding) ECV, which depends on or may be augmented by the amount and size of the ghost cells. The collision counter cannot give direct insights into the state of the simulation but allows estimation of remaining simulation time.

A graphical user interface (GUI) enables the user to interact with the simulation. As shown in figure 2.15 it allows for passive monitoring of the progress as well as premature termination if the simulation is deemed to have reached convergence. Future work is recommended to allow interactive adjustment of the velocity magnitudes u_{att} and u_{rep}. At the current stage, these must be determined a-priori. Although they do not need to be constant throughout the simulation, selecting an appropriate set of parameters and time points is iterative and inefficient by nature. Additionally, dynamic adjustment based on certain metrics similar to the convergence criteria may allow for unsupervised simulations.

2.5.3 Applying the packing algorithm

Packing of cardiomyocytes into sheetlets

Cardiomyocytes are generated as ellipses that match the size and shape distributions found in figure 2.11 and their orientation is uniformly sampled from $[0, 2\pi)$. Using ellipses has the advantage of denser packing than with more awkwardly shaped cells that have protruding edges. Ellipses can also be represented accurately using fewer vertices.

Three regimes are defined: First, a relatively large velocity is prescribed to quickly move the objects towards the centre. Then, a moderate velocity corresponding to a displacement of less than $5\,\%$ of the average bounding radius is used. This allows the objects near the origin to come close enough to each other to pack effectively. For these two cases the attraction velocity magnitude is set to be twice the repulsion velocity, i.e. $u_{\mathrm{att}} = 2u_{\mathrm{rep}}$. Finally, when the target ECV has been reached, the attraction velocity is set to zero and u_{rep} is reduced to a very small value that allows the objects to “wiggle” into place and resolve most remaining intersections.

The resulting packing can be seen in figure 2.16. It shows good visual agreement between the synthesised sheetlet and the one based on histology, both in terms of ECV and distribution of ECS. Thanks to the use of a buffer zone around each cell and the final repulsion steps, the post-processed objects do not overlap.

Packing of sheetlets

To generate a simulation substrate of a size corresponding to an imaging voxel, sheetlet objects can be packed together using the same algorithm as described above. The sheetlet objects are constructed randomly as highly eccentric ellipses, however rounded rectangles would also be appropriate. The simplest and easiest-to-pack configuration consists of polygons with parallel major axes. Based on histological data, their thickness should equal several cardiomyocyte diameters. An example tissue is shown in the wide-field microscopy in figure 2.17. The histology is taken from systolic-like tissue, which shows the shear layers as large gaps. An example of an automatic packing is also shown in the figure. Due to the difficulty of packing these rigid objects, the resulting ECV is much larger than expected. To account for this, the sheetlet objects are thickened using the algorithm from section 2.3.5.

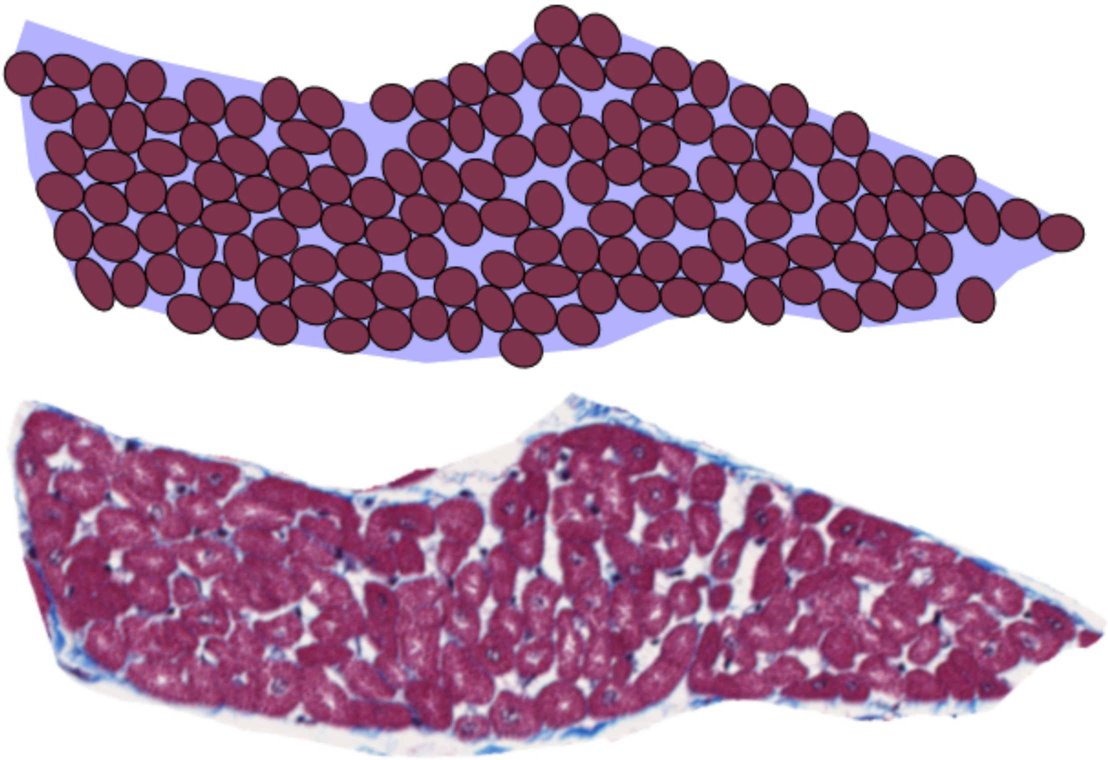

Figure 2.16: Myocyte packing result **(Top)** compared with the histology image of the target sheetlet **(Bottom)**. Good agreement is found between the two sheetlet geometries in terms of both overall ECV as well as distribution of ECS.

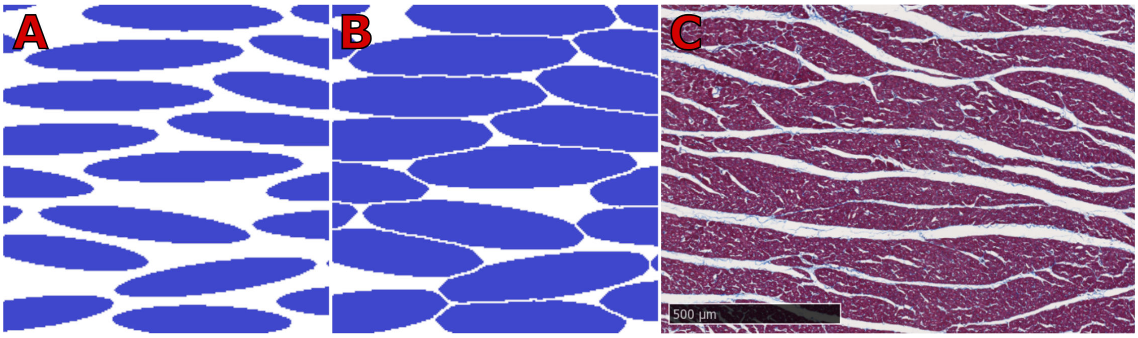

Figure 2.17: Sheetlet packing result **(A–B)** compared with a histology image **(C)** that serves as the desired outcome. **(A)** shows the original output of the packing simulation. The resulting sheetlet polygons were then thickened to create the objects in **(B)**.

2.6 Discussion

This chapter reviewed the myocardial microstructure and presented methods to construct a virtual model of myocardial tissue. Key components were identified and the myocardium subsequently reduced to two distinct compartments: intra-cellular space (ICS) and extra-cellular space (ECS). These compartments are modelled as regions Ω with respective bulk diffusion coefficients D_0. Their infinitely-thin boundaries Γ represent the cell membranes, to which a constant permeability κ can be assigned.

An accurate model of the myocardium is essential for numerical simulations of diffusion in silico. The substrate constructed in this chapter is histology-based and several critical steps were taken to construct a three-dimensional model that includes features like transmural rotation of fibres and realistic distribution of extra-cellular space (ECS).

However, the model still has some limitations: Due to the size of the ROI of a manually segmented microscopy image, the substrate at the size of a DT-CMR imaging voxel is represented by a tissue building block that is replicated and transformed to fill the domain (see section 2.3.4). The geometry also does not include complex cardiomyocyte shapes or their branching. These effects are however expected to be small compared to the prohibitive effort of accounting for such detail at this stage. Instead, cardiomyocytes are assumed to be cylinders with arbitrary cross-sections. These cylinders, represented as triangulated polyhedra, are parallel within the ROI and their orientation changes with every copy of the ROI in the transmural direction.

The deep learning–based methods developed in this work may eventually make possible the automatic segmentation of cardiomyocytes in large-scale microscopy images. However, only a small set of manually annotated histology images was available for use as training data, so the present implementation has shown mixed success. Alternatively, classical image processing techniques allow for processing of microscopy slices from new data sets that have not been annotated. Black box approaches using existing automatic tools, such as ilastik (S. Berg et al., 2019), have been used successfully by Wilson et al. (2021). Finally, a simulation tool was proposed to synthesise a dense packing of cardiomyocytes, represented as arbitrary polygons. All of these methods are currently still limited to 2D.

In the future, extension of these automatic methods to 3D is desirable. For example, the 2D sheetlets can be packed on several parallel planes in the image-normal direction and lofted together. Generation of three-dimensional cardiomyocytes can then be achieved through 3D packing. Additionally the distribution of tissue parameters throughout the voxel and the myocardium needs to be considered. According to Campbell et al. (1987) and Gerdes et al. (1986), cardiomyocyte sizes differ depending on the location in the heart. A homogeneous model cannot be used when transitioning from simulations of a single voxel to many voxels, made necessary when comparison with in-vivo or ex-vivo DT-CMR imaging is desired for validation.

Chapter 3

Simulating Diffusion Tensor Imaging

Contents

3.1 Introduction

The aim of this chapter is to introduce a method of numerically simulating diffusion tensor imaging. First, a minimal but essential background of magnetic resonance imaging (MRI) is provided in section 3.2. Section 3.3 is dedicated to solving the governing equations efficiently using continuum methods and a GPU-based simulator. Finally, section 3.4 presents results of the simulator's performance and a simulation of diffusion-weighted signal.

3.2 Diffusion MRI physics

In this section no attempts are made to explain nuclear magnetic resonance (NMR). The textbook *Principles of Nuclear Magnetic Resonance Microscopy* by P. T. Callaghan (1993) offers an excellent introduction to the topic. Neither will there be any extensive discussions of the broad fields of diffusion magnetic resonance imaging (MRI) or diffusion tensor imaging (DTI). Instead, the section is focussed on providing an overview of the relevant governing equations necessary for developing and interpreting numerical simulations of diffusion MRI.

3.2.1 Nuclear magnetic resonance

The behaviour of ^{1}H spins is governed by the laws of quantum mechanics. Fortunately this description is not necessary to explain NMR and MRI, which are classical phenomena (Hanson, 2008). From here on spins are considered to be magnetisation vectors $\boldsymbol{m}$. The forthcoming equations take a macroscopic view and consider an ensemble of spins with a net magnetisation $\boldsymbol{M} = [\,M_x \quad M_y \quad M_z]$ and initial magnitude M_0.

The Bloch equations (3.1), developed by Bloch (1946), describe the evolution of magnetisation $\boldsymbol{M}(\boldsymbol{x}, t)$,

$$\frac{\partial \boldsymbol{M}}{\partial t} = \gamma \boldsymbol{M} \times \boldsymbol{B} - \left(\frac{M_x \hat{\boldsymbol{\imath}} + M_y \hat{\boldsymbol{\jmath}}}{T_2} + \frac{(M_z - M_0)\, \hat{\boldsymbol{k}}}{T_1} \right), \tag{3.1}$$

with magnetic field $\boldsymbol{B}(\boldsymbol{x}, t) = [\,B_x(\boldsymbol{x}, t) \quad B_y(\boldsymbol{x}, t) \quad B_0 + B_z(\boldsymbol{x}, t)]$. Here B_0 is the time-invariant field of the scanner and the $B_{\{x,y,z\}}(\boldsymbol{x}, t)$-terms account for RF pulses and magnetic field gradients $\boldsymbol{G}(t)$, which are used to interact with the spins. The equations also account for magnetisation decay due to T1 (transverse) and T2 (longitudinal) relaxation through their respective time constants T_1 and T_2. In this work magnetisation decay is not considered. For that special case of $T_1, T_2 \to \infty$, equation (3.1) recovers Lamor precession, where the angular velocity of the spins only depends on the local magnetic field strength and the gyromagnetic ratio γ of ^{1}H. As a result, the dynamics of magnetisation $\boldsymbol{M}$ are limited to the transverse plane and thus its components M_x and M_y only. This is often written in complex notation as $M_{xy} = M_x + \mathrm{i} M_y$.

Torrey (1956) extended equation (3.1) by adding a diffusion term. The resulting Bloch–Torrey equations

$$\frac{\partial \boldsymbol{M}}{\partial t} = \gamma \boldsymbol{M} \times \boldsymbol{B} - \left(\frac{M_x \hat{\boldsymbol{\imath}} + M_y \hat{\boldsymbol{\jmath}}}{T_2} + \frac{(M_z - M_0)\, \hat{\boldsymbol{k}}}{T_1} \right) + \boldsymbol{\nabla} \cdot (\mathbf{D} \boldsymbol{\nabla} \boldsymbol{M}) \tag{3.2}$$

consist of two parts: the original Bloch equations, which describe the magnetisation dynamics as a result of external influences; and the diffusion operator $\boldsymbol{\nabla} \cdot (\mathbf{D} \boldsymbol{\nabla})$, which models the transport of magnetisation as a result of the diffusion of ^{1}H in H_2O. The Bloch–Torrey equations can either be considered a vector equation* or alternatively three linked scalar equations for the three components of the magnetisation vector. The notation using $\boldsymbol{M}$ implies that the diffusion term operates on each component of $\boldsymbol{M}$ separately as it is a scalar operator.

3.2.2 Diffusion encoding

Through application of carefully designed pulse sequences with gradient waveform $\boldsymbol{G}(t)$, it is possible to make the NMR signal sensitive to intrinsic parameters of equation (3.2). The

---

*This requires rewriting of the relaxation terms using matrices.

shape of the waveform and timings and strengths of the RF pulses depend on the specific imaging requirements as described by Bernstein et al. (2004). In the absence of relaxation, equation (3.2) suggests that the only way to observe a loss of magnetisation is through diffusion. This is the basis for diffusion encoding, or diffusion weighted imaging (DWI).

Stejskal et al. (1965) were the first to propose this. After tipping a component of magnetisation into the transverse plane, application of two equal gradients separated by a 180° RF pulse causes an echo at time TE whose strength depends on the distance that spins have displaced between the two gradients. While the magnetic field gradient is active, the angular velocity of spins depends on their positions along the gradient direction. This imparts a phase gradient on the spins, which they retain when the gradient is switched off. For stationary spins, the second gradient reverses the phase offset imparted by the first gradient when the 180° rotation is accounted for. If a spin has moved during the diffusion time Δ between the two gradients, however, it will retain a net phase lag ϕ. The incoherent nature of diffusion means that the summation of the associated phases accrued results in a signal attenuation, A, which is measured in relation to the reference signal S_0:

$$A = \frac{S}{S_0} = \left|\langle \exp(\mathrm{i}\phi) \rangle\right| . \tag{3.3}$$

From this, the apparent diffusion coefficient (ADC, or D_{ADC}) in the imaging voxel can be inferred via

$$A = \exp(-bD_{\mathrm{ADC}}) , \tag{3.4}$$

where the b-value is a measure of the amount of diffusion weighting applied by the sequence (Le Bihan, 2010), defined through the following double-integral:

$$b = \gamma^2 \int_0^{\mathrm{TE}} \left[\int_0^t \boldsymbol{G}(\tau) \, \mathrm{d}\tau \right] \mathrm{d}t \tag{3.5}$$

The signal can also be interpreted as the Fourier transform of the averaged diffusion propagator U with wave number/vector $\boldsymbol{q} = \gamma\delta\boldsymbol{G}$:

$$S(t, q) = \int U(\boldsymbol{x}, t; \boldsymbol{x}_0) \exp(\mathrm{i}\boldsymbol{q}(t) \cdot \boldsymbol{x}(t)) \, \mathrm{d}\boldsymbol{x} \tag{3.6}$$

A more detailed explanation of the *Fundamentals of diffusion MRI physics* is presented by Kiselev (2017).

Basser et al. (1994) extended this concept to three dimensions by realising that the signal can be sensitised to diffusion along different directions inside the imaging voxel. This allows for the calculation of a diffusion tensor $\mathbf{D}$,

$$\mathbf{D} = \begin{bmatrix} D_{xx} & D_{xy} & D_{xz} \\ D_{yx} & D_{yy} & D_{yz} \\ D_{zx} & D_{zy} & D_{zz} \end{bmatrix} , \tag{3.7}$$

Table 3.1: Components of the normalised magnetic gradient vector $\boldsymbol{G} = [G_x \quad G_y \quad G_z]$ for six DT-CMR encoding directions. Non-collinearity between the gradient directions is required to reconstruct a diffusion tensor.

G_x	G_y	G_z
1	1	0
1	-1	0
1	0	1
1	0	-1
0	1	1
0	1	-1

which quantifies not only the amount of diffusion inside the voxel but also its "shape" and directionality. Through eigendecomposition, the eigenvalues $\lambda_{1,2,3}$ and corresponding eigenvectors $\boldsymbol{e}_{1,2,3}$ are found. Common metrics for quantifying the diffusion tensor are the mean diffusivity (MD),

$$\mathrm{MD} = \langle \lambda \rangle = \mathrm{trace}(\mathbf{D})/3 = \frac{\sum_i \lambda_i}{3}\,, \tag{3.8}$$

and the fractional anisotropy (FA),

$$\mathrm{FA} = \sqrt{\frac{3}{2}\frac{\sum_i (\lambda_i - \langle\lambda\rangle)^2}{\sum_i \lambda_i^2}}\,. \tag{3.9}$$

The mathematics of this are reviewed by Kingsley (2006a,b,c). The diffusion tensor is often visualised using superquadric glyphs (Ennis et al., 2005; Kindlmann, 2004).

The diffusion tensor is symmetric, i.e. $D_{ij} = D_{ji}$, resulting in 6 unique apparent diffusivities. Instead of the single b-value in equation (3.4), measuring in at least 6 orthogonal directions (plus one reference measurement of S_0) is required, resulting in the $\mathbf{b}$-tensor (Kingsley, 2006a,b,c). Table 3.1 shows the 6 gradient directions used in this work. By least squares fitting or other inversion methods, equation (3.10)

$$A = \exp(-\sum_i \sum_j \mathbf{b}_{ij}\mathbf{D}_{ij}) \tag{3.10}$$

can be solved to provides the diffusion tensor $\mathbf{D}$. This method, diffusion tensor imaging (DTI), has reached maturity in neuroimaging, where it is widely used for determining white matter pathways (Le Bihan et al., 2012), and has gained recent popularity in the heart, where it is called diffusion tensor cardiovascular magnetic resonance (DT-CMR). Please consult the textbook *Diffusion MRI* by Jones (2010) for an excellent treatment of DTI.

Three pulse sequences typical for DT-CMR are considered in this work: the classical Stejskal–Tanner pulse gradient spin echo (PGSE) sequence (Stejskal et al., 1965); the motion-compensated spin echo (MCSE) sequence, particularly the second-order motion-compensated sequence (M2-SE) presented by Welsh et al. (2015); and the stimulated echo

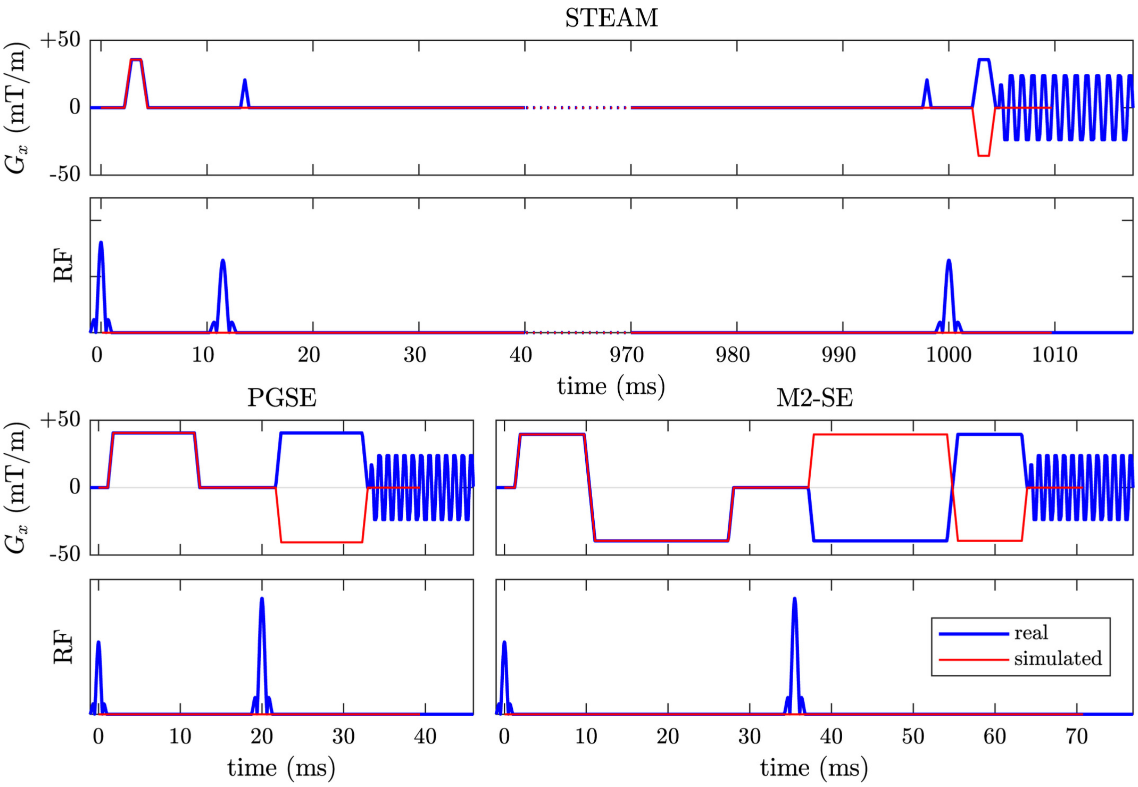

Figure 3.1: Comparison of three actual ("real") and idealised ("simulated") pulse sequences used in this work. The gradient waveform G_x is plotted together with any RF pulses for the sequence types: PGSE, M2-SE, and STEAM. The single 180° pulse (PGSE, M2-SE) and the two 90° pulses (STEAM) are simulated by inverting the polarity of the subsequent gradient(s). [*Reproduced with permission from (Rose et al., 2019c).*]

acquisition mode (STEAM) sequence (Reese et al., 1995). They are all shown in figure 3.1. Only idealised sequences, that is sequences without auxiliary gradients (e.g. slice selection), are simulated. Omitting these gradients has negligible effect on b-value and thus diffusion weighting. All RF pulses and the readout itself are considered instantaneous. This could be improved in the future and is not expected to have a large penalty in terms of simulation time, but again the effect of this assumption is expected to be minimal. The 180° RF pulse (spin echo sequences) or the pair of 90° RF pulses (stimulated echo sequence) are equivalently modelled by negating the sign of the subsequent gradients.

3.2.3 Generating an idealised pulse sequence

The sequences in figure 3.1 are simplified versions of the true pulse sequences that are exported by scanner software. They have been manually reduced to their key timing parameters. Figure 3.2 shows schematics of the three sequence types.

To facilitate simulations that involve varying a given parameter, such as a study involving Δ or b, a tool to automatically generate pulse sequences is useful. Not only

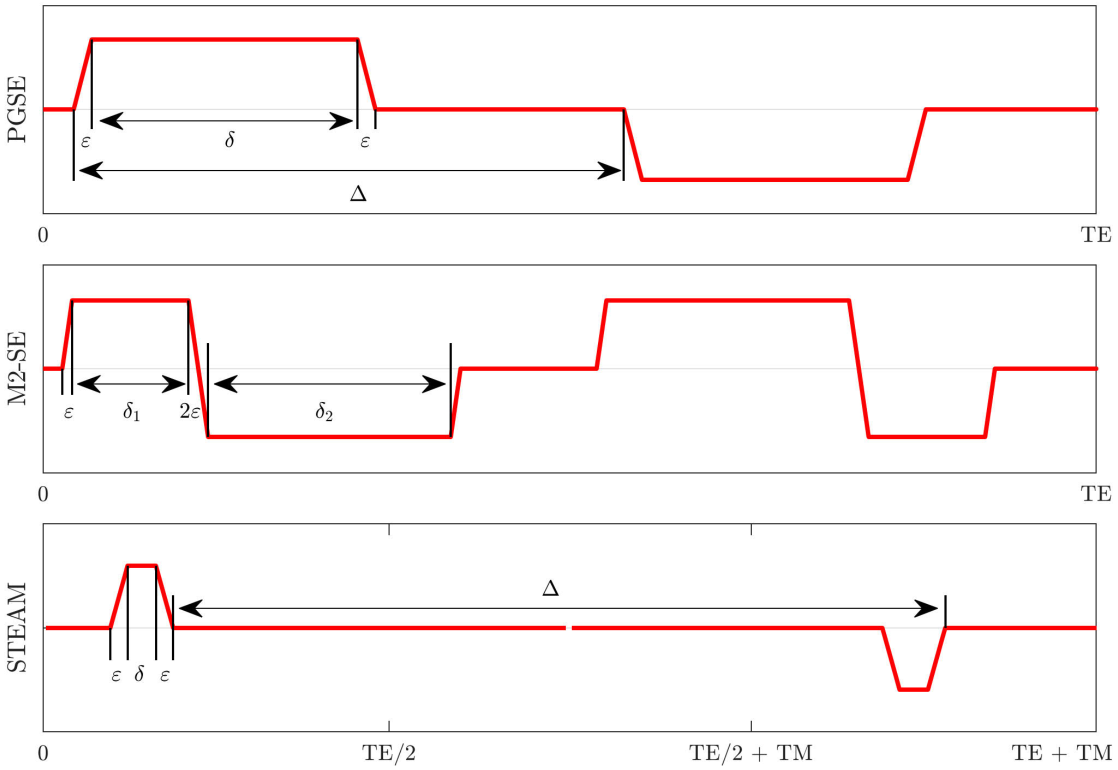

Figure 3.2: Schematic diagram describing the three pulse sequences used in this work and shown in figure 3.1. Only the timing parameters (x-axis) are labelled. The gradient strength of the waveforms is shown on the y-axis and all non-zero gradients have the same flat-top gradient strength $G_{\max}$. [*Reproduced with permission from (Rose et al., 2019c).*]

does this accelerate the turn-around time of simulations, it also allows to simulate a wider space of parameters including unphysical ones that the scanner simulation may report as incompatible.

For all sequences, the gradients are simulated at the maximum gradient strength $G_{\max}$ that is available in the scanner. This also fixes the gradient ramp-up and ramp-down times ϵ, which are computed based on the hardware-specific slew rate $\varepsilon = G/\epsilon$.

For the purpose of sequence generation, the PGSE and STEAM sequence are treated equally as bipolar gradient sequences. They can be consider as “simple” sequences that have a pair of opposing trapezoidal gradients. As a result, they only differ by the prescribed parameters, in particular ϵ and most notably Δ. Both sequences need to satisfy the following condition:

$$b = (\gamma G)^2 \left(\delta(\Delta - \delta/3) + 1/30\epsilon^3 - 1/6\delta\epsilon^2\right) \tag{3.11}$$

This equation can be solved for any of the parameters through rearranging. Some are more straightforward to evaluate than others, for example solving for δ/ϵ requires the quadratic/cubic formula. All parameters are limited to the positive value when computing the square root. Complex numbers that can arise may be reduced to the real part *iff* the complex norm is sufficiently small to suggest that the imaginary part is likely due to numerical errors.

The advantage of the STEAM sequence is that it allows for long diffusion times Δ. Varying this parameter is straightforward and only requires finding an appropriate value for δ given the constant $G = G_{\max}$ (from which ϵ can also be derived given the scanner slew rate).

As the diffusion time Δ becomes shorter (and parameters approach those typical for PGSE sequences), the target b can often no longer be satisfied with the gradient shape constraints in place. Then, a different objective for sequence generation needs to be considered. Consider the relative gradient durations in figure 3.1, where δ and Δ are of similar magnitude. Instead of specifying a target Δ, values for δ must be iterated through to find the combination of parameters that minimises the echo time TE. Another constrain is that $\Delta \leq 2\epsilon + \delta + \alpha_{180^\circ}$, where α_{180° is the minimum duration of a 180° RF pulse. While this is not simulated in the idealised sequence, the constraint ensures a more realistic timing of gradients.

The more complicated motion-compensated sequences (MCSE) require a different treatment. The equation for b-value of the M2-SE sequence that all parameters need to satisfy is[†]

$$\begin{aligned} b = \gamma^2 G^2 \Bigg[& \delta_2^2(\Delta + \tau) - \frac{\delta_2 \tau^2}{6} + \frac{49\tau^3}{60} - \frac{\delta_2^3}{3} \\ & + \frac{(\tau^2 - \Delta\tau + 2\Delta\delta_2)^3 - 12\delta_2^3(\Delta+\tau)^3}{12(\Delta + 2\delta_2 - \tau)^3} \cdot \frac{\delta_2^2(\Delta+\tau)^2(\Delta+3\delta_2)}{(\Delta+2\delta_2-\tau)^2} \\ & - \frac{\tau^2(\tau^2 - \Delta\tau + 2\Delta\delta_2) + 3\delta_2^2(\Delta+\tau)(2\Delta+\delta_2+2\tau)}{3(\Delta+2\delta_2-\tau)} \Bigg] . \end{aligned} \tag{3.12}$$

This corresponds to the M2-SE implementation of constant amplitude and variable pulse widths, related by

$$\delta_2 = \delta_1 \frac{\Delta - \tau}{\Delta - 2\delta_1 + \tau} , \tag{3.13}$$

as shown in (Welsh et al., 2015, fig. 9). At present, the symbolic mathematics toolbox in MATLAB is used to solve for the different parameters when generating MCSE sequences. However, a more iterative approach may be necessary because some combinations of parameters are not always satisfiable without some tolerances. The goal is to minimise echo time (TE) in order to reduce motion sensitivity and T_2-related signal loss.

3.3 A GPU-accelerated Bloch–Torrey simulator

For complicated domains like a model of cardiac tissue described in chapter 2 the solution to the Bloch–Torrey equations (3.2) is not trivial. Exact analytical solutions exist (Moutal

---

[†] Equation (3.12) is developed in (Welsh et al., 2015, eqn. 16). In the original paper, it contains a missing closing parenthesis which has been corrected here.

et al., 2020), but these are limited to special cases. Numerically solving the Bloch–Torrey equations allows us to simulate for example diffusion-weighted images and compute a diffusion tensor from the magnetisation vector in the domain. Several approaches exist and can be grouped into two categories: particle-based methods like the Monte Carlo random walk (MCRW), which will be discussed later in chapter 5; and continuum solution methods. The latter are well understood and can be very accurate. As such they provide a means to verify random walk approaches. Continuum solutions are however relatively computationally expensive and for large three-dimensional problems the effort required to obtain a solution that is accurate to within a few percent (random walk) rather than machine-level precision (continuum solution) makes random walks the method of choice. To overcome the large computational effort of continuum solutions, acceleration with GPUs is considered. As shown below, the problem lends itself to parallel processing.

For this work, efficient means to compute continuum solutions are investigated for two reasons: Firstly, it was considered essential to provide a means to validate the MCRW simulations with minimal computational effort; Secondly, with continuous improvement in GPU technology it is not clear where the boundary between choosing a continuum solution vs a random walk approach will lie in the future.

To solve the governing equations, the domain must first be discretised. The exact procedure for this depends on the continuum method applied: finite difference (FDM), finite volume (FVM), or even finite element (FEM) methods all have their unique approach. However, for the sake of this discussion, they all assume that the solution variable U is somehow described at discrete locations in space, which will be called *cells* for generality. Note that "cell" in the context of continuum methods in this chapter 3 refers to a discretised node/volume/element in FDM/FVM/FEM and *not* a biological cell. In fact, given a discretisation of even modest spatial resolution, a cardiomyocyte is expected to be divided into multiple of these cells.

Omission of the relaxation terms in equation (3.2) allows for the study of the magnetisation $M_{xy}(t) = M_x(t) + \mathrm{i}M_y(t)$ only in the transverse xy plane. The use of a complex variable M_{xy} only simplifies the notation and not calculation because nonetheless two solutions to the diffusion equation are required, separately for M_x and M_y. The method of updating a generic scalar quantity U (M_i) throughout time will be described in the remainder of this section.

Before proceeding, the interaction between M_x and M_y during application of gradients and RF pulses needs to be briefly covered. The initial 90° pulse provides the initial condition and can be modelled as $M_{xy} = M_x = 1$ (real). A 180° RF pulse is equivalent to $M_{xy}^{n+1} = M_x^n - \mathrm{i}M_y^n$, i.e. the flipping of y-magnetisation. Approximating the pulses as instantaneous is acceptable since for most cases the simulation time step δt is of similar magnitude as the duration of the RF pulse. As such, the desired change in magnetisation is ensured without having to fully resolve the pulse. This trivial treatment of the $\gamma \boldsymbol{M} \times \boldsymbol{B}$ term in equation (3.2) can be implemented efficiently and will not be discussed further in this work. For the purposes of GPU implementation, the CUDA Thrust library is used for the magnetisation dynamics, as these are simple transforms of the magnetisation vector. This high-level library hides the intricate details of the GPU architecture.

3.3.1 Continuum solution to the diffusion equation

The diffusion term of equation (3.2) corresponds to the right-hand side of the diffusion equation (3.14). The operator $\boldsymbol{\nabla} \cdot (\mathbf{D}\boldsymbol{\nabla})$ can be expressed as a double summation:

$$\frac{\partial U}{\partial t} = \boldsymbol{\nabla} \cdot (\mathbf{D}\boldsymbol{\nabla} U) = \sum_{i=1}^{3} \sum_{j=1}^{3} \frac{\partial}{\partial x_i} \left(\mathbf{D}_{ij} \frac{\partial U}{\partial x_j} \right) . \tag{3.14}$$

Consider a *scalar* diffusion coefficient $D(\boldsymbol{x})$. Note that this is not the apparent diffusivity in equation (3.4) but the underlying diffusion coefficient D_0 from section 2.3.1. In the case of isotropic but inhomogeneous diffusion, the divergence and gradient operators can be expanded and thus equation (3.14) for m dimensions becomes

$$\frac{\partial U(\boldsymbol{x},t)}{\partial t} = \sum_{i=1}^{m} \frac{\partial D(\boldsymbol{x})}{\partial x_i} \frac{\partial U(\boldsymbol{x},t)}{\partial x_i} + D(\boldsymbol{x}) \frac{\partial^2 U(\boldsymbol{x},t)}{\partial (x_i)^2} . \tag{3.15}$$

The diffusion operator is separable and can be solved for $\partial U/\partial t$ in m passes along axis i of the m-dimensional reference frame. As seen later, this has considerable (positive) performance implications for the algorithm of choice, especially on GPUs.

At the domain boundaries with normal vector $\boldsymbol{n}$, isolating (zero-flux) boundary conditions are used:

$$\frac{\partial U}{\partial \boldsymbol{n}} = 0 . \tag{3.16}$$

The internal boundaries, i.e. cardiomyocyte membranes, need to enforce that the flux matches the permeability κ:

$$\frac{\partial U}{\partial \boldsymbol{n}} \sim \kappa . \tag{3.17}$$

Note that the diffusion equation locally reduces to the heat equation

$$\frac{\partial U}{\partial t} = D_0 \boldsymbol{\nabla}^2 U \tag{3.18}$$

inside each compartment, where D_0 is the local constant scalar diffusion coefficient. This is a result of the compartment model described in section 2.3.1. The internal boundary conditions at the compartment barriers then enforce the required flux (permeability of the membrane). A discretisation of equation (3.18) could be implemented as a special treatment in the source code, but the additional instructions from equation (3.15) are not

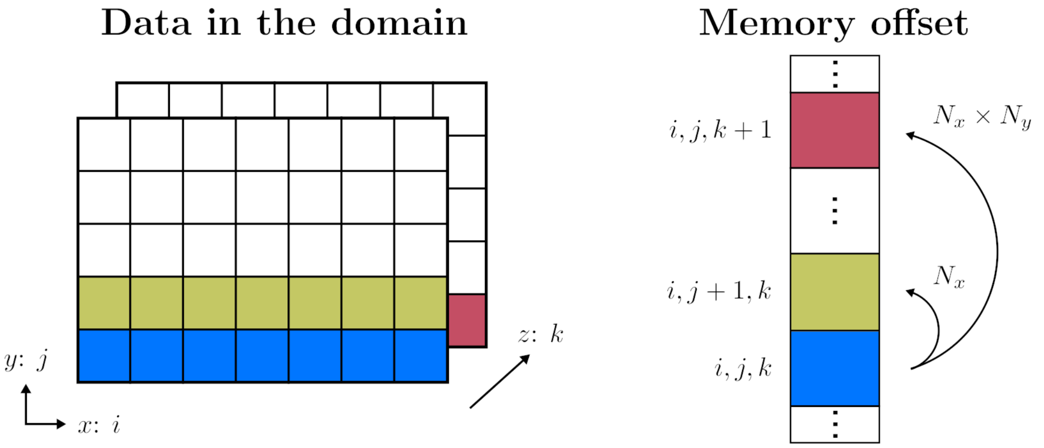

Figure 3.3: Multi-dimensional data **(Left)** and its linear layout in computer memory **(Right)**. Elements of U with coordinates $\boldsymbol{x} = [x \quad y \quad z]$ in a grid of size $N_x \times N_y \times N_z$ are indexed at integer multiples i, j, k. Data is stored contiguously (offset of 1) along x and neighbouring elements can be retrieved by an offset in linear memory of N_x $(j \to j+1)$ and $N_x \times N_y$ $(k \to k+1)$.

a bottleneck. Instead, keeping one discretisation aids readability and maintainability of the code.

The temporal discretisation and time stepping uses an explicit (Euler) scheme. For a given time step Δt, this results in

$$\frac{\partial U}{\partial t} = \frac{U^{n+1} - U^{n}}{\Delta t} \,. \tag{3.19}$$

This simple forward-time scheme is applied for both FDM and FVM described below, which are concerned with approximating the right-hand side of the diffusion equation. For the parameters used in this work, the time step is typically small. As such, more expensive approaches like implicit methods or higher-order schemes are not needed to ensure numerical stability or accuracy. J.-R. Li et al. (2014) applied an adaptive time-stepping method to simulations of diffusion MRI, but such methods are more complicated to implement on the GPU architecture that is targeted here.

3.3.2 Considerations regarding GPU memory access

As with most computer codes running on modern hardware, the main bottleneck is memory access (Burger et al., 1996). At each time step, the cost of executing the few operations at each data point is negligible compared to the time it takes to read the data involved in the calculation and writing the result back into memory. Because computer memory is linear, another problem occurs. Higher-dimensional operators such as $\boldsymbol{\nabla}$ need to read data from memory that is many entries away from the centre of the stencil, leading to strided memory access. This is visualised in figure 3.3.

The Laplacian operator $\boldsymbol{\nabla}^2$ that occurs in equation (3.18) and its finite difference implementation using a stencil of neighbouring points (section 3.3.3) is similar to image kernel convolution (Semmlow, 2004). Efficient methods exist in CUDA to carry out these operations, however this has two problems: it is not available for 3D data, and it is limited to homogeneous D. Another approach is to use texture memory (Wilt, 2013), which optimises multi-dimensional memory access for data locality by means of space filling curves. However this is less optimal than using a custom-designed CUDA kernel, because texture memory is only available for 1D and 2D operators, requiring significant refactoring of the instructions. Instead, separate 1D passes along the considered dimensions as permitted by equation (3.15) are used to optimise linear computer memory access. Section 3.3.3 considers the numerical schemes to solve the diffusion equation in 1D.

Using the standard memory layout, data for cells in the 3D grid is arranged linearly (figure 3.3). In the context of GPUs, there are different types of memory that threads have access to (Wilt, 2013). These are, in increasing order of threads access speeds,

$$\text{(fastest)} \quad \text{registers} > \text{shared} > \text{device/global} \gg \text{host} \quad \text{(slowest)}\,. \tag{3.20}$$

Host memory is very slow to access. It is inaccessible to the threads and needs to be explicitly copied to device memory. For this reason, operations are solely done on device memory and data is only copied between device and host when loading from or writing to disk. Global reads inside a kernel stall the execution and require about 3 to 4 cycles to execute. It is therefore advantageous to refactor the code to carry out all reads at the start and all writes at the end in consecutive statements. The following operations should then be register-only computations that do not depend on the successful fetch of global memory. Examples of such efficient filler instructions are: kernel logistics and housekeeping that depend only on the thread index; unpacking and processing of input data structures which are passed by value into registers on kernel call.

It is important to understand how threads are organised on the GPU. A full explanation of this can be found in the book by Wilt (2013). Each thread is executed in a kernel grid whose dimensions need to be provided to CUDA. It is customary to schedule one thread per data point in a grid with the same dimensions as the data on which it operates. Threads are grouped together in thread blocks (with a maximum of 1024 threads per block) and executed in “warps” of 32 threads. These numbers apply to GPU devices with compute capability 2.0 and larger. On the hardware, blocks are scheduled to run on the streaming multiprocessors (SM), each of which contains a fast cache called “shared memory” as well as a certain number of registers for fast local storage.

Each access to global memory loads 32 (equal to the warp size) consecutive values along the x direction of the *memory.* When threads operate along the x direction of the *domain*, they load data consecutively from memory and thus access is coalesced. This leads to a high effective memory bandwidth, where threads can load data to fast shared

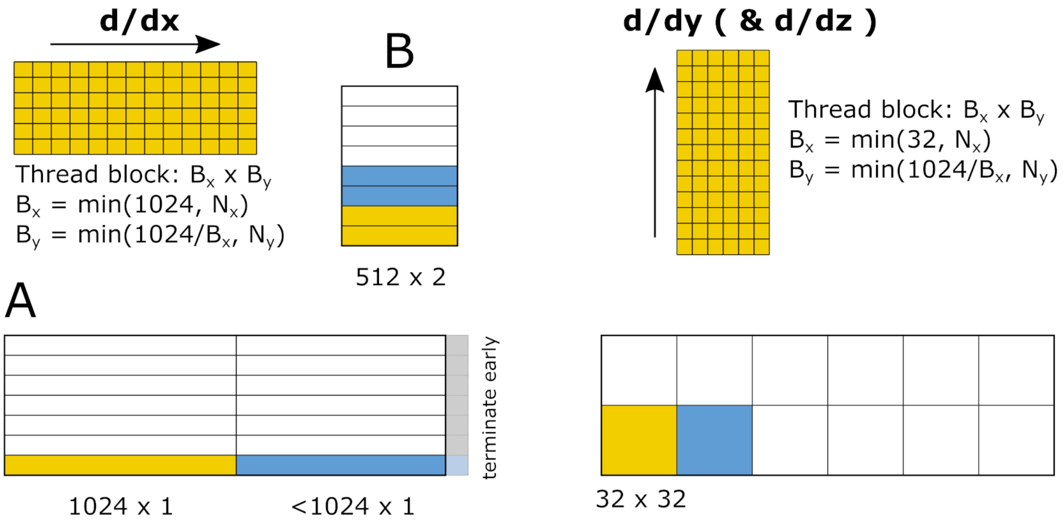

Figure 3.4: GPU kernel logistics to optimise memory access along different directions. Each thread block contains 1024 threads. **(Left)** Operating on data with $(\partial/\partial x)$ requires no special consideration and a one-dimensional thread block is used. For a significantly large x-dimension of the domain such as in (A), thread blocks can be arranged as 1D pencils. Domains that are shorter in x than the maximum block size cause the block dimension to "wrap around" (B). **(Right)** Due to a warp size of 32, operators $(\partial/\partial y)$ and $(\partial/\partial z)$ require a thread block with 32 threads in x. This results in a block size of 32×32.

memory. When naïvely operating along the y or z direction however, each thread causes 31 unnecessary memory accesses. This is prevented by organising kernel launches along these dimensions differently as seen in figure 3.4. Using the described access patterns has the same effect as (costly) reshaping the data before each pass.

3.3.3 Numerical schemes for the finite difference and volume methods

Finite difference method

The idea behind the finite difference method (FDM) is to approximate derivatives of a quantity, which are its local gradients, using the differences in quantity between neighbouring nodes:

$$\frac{\partial U}{\partial t} = \frac{\partial D}{\partial x}\frac{\partial U}{\partial x} + D\frac{\partial^2 U}{\partial x^2} \approx \frac{\Delta D}{\Delta x}\frac{\Delta U}{\Delta x} + D\frac{\Delta^2 U}{\Delta x^2} \tag{3.21}$$

The set of nodes/cells being used is called the stencil, illustrated in figure 3.5. The approximation of the derivatives is done using Taylor expansion (Özişik et al., 2017). Ignoring the truncation error of $\mathcal{O}(\Delta x)$, a finite difference approximation of equation (3.15) is

$$\frac{\partial U}{\partial t} \approx \frac{D_{i+1} - D_{i-1}}{\Delta x}\frac{U_{i-1} - U_{i+1}}{\Delta x} + D_i\frac{U_{i-1} - 2U_i + U_{i+1}}{\Delta x^2}\,. \tag{3.22}$$

The zero-flux boundary condition (equation (3.16), $\partial U/\partial x = 0$) is approximated using

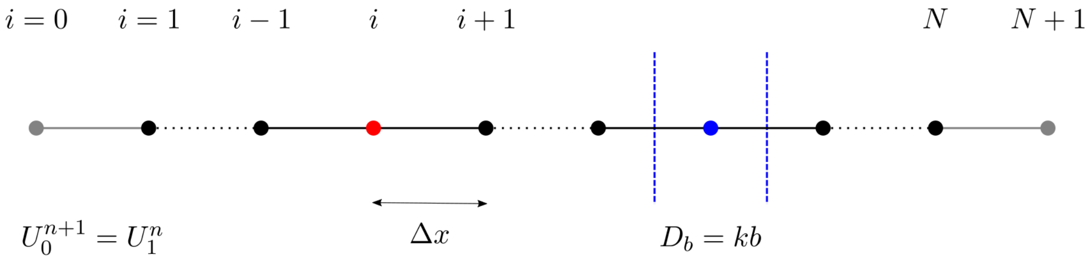

Figure 3.5: Schematic of the finite difference scheme. The domain is divided into N nodes spaced Δx apart. The concentration at U_i (red) is updated according to equation (3.22) using the 3-point stencil $\{i-1, i, i+1\}$. Ghost nodes (grey) at the domain ends enforce the zero-flux boundary condition, while barrier nodes (blue) are assigned reduced diffusion coefficient D_b to model the membrane with permeability κ.

a first-order treatment

$$\frac{\partial U}{\partial x} \approx \frac{U_1 - U_0}{\Delta x} \,. \tag{3.23}$$

To accommodate this, halo nodes/ghost cells are introduced at $i = 0$ and $i = N + 1$ for N cells in the domain. The boundary condition results in $U_0^n = U_1^{n-1}$, and similarly $U_{N+1}^n = U_N^{n-1}$. In other words, the halo nodes are updated to have the same concentration as the neighbouring (internal) node at the start of the new time step.

Cardiomyocyte membranes are internal interfaces that satisfy equation (3.17). As with the boundary condition in equation (3.23), the FDM has no natural mechanism for enforcing these fluxes. Permeability can be introduced through a separate numerical scheme at the affected nodes in the stencil, however this leads to awkward formulation and difficult implementation. A more complex algorithm also results in sub-optimal GPU code. Another (better) option is to use the definition of permeability in equation (2.3):

$$\kappa \equiv \lim_{\substack{b \to 0, \\ D_b \to 0}} \left(\frac{D_b}{b} \right) . \tag{2.3 [reproduced]}$$

A consistent interface condition is achieved though a finite approximation to this limit. The membrane is thus represented not as an interface but as a thin region of thickness $b = \Delta x$ (spacing between nodes) and reduced diffusion coefficient $D_b = \kappa / b$. For a discretised domain, the outer-most node of each intra-cellular region is designated as the membrane. This avoids polluting the possibly small gaps of ECS between cardiomyocytes. For a sufficiently small spatial resolution, the effective reduction of myocyte size is negligible.

Finite volume method

The finite volume method (FVM) has an advantage over the finite difference formulation. As shown previously, there are limitations in how the FDM applied to the diffusion equation can represent discontinuities in the diffusion coefficient. The FVM overcomes this naturally

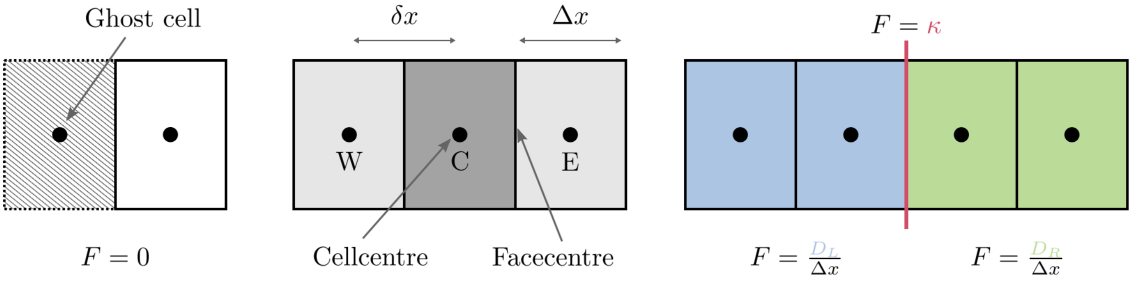

Figure 3.6: Schematic of the finite volume scheme. The domain is divided into cells of size Δx, with their cell centres (C) spaced δx apart (for constant sizes, $\Delta x = \delta x$). Information with the neighbouring cells left (W) and right (E) is exchanged through the cell faces. The flux F at these faces is either dependent on the diffusion coefficient D_0 or prescribed ($F = \kappa$, or $F = 0$).

by dividing the domain into volumes (cells) and equating fluxes through the cell faces. All information is communicated through the cell faces, which can be made to coincide with membranes at the cardiomyocyte boundaries leading to infinitely thin membranes. Figure 3.6 shows a schematic of the FVM in 1D. The current (central) cell is denoted by C and its neighbours on the left (west) and right (east) use the subscripts W and E.

As with the FDM, the description below only offers a brief explanation of the method as far as it is relevant to the final implementation in the Bloch–Torrey solver. Anyone interested in a more detailed treatment, especially the mathematical underpinnings and derivation of the equations presented below, should consult the book by Versteeg et al. (2007).

The FVM uses a conservation approach. Instead of calculating the differences explicitly as was done in the FDM, the change in quantity U inside the finite volume is considered instead. Through conservation laws, all changes in U ($\frac{\partial U}{\partial t}$) must be the result of concentration exiting and entering the volume[‡]:

$$\left(\frac{\partial U}{\partial t}\right)_C = a_W U_W + a_E U_E - a_C U_C \tag{3.24}$$

where $a_{W|E} = \frac{DA}{\Delta x}$. This takes advantage of the constant spacing and size of cells in the domain and would need to be adjusted to the specific geometry if variable spacing were used. Setting $A = 1$ omits the face area, which in 1D equals unity by definition. Furthermore $a_C = a_W + a_E$ leads to the formulation

$$\left(\frac{\partial U}{\partial t}\right)_C = \underbrace{\frac{D}{\Delta x}}_{=F}\left(U_W - 2U_C + U_E\right). \tag{3.25}$$

Note the similarity to the FDM in equation (3.22).

The quantity F in equation (3.25) represents the flux through the cell faces. Due to the two-compartment model, D is constant between cells except at membranes. This can

---

[‡] Source terms that account for concentration being created or destroyed inside a cell are ignored here.

be used to identify interfaces where κ should be used instead. In the code implementation, F is not factored out and the formulation is kept closer to equation (3.24). The membrane permeability can be used as a drop-in replacement for F.

At the boundaries, there is no need for ghost/halo cells. As with the internal boundaries, the no-flux condition can be imposed directly by setting $F = \kappa = 0$. However for ease of implementation halo cells *are* used with a special value for the diffusion coefficient, $D =$ `NAN` (not-a-number). This has two advantages: it results in a similar domain to the FDM implementation, thus allowing for re-use of code and interchangeability of the diffusion operator; it also enables using the value of ΔD to conditionally set the face velocity (=flux) to zero instead of requiring a different implementation at the boundaries (recall the similar reasoning in the FDM in the context of GPU optimisation).

3.4 Numerical results

3.4.1 Simulating a 3D stack of confocal microscopy images

An advantage of continuum methods over random walks is that no precise geometries need be prescribed. FVM can simulate the diffusion/Bloch–Torrey equations directly in a histology image of low resolution or poor-quality segmentation. For example, individual membranes need not be identified exactly as would be required for MCRW methods. The effect of “smeared” membranes inside bulk regions of ICS could for example be modelled through a reduced D_{ICS}.

Here, a segmented stack of confocal microscopy images from figure 2.5 (Seidel et al., 2016) is used as the domain, seen in figure 3.7. The original image stack has a size of $1024 \times 1024 \times 293\,\mu\text{m}^3$ and isotropic imaging resolution of $0.2\,\mu\text{m/px}$. A cube of size $200 \times 200 \times 200$ $(= 8 \times 10^6)$ cells and side length $40\,\mu\text{m}$ is extracted from the centre of the stack and simulated using the FDM implementation described in section 3.3.3. Compartment diffusion coefficients were set to $D_{\text{ICS}} = 1\,\mu\text{m}^2/\text{ms}$ and $D_{\text{ECS}} = 3\,\mu\text{m}^2/\text{ms}$ and the interface between ICS and ECS is fully permeable ($\kappa = \infty$).

Figure 3.7 also shows a volume rendering of the concentration in the domain. It has been clipped so that it only shows values larger than three standard deviations of a Gaussian distribution for the same simulation time. Without this post-processing it would be difficult to view the distribution near the initial spike, where the shape of the PDF has most relevance. Anisotropic spread of the concentration can be appreciated, caused by the heterogeneity of the diffusion coefficient. This results in local preferred directions of diffusion along the cardiomyocytes.

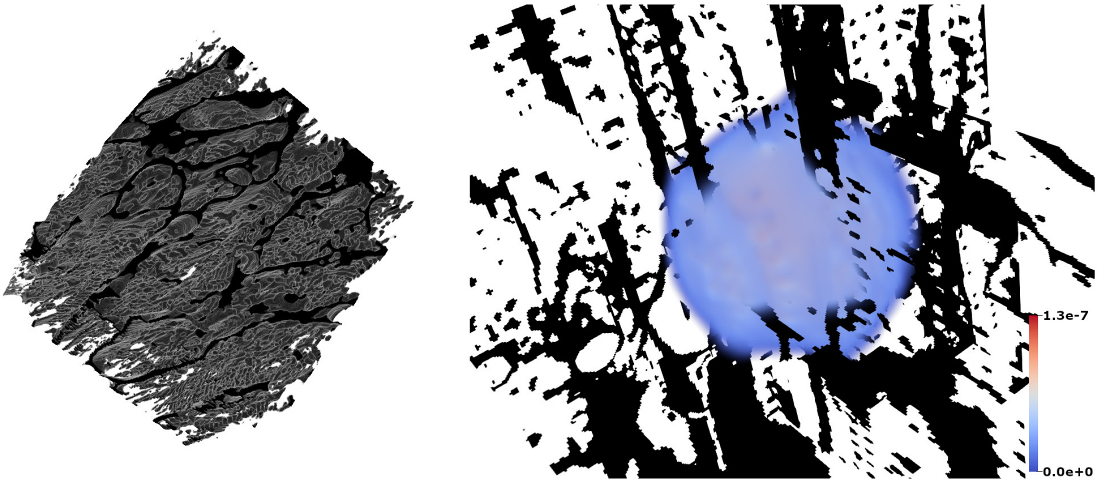

Figure 3.7: Input geometry for GPU-based Bloch–Torrey simulation **(Left)** and resulting 3D distribution of concentration after an initial spike at the centre **(Right)**. The geometry shows the extra-cellular space (ECS) in black. The volume rendering of concentration is thresholded to a value of three standard deviations of the corresponding Gaussian distribution. [*Input geometry kindly provided by T. Seidel, part of the data set from (Seidel et al., 2016).*]

3.4.2 Accurate representation of discontinuities

Here, a FVM study is carried out to investigate the convergence of one-dimensional solutions with an increase in number of cells in the domain. Two membranes are present in the domain and during meshing/discretisation care is taken to place a cell face at these exact locations. This results in slight differences in Δx in the regions (compartments) between membranes, but ensures a consistent membrane location irrespective of discretisation. As the current GPU implementation does not allow for variable spacing at this time, the MATLAB code from previous work (Rose et al., 2018e) is used instead. The code (appendix B.2.1) is based on the finite volume MATLAB toolbox FVTool (Eftekhari, 2021).

A constant diffusion coefficient of unity (all parameters are normalised) and a high permeability of 0.4 are selected. The simulation is carried out over 100 time steps until (normalised) time 100, using an implicit time stepping scheme. An initial spike in concentration is set in the centre of the domain. Due to the irregular mesh, the cell centres do not all coincide. Since the FVM assumes a constant distribution of the quantity of interest inside each volume, the cell that contains $x_0 = 50$ is assigned the initial value of $1/\Delta x$ (such that $\int U \, \mathrm{d}x = 1$).

Figure 3.8 shows the final distribution of concentration. The overall shape of the distribution is well captured even for a low number of cells. At the membranes, a “smearing“ of the concentration is observed at low resolutions. This effect is more prominent at the membrane closer to the initial location of concentration, where the gradient $\partial U/\partial x$ and thus the step change in concentration across the cell face is larger.

A sufficiently converged solution can be assumed at the highest number of points, $N_x =$

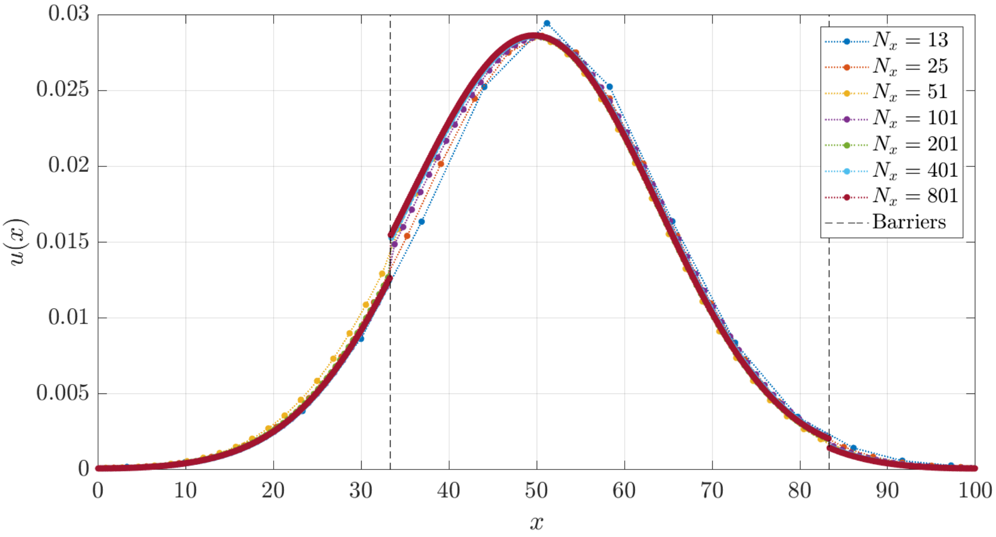

Figure 3.8: Effect of spatial resolution on location of maximum concentration and accurate representation of membranes in the finite volume method (FVM). The initial spike in concentration is in the cell containing $x_0 = 50$.

801. From $N_x > 101$ the solutions only differ slightly and capture all features of the distribution. In general, the resolution required for a converged solution is problem dependent. Based on this study with $\Delta t \sim D \sim \mathcal{O}(1)$, it is suggested to use a cell size of $\mathcal{O}(1)$.

3.4.3 Signal loss along different gradient directions

Until now, the applications of the continuum methods have focused on solutions to the diffusion equation. This is an important aspect of the Bloch–Torrey equations and especially diffusion-weighted methods like DT-CMR. However, the magnetisation dynamics in response to the pulse gradients needs to be considered too. Below, the GPU-based Bloch–Torrey simulator is applied to a realistic DT-CMR problem. The finite difference method (FDM) is employed for these simulations, published previously (Rose et al., 2019d).

Using the automatic segmentation techniques described in section 2.4.2, regions of intra- and extra-cellular space are identified in a wide-field microscopy image of swine histology. The domain is seen in figure 3.9. The images have resolution $\Delta x = 0.5\,\mu\text{m/px}$. A region of interest of $1760 \times 1760\,\text{px}^2$ is selected as simulation domain. Boundary effects (Hwang et al., 2003) due to the zero-flux boundaries at the domain ends are mitigated by discarding the outer-most 10 % of the domain on all sides. The boundary pixels of ICS regions are assigned a reduced diffusion coefficient $D_b = \kappa/\Delta x$ as required by equation (3.17) to model the cardiomyocyte membrane with permeability $\kappa = 0.005\,\mu\text{m/ms}$. Diffusion coefficients in the ICS and ECS are set to $D_{\text{ICS}} = 1\,\mu\text{m}^2/\text{ms}$ and $D_{\text{ECS}} = 2\,\mu\text{m}^2/\text{ms}$ respectively.

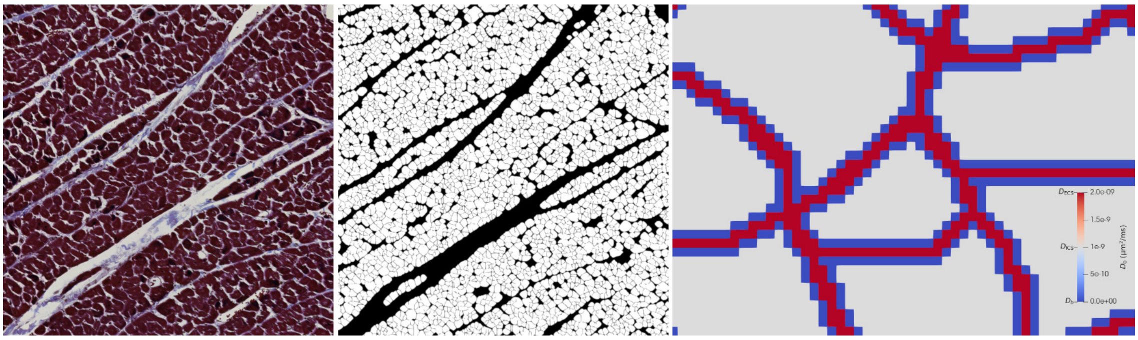

Figure 3.9: Original histology image **(Left)** and automatically-segmented simulation domain **(Middle)** for simulations with the finite difference method (FDM). A subset of the domain **(Right)** is used to illustrate the three different types of finite difference cells: Extra-cellular space (ECS, red), intra-cellular space (ICS, grey), and membrane (part of ICS, blue). [*Parts of this figure were presented in (Rose et al., 2019d).*]

To model the DT-CMR signal in the domain, a full STEAM sequence with $\Delta = 1\,\mathrm{s}$ and b-value $450\,\mathrm{ms}/\mathrm{\mu m}^2$ is simulated. As described in section 3.3, the transverse magnetisation $\boldsymbol{M} = M_x\hat{\boldsymbol{\imath}} + M_y\hat{\boldsymbol{\jmath}}$ has initial condition $\boldsymbol{M} = 1\hat{\boldsymbol{\imath}}$ everywhere in the domain as a result of the 90° RF pulse. Three different gradient directions ($G_{xx} = G\hat{\boldsymbol{\imath}}$, $G_{yy} = G\hat{\boldsymbol{\jmath}}$, and $G_{xy} = G/\sqrt{2}(\hat{\boldsymbol{\imath}} + \hat{\boldsymbol{\jmath}})$) are simulated, from which a 2×2 diffusion tensor can be constructed. This is further discussed later in section 6.4.1 and instead the qualitative results are analysed here. Figure 3.10 shows the magnitude of $\boldsymbol{M}$ in the domain at the time of echo. The effect of microstructure on local signal loss is appreciable. This region of interest was chosen specifically to contain large shear layers between the sheetlets. It is clear from figure 3.9 that the orientation of these shear layers have an orientation of less than 45° with respect to the x-axis. This is corroborated by a high signal loss along the G_{xy} gradient direction. Such a signal loss is the result of increased diffusion, in turn caused by reduced local hindrance in ECS. The minimised signal loss inside the cardiomyocytes as a result of

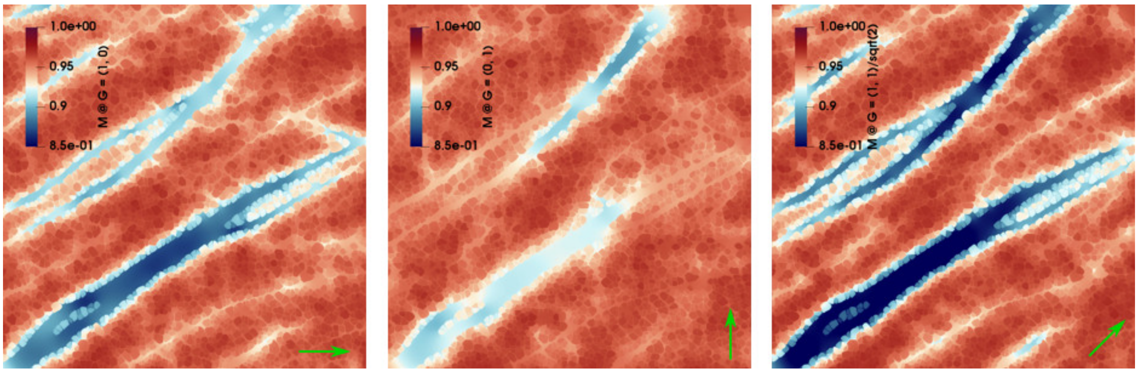

Figure 3.10: Loss of transverse magnetisation $\boldsymbol{M}$ as a result of different DT-CMR gradient directions $\boldsymbol{G}$, indicated by the green arrow in the bottom right corner. The domain is the same as in figure 3.9. Low values of $\|\boldsymbol{M}\|$ indicate a high signal loss, corresponding to low (local) restriction and thus high apparent diffusion in that gradient direction.

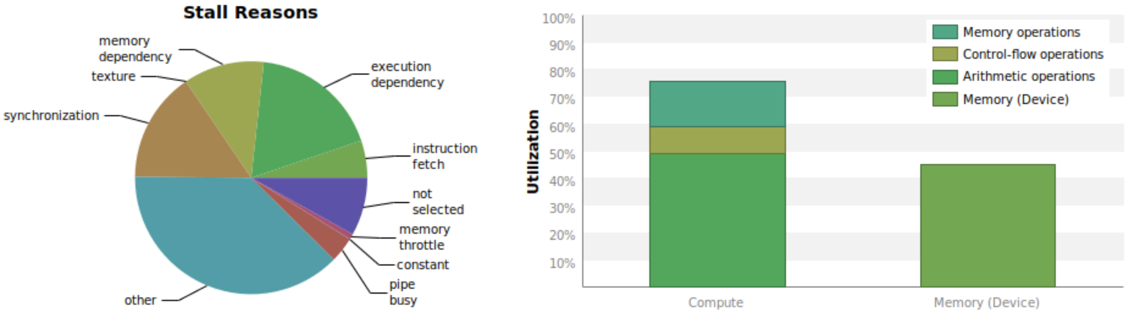

Figure 3.11: GPU performance results from the NVIDIA profiler. **(Left)** Pie chart of reasons for threads to stall during execution. The largest share is labelled "other", followed by "execution dependency" and "synchronisation". **(Right)** Compute and device memory utilisation.

restricted diffusion can also be observed.

3.4.4 GPU performance

The simulations in section 3.4.1 were profiled to assess the performance and quality of the GPU code. While the simulations above were executed on a designated remote workstation fitted with an NVIDIA Quadro P6000 GPU, profiling was done on a local workstation containing an NVIDIA Quadro M4000. The M4000 was selected as a mid-range professional desktop graphics card to also demonstrate feasibility of such simulations on non-dedicated computing hardware like HPC systems or high-end workstations. The operating system was Linux (Ubuntu 18.04) and code was compiled using the CUDA Toolkit 10. Even though the precision of variables in the simulation can be selected at compile time, single precision is used for all data as this is the most supported data type on GPUs. Given the high performance penalty that comes with performing double precision arithmetic on modern GPUs[§], there is no advantage to be gained from additional precision. In fact, spatial and temporal resolution are most likely more important for accurate simulations than the floating point precision of variables.

Figure 3.11 shows the results from the NVIDIA profiler. According to the pie chart in figure 3.11 (Left) the primary reason for stalling, i.e. when threads must halt and cannot be utilised 100 %, is "other". This suggests that the kernel is almost fully optimised. Stalling due to synchronisation is unavoidable to ensure all threads have written to the shared memory before each thread makes use of the cached information from neighbouring elements. Figure 3.11 (Right) shows the pipeline utilisation. The compute utilisation is relatively high for a complex kernel like the one being profiled here. The effective GPU memory bandwidth of the Quadro M4000 is reported as 93 GB/s, compared to its theoretical peak bandwidth of 192 GB/s. This low utilisation of <50 % is possibly a result

---

[§] The NVIDIA Tesla series (now branded "Data Centre GPUs") is capable of efficient double precision calculations.

of overfull caches. As expected from the discretisation in equation (3.22) a total of 6 variables, namely $D_{i-1,i,i+1}$ and $U_{i-1,i,i+1}$, need to be read to compute a single update to U_i.

The average kernel runtime amounted to 5 ms. This is the time to execute a single diffusion pass along one of the three dimensions. For this specific case with the given domain size of 200^3 and a resolution of $\Delta x = 0.2\,\mu\mathrm{m/px}$, the maximum time step for numerical stability is bound by $\Delta t \leq \frac{\Delta x^2}{2\max(D)} = 0.01\,\mathrm{ms}$. Three diffusion passes are required in 3D, which amounts to a total kernel runtime of 1500 s. Even factoring in other smaller compute overheads, this is a good result.

Simulations of an initial concentration spike, which computes the diffusion propagator $U(\boldsymbol{x}_0 \to \boldsymbol{x}; t)$, only require a relatively small domain around the initial location $\boldsymbol{x}_0$. For problems like those in section 3.4.3 however, a domain large enough to avoid significant boundary effects is required. That work was carried out in 2D as a result. If one wanted to simulate DT-CMR at the scale of a typical imaging voxel, the computational cost quickly becomes a limiting factor. In 3D, the total memory size becomes a limitation too and the execution time is no longer feasible. For those cases, it is recommended to limit analysis to 2D or rely on random walk methods.

3.5 Discussion

This chapter introduced the basic theory and underlying equations for diffusion-weighted imaging (DWI) and, more specifically, diffusion tensor imaging (DTI) or DT-CMR as it is called in the context of cardiovascular magnetic resonance. With the exception of analytical methods that are to be covered in chapter 4, modelling DT-CMR boils down to numerically solving the Bloch–Torrey equations (3.2). These fundamental equations govern the dynamics of the magnetisation vector $\boldsymbol{M}$. For the time being, relaxation effects are ignored and the Bloch–Torrey equations are reduced to precession in the transverse plane. Inclusion of relaxation mechanisms would cause the dephasing of spins over time and lead to a loss of M_{xy}.

Section 3.3 described a simulator for efficiently carrying out these numerical calculations using a continuum solution approach. Both finite difference (FDM) and finite volume methods (FVM) were presented. The use of GPU hardware allows for significant acceleration of these compute-intensive solution approaches. To harness the available processing power of such hardware, knowledge of the GPU platform and its limitations is required. As shown in section 3.3.2, the diffusion operator $\boldsymbol{\nabla} \cdot (\mathbf{D}\boldsymbol{\nabla})$ requires information from neighbouring points of the discretised domain. Due to the intricacies of GPU memory access patterns, the diffusion operator was split into separate passes along the different Cartesian directions.

While targeting GPU architecture directly has shown to involve a significant investment of code development, it offers several benefits. For example, a well-designed parallel algorithm executed on a GPU will outperform code on a CPU. While modern CPU cores can have high clock speeds in excess of 4 GHz, the large number of (slower) GPU cores offer superior performance in parallel. In addition, GPUs are easy to retro-fit to existing workstations to enable even older machines to run simulations where high performance computing clusters are not available. Such simulations could also be integrated into other workflows where GPUs are already used, for example the processing of histology images.

In order to simulate realistic DT-CMR acquisitions, the pulse sequences need to be accurately represented. Section 3.2.3 presents a tool to automatically generate gradient waveforms for the three common DT-CMR sequence types PGSE, M2-SE, and STEAM. This allows for rapid turnaround in parameter studies that consider the variation of pulse sequence parameters.

Chapter 4

Analytical Methods

Contents

4.1 Introduction

Previously in chapter 3, classical techniques from continuum mechanics were employed to solve the Bloch–Torrey equations (3.2), or more specifically the diffusion equation (3.14), using finite difference or finite volume methods. These techniques rely on discretisation of space and time. Highly (spatially and temporally) resolved solutions require a considerable amount of computational effort to simulate as both the number of degrees of freedom increases and the time step decreases. Furthermore, care must be taken to discretise the domain correctly and respect discontinuities at interfaces. In the case of the finite difference method the treatment of barriers is even more complicated, either through use of (at least) one interface node or special interface treatment.

Analytical methods are a promising approach to overcome these drawbacks but are often limited to simplified problems. However, by reducing the complex diffusion in a microstructure of multiple compartment types to a more elementary form allows us to do two things: Firstly, the complex interplay of contributions to the diffusion signal can be detangled by focusing on a domain that is easier to understand. Secondly, it enables the verification of other, model-based methods, particularly the Monte Carlo random walk methods discussed later in chapter 5.

In this chapter, methods are presented to obtain the semi-analytical solution to the diffusion equation in a 1D layered medium with permeable barriers. First, the domain properties and limitations as well as the problem definition are described in section 4.2. The solution involves finding the roots of a complex transcendental equation, which is accomplished using a novel method presented in section 4.3. Lastly, the numerical approximation of the semi-analytical solution is compared to known, truly analytical solutions in section 4.4 to perform a sensitivity study that quantifies errors which may arise in practice.

4.2 Analytical solutions to diffusion in layered media

The one-dimensional diffusion equation (3.14) applied to layered media, i.e. with piecewise constant diffusion coefficient $D(x)$, is

$$\frac{\partial U}{\partial t} = \frac{\partial}{\partial x}\left(D\frac{\partial U}{\partial x}\right). \tag{4.1}$$

The variable $U = U(x, t; x_0)$ represents the probability of moving from position x_0 to x during time t. It is often referred to as the diffusion propagator. In this example, the initial condition is given by

$$U(x, 0) = \delta(x - x_0) \tag{4.2}$$

with δ the Dirac function.

4.2.1 Description of the 1D domain

As described in chapter 2, the myocardium like other biological tissue is often modelled as a bi-compartmental system with two distinct types of compartments (intra- and extra-cellular space) and their respective diffusion coefficients D_{ICS} and D_{ECS}, as well as membranes with a fixed permeability κ that separate these compartments. While this model is followed for applications to DT-CMR in this work, such limitations are not imposed by the method in this chapter and an arbitrary choice of D and κ for each compartment/membrane is allowed.

For typical diffusion length scales, diffusion in the direction parallel to the cardiomyocytes is much less restricted than in the perpendicular direction. As a result, useful information can be extracted from 2D simulations. By constructing a domain from characteristic compartment length scales, 1D analysis may also provide new insights into the diffusion processes of the tissue under consideration, especially in studying the effect of permeability. For example, later in chapter 5 the analytical solution developed in this chapter is used to verify random walk models for membrane transit. Simulations in 1D can also be used to quantify restriction along specific directions in tissue, for example the slight restriction introduced by intercalated discs along the long axis of the cardiomyocytes.

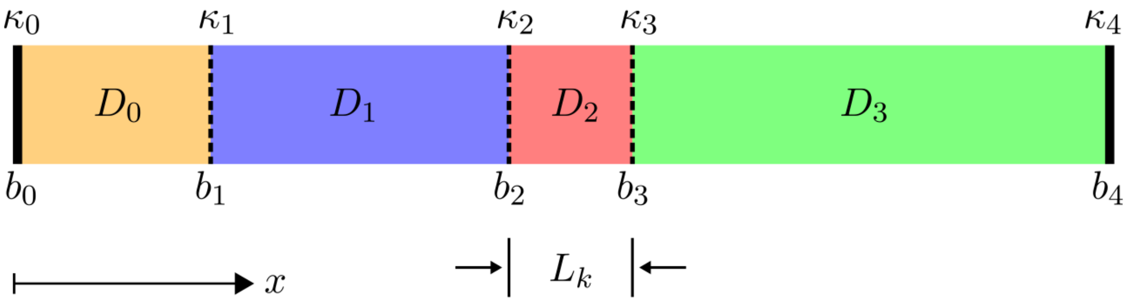

Figure 4.1: Schematic of an example domain of a 1D layered medium. There are $m = 4$ compartments with indices k, separated by $m + 1$ barriers. Index k refers to the left barrier of a compartment. Uniquely defining parameters are the barrier locations b_k, starting at $b_0 = 0$, and corresponding compartment lengths $L_k = b_{k+1} - b_k$, diffusion coefficients D_k, and permeabilities κ_j. At the domain ends, zero-flux boundary conditions ($\kappa_0 = \kappa_m = 0$) are enforced.

Figure 4.1 shows an example 1D domain. It can be used to explain the nomenclature used throughout chapter 4. The compartment barrier locations b_k and corresponding sizes L_k, diffusion coefficients D_k, and barrier permeabilities κ_k uniquely define the problem. It is possible to specify non-zero permeabilities at the domain ends. This is rarely done in practice however, because for most applications the concentration should not disappear from the domain. Setting $\boldsymbol{\nabla} U = \kappa$ at the domain ends corresponds to a solution in a small region of interest, a finite interrogation window $[b_0, b_m]$ inside an infinite domain. However, as shown later, doing so prohibits any meaningful steady-state analysis. As a result, a zero-flux Neumann boundary condition ($\boldsymbol{\nabla} U = 0$) is imposed for all practical applications in this work.

4.2.2 Spectral analysis of the diffusion operator

As a result of the wide range of applications of diffusion simulations, one-dimensional diffusion in heterogeneous domains has been studied extensively in the literature. Common techniques involving Green's function, Laplace transforms, or spectral decomposition are summarised by Hahn et al. (2012, ch. 10).

The solution assumes that space and time in equation (3.14) are separable, thus resulting in the ansatz

$$U(x,t) = u(x)e^{-\lambda t} \,. \tag{4.3}$$

Spectral decomposition is used to find the eigenvalues λ_n and eigenmodes $\nu_n(x)$ of the diffusion operator (Tanner, 1978). With them the diffusion propagator can be calculated by summation:

$$U(x,t;x_0) \approx \sum_{n=1}^{N} e^{-\lambda_n t} \nu_n(x) \nu_n(x_0) \,. \tag{4.4}$$

The piece-wise constant diffusion coefficient D_k allows to assert that the diffusion operator $\nabla(D\nabla)$ is self-adjoint. The orthogonality that follows from it guarantees that the solution is the sum of all weighted modes. The eigenvalue problem is reduced to a Helmholtz equation

$$D_k\, u'' + \lambda u = 0 \quad \forall x \in [b_k, b_{k+1}] \tag{4.5}$$

whose general solution is

$$u(x) = C_1 \sin(\sqrt{\lambda/D_k}x) + C_2 \cos(\sqrt{\lambda_k/D_k}x)\,. \tag{4.6}$$

Moutal et al. (2019) present an elegant approach to this. The original derivation can be found in Sec. 2.1 of their paper, but a summary is outlined here which adheres to the notation in the rest of this work. It involves the complex transcendental equation

$$F(\lambda) := \begin{bmatrix} \kappa_m/\sqrt{\lambda D_{m-1}} & 1 \end{bmatrix} \mathcal{T}(\lambda) \begin{bmatrix} 1 \\ \kappa_0/\sqrt{\lambda D_0} \end{bmatrix} = 0\,, \tag{4.7}$$

whose roots are defined as the eigenvalues λ in equation (4.4). The term $\mathcal{T}(\lambda)$ represents a matrix (defined below). Through right- and left-multiplication with the column and row vectors, which introduce the domain boundary conditions at boundaries $b_{0,m}$ the scalar F is obtained. The equation for $\mathcal{T}(\lambda)$ with auxiliary matrices $\mathcal{R}$ and $\mathcal{T}$ is

$$\mathcal{T}(\lambda) = \mathcal{R}_{m-1}(\lambda) \left(\prod_{k=0}^{m-2} \mathcal{M}_{k,k+1}(\lambda)\mathcal{R}_k(\lambda) \right)\,, \tag{4.8a}$$

$$\mathcal{R}_k(\lambda) = \begin{bmatrix} \cos(L_k\sqrt{\lambda/D_k}) & \sin(L_k\sqrt{\lambda/D_k}) \\ -\sin(L_k\sqrt{\lambda/D_k}) & \cos(L_k\sqrt{\lambda/D_k}) \end{bmatrix}\,, \tag{4.8b}$$

$$\mathcal{M}_{k,k+1}(\lambda) = \begin{bmatrix} 1 & \sqrt{\lambda D_k}/\kappa_{k,k+1} \\ 0 & \sqrt{D_k/D_{k+1}} \end{bmatrix}\,. \tag{4.8c}$$

For all the compartments $k \in \{0, ..., m-1\}$, each $\mathcal{R}(\lambda)$ matrix ensures that the solution is satisfied throughout the entire domain. While $\mathcal{R}$ appears like a rotation matrix, it actually originates from equation (4.6) with respect to either side of compartment k. The matrix $\mathcal{M}$ serves to satisfy the flux conditions at the internal barriers with membrane permeabilities $\kappa_{k,k+1}$. This notation involving the indices k from both compartments that the barrier separates is copied from Moutal et al. (2019) only in this instance, in order to keep equation (4.8c) similar to that in (Moutal et al., 2019, eqn. 15). Elsewhere in this work, κ_k is used to mean the boundary on the left of compartment k.

Only non-trivial cases are considered. As such, the permeability values are required to be in the range $0 < \kappa_k < \infty$. In that case, there exist a countably infinite number of real, non-negative, and simple eigenvalues (Moutal et al., 2019), which are ordered:

$$0 \leq \lambda_1 < \lambda_2 < \ \dots\,, \quad \lambda_n \to \infty \tag{4.9}$$

All these need to be found to recover the exact solution through the eigenfunction expansion in equation (4.4). From a practical perspective, the solution will therefore always be an

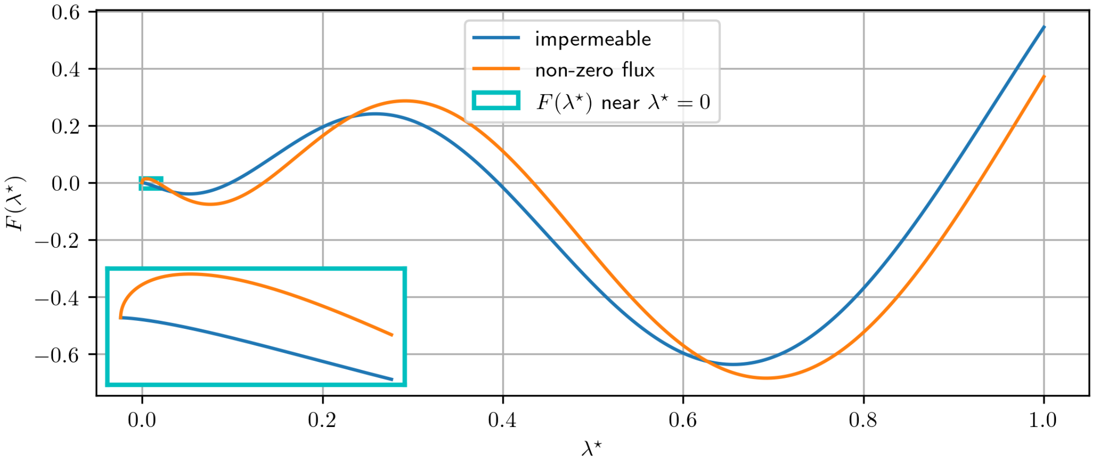

Figure 4.2: Effect of domain boundary conditions (BCs) on the behaviour of $F(\lambda)$ from equation (4.7) near zero. An arbitrary domain with two types of barriers at the domain ends is used: impermeable ($\kappa = 0$, as used throughout this work) and permeable ($\kappa > 0$, labelled "non-zero flux"). The running variable $\lambda^\star$ is used instead of λ, which is reserved for the roots of F. In the impermeable case $\mathrm{d}F/\mathrm{d}\lambda^\star = 0$ at the origin, but in the permeable case a discontinuity $\mathrm{d}F/\mathrm{d}\lambda^\star \to \infty$ develops as $\lambda^\star \to 0$.

approximation as one cannot take an infinite number of eigenvalues. As shown later in section 4.4.1 the relative importance of higher eigenvalues in the summation in equation (4.4) reduces with increasing solution time t. A sensible truncation point is problem-specific and needs to be chosen based on experience. For the domains in this work, $n_{\max}$ is usually $\mathcal{O}(10^3)$. Note that due to the first eigenvalue $\lambda_1 = 0 \iff \kappa_0 = \kappa_m = 0$. This eigenvalue corresponds to a constant eigenmode that describes the steady-state solution. The effect of domain boundary conditions $\kappa_{\{0,m\}}$ is illustrated in figure 4.2. It plots $F(\lambda^\star)$ near zero for a case with impermeable domain ends ($\kappa = 0$) and with finite, non-zero permeability. In the former case the function approaches $F = 0$ with $\mathrm{d}F/\mathrm{d}\lambda^\star \to 0$, while the latter case results in a discontinuity of $\mathrm{d}F/\mathrm{d}\lambda^\star \to \infty$.

As shown later, calculating the eigenvalues is computationally expensive. However, for a given domain with fixed parameters this only needs to be done once. The eigenvalues then fully characterise the solution. Evaluation of the solution requires the eigenmodes to be evaluated at the desired locations inside the domain. A high number of linearly-spaced query points $x_q \in [0, b_m]$ is used to discretise the domain and obtain the eigenmodes $\nu(x_q)$ by solving equation (4.5) as done by Moutal et al. (2019).

4.2.3 Behaviour of the transcendental equation

The eigenvalues λ of the diffusion operator are the roots of $F(\lambda^\star)$ in equation (4.7). The auxiliary variable $\lambda^\star$ is used when F is evaluated on a continuous range to differentiate the running variable from the distinct eigenvalues. There is a singularity in equation (4.7)

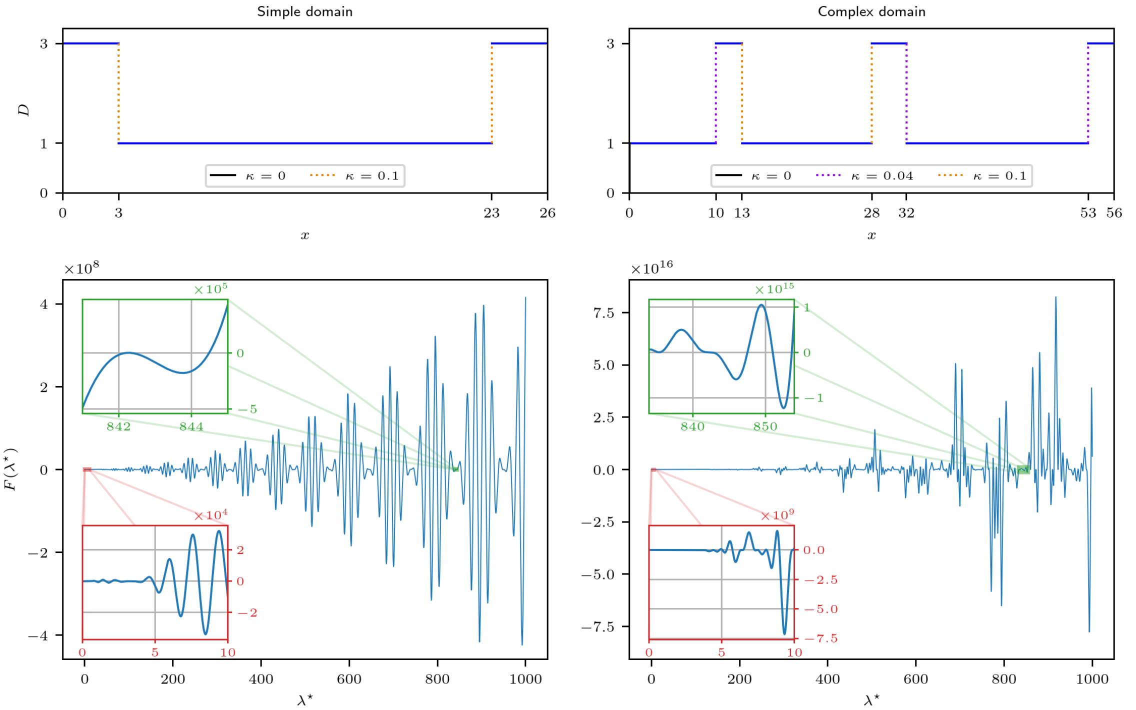

Figure 4.3: Function $F(\lambda^\star)$ plotted for two different domains. Each plot shows $F(\lambda^\star)$ until $\lambda^\star_{\text{max}} = 10^3$ and zooms in on regions near zero (red) and at high values of $\lambda^\star$ (green). These inset axes highlight the high oscillations that this function exhibits at different scales and the overall difference in magnitude that make root finding difficult.

at $\lambda^\star = 0$ for $\kappa = 0$. This can cause numerical problems when attempting to find the roots located very close to the origin.

A small modification to equation (4.7) is made in an attempt to improve the behaviour in the vicinity of $\lambda^\star = 0$. Only considering the cases $\lambda^\star > 0$ would result in failing to find all other eigenvalues $0 < \lambda_2 \ll 1$. This requires the evaluation of F in the range $\lambda^\star \in [\varepsilon, \infty]$ for some arbitrary ε, usually machine precision $\mathcal{O}(10^{-16})$. An alternative approach is as follows:

Since $F(\lambda_1) = F(0) := 0$ holds for the chosen boundary conditions, the roots of an alternative function, $\hat{F}(\lambda^\star) = \lambda^\star \cdot F(\lambda^\star)$, are found instead. This does not alter the location of the roots λ_n and has little effect on the root finding process. To improve readability, the "hat" is dropped and F used to mean $\hat{F}$ henceforth.

Figure 4.3 shows $F(\lambda^\star)$ for two domains: A simple three-compartment system resembling a cell surrounded by small extra-cellular gaps; and a larger domain representing an array of neighbouring cells with more arbitrary lengths and different membrane permeabilities. For the first case, the oscillatory, periodic nature of the function becomes apparent. As the domain becomes more complex and more unique values of L_k, D_k, and κ_k are used, more frequencies appear in F. The added domain complexity also increases the amplitude of the function significantly.

Moutal et al. (2019) observed an apparent behaviour of $F(\lambda^\star)$, namely that there are no double roots ($F'(\lambda) \neq 0$), no saddle points, and that (at the extrema) $F''(\lambda) \cdot F(\lambda) < 0$ (all minima $[F'' > 0]$ on one side $[-F]$, all maxima $[F'' < 0]$ on the other side $[+F]$ of the x-axis). This conjecture observed by Moutal et al. (2019, pp. 16–17) was also confirmed numerically in this investigation. Attempts to prove this analytically by induction, starting with a simple two-compartment case, have failed to offer a definitive proof for this behaviour.

The large magnitudes and gradients of $F(\lambda^\star)$ may pose problems with root finding. The use of transforms to scale equation (4.7) was investigated in an attempt to mediate some of the issues encountered. The "logicle" transform (Parks et al., 2006) was ruled out because it relies on too many parameters that need to be carefully selected on a case-by-case basis. Linear transformation in x (stretching) and/or y (scaling), meaning the domain and range of the function $F(\lambda^\star)$, is possible but not very useful due to the nature of floating point numbers. Anecdotally, scaling in x helps in certain circumstances when numerical error at large $\lambda^\star$ values causes problems locating the exact root. However, these numerical phenomena need to be accepted since transforming back to the original x-scale will introduce similar problems. Likewise, Moutal et al. (2019) observed that two roots may numerically collapse to the same root due to numerical(in)accuracy. Therefore, while scaling may help with robustness of the algorithm, it does not help with overall accuracy.

Non-linear transformations of F into $\bar{F}$ like clipping to a threshold, i.e. $\bar{F} = \text{sign}(F) \cdot \min(F_{\max}, |F|)$, or normalising the function, i.e. $\bar{F} = \text{sign}(F) \cdot 1$, are other possible approaches. They both help avoid the large vertical scales, but introduce discontinuities. These prevent methods relying on the derivative of F and the smoothness of the function, which helps approach and find the small extrema near $F \approx 0$. These methods also mean that the roots are now dependent on the interrogation window/step size. Overall, the global shape of F is too dependent on parameters to find something else. As a result, it was decided to not make use of transformations.

4.3 An efficient and convergent root finding algorithm

Considering the highly non-linear nature of equation (4.7), it quickly becomes apparent that no closed-form expression for the eigenvalues exists. The roots of the transcendental equation must therefore be found numerically, making the approach semi-analytical. Inspecting the behaviour of $F(\lambda^\star)$ even for simple domains as shown in figure 4.3 also suggests that traditional root finding techniques may not be suitable. Besides, evaluating F can be computationally expensive as the number of layers in the domain increases, due to the need for repeated matrix multiplication involving λ. As such, an efficient algorithm was developed without sacrificing accuracy and robustness in finding the roots.

In their paper, Moutal et al. (2019) find the roots of F using a novel and efficient algorithm specifically tailored to the problems they considered. It marches along $\lambda^\star$ with a variable step size and looks for sign changes in F to determine an approximate root location in the given interval. The algorithm relies on the apparent property of $F(\lambda^\star)$, also described above, that any two roots are separated by a local extremum ($F' = 0$, obtained numerically by evaluating F at $\lambda^\star \pm \epsilon$) in order to locally refine the function. While their method is very fast, investigations performed as part of this work have found that the approach can sometimes lead to missing (and occasional duplicate) roots, primarily in regions with many closely-spaced roots and roots between extrema of low relative magnitude (compared to $\max(|F|)$ in the surrounding region). Furthermore, the dependence on user-defined tolerances and an initial guess for the step length also makes the approach by Moutal et al. (2019) error-prone and not suitable for parameter studies, where manual input for each choice of parameters is cumbersome.

4.3.1 Chebyshev interpolation

The problem requires that all roots of the function up to $\lambda^\star_{\text{max}}$ be found. To achieve this, a viable approach is to fit F with a function whose roots can be computed reliably.

Initially, attempts were made to evaluate the function at different levels of refinement and perform piece-wise fitting using simple polynomials of varying degrees whose roots are easily calculable. However, the fit is often poor and not guaranteed to converge. This may be explained by the fact that the polynomial degree of the fit depends on the number of roots in the (sub)domain, something that is not known a priori.

Given that the function is smooth and continuously differentiable, it lends itself to interpolation with Chebyshev polynomials. In fact, convergence is guaranteed for Lipschitz continuous functions (Aurentz et al., 2017). This solves the problem of the function being highly oscillatory and having a much larger vertical than horizontal scale.

In this work ChebPy (Richardson et al., 2021) is used. It is a Python implementation of the popular MATLAB package Chebfun (Battles et al., 2004; Driscoll et al., 2014), is used. To improve reproducibility, the decision was taken to not rely on the proprietary software MATLAB, because Chebfun does not work in Octave due to lack of support for MATLAB-style classes and object-orientated programming in general. Instead Python was used, which is easily and freely available. Through code inspection (both ChebPy and Chebfun are open-source), contribution to the ChebPy source code, and comparison with a custom MATLAB version that utilises the same algorithm but with Chebfun as backend, it was ensured that the crucial parts of Chebfun were present and reliably implemented.

Using ChebPy, $F(\lambda^\star)$ can be interpolated with Chebyshev polynomials $C(\lambda^\star)$. For a given interval in $\lambda^\star$, the number of Chebyshev coefficients is determined automatically (Aurentz et al., 2017). After a fit has been obtained for the interval, the extrema of the newly obtained Chebyshev polynomial are computed. These extrema then serve as

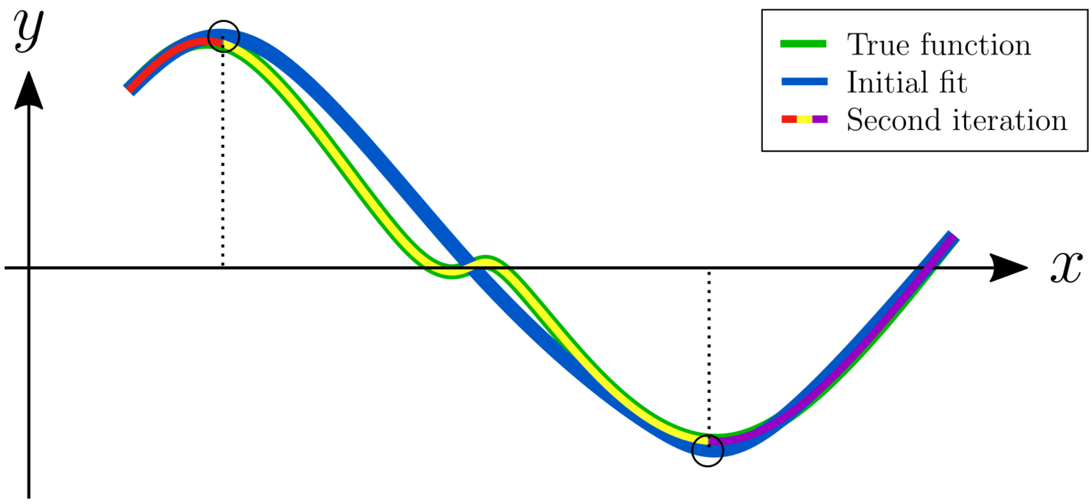

Figure 4.4: Graphical explanation of the recursive Chebyshev interpolation algorithm. Consider an arbitrary smooth function $y(x)$. Its initial interpolation approximates the extrema of larger magnitude well, but fails to recognise the two low-magnitude extrema near $y = 0$. The next iteration operates on intervals defined by the previously-found extrema.

initial condition for the next step of the iteration. Figure 4.4 illustrates this refinement algorithm.

Figure 4.5 shows the Chebyshev coefficients and function values for $C(\lambda^\star)$, $\lambda^\star \in [0, 10^4]$. The initial global fit of $\lambda^\star$ over the entire $\lambda^\star$-range shows a poor fit near zero. The fact that F

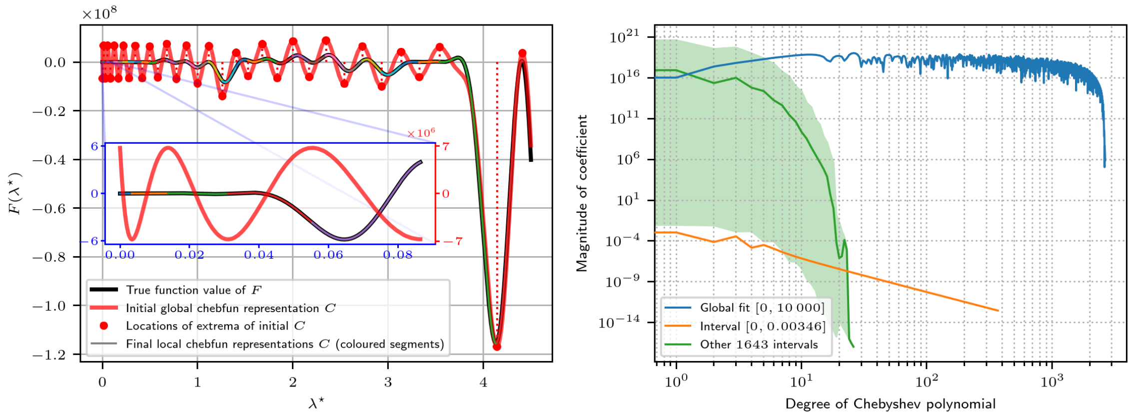

Figure 4.5: Interpolation of $F(\lambda^\star)$ on the "Complex" domain from figure 4.3 using Chebyshev polynomials $C(\lambda^\star)$. **(Left)**: The global fit over the entire range $[0, 10^4]$ shows large oscillations and a poor fit for $\lambda^\star < 5$. Splitting the function into subintervals (each shown in a different colour) bounded by the extrema of C_{global} allows for a more accurate fit. **(Right)**: Chebyshev coefficients of C. The global approximation requires a large polynomial degree with a late drop in coefficient magnitude, while the local approximations converge much faster. The first interval near $\lambda^\star = 0$ shows a slow but steady drop in magnitude, but the coefficients of the other 1643 intervals converge quickly. The solid line represents the median, while the shaded region is bound by the minima and maxima of all local fits. The spike near the tail occurs because most coefficients end at 20.

is composed of trigonometric functions may be the reason why initial attempts to interpolate were relatively unsuccessful. When interpolating on subintervals of $[0, \lambda^\star_{\max}]$ (split at the extrema of the global approximation), there is a significant reduction in polynomial degree and an improved fit. The poor convergence in the first subinterval $[0, 0.00346]$ is due to the careful chopping algorithm of the automatic constructor, which does not find a suitable numerical plateau despite the low absolute magnitude of the coefficients (Aurentz et al., 2017). This could be mediated by choosing a lower tolerance.

4.3.2 Recursive root finder

Any well-behaved function without repeated roots, as considered in this work, has at most one root between subsequent local extrema. This forms the basis of the root finding algorithm. It is similar to the observation by Moutal et al. (2019) that there is exactly one extremum between roots, but the presented algorithm does not rely on a function to have such a property. In fact, the algorithm is suitable for any function $f(x)$ provided it is smooth and has simple roots. Three requirements to a good root finder are:

R1. It has to be fast and scale well with $x_{\max}$ (in this case $\lambda^\star_{\max}$),

R2. It must find all roots (to a given tolerance ε),

R3. It should not rely on a-priori parameter selection (except ε).

As stated previously, an initial global interpolation C is obtained and divided into smaller subintervals by splitting at the extrema of C. This procedure is done recursively, providing a convergence mechanism. In addition, as seen in figure 4.4, this avoids missing features by subdividing the function into more manageable chunks. It also has the added benefit that it is computationally less expensive to operate on many small interpolations than on one big function, especially if the algorithm were to be parallelized. Figure 4.5 gives an indication of the size of the global and local polynomials. The procedure introduced here is described in algorithm 4.1. The recursive component can be found in line 10, while the Chebyshev interpolation is carried out in line 17.

The algorithm is implemented as a wrapper around the `chebfun` function in ChebPy. In theory it is possible to implement this closer to the spirit of Chebfun, i.e. use internal breakpoints to partition the domain (Driscoll et al., 2014) and employ the `roots` routine to find the zeros of $C(\lambda^\star)$. However, it was found that more stringent checks are needed to save extra work and avoid re-computing intervals, and to ensure no gaps in the domain occur where roots could hide. The latter is particularly important when roots are closely spaced. This additional logic is not described here, but can be seen in the source code (appendix B.2.3).

Algorithm 4.1: Core procedures of the root finding algorithm. The function SUBDIVIDE in algorithm 4.1 serves as the entry point and is recursively called in algorithm 4.1. The function FIND_EXTREMA performs the Chebyshev interpolation in algorithm 4.1. For all other functions that are not listed here, a trivial implementation is assumed.

```
Input: A function $F(\lambda^\star)$; an initial set of breakpoints $[\lambda^\star_{\min}, \lambda^\star_{\max}]$
Output: A new set of breakpoints where the intervals contains no additional extrema

SUBDIVIDE($F(\lambda^\star)$, $[0, 10^4]$)          ▷ Entry point with a common value for $\lambda^\star_{\max}$

function SUBDIVIDE($F$, oldpoints)
    intervals ← PAIRS(oldpoints)          ▷ Convert into list of interval end point pairs
    newpoints ← $\emptyset$          ▷ Initially empty
    for $[\text{left}, \text{right}]$ in intervals do          ▷ Operate on one pair at a time
        extrema ← FIND_EXTREMA($F$, left, right)
        if extrema equal to $[\text{left}, \text{right}]$ then          ▷ Exit condition
            APPEND(newpoints, extrema)          ▷ Store this interval
        else
            listofpoints ← SUBDIVIDE($F$, extrema)          ▷ Recurse
            EXTEND(newpoints, listofpoints)          ▷ Store the list of intervals
        end if
    end for
    return newpoints          ▷ A new list of interval end point pairs
end function

function FIND_EXTREMA($F$, a, b)
    $C$ ← chebfun($F$, $[a, b]$)          ▷ Adaptive construction of chebfun
    $C'$ ← $\mathrm{d}C/\mathrm{d}x$          ▷ Compute the derivative of chebfun
    extrema ← $x \quad \forall \quad C'(x) = 0$          ▷ Extrema are the roots of $C'$
    return UNIQUE($[a, \text{extrema}, b]$)          ▷ Consider end points as extrema, too!
end function
```

Once all intervals of interest are found, the single root is computed in each interval $[\lambda^\star_L, \lambda^\star_R]_j$ (if one exists, as determined by $F(\lambda^\star_{L,j}) \cdot F(\lambda^\star_{R,j}) < 0$) using Brent's algorithm* (Brent, 1971). Double roots cannot be found using this method, but as discussed earlier the eigenvalues are simple. In addition $\lambda_1 = 0$ needs to be enforced in the first interval, where the algorithm otherwise would not search for a root since $F(\lambda^\star_{L,1}) = F(\lambda_1) = 0$. An example of the resulting root locations is given in figure 4.6, which compares the initial estimation based on C_{global} and after convergence of the root finding algorithm. The histogram indicates, for this specific F, the density of extrema and roots. It is observed that F has the same number of extrema as roots. The figure also shows where the global fit C_{global} fails to find the roots (and extrema). Most roots are missed in $[0, 500]$ and the number decreases as $\lambda^\star$ increases.

---

*The SciPy (Virtanen et al., 2020) implementation of Brent's algorithm, `brentq`, was used.

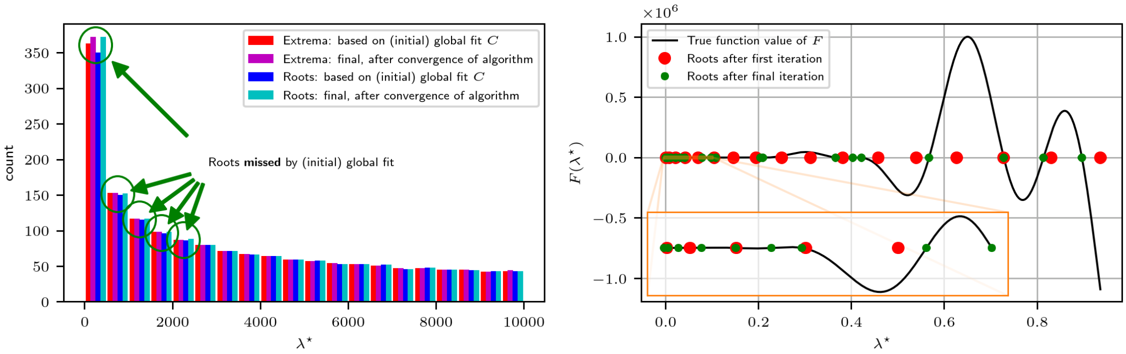

Figure 4.6: Different iterations of the root finding algorithm. Shown are the initial guess based on the global Chebyshev interpolation and the final locations after convergence. **(Left)**: Histogram of extrema and roots of F. The initial global fit C_{global} is insufficient to represent the function and find all of its roots. The recursive element in the root finder finds additional extrema and roots until convergence. Regions where the initial global fit fails to find roots are indicated. A large number of roots (and missed ones) are located at $\lambda^\star < 10^3$. **(Right)**: Behaviour of $F(\lambda^\star)$ and locations of roots near 0, showing that many roots are missed in $[0, 1]$ initially.

To avoid problems with what was describe in figure 4.4 a final splitting and interpolation of the subdomains could be implemented. This would ensure that the algorithm has in fact converged for intervals of large horizontal scale between extrema.

4.4 Verification of the analytical solution

As described above, the eigenvalues (roots of equation (4.7)) are found numerically up to λ_{max}. The solution $U(x_q, t)$ is then evaluated by summation of the series in equation (4.4) and is therefore semi-analytical. As a consequence, numerical errors introduced by the root finding procedure manifest themselves as errors in the solution. Here, these errors are quantified using two approaches: comparison with a known solution and sensitivity analysis.

4.4.1 Known solutions

Consider diffusion in a single compartment, defined by the (non-dimensional) parameters $D_0 = 0.5$, $L = 2$, and $x_0 = 1$. For this case of parallel plates (Tanner et al., 1968), the eigenvalues are known to be

$$\lambda_n = \left(\frac{n\pi}{L}\right)^2 D_0 \tag{4.10}$$

and the eigenmodes are

$$\nu_n(x) = \sqrt{a_n}\cos\left(\frac{n\pi}{L}x\right) \tag{4.11}$$

with $a_0 = \frac{1}{L}$ and $a_{n>0} = \frac{2}{L}$. This is used to verify that the root finding algorithm returns all roots and to test the accuracy of those roots. With strict tolerances, $\mathcal{L}_\infty$ and $\mathcal{L}_2$ norms

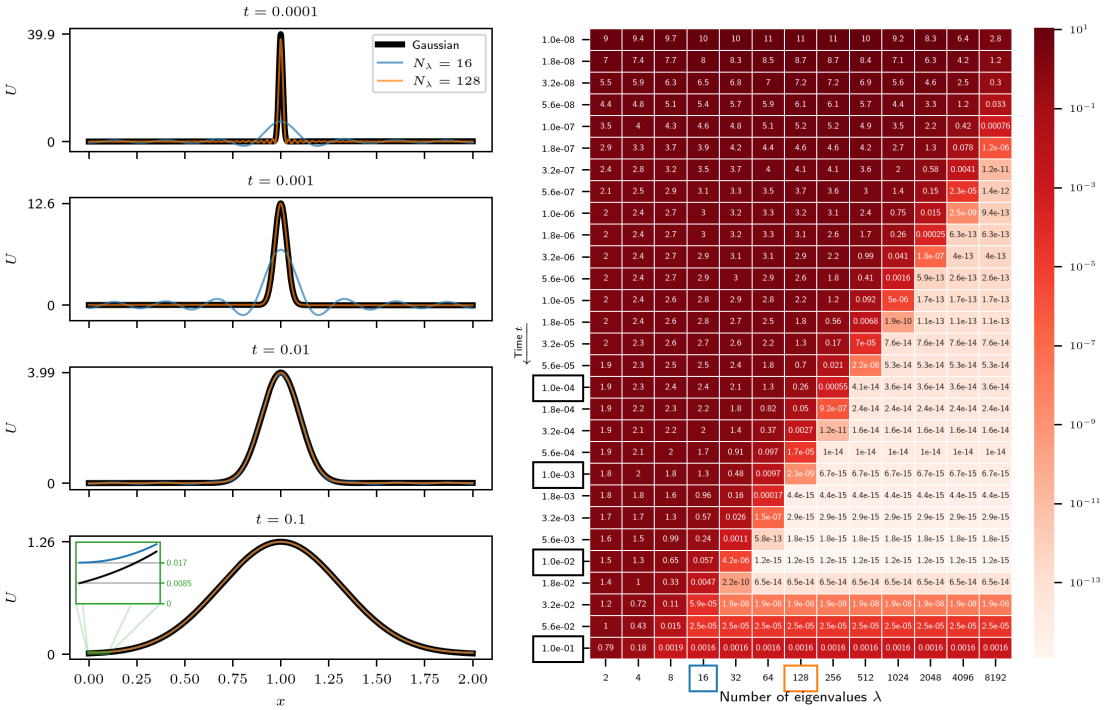

Time t	2	4	8	16	32	64	128	256	512	1024	2048	4096	8192
1.0e-08	9	9.4	9.7	10	10	11	11	11	10	9.2	8.3	6.4	2.8
1.8e-08	7	7.4	7.7	8	8.3	8.5	8.7	8.7	8.4	7.1	6.3	4.2	1.2
3.2e-08	5.5	5.9	6.3	6.5	6.8	7	7.2	7.2	6.9	5.6	4.6	2.5	0.3
5.6e-08	4.4	4.8	5.1	5.4	5.7	5.9	6.1	6.1	5.7	4.4	3.3	1.2	0.033
1.0e-07	3.5	4	4.3	4.6	4.8	5.1	5.2	5.2	4.9	3.5	2.2	0.42	0.00076
1.8e-07	2.9	3.3	3.7	3.9	4.2	4.4	4.6	4.6	4.2	2.7	1.3	0.078	1.2e-06
3.2e-07	2.4	2.8	3.2	3.5	3.7	4	4.1	4.1	3.6	2	0.58	0.0041	1.2e-11
5.6e-07	2.1	2.5	2.9	3.1	3.3	3.5	3.7	3.6	3	1.4	0.15	2.3e-05	1.4e-12
1.0e-06	2	2.4	2.7	3	3.2	3.3	3.2	3.1	2.4	0.75	0.015	2.5e-09	9.4e-13
1.8e-06	2	2.4	2.7	3	3.2	3.3	3.1	2.6	1.7	0.26	0.00025	6.3e-13	6.3e-13
3.2e-06	2	2.4	2.7	2.9	3.1	3.1	2.9	2.2	0.99	0.041	1.8e-07	4e-13	4e-13
5.6e-06	2	2.4	2.7	2.9	3	2.9	2.6	1.8	0.41	0.0016	5.9e-13	2.6e-13	2.6e-13
1.0e-05	2	2.4	2.6	2.8	2.9	2.8	2.2	1.2	0.092	5e-06	1.7e-13	1.7e-13	1.7e-13
1.8e-05	2	2.4	2.6	2.8	2.7	2.5	1.8	0.56	0.0068	1.9e-10	1.1e-13	1.1e-13	1.1e-13
3.2e-05	2	2.3	2.6	2.7	2.6	2.2	1.3	0.17	7e-05	7.6e-14	7.6e-14	7.6e-14	7.6e-14
5.6e-05	1.9	2.3	2.5	2.5	2.4	1.8	0.7	0.021	2.2e-08	5.3e-14	5.3e-14	5.3e-14	5.3e-14
1.0e-04	1.9	2.3	2.4	2.4	2.1	1.3	0.26	0.00055	4.1e-14	3.6e-14	3.6e-14	3.6e-14	3.6e-14
1.8e-04	1.9	2.2	2.3	2.2	1.8	0.82	0.05	9.2e-07	2.4e-14	2.4e-14	2.4e-14	2.4e-14	2.4e-14
3.2e-04	1.9	2.1	2.2	2	1.4	0.37	0.0027	1.2e-11	1.6e-14	1.6e-14	1.6e-14	1.6e-14	1.6e-14
5.6e-04	1.9	2.1	2	1.7	0.91	0.097	1.7e-05	1e-14	1e-14	1e-14	1e-14	1e-14	1e-14
1.0e-03	1.8	2	1.8	1.3	0.48	0.0097	2.3e-09	6.7e-15	6.7e-15	6.7e-15	6.7e-15	6.7e-15	6.7e-15
1.8e-03	1.8	1.8	1.6	0.96	0.16	0.00017	4.4e-15	4.4e-15	4.4e-15	4.4e-15	4.4e-15	4.4e-15	4.4e-15
3.2e-03	1.7	1.7	1.3	0.57	0.026	1.5e-07	2.9e-15	2.9e-15	2.9e-15	2.9e-15	2.9e-15	2.9e-15	2.9e-15
5.6e-03	1.6	1.5	0.99	0.24	0.0011	5.8e-13	1.8e-15	1.8e-15	1.8e-15	1.8e-15	1.8e-15	1.8e-15	1.8e-15
1.0e-02	1.5	1.3	0.65	0.057	4.2e-06	1.2e-15	1.2e-15	1.2e-15	1.2e-15	1.2e-15	1.2e-15	1.2e-15	1.2e-15
1.8e-02	1.4	1	0.33	0.0047	2.2e-10	6.5e-14	6.5e-14	6.5e-14	6.5e-14	6.5e-14	6.5e-14	6.5e-14	6.5e-14
3.2e-02	1.2	0.72	0.11	5.9e-05	1.9e-08	1.9e-08	1.9e-08	1.9e-08	1.9e-08	1.9e-08	1.9e-08	1.9e-08	1.9e-08
5.6e-02	1	0.43	0.015	2.5e-05	2.5e-05	2.5e-05	2.5e-05	2.5e-05	2.5e-05	2.5e-05	2.5e-05	2.5e-05	2.5e-05
1.0e-01	0.79	0.18	0.0019	0.0016	0.0016	0.0016	0.0016	0.0016	0.0016	0.0016	0.0016	0.0016	0.0016

Figure 4.7: Verification cases of diffusion between plates at different times and with different number of eigenvalues. Conversion from number of eigenvalues to $\lambda^\star_{\text{max}}$ is trivially done with equation (4.10). Left: Short-time solutions show oscillations at lower (insufficient) number of eigenvalues. At longer times, the tail of the distribution deviates from the Gaussian due to the zero-flux condition at the plates. Right: Heat map of the error, calculated as the area between the curves U and $G = U_{\text{Gauss}}$. Since $\int U\,\mathrm{d}x = 1$, an error $\ll 1$ is required for an acceptable solution. Note that the time on the y-axis is increasing from top to bottom to match the plots on the left.

have values of 10^{-17} for the error of all λ_n up to $n = 91$. The difference is larger than zero for most roots, because $F(\lambda_n)$ itself does not evaluate to zero due to numerical error (of the order of 10^{-10}, increasing with λ).

At short times, when the concentration has not reached the barriers at $x = x_0 \pm 1$, the solution should match a Gaussian (normal) distribution with mean $\mu = x_0$ and variance $\sigma^2 = 2D_0 t$ (or simply $\sigma^2 = t$ since $D_0 = 0.5$). Recall the definition of the diffusion propagator. For a homogeneous medium without barriers, it satisfies the Gaussian distribution

$$U(x, t > 0) = \frac{1}{\sigma\sqrt{2\pi}} \exp\left(-\frac{1}{2}\left(\frac{x - x_0}{\sigma}\right)^2\right). \tag{4.12}$$

This occurs until time $t = T$ where $T \ll \frac{(x-x_0)^2}{2D_0} = 1$. At very short times $t \ll T$, the solution $U(x_q, t)$ displays oscillations as seen in figure 4.7. For cases like this, a larger number of roots is typically required to remove the artefactual oscillations.

The relationship between time t and the number of eigenvalues required to accurately represent the solution at t is complicated as can be observed in the heat map in figure 4.7.

For very short times $t < 10^{-7}$, this requires $N_\lambda \gg 10^4$ eigenvalues for an acceptable error. As t is increased, large eigenvalues become less important to the solution. Compared to a solution with $N_\lambda \to \infty$, this would continue until a steady-state is reached and only the first eigenvalue/mode is necessary to represent the solution. However, comparison to the Gaussian reference solution instead reveals that the effective T occurs near $t > 10^{-2}$ when the error increases irrespective of the number of eigenvalues used. This is due to the Gaussian approximation based on free diffusion diverging from the true solution for diffusion between parallel plates as described in equations (4.10) and (4.11). The time at which the error becomes unacceptable may be estimated using the error function (erf).

The solution at short times displays negative values for $U(x,t)$. An attempt to solve this by Fejér summation (Fejér, 1903) corrects the negative values but leads to poor convergence overall and a much lower peak at $x_{q,0}$.

4.4.2 Sensitivity analysis

In section 4.4.1 it was shown that a large number of eigenvalues are needed to accurately represent a solution, especially at shorter times. Here, the effects that numerical error in the root finding has on the accuracy of the diffusion solution are investigated by means of a sensitivity study. Two types of error are considered: inaccuracies in the root locations and missed roots. The results are shown in figure 4.8.

All 3021 eigenvalues in $\lambda^\star \in [0, 10^5]$ are modified by multiplying them with random perturbations of order $\mathcal{O}(\epsilon)$ in the range 0 to 0.5 %. For each value of $\epsilon_{\max}$ 10 repetitions are performed, each time drawing all perturbations to the eigenvalues randomly from $[0, \epsilon_{\max}]$. The resulting solutions U are plotted in figure 4.8 at different time points. Large fluctuations in U (including unphysical negative values) can be observed for $t = 10^{-4}$ and $t = 10^{-3}$ in the tail of the distribution. At $t = 10^{-2}$ the error also manifests itself as a flattening of the peak at x_0 and a slight asymmetric shift away from the reference solution. In all cases the discontinuity at the barriers is respected and the error is not symmetric about x_0.

The right half of figure 4.8 shows the effect of missing roots altogether. For each eigenvalue i, λ_i and ν_i are removed from the series solution in equation (4.4). Here, only the first 100 eigenvalues are considered, since higher eigenvalues have diminishing influence. A similar behaviour to figure 4.7 can be observed regarding the relationship between time t and eigenvalues. In the heat map the error magnitudes vary periodically with eigenvalue index. This is most likely explained by the eigenfunction for this specific $F(\lambda)$, which contains periodic elements similar to those in equation (4.7).

4.4.3 Error guarantees

One can verify that all roots have been found within a given range by checking the sign change of the eigenmodes. It is important to use a large number of query points to capture

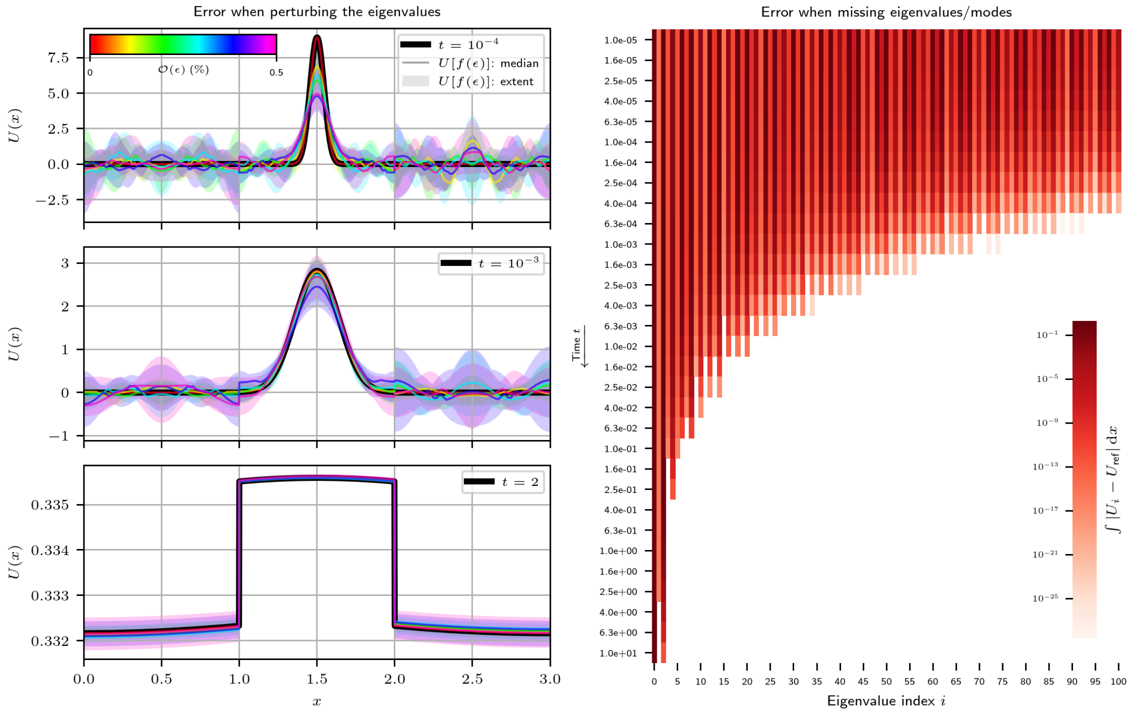

Figure 4.8: Sensitivity of analytical solution U to errors in the eigenvalues. The considered domain has three compartments with parameters $L = 10$, $D = 1$, and $\kappa = 0.1$. In total, 3021 eigenvalues are found in $\lambda^\star \in [0, 10^5]$. **(Left)**: All eigenvalues were perturbed with random errors (uniform between 0 and $\mathcal{O}(\epsilon)$). Shown are 6 different values of ϵ_{max} in the range 0 to 0.5 %. The plotted solutions for each ϵ-value are the maximum extent and median of U of each 10 random repetitions. **(Right)**: Sensitivity of the solution at different time points to a single eigenvalue i missing. The error is the area (integral) between the reference and modified solution and $\int U \, \mathrm{d}x = 1$.

the sign change accurately. Alternatively, applying Chebyshev interpolation and finding the roots of the interpolant using the same method as used in section 4.3 might provide more reliable results. Throughout this work, checks were always performed to ensure that all roots are found and the solver tolerances have been adjusted if necessary.

4.5 Discussion

An analytical solution for diffusion in one-dimensional arbitrary layered media was presented. This approach is based on the spectral decomposition of the diffusion operator, for which the eigenvalues need to be determined numerically from equation (4.7). By means of a novel root finding algorithm that uses recursive Chebyshev polynomial interpolation it is possible to efficiently find all these eigenvalues up to machine accuracy. A rigorous analysis was carried out to study the errors in the solution which is semi-analytical by nature. The analytical solution can be used as reference solution for other methods, for example to verify statistical models in Monte Carlo random walk simulations. In this work, this is done later in section 6.3. Note also that recently Moutal et al. (2020) extended their method to diffusion MRI in periodic media.

The results of this chapter have implications beyond application to diffusion in biological tissue. For example, diffusion of colloidal fluids in porous media (Kärger, 1985, 2012) shares similarity with biological tissue. Additionally, heat transfer problems can often be reduced to 1D. The root finding algorithm presented here is novel and may find universal application to general root finding procedures.

Chapter 5

Diffusion as a Random Walk Process

Contents

5.1 Introduction

Random walks are widely used to model the underlying stochastic processes in a range of applications, such as astrophysics (Chandrasekhar, 1949), diffusion in porous media (Kärger et al., 2012), and statistical finance (Scalas, 2006). Their validity and mathematical underpinning are well-explained in the review by Chandrasekhar (1943). Regarding the context of modelling diffusion in biological tissue, the textbook *Random Walks in Biology* (H. C. Berg, 1993) offers a good description of the basic concepts of a random walk.

Section 5.2 presents a general description of the approach, first in free diffusion and then near barriers. A thorough derivation for the correct treatment of walker-barrier interactions is then discussed in section 5.3. The numerical implementation is finally presented in section 5.4.

5.2 General approach

Consider a heterogeneous layered medium with scalar compartment-specific diffusion coefficient $D(\boldsymbol{x})$. The diffusion equation in equation (3.14) becomes

$$\frac{\partial U}{\partial t} = \boldsymbol{\nabla} \cdot (D \boldsymbol{\nabla} U) \ . \tag{5.1}$$

Its solution with initial condition $\delta(\boldsymbol{x} - \boldsymbol{x}_0)$ may be obtained by considering an ensemble of N_p massless, non-interacting particles* initially located at $\boldsymbol{x}_0$ performing a (discrete time) random walk. Again, equation (3.14) can be reduced locally to the heat equation

$$\frac{\partial U}{\partial t} = D_0 \boldsymbol{\nabla}^2 U \tag{3.18 [reproduced]}$$

inside each compartment with local diffusion coefficient D_0. The boundary conditions at the compartment barriers enforce the permeability of these membranes through an appropriate flux $D\boldsymbol{\nabla}U$ to “link” the solutions from separate compartments.

Unlike previously in chapters 3 and 4, where the solution $U(\boldsymbol{x}, t)$ described the concentration density in space and time, U now equivalently denotes the probability of finding a particle at a given position and time. Each walker, initially located at $\boldsymbol{x}(0)$, moves according to

$$\boldsymbol{x}(N_t \delta t) = \boldsymbol{x}(0) + \sum_{n=1}^{N_t} \delta \boldsymbol{x}(D(\boldsymbol{x}), \delta t) \tag{5.2}$$

where the N_t random steps $\delta \boldsymbol{x}$ of duration δt are statistically independent and scale with $\sqrt{D(\boldsymbol{x})\, \delta t}$.

5.2.1 Stepping in time and space

Let us limit ourselves briefly to homogeneous media with constant diffusion coefficient D_0 everywhere. This describes the behaviour of walkers away from barriers. In this case, the most basic example of a random walk is a one-dimensional walker originally located at the origin moving by either $+1$ or -1 every time step. Eventually, the walker will have covered every position in $\mathbb{Z}$. The unit step length implies $D\, \delta t = 0.5$, because $|\delta x| = \sqrt{2 D_0\, \delta t}$. This elementary example of “walking on a grid” uses constant stepping without resting.

Another approach is to draw the step length δx directly from the diffusion propagator, i.e. a normal distribution with variance $\sigma^2 = 2 D_0\, \delta t$. This results in a walk in $\mathbb{R}$. The advantage is obvious and clearly visible in figure 5.1: Fewer walkers and steps are needed to recover the propagator, because each step already satisfies the solution. As the number of steps is increased for the same diffusion time, the random walk that uses constant steps

---

*The choice of N_p is problem-specific and needs to be large enough to achieve a converged result. This will be addressed in section 6.2.2.

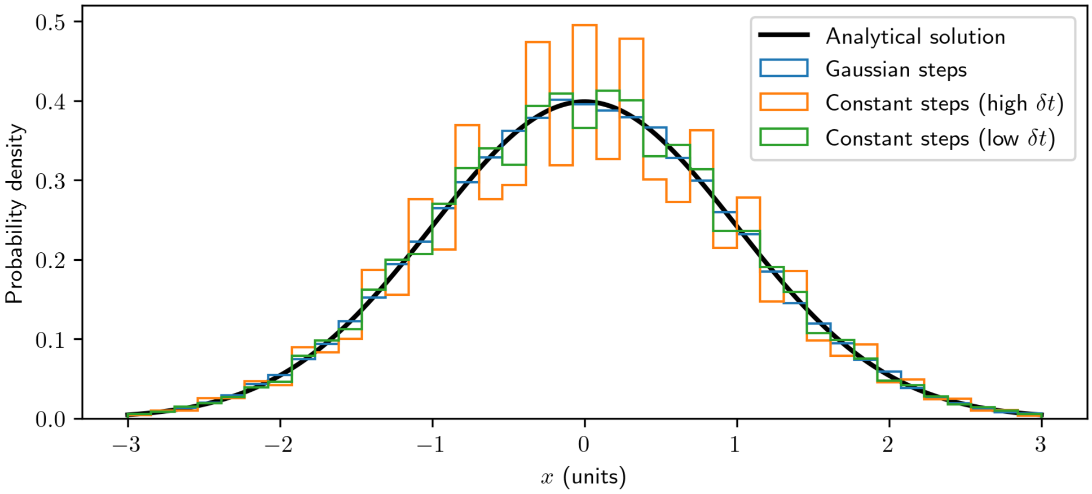

Figure 5.1: Effect of the different choices of random step length in 1D. All walkers were initially located at the origin and stepped with either normally-distributed or fixed step lengths. The histograms show final walker positions, compared with a Gaussian distribution. As expected, the normally-distributed steps match the target distribution well. Using (too few) constant steps causes a non-smooth histogram due to the finite number of positions. Increasing the temporal resolution results in convergence.

converges to the Gaussian distribution. As shown later, stepping with constant length and random direction is necessary in the presence of permeable barriers.

In higher dimensions the elementary random walk with constant steps results in 4 (2D) or 8 (3D) unique step vectors. These stencil points are all equally likely to occur. Alternatively, one may consider a circle or sphere of radius $R = \sqrt{2nD_0\,\delta t}$ for an n-dimensional random walk. The two-dimensional case is shown in figure 5.2. Given a random step direction, each

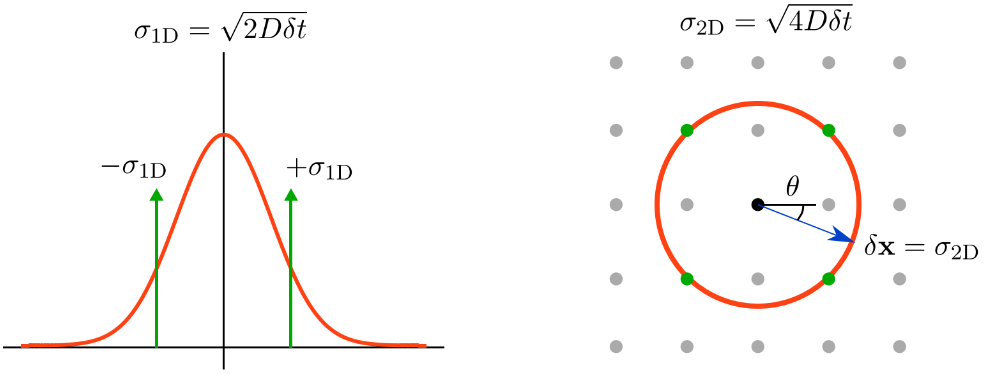

Figure 5.2: Different ways to draw random steps. **(Left)** In 1D, using a constant step length of $\sigma_{1\mathrm{D}}$ results in two steps $\pm\sigma_{1\mathrm{D}}$. Steps can also be drawn from a normal distribution. **(Right)** In 2D, the constant step length is $\sigma_{2\mathrm{D}}$. It can be drawn either with a uniformly-distributed orientation θ or by randomly selecting from 4 points on a grid. Alternatively, normally-distributed lengths are possible too by drawing the two step vector components from a Gaussian.

point is equally probable. In 2D the random orientation of the step needs to be uniformly distributed in $[0, 2\pi)$. In 3D a correct choice of random variables is required to ensure uniform sampling of the sphere's surface. Instead of (maybe intuitively) sampling the spherical coordinates θ (polar angle) and φ (azimuth angle) in their respective ranges $[0, \pi]$ and $[0, 2\pi)$, they must instead be drawn from two uniform random variables u and v both in $[0, 1)$ and computed as $\theta = \cos^{-1}(2u - 1)$ and $\varphi = 2\pi v$ (Fieremans et al., 2008). In an extension to the 1D case, all 2 or 3 Cartesian step vector components can also be drawn from independent Gaussian distributions. In summary, the following step types are possible:

- Fixed step length and random orientation, generated by
    - randomly sampling a circle/sphere in 2D/3D, or
    - randomly drawing each step vector component as ±1 and scaling;
- Gaussian step length and orientation, generated by
    - randomly drawing normally-distributed step vector components.

All these approaches have different rates of convergence as the number of walkers and time steps increases. Not only must the random walk recover the underlying diffusion coefficient D_0 from the mean squared displacement (MSD) at time t in isotropic, homogeneous media via ensemble averaging

$$\mathrm{MSD} = \langle |\boldsymbol{x}(t) - \boldsymbol{x}(0)|^2 \rangle = \frac{1}{N_p} \sum_{p=1}^{N_p} |\boldsymbol{x}_p(t) - \boldsymbol{x}_p(0)|^2 \equiv 2nD_0 t\,, \tag{5.3}$$

but it also has to sample inhomogeneous spaces effectively and uniformly. For example, constant stepping quickly recovers the MSD as the number of walkers increases even with a relatively low number of steps, but suffers from only sampling a (small) finite set of points. This is especially true if walkers are initially located at a common origin or seeded in a grid. In such a case an initial transient phase of the walker dynamics needs to be simulated. This can be avoided by true random seeding, i.e. drawing positions from a uniform distribution.

Furthermore, Powles et al. (1992) suggest a step limit of $\delta x \ll L$ for some characteristic geometric length scale L. However, this can still lead to bias in the results if the characteristic length (for example the cell diameter) is much larger than other features that the simulation is supposed to sense like irregular membrane shapes Γ.

A hybrid treatment may be possible where only walkers that are sufficiently far away from barriers execute Gaussian steps, thereby improving convergence while enabling

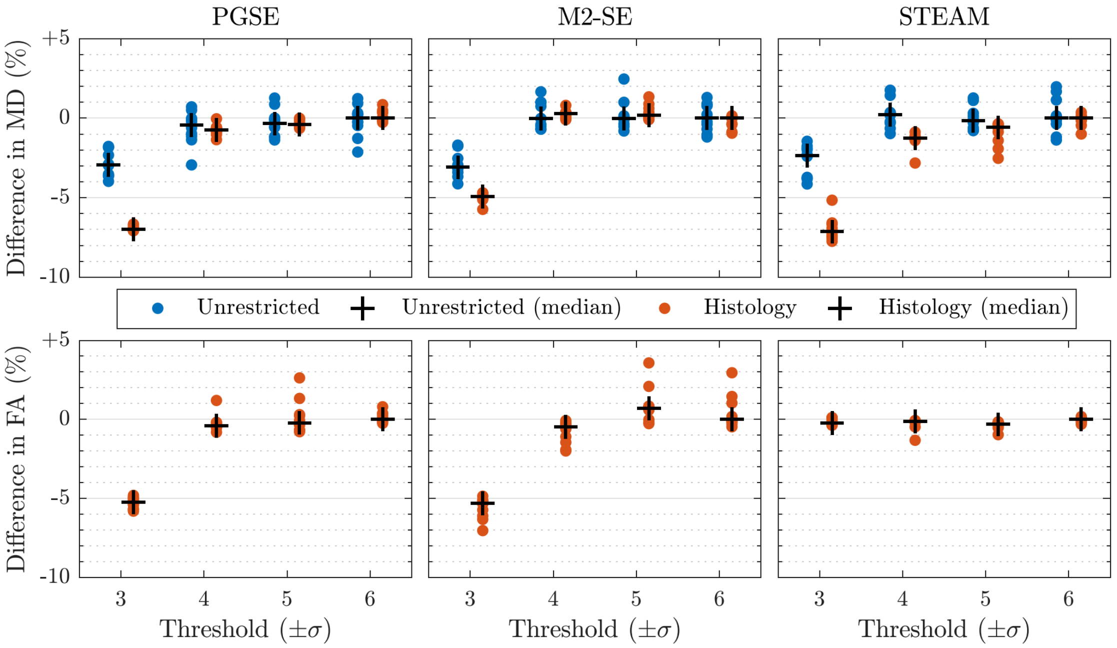

Figure 5.3: Convergence of apparent diffusion parameters for different thresholds for a truncated Gaussian step length. Both free (unrestricted) and restricted (histology-based) geometries are considered. FA is not shown for free diffusion as it is ill-defined. [*Reproduced with permission from (Rose et al., 2019c).*]

permeable membranes. If a maximum length for the step of e.g. 5 standard deviations[†] of the distribution is chosen, all walkers within that distance of the barrier carry out uniform steps. During the simulation the random walk may also be arbitrarily paused to coarsen or refine the time step δt. This is advantageous if the temporal resolution needs to be varied during some time interval, for example due to the application of very short magnetic gradients in the otherwise long STEAM sequence. In any case, conditional sub-stepping is prohibited. Changing between step types has to be determined before the step is drawn and cannot be done only if a step is found to intersect the barrier. Since substeps must not be forced to follow the bulk direction of the original step, conditional sub-stepping would introduce a conditional probability that biases the random walk against walking towards barriers.

In figure 5.3 the effect of drawing step lengths from a truncated normal distribution with increasing bounds is studied. Both free diffusion and diffusion in a histology-like (section 2.3.4) domain are simulated. For a truncation to a short maximum step length of $\pm 3\sigma$ significant errors are observed in the random walk and resulting DT-CMR parameters. As a result, truncation should be done such that $\delta x \geq 4\sigma$ even though $\pm 3\sigma$ already contains 99.7 % of step lengths.

[†] This corresponds to 1 in 1 744 278 steps being rejected. As shown in figure 5.3, this results in negligible bias in the random walk.

5.2.2 Distinction between walkers and spins

It is important to correctly define what a walker is. While the analogy is often found in MRI literature, random walkers are *not* directly equivalent to water molecules or spins. There are $\mathcal{O}(10^{25})$ H_2O-molecules in a litre of fluid. For common imaging voxel sizes of $1\,\mathrm{mm}^3$, this would require simulating $\mathcal{O}(10^{16})$ walkers. Given the Boltzmann distribution

$$\frac{N^+}{N^-} = \exp(-\frac{\Delta E}{kT}) \tag{5.4}$$

and the Zeeman effect

$$\Delta E = \gamma \hbar B_0 \tag{5.5}$$

the net number of spins in the voxel can be estimated. For a 3 T field at room temperature, this results in $N^+/N^- = 1 - 2.1 \times 10^{-5}$. While this is *almost* unity, the large number of H_2O-molecules still means that there are $\mathcal{O}(10^{11})$ measurable spins—an unmanageable amount for directly simulating each spin.

The random walk models Brownian motion as a solution to the diffusion equation. In fact, the random walk is simply another approach to solving the diffusion equation. For example, the jump probabilities in the random walk using constant step lengths find analogy in the 3-point stencil used in the finite difference scheme in section 3.3.3. Like in the continuum approach, where space is discretised into cells, magnetisation can be assigned to an *ensemble* of spins represented by a single walker. In reality each water molecule on average experiences $\mathcal{O}(10^{14})$ collisions per second (Feynman et al., 1964, sec. 41-1), which is neglected by assuming their statistical independence. Further, simulation of the complex molecular interaction with the tissue such as lipid bilayers (cell membranes) requires modelling molecular dynamics with software such as Smoldyn (Andrews et al., 2010) or MCell (Kerr et al., 2008; Stiles et al., 2001).

For the purposes of MR simulations, a walker represents a spin ensemble that contributes with equal weight to the diffusion signal. During the experiment, each walker collects phase ϕ as a result of the magnetic gradients (time-discretised into N_t intervals of duration δt and strength $\boldsymbol{G}$):

$$\phi(N_t\,\delta t) = \gamma \sum_{n=1}^{N_t} \boldsymbol{G}(n\,\delta t) \cdot \boldsymbol{x}(n\,\delta t)\,\delta t\,. \tag{5.6}$$

The resulting signal magnitude at readout is then computed by combining the phase ϕ_p of each of the N_p walkers with index p via

$$S = \frac{1}{N_p} \left| \sum_{p}^{N_p} e^{-\mathrm{i}\phi_p} \right| \tag{5.7}$$

where $\mathrm{i} = \sqrt{-1}$. Note that equation (5.7) is a discretised versions of equation (3.3). To accurately reflect the image acquisition, only walkers that are inside the imaging voxel at the time of echo are included. To account for this loss of concentration over diffusion time T, additional walkers need to be seeded in a buffer zone of size $\sqrt{2nDT}$ around the imaging voxel.

In the narrow pulse approximation (NPA) (P. T. Callaghan, 2010), co-simulation of the phase is not required. Instead, pure diffusion simulations can be carried out and post-processing based on the distances that the walkers have diffused. Equation (5.6) can be replaced with

$$\phi(\Delta) = q\hat{\boldsymbol{g}} \cdot \big(\boldsymbol{x}_p(\Delta) - \boldsymbol{x}_p(0)\big) \tag{5.8}$$

and the phase corresponding to instantaneous gradients with direction $\hat{\boldsymbol{g}}$ and wave number q can be calculated. Care must be taken to ensure the simulated time is not the full sequence from RF pulse to echo, but that diffusion happens only for a duration of Δ to comply with the NPA.

5.2.3 Stepping in the presence of barriers

Equation (5.2) describes a general random walk. Previously section 5.2.1 discussed stepping in regions where the diffusion propagator is Gaussian. Barriers such as cell membranes hinder or restrict diffusion, leading to non-Gaussian effects such as kurtosis and other deviations from the Gaussian distribution. When interacting with a barrier, each time step the net displacement vector $\delta\boldsymbol{x}$ is composed of a series of sub-steps $\delta\boldsymbol{x}_m$ that depend on the local environment and together make up the full step

$$\delta\boldsymbol{x} = \sum_m \delta\boldsymbol{x}_m \,. \tag{5.9}$$

This ensures that even complex interactions are handled correctly. For example, a walker located inside an impermeable cube near one of its corners may reflect off multiple faces in succession during the same time step. Later in section 5.4 a numerical implementation of this substepping is described.

In general, the interaction is resolved by first computing a probability of transit p_t, whose value is constant and deterministic, and then drawing a random number $\mathcal{U} \in [0, 1)$ to compare to p_t:

$$\delta\boldsymbol{x}_{m+1} = \begin{cases} \text{transit} & \text{if } \mathcal{U} < p_t, \\ \text{reflection} & \text{otherwise.} \end{cases} \tag{5.10}$$

While specular reflection is used in this work, other interactions are also possible. In particular, random scattering warrants further investigation given the imperfect membrane surface in real tissue.

For ease of explanation, let us introduce the one-dimensional simple single-barrier encounter shown in figure 5.4. Extension to higher dimensions is trivial and will be

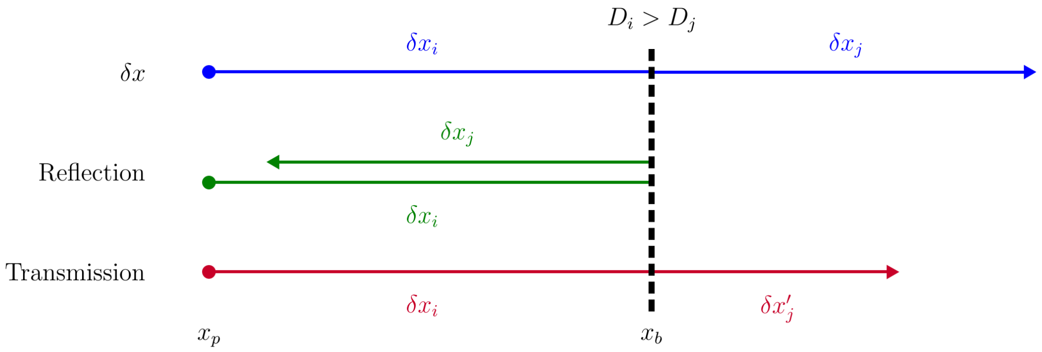

Figure 5.4: Illustration of the behaviour of a single walker at x_p performing a random step δx towards a barrier at x_b. Initially, the step is divided into δx_i and δx_j. Depending on the transit decision, the walker is either reflected elastically ($x = x_p + \delta x_i - \delta x_j$) or enters the new compartment with $D_j < D_i$. In the latter case, the remaining step after transit is modified to $\delta x'_j$ following equation (5.12) such that entering a compartment with lower/higher diffusion coefficient decreases/increases δx_j.

discussed later. If a walker currently residing in compartment i attempts to cross into compartment j through a barrier at x_b, the step is divided into

$$\delta x = \delta x_i + \delta x_j \tag{5.11}$$

such that $\delta x_i = x_b - x_p$. Upon entering the new compartment with a different diffusion coefficient $D_j \neq D_i$, the remaining step length δx_j over the duration $\delta t_j = \frac{\delta x_j}{\delta x} \delta t$ needs to be adjusted to preserve a constant step size $\sqrt{2\,\delta t}$ normalised by the diffusion coefficient (Szafer et al., 1995):

$$\delta x'_j = \delta x_j \sqrt{\frac{D_j}{D_i}}\,. \tag{5.12}$$

An alternative but equivalent formulation of this condition is

$$\sqrt{\delta t_j} = \sqrt{\delta t} - \sqrt{\delta t_i}\,, \tag{5.13}$$

which relates the times spent on each sub-step by

$$\frac{\delta x_i}{\sqrt{2 D_i\,\delta t}} + \frac{\delta x_j}{\sqrt{2 D_j\,\delta t}} = 1\,. \tag{5.14}$$

In addition to the step modification in equation (5.12), another condition needs to be satisfied. The probabilities of crossing from either side to the other, i.e. $p_{t,(i\to j)}$ and $p_{t,(j\to i)}$, must be augmented by the relative compartment diffusion coefficients, even in the absence of a membrane, via

$$\frac{p_{t,(i\to j)}}{p_{t,(j\to i)}} = \sqrt{\frac{D_j}{D_i}}\,. \tag{5.15}$$

As noted by Szafer et al. (1995), this “interface reflection” is required even as $\kappa \to \infty$.

5.3 Analysis of membrane transit models

A number of different methods have been proposed in literature to calculate the probability of transit p_t in equation (5.10) based on some or all of the membrane and tissue properties:

$$p_{t,(i\to j)} = f\left(\delta x_i, \delta x_j, D_i, D_j, \kappa_{i,j}\right) . \tag{5.16}$$

In this work these are referred to as transit models, represented by some to-be-determined function f in equation (5.16). This rather long section is devoted to an analysis of existing models and their validity.

The ultimate aim of any such transit model is to accurately represent the *leather* boundary condition in equation (5.17), which Powles et al. (1992) named after Tanner (1978):

$$D_i \left.\frac{\partial U}{\partial x}\right|_L = \kappa_{i,j}\left(U|_R - U|_L\right) . \tag{5.17}$$

Here, U is the particle density and the evaluation limits L and R indicate that the concentration and its gradient should be evaluated infinitesimally to the left (on the side of compartment i) or right (compartment j) of the interface. Fick's first law (Fick, 1855) states that the flux $\boldsymbol{J}$ is related to the gradient in concentration by

$$\boldsymbol{J} = -D\boldsymbol{\nabla}U\,, \tag{5.18}$$

where the sign indicates the direction of the flux vector with magnitude J. Since there is no accumulation of concentration/walkers inside the barrier, the flux must remain the same on either side, i.e.

$$D_i \left.\frac{\partial U}{\partial x}\right|_L = D_j \left.\frac{\partial U}{\partial x}\right|_R . \tag{5.19}$$

These two relations above (equations (5.17) and (5.19)) are illustrated in figure 5.5 by considering the concentration distribution $U(x)$ across a permeable membrane. In this example, the membrane is described as having small but finite width b and reduced diffusion coefficient D_b (such that it satisfies equation (2.3) for a given κ). On the left and right sides of the membrane are compartments with respective diffusion coefficients D_L and D_R. The concentration on the left side is higher than on the right. This can be seen from the slopes of the two curves at $x_b \pm \frac{b}{2}$. According to equation (5.19) the fluxes into and out of the membrane have to be equal, and thus the lower gradient $\mathrm{d}U/\mathrm{d}x$ on the left is compensated for by a larger D_L. Within the membrane, the concentration gradient is assumed constant. As $b \to \infty$, the finite membrane becomes a discontinuity in U seen in the top right smaller plot. This step change in U across the membrane disappears as $\kappa \to \infty$ and the boundary condition in equation (5.17) becomes trivial (Moutal et al., 2019).

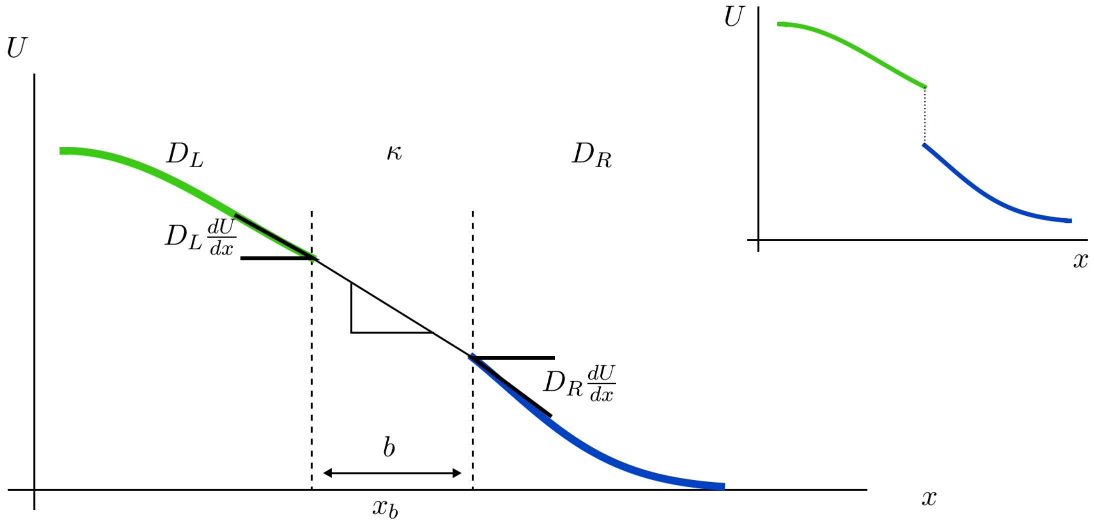

Figure 5.5: Discontinuity of concentration U across a permeable membrane. Inside it, the concentration gradient is constant over its fixed width b. When representing the membrane as infinitesimally thin, this gradient reduces to a discontinuity in concentration across it.

5.3.1 Models found in literature

Besides models where a constant probability of transit is prescribed based on experience or calibration, such as in the work by Hall et al. (2016), the general approach is to derive p_t from first principles.

First, consider the case of a fully permeable barrier which often appears in heat transfer problems when two materials of different conductivities (or thermal diffusivities) D_i and D_j, are in contact. In this case, Maruyama (2017) presents an elegant interpretation of the behaviour of random walkers, likened to transitioning between media of different viscosities. The expression for the probability of transmission from region i to region j,

$$p_{t,(i\to j)} = \min\left(1, \sqrt{\frac{D_j}{D_i}}\right) , \tag{5.20}$$

was first derived by Bechtold et al. (2011) and corresponds to a one-sided step rejection that satisfies equation (5.15).

The case of a finite membrane permeability was well-studied by Powles et al. (1992). The authors consider a constant diffusion coefficient D (i.e. $D_i = D_j$) and a discrete lattice of equidistant points to derive p_t for a barrier located on a grid point. Note that Powles et al. use permeability coefficient $\mathcal{P} = \kappa/D$. Fieremans et al. (2010) extended this approach to walkers performing uniform steps located at arbitrary positions x_p in the vicinity of the boundary. By neglecting higher-order terms in the derivation (compare to the Taylor expansion in section 5.3.2), Fieremans et al. present a transit probability

$$p_{t,(i\to j)} = \frac{2\kappa_{i,j}\,\delta x_i}{D_i + 2\kappa_{i,j}\,\delta x_i} \tag{5.21}$$

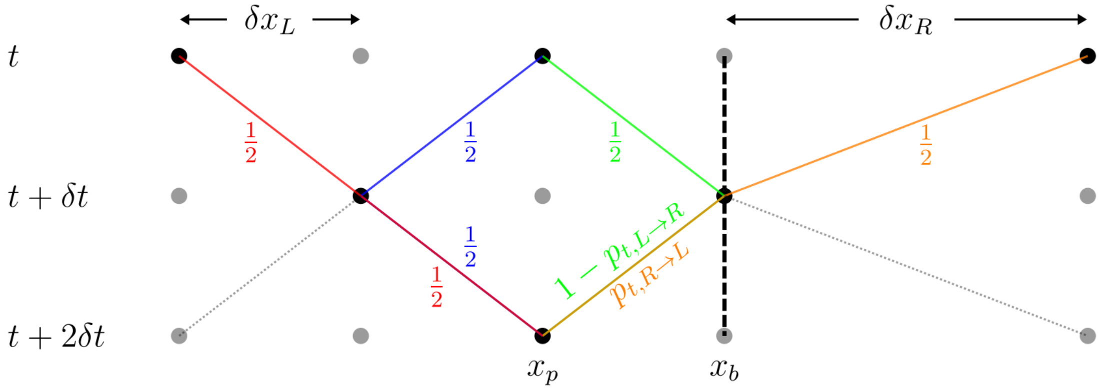

Figure 5.6: A grid of walker positions x and jump probabilities p near a permeable barrier located at x_p. The concentration at x_p, i.e. $U(x_p, t+2\delta t)$, is composed of the contribution of three different walker positions at time t (two time steps prior) through four different paths. The green path reflects at the barrier with probability $1-p_{t,L\to R}$, while the orange path passes through the barrier with transit probability $p_{t,R\to L}$.

for different diffusion coefficients ($D_i \neq D_j$) on either side of the barrier, where δx_i is the distance from x_p to the barrier x_b. The authors note a limit on δt such that $p_t \ll 1$. In numerical simulations, a value of $p_t = 0.01$ is used (Fieremans et al., 2010).

5.3.2 Transit model derivation

The work by Powles et al. (1992) presents a derivation of the transit probability p_t for walker positions on a lattice based on a constant step length in the entire domain. Here, domains are considered where the diffusion coefficient may differ between compartments. As such, the probability of transit is re-derived for the domain in figure 5.6 considering the different step lengths.

Consider the probability of finding a walker at x_p as the sum of probabilities of neighbouring walkers jumping to x_p. Away from interfaces, this results in

$$U(x_p, t+\delta t) = \frac{1}{2}U(x_p - \delta x, t) + \frac{1}{2}U(x_p + \delta x, t) \tag{5.22}$$

and can be visualised by Pascal's triangle. Selecting x_p to be near a barrier at x_b (see figure 5.6 for the possible paths of walkers to reach this position) results in additional terms involving p_t (both $p_{t,L\to R}$ and $p_{t,R\to L}$). In the limit of fully -permeable membranes with $\kappa \to \infty$, these p_t terms would tend to 0.5 *iff* $D_i = D_j$. The barrier location is chosen to coincide with a grid point. A walker located here will proceed left/right according to the appropriate probability of transit. The contributions of different $U(x,t)$ terms to $U(x_p, t+2\delta t)$ in figure 5.6 (with the path colour indicated) are

$$\begin{aligned} U(x_p, t+2\delta t) = &\underbrace{\frac{1}{4}U(x_p - 2\delta x_L, t)}_{\text{free (red)}} + \underbrace{\frac{1}{4}U(x_p, t)}_{\text{free (blue)}} \\ &+ \underbrace{\frac{1-p_{t,L\to R}}{2}U(x_p, t)}_{\text{reflection (green)}} + \underbrace{\frac{p_{t,R\to L}}{2}U(x_p + \delta x_L + \delta x_R, t)}_{\text{transit (orange)}} . \end{aligned} \tag{5.23}$$

One may now express x_p relative to x_b, e.g. the contribution of the orange path from the right side of the barrier is reformulated as

$$U(x_p + \delta x_L + \delta x_R, t) = U(x_b + \delta x_R, t) . \tag{5.24}$$

Applying this to all terms results in

$$\begin{aligned} U(x_b - \delta x_L, t+2\delta t) = &\frac{1}{4}U(x_b - 3\delta x_L, t) + \frac{1}{4}U(x_b - \delta x_L, t) \\ &+ \frac{1-p_{t,L\to R}}{2}U(x_b - \delta x_L, t) + \frac{p_{t,R\to L}}{2}U(x_b + \delta x_R, t) . \end{aligned} \tag{5.25}$$

This allows us to perform a Taylor series expansion of every term U, namely

$$U(x+a, t+b) = U(x,t) + \frac{\partial U}{\partial x}\frac{a^1}{1!} + \frac{\partial^2 U}{\partial x^2}\frac{a^2}{2!} + \frac{\partial U}{\partial t}\frac{b^1}{1!} + \text{H.O.T.} . \tag{5.26}$$

The expansion is carried out in time t, with $\partial U/\partial t = \dot{U}$, and around the barrier location x_b, where care is taken to expand infinitesimally to the left and right of the barrier as appropriate. This yields

$$\begin{aligned} &U|_L - \delta x_L \left.\frac{\partial U}{\partial x}\right|_L + \frac{\delta x_L^2}{2}\left.\frac{\partial^2 U}{\partial x^2}\right|_L + 2\delta t \dot{U}_L \\ &= \frac{1}{4}\left(U|_L - 3\delta x_L \left.\frac{\partial U}{\partial x}\right|_L + \frac{9\delta x_L^2}{2}\left.\frac{\partial^2 U}{\partial x^2}\right|_L\right) \\ &+ \frac{1}{4}\left(U|_L - \delta x_L \left.\frac{\partial U}{\partial x}\right|_L + \frac{\delta x_L^2}{2}\left.\frac{\partial^2 U}{\partial x^2}\right|_L\right) \\ &+ \frac{1-p_{t,L\to R}}{2}\left(U|_L - \delta x_L \left.\frac{\partial U}{\partial x}\right|_L + \frac{\delta x_L^2}{2}\left.\frac{\partial^2 U}{\partial x^2}\right|_L\right) \\ &+ \frac{p_{t,R\to L}}{2}\left(U|_R + \delta x_R \left.\frac{\partial U}{\partial x}\right|_R + \frac{\delta x_R^2}{2}\left.\frac{\partial^2 U}{\partial x^2}\right|_R\right) . \end{aligned} \tag{5.27}$$

Higher-order terms (H.O.T.) resulting from the Taylor expansion can be omitted, but their significance should be remembered as δx increases. Grouping the elements of equation (5.27) by terms of U and its derivatives gives

$$\begin{aligned} \dot{U}_L\,(2\delta t) = U|_L &\left(-1 + \frac{1}{4} + \frac{1}{4} + \frac{1}{2} - \frac{p_{t,L\to R}}{2}\right) + U|_R\left(\frac{p_{t,R\to L}}{2}\right) \\ &+ \left.\frac{\partial U}{\partial x}\right|_L \delta x_L \left(1 - \frac{3}{4} - \frac{1}{4} - \frac{1}{2} + \frac{p_{t,L\to R}}{2}\right) + \left.\frac{\partial U}{\partial x}\right|_R \delta x_R \left(\frac{p_{t,R\to L}}{2}\right) \\ &+ \left.\frac{\partial^2 U}{\partial x^2}\right|_L \delta x_L^2 \left(-\frac{1}{2} + \frac{9}{8} + \frac{1}{8} + \frac{1}{4} - \frac{p_{t,L\to R}}{4}\right) + \left.\frac{\partial^2 U}{\partial x^2}\right|_R \delta x_R^2 \left(\frac{p_{t,R\to L}}{4}\right) . \end{aligned} \tag{5.28}$$

This can be further simplified to

$$\begin{aligned}\dot{U}_L\,(2\delta t) = {} & U|_L \left(\frac{p_{t,L\to R}}{2}\right) + U|_R \left(\frac{p_{t,R\to L}}{2}\right) \\ & + \left.\frac{\partial U}{\partial x}\right|_L \delta x_L \left(-\frac{1}{2} + \frac{p_{t,L\to R}}{2}\right) + \left.\frac{\partial U}{\partial x}\right|_R \delta x_R \left(\frac{p_{t,R\to L}}{2}\right) \\ & + \left.\frac{\partial^2 U}{\partial x^2}\right|_L \delta x_L^2 \left(1 - \frac{p_{t,L\to R}}{4}\right) + \left.\frac{\partial^2 U}{\partial x^2}\right|_R \delta x_R^2 \left(\frac{p_{t,R\to L}}{4}\right) .\end{aligned} \tag{5.29}$$

The heat equation (3.18), expressed in 1D as

$$\dot{U} = \frac{\delta x^2}{2\delta t}\frac{\partial^2 U}{\partial x^2} , \tag{5.30}$$

is subsequently applied in L to remove the time derivative:

$$\begin{aligned}\cancel{\dot{U}_L\,(2\delta t)} = {} & U|_L \left(\frac{p_{t,L\to R}}{2}\right) + U|_R \left(\frac{p_{t,R\to L}}{2}\right) \\ & + \left.\frac{\partial U}{\partial x}\right|_L \delta x_L \left(-\frac{1}{2} + \frac{p_{t,L\to R}}{2}\right) + \left.\frac{\partial U}{\partial x}\right|_R \delta x_R \left(\frac{p_{t,R\to L}}{2}\right) \\ & + \left.\frac{\partial^2 U}{\partial x^2}\right|_L \delta x_L^2 \left(\cancel{1} - \frac{p_{t,L\to R}}{4}\right) + \left.\frac{\partial^2 U}{\partial x^2}\right|_R \delta x_R^2 \left(\frac{p_{t,R\to L}}{4}\right) .\end{aligned} \tag{5.31}$$

Equations (5.17) and (5.19) can be combined to form

$$D_L \left.\frac{\partial U}{\partial x}\right|_L = D_R \left.\frac{\partial U}{\partial x}\right|_R = \kappa(U|_R - U|_L) . \tag{5.32}$$

By differentiating equation (5.19) one more time with respect to x while noting that $\partial U/\partial x = 0$ (only non-zero *across* the barrier), the following additional relation is obtained:

$$D_L \left.\frac{\partial^2 U}{\partial x^2}\right|_L = D_R \left.\frac{\partial^2 U}{\partial x^2}\right|_R . \tag{5.33}$$

Next, equation (5.15) relates the two probabilities $p_{t,L\to R}$ and $p_{t,R\to L}$ as a ratio $\sqrt{D_L/D_R}$. These three relations, namely equations (5.15), (5.32) and (5.33), are substituted into equation (5.31). Appreciating that the step lengths are $\delta x = \sqrt{2D\,\delta t}$ allows switching from δx_R to δx_L through multiplication with $\sqrt{D_L/D_R}$. With these techniques, everything can be expressed in terms of $U|_L$, $(\partial U/\partial x)_L$, and $(\partial^2 U/\partial x^2)_L$ as well as $p_{t,L\to R}$ and δx_L.

Equations (5.32) and (5.33) introduced the permeability κ, originally from equation (5.17), into the resulting equation involving p_t. The final rearranged expression

$$\begin{aligned} 0 = {} & 2p_t \left(1 - \sqrt{\frac{D_L}{D_R}}\right) U|_L \\ & + 2\left(\left(1 - \left(1 + \frac{D_L}{D_R}\right) p_t\right) \delta x_L - p_t \sqrt{\frac{D_L}{D_R}} \frac{D_L}{\kappa}\right) \left.\frac{\partial U}{\partial x}\right|_L \\ & + p_t \left(1 - \sqrt{\frac{D_L}{D_R}}\right) \delta x_L^2 \left.\frac{\partial^2 U}{\partial x^2}\right|_L \end{aligned} \tag{5.34}$$

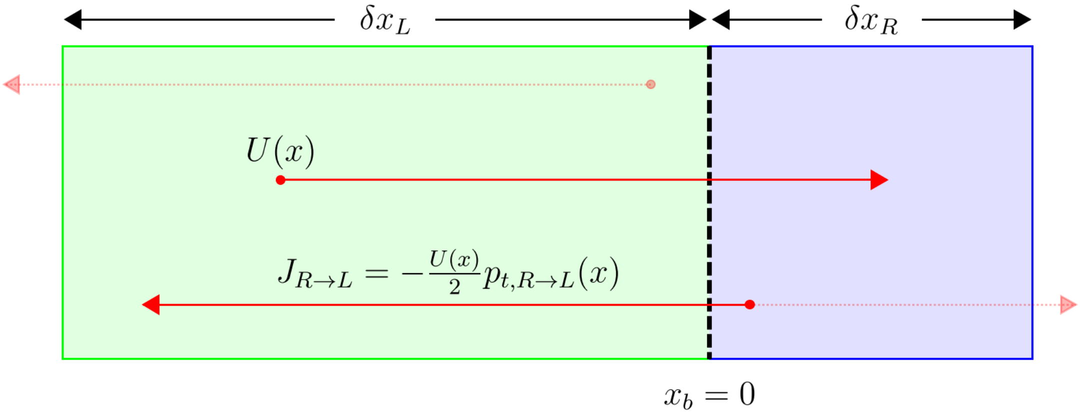

Figure 5.7: A graphical explanation of the flux analysis around two compartments ($D_L > D_R$) separated by a permeable barrier with asymmetric transit probabilities $p_{t,L\to R}$ and $p_{t,R\to L}$. The control volume is bounded by the step lengths δx on either side. Walkers located inside this volume at a point with concentration/density $U(x)$ add to the flux component J with their weighted contribution $\pm U(x) p_t(x)$, provided they step towards the barrier (accounted for by the factor $\frac{1}{2}$).

thus needs to be solved for p_t as a function of D, κ, and δx to obtain the transit model that equation (5.16) postulates. The model in equation (5.21) as derived by Fieremans et al. (2010) relies on ignoring the terms associated with U and $\partial^2 U/\partial x^2$. However, in the general case no statements about the magnitude of these terms can be made. The former omission of U-terms is only valid provided $p_t \to 0$ or $D_L/D_R \to 1$, while ignoring the $\partial^2 U/\partial x^2$-terms additionally requires $\delta x \to 0$. It is important to recognise that equation (5.34) recovers

$$p_t = \frac{2\kappa\delta x}{D + 2\kappa\delta x} \tag{5.35}$$

in the case of equal diffusion coefficients $D_L = D_R$. Equation (5.35) is an alternative but equivalent formulation of the expression derived by Powles et al. (1992).

5.3.3 Flux analysis

As will be demonstrated numerically later in section 6.3, the transit model formulation in equation (5.21) is inconsistent and causes errors at large δt. For now, a theoretical approach is taken and this error is analysed by considering the flux at any given point in time.

Figure 5.7 shows the control volume around a barrier bounded by the maximum step length δx on either side. Note the difference between the running variable x (and its differential $\mathrm{d}x$) and the finite step length δx.

The net flux $\boldsymbol{J} = -D\boldsymbol{\nabla} U$ in equation (5.18) can be split into its individual bidirectional (or opposing) components, i.e. the amount of walkers/concentration crossing from left to right and from right to left, whose signed sum equals J along the unit vector $\hat{\boldsymbol{J}}$. Their magnitudes are given by

$$J_{L\to R} = \frac{1}{\delta t}\int_{-\delta x_L}^{0} +\frac{U(x)}{2} p_{t,L\to R}(x)\,\mathrm{d}x\,, \tag{5.36a}$$

$$J_{R\to L} = \frac{1}{\delta t}\int_{0}^{\delta x_R} -\frac{U(x)}{2} p_{t,R\to L}(x)\,\mathrm{d}x\,. \tag{5.36b}$$

The integral bounds on the two sides cover the farthest that a walker can be located away from the boundary on either side in order for its step δx to interact with the barrier. While the concentration density $U(x)$ in general depends on position x, this dependency is ignored here because of the assumption that U is constant in the domain for the steady-state case. The factor $\frac{1}{2}$ accounts for the fact that only half the walkers are expected to step *towards* the barrier. The $\pm$ signs are included to designate the directionality of the flux components J such that (loosely speaking) $\sum J = \boldsymbol{J}$. For simplicity, this is omitted and only *magnitudes* are used. The terms U and δt are also cancelled and henceforth the probability integrals F is used, shown here for an arbitrary transition between regions with placeholder indices A and B:

$$F_{A\to B} = \int p_{t,A\to B}(x)\,\mathrm{d}x\,. \tag{5.37}$$

The steady-state solution requires the net flux $\sum J = 0$, i.e. $F_{L\to R} = F_{R\to L}$. If not, an imbalance in $U(x)$ will develop. If the diffusion coefficients on both sides are equal ($D_L = D_R = D$), the models considered in this work reduce to $p_{t,L\to R} = p_{t,R\to L}$. Furthermore, by definition $\delta x_L = \delta x_R$ and hence $\sum J = 0$ follows from equation (5.36a) being equal to equation (5.36b). Next, the different models for the non-trivial case $D_L \neq D_R$ are considered.

Interface model

In the case of an infinitely permeable membrane, consider the interface model in equation (5.20). The asymmetric transit probability was first mentioned by Szafer et al. (1995) for the limit $\kappa \to \infty$ and explicitly derived for any interface by Maruyama (2017). The probability of transit for interfaces with discontinuous diffusion coefficient D is thus given by

$$p_{t,L\to R} = \min\left(1, \sqrt{\frac{D_R}{D_L}}\right)\,, \tag{5.38a}$$

$$p_{t,R\to L} = \min\left(1, \sqrt{\frac{D_L}{D_R}}\right)\,. \tag{5.38b}$$

For this interface model, the probabilities p_t do not depend on x but only on D as seen from equation (5.38). As a result, p_t can be removed from the integral in equation (5.36)

Table 5.1: The two cases of unequal diffusion coefficients D_L and D_R across an interface, as considered in equation (5.38), and their corresponding probabilities of transit p_t and resulting fluxes F.

Diffusion coefficients	$p_{t,L\to R}$	$p_{t,R\to L}$	$F = F_{L\to R} = F_{R\to L}$
$D_L > D_R$	$\sqrt{\frac{D_R}{D_L}}$	1	$\sqrt{2D_R\,\delta t}$
$D_L < D_R$	1	$\sqrt{\frac{D_L}{D_R}}$	$\sqrt{2D_L\,\delta t}$

and the result is then simplified to

$$F_{L\to R} = p_{t,L\to R} \int_{-\delta x_L}^{0} \mathrm{d}x = p_{t,L\to R}\,\delta x_L = p_{t,L\to R}\sqrt{2D_L\,\delta t}\,, \tag{5.39a}$$

$$F_{R\to L} = p_{t,R\to L} \int_{0}^{\delta x_R} \mathrm{d}x = p_{t,R\to L}\,\delta x_R = p_{t,R\to L}\sqrt{2D_R\,\delta t}\,. \tag{5.39b}$$

To remove the awkward min-operator for p_t in equation (5.38), consider the two distinct cases in table 5.1 separately. For both combinations of p_t values it is clear that $F_{L\to R} = F_{R\to L} = F$. In fact, $F = \sqrt{2D_{\min}\,\delta t}$ where $D_{\min} = \min(D_L, D_R)$ which can also be observed in numerical simulations with $\kappa = \infty$.

Membrane model

Fieremans et al. (2010) introduce two probabilities of transit p_t, going from L to R and from R to L, as

$$p_{t,L\to R} = \frac{2\kappa s_L}{D_L + 2\kappa s_L} \approx \frac{2\kappa s_L}{D_L}\,, \tag{5.40a}$$

$$p_{t,R\to L} = \frac{2\kappa s_R}{D_R + 2\kappa s_R} \approx \frac{2\kappa s_R}{D_R}\,. \tag{5.40b}$$

Each p_t depends on the diffusion coefficient D_0 of the original compartment that the attempted transit originated from, and the distance s from the step origin to the barrier at x_b. Since $x_b = 0$, this results in $s_L \in [-\delta x_L, 0]$ and $s_R \in [0, \delta x_R]$ respectively. The (signed) value of s is therefore equal to $\mp x$. Note that the simplification ($\approx$) on the right-hand sides of equation (5.40) only applies if $2\kappa s \ll D$.

General case Using the full, non-approximated term for p_t from equation (5.40) and substituting it into equation (5.37) results in

$$F_{L\to R} = \int_{-\delta x_L}^{0} p_{t,L\to R}(x)\,\mathrm{d}x = \int_{-\delta x_L}^{0} \frac{x}{x - \frac{D_L}{2\kappa}}\,\mathrm{d}x\,, \tag{5.41a}$$

$$F_{R\to L} = \int_{0}^{\delta x_R} p_{t,R\to L}(x)\,\mathrm{d}x = \int_{0}^{\delta x_R} \frac{x}{x + \frac{D_R}{2\kappa}}\,\mathrm{d}x\,. \tag{5.41b}$$

These integrals can be solved by a change of variables, i.e. $x = \zeta \pm \frac{D}{2\kappa}$, turning equation (5.41) into

$$F_{L\to R} = \int_a^b \frac{\zeta + \frac{D_L}{2\kappa}}{\zeta}\,\mathrm{d}\zeta = \left[\zeta + \frac{D_L}{2\kappa}\ln(\zeta)\right]_a^b , \tag{5.42a}$$

$$F_{R\to L} = \int_a^b \frac{\zeta - \frac{D_R}{2\kappa}}{\zeta}\,\mathrm{d}\zeta = \left[\zeta - \frac{D_R}{2\kappa}\ln(\zeta)\right]_a^b . \tag{5.42b}$$

Changing variables back to x gives

$$\begin{aligned} F_{L\to R} &= \left[x - \frac{D_L}{2\kappa} + \frac{D_L}{2\kappa}\ln\left(x - \frac{D_L}{2\kappa}\right)\right]_{-\delta x_L}^{0} \\ &= \delta x_L + \frac{D_L}{2\kappa}\left(\ln\left(-\frac{D_L}{2\kappa}\right) - \ln\left(-\delta x_L - \frac{D_L}{2\kappa}\right)\right) , \end{aligned} \tag{5.43a}$$

$$\begin{aligned} F_{R\to L} &= \left[x + \frac{D_R}{2\kappa} - \frac{D_R}{2\kappa}\ln\left(x + \frac{D_R}{2\kappa}\right)\right]_{0}^{\delta x_R} \\ &= \delta x_R + \frac{D_R}{2\kappa}\left(\ln\left(\frac{D_R}{2\kappa}\right) - \ln\left(\delta x_R + \frac{D_R}{2\kappa}\right)\right) . \end{aligned} \tag{5.43b}$$

Since $F_{L\to R}$ and $F_{R\to L}$ here depend on D_L and D_R respectively, and because F cannot be reduced further, it is concluded that $F_{L\to R} \neq F_{R\to L}$ and thus $\sum J \neq 0$. This means that the step is not balanced and the model is invalid in the general case.

Special case A sufficiently small time step δt permits solving for the simplified expression of p_t. The integrals in equation (5.41) now become trivial to solve and one gets

$$\begin{aligned} F_{L\to R} &= \int_{-\delta x_L}^{0} p_{t,L\to R}(x)\,\mathrm{d}x = \frac{2\kappa}{D_L}\int_{-\delta x_L}^{0} -x\,\mathrm{d}x \\ &= \frac{2\kappa}{D_L}\left[-\frac{1}{2}x^2\right]_{-\delta x_L}^{0} = \frac{\kappa\,\delta x_L^2}{D_L} = 2\kappa\,\delta t , \end{aligned} \tag{5.44a}$$

$$\begin{aligned} F_{R\to L} &= \int_{0}^{\delta x_R} p_{t,R\to L}(x)\,\mathrm{d}x = \frac{2\kappa}{D_R}\int_{0}^{\delta x_R} x\,\mathrm{d}x \\ &= \frac{2\kappa}{D_R}\left[\frac{1}{2}x^2\right]_{0}^{\delta x_R} = \frac{\kappa\,\delta x_R^2}{D_R} = 2\kappa\,\delta t . \end{aligned} \tag{5.44b}$$

Hence, $F_{L\to R} = F_{R\to L} = F = 2\kappa\,\delta t$ (this was also confirmed in simulations with small δt) and the model will retain the steady-state solution. Recall that the simplification in equation (5.40) above requires that $2\kappa\,\delta s \ll D$. This requirement can be recast to

$$1 \ll \frac{2\kappa\sqrt{2D\,\delta t}}{D} = \sqrt{\frac{8\kappa^2\,\delta t}{D}} . \tag{5.45}$$

This shows that the threshold at which a significant error in the fluxes occurs increases with κ and δt and decreases with D. This is in line with observations in figure 6.11 later on.

Asymmetric interface reflection

As originally stated by Szafer et al. (1995), the interface reflection condition in equation (5.15) must be respected even as $\kappa \to \infty$. This is satisfied intrinsically in equation (5.38). Following from equation (5.40), the ratio of probabilities

$$\frac{p_{t,L\to R}}{p_{t,R\to L}} = \frac{2\kappa\,\delta x_{i,L}}{D_L + 2\kappa\,\delta x_{i,L}} \div \frac{2\kappa\,\delta x_{i,R}}{D_R + 2\kappa\,\delta x_{i,R}} = \frac{\delta x_{i,L}}{\delta x_{i,R}} \frac{D_R + 2\kappa\,\delta x_{i,R}}{D_L + 2\kappa\,\delta x_{i,L}} \tag{5.46}$$

is undefined in the limit

$$\lim_{\kappa\to\infty} \frac{p_{t,L\to R}}{p_{t,R\to L}} = \frac{\delta x_{i,L}}{\delta x_{i,R}} \lim_{\kappa\to\infty} \frac{D_R + 2\kappa\,\delta x_{i,R}}{D_L + 2\kappa\,\delta x_{i,L}} \to \frac{\infty}{\infty}\,. \tag{5.47}$$

Following L'Hôpital's rule yields

$$\frac{\frac{\mathrm{d}}{\mathrm{d}\kappa}(D_R + 2\kappa s_{R\to L})}{\frac{\mathrm{d}}{\mathrm{d}\kappa}(D_L + 2\kappa s_{L\to R})} = \frac{2s_{R\to L}}{2s_{L\to R}}\,, \tag{5.48}$$

which means that the ratio of probabilities

$$\lim_{\kappa\to\infty} \frac{p_{t,L\to R}}{p_{t,R\to L}} \to \frac{\delta x_{i,L}}{\delta x_{i,R}} \frac{s_{R\to L}}{s_{L\to R}} = 1 \tag{5.49}$$

approaches unity in the limit of $\kappa \to \infty$ instead of $\sqrt{D_R/D_L}$ as required. This might explain why the model appears to break down as the time step restriction is exceeded either by increasing δt or κ as done in figure 6.11.

Another observation regarding equation (5.21) is that it does not handle the extreme case of $D_j = 0$ appropriately (p_t should also be zero in that case). Such a situation may be visualised as the limit case of a *very* viscous medium, the analogy proposed by Maruyama (2017). Since walkers are permitted to enter compartments with diffusion coefficient of zero, they will undoubtedly become trapped there. While equation (5.15) causes the remaining step length in the new compartment to be $\delta x'_j = 0$ and thus places it infinitesimally to the other side of the barrier, the walker has nonetheless entered a region where every subsequent step has length zero.

5.3.4 Alternative ways to model membranes

As shown previously, modelling an infinitesimally thin permeable interface with a step change in diffusion coefficient can be challenging. The discontinuity in the random walk requires correct treatment and not all choices of model or model parameter are always appropriate. When considering compartments with differing diffusion coefficients $D_L \neq D_R$, no *consistent* closed-form expression was found to represent the membrane with a correct permeability. Here, different and perhaps more pragmatic approaches to modelling such a membrane for random walk simulations are presented. The two types are shown in figure 5.8 and explained below.

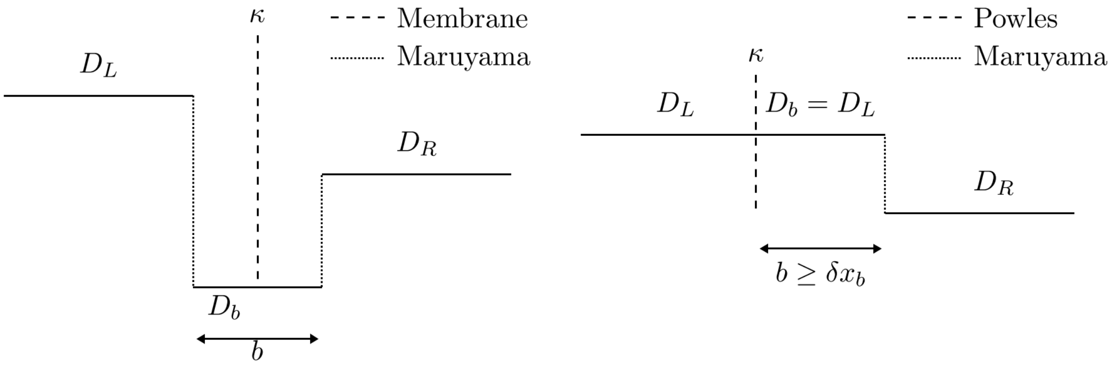

Figure 5.8: Alternative ways to model a membrane. **(Left)** As a highly viscous layer: The thickness b and diffusion coefficient D_b need to be chosen to satisfy equation (2.3). **(Right)** As a buffer region: The membrane between two compartments is represented as a buffer region

Membrane as a highly viscous layer

Biological membranes have a negligible thickness of two lipid molecules (section 2.2). Similar to what was implemented for the FDM simulations in section 3.3.3, the membrane can be approximated as a region of finite thickness and reduced diffusion coefficient. An illustration of the membrane model is shown in figure 5.8 (Left). Following the interpretation of Maruyama (2017), the region is a highly viscous layer that impedes motion similar to how a cell membrane may impede transit.

Care needs to be taken to correctly account for the modification to the domain. The size of the ECS and ICS must not be affected by this additional third region. One would need to decide on the treatment of walkers when diffusion gradients are applied, in particular the global position of the walker needs to be considered. Immediately it seems that the walker position needs to be fixed to the membrane position until it exits the region. In the case of 2D/3D simulations, more needs to be considered. To accelerate simulations and avoid transverse motion during the transit, a co-simulation might be a good idea. Then, walkers would need to perform a 1D random walk in the membrane-perpendicular direction.

The values of D_b and b need to be chosen somewhat arbitrarily provided they satisfy the value of κ. One may attempt to construct the layer to ensure minimal disruption and thus reduce b as much as possible. However, no choice of parameters can yield a buffer region that can be crossed in a single step. For a sensible choice of D_b and b, the value of D_b will be significantly less than D_L and D_R. As a result of the ratio between these values and equation (5.20), reflection can only occur when entering the buffer region but never when exiting. The remaining step $\delta x_j'$ inside the barrier is required to equal b:

$$\delta x_j' = b = \delta x_j \sqrt{\frac{D_b}{D_i}} \tag{5.50a}$$

$$\delta x_j = (1-t)\sqrt{2D_i\,\delta t} \tag{5.50b}$$

$$b = \frac{D_b}{\kappa} = (1-t)\sqrt{2D_b\,\delta t} \tag{5.50c}$$

$$1-t = \frac{1}{b}\sqrt{\frac{D_b}{2\delta t}} \tag{5.50d}$$

It is therefore not possible to satisfy this for all walkers with arbitrary intersection point t.

Due to the linear relation between b and D_b but the non-linear relation between D_b and δx, the smaller b is the more steps of duration δt it takes to cross the region. This means walkers effectively become trapped in the region for longer. If sufficiently many walkers are available, this is not a problem. However, if the proportion of trapped walkers becomes significant compared to the total number of walkers (for example if a lot of barriers are present or N is generally low), this can cause problems.

Membrane as a double-interface buffer region

Another approach altogether is to rely on the two functioning models presented previously in combination with a buffer region that separates the interface between the two regions with differing diffusion coefficients from the permeable membrane. This considers the two types of restriction that the walker experiences when crossing a membrane, separately. Figure 5.8 (Right) illustrates the approach.

Previously in sections 5.3.2 and 5.3.3 it was shown that the transit model for a permeable membrane separating compartments with equal diffusion coefficients ($D_L = D_R$) can be accurately represented by equation (5.21) as described by Powles et al. (1992). Under these conditions, the expression is well-behaved since it correctly respects $\kappa = 0$ (impermeable) as well as $\kappa \to \infty$ ($p = 1$, fully permeable, i.e. no barrier). On the other hand, the transit through a membrane-free interface between compartments of different diffusion coefficients can be accurately represented with the model by Maruyama (2017), given in equation (5.20), as it satisfies the asymmetric interface condition in equation (5.15).

For the double-interface model, the buffer zone should be the size of one step, equal to $\delta x_{\max} = b = \sqrt{2D_b\,\delta t_{\max}}$. Hence $\delta t_{\max} = \frac{b^2}{2D_b} = \frac{b}{2\kappa}$ and thus $b_{\min} = 2\kappa\,\delta t$. This minimum value for the buffer width ensures that walkers only cross a single interface per time step.

Similar to the case of a more viscous membrane region, it is important to realise the effect of this domain modification. The addition of a buffer zone alters the geometry slightly, and care must be taken for how walkers inside that zone are treated. However, due to the fact that the buffer region has a similar diffusion coefficient, it is possible to incorporate this region as a sub-set of either ECS or ICS. Representing the transit as a

1D co-simulations is also possible, as was previously discussed for the model of a viscous layer.

5.4 Monte Carlo random walk simulator

Previously, the mathematical aspects of the random walk process were described for a single walker, which is executed N_p times per experiment. In particular, it was discussed how random steps are drawn and what the probability of transit is for a given walker-membrane interaction. This section now focuses on the numerical implementation and its application to Monte Carlo random walk (MCRW) simulations. After introducing the algorithm in section 5.4.2, the specific software implementations that were written in this project are described in sections 5.4.3 and 5.4.4.

We will find that many of the employed techniques are similar to those used in computer graphics. For example, determining the path of a walker during a time step is almost equivalent to the ray tracing problem. The textbooks *Real Time Rendering* (Akenine-Möller et al., 2008) and *Graphics Gems IV* (Heckbert, 1994) are great starting points for readers interested in the algorithms.

5.4.1 A brief review of existing simulators

The toolbox Camino (P. A. Cook et al., 2006) is a popular software in neuroimaging. Besides many advanced tools for image reconstruction and data processing it offers data synthesis through random walk simulations (Hall et al., 2009). It is capable of simulating simple analytical shapes as well as arbitrary, mesh-based geometries (Panagiotaki et al., 2010). This makes it a good reference tool that is often used in benchmarks. However, the generality means it is not always the optimal tool of choice.

Other groups (K.-V. Nguyen et al., 2018; Rafael-Patino et al., 2020; Yeh et al., 2013) have presented custom simulators with varying aims, advantages, and limitations. For example, K.-V. Nguyen et al. (2018) present a GPU-accelerated random walk simulator that is claimed as highly efficient, but the source code has not been made available. The recently released code by Rafael-Patino et al. (2020) is targeted at highly-realistic mesh substrates, focussed on microstructural features of brain white matter. H.-H. Lee et al. (2021) use a custom GPU code for random walks in voxelised domains representative of axonal cells.

The decision was taken to develop an in-house solver in order to target it at cardiac tissues and in general DT-CMR. Through increased control over the source code of the simulation, different biophysical models and other adjustments can be made.

Another approach for DWI simulations is to use existing particle/molecular simulators to solve the diffusion of spins and then apply the pulse sequence as a post-processing step. For example, Bates et al. (2017) used Smoldyn (Andrews et al., 2010) and Berry

Algorithm 5.1: Basic procedure of any Monte Carlo random walk implementation. The outer for-loop (algorithm 5.1) iterates over the N_p walkers. The inner while-loop (algorithm 5.1) marches through time. The procedure in algorithm 5.1 is implementation-specific.

```
procedure RandomWalk
    for $i \in \{1, ..., N_p\}$ do                            ▷ Walker loop
        $\boldsymbol{x}_i \leftarrow \boldsymbol{x}(0)$        ▷ Initial seeding
        while $t < T$ do                                       ▷ Time loop
            $\delta\boldsymbol{x} \leftarrow$ RANDOM_STEP($D$)          ▷ Random stepping
            $\boldsymbol{x}_i \leftarrow \boldsymbol{x}_i +$ RESOLVE_STEP($\delta\boldsymbol{x}$)   ▷ Interaction with the substrate
        end while
    end for
end procedure
```

et al. (2018) used MCell (Kerr et al., 2008). The implications of this are twofold: A clear advantage is that reliable diffusion solutions can be obtained without major software development effort, while the major disadvantage is the reliance on general code that may not support MR co-simulation or suffer a performance penalty.

5.4.2 Algorithm and parallelisation

In general the MCRW algorithm follows the pseudo-code in algorithm 5.1. At the beginning of the simulation, walkers are seeded inside the domain. This can be done randomly using a uniform distribution over the extent of the domain or at a given spatial point if comparison to reference solutions from chapters 3 and 4 is desired. Every walker then has to execute a series of time steps, each of which needs to be resolved to account for the interaction of the walker with the features of the substrate. Converting algorithm 5.1 into real code for cases beyond free diffusion requires consideration of possible numerical inaccuracies. The details of this are discussed for two substrate types in section 5.4.3 (voxelised domain) and section 5.4.4 (surface mesh domain). If a large number of walkers N_p is to be simulated, an efficient implementation is also required.

At every time step, a random step is drawn and the resulting path is resolved as a series of sub-steps (compare equation (5.9)) if one or more membranes are encountered in the substrate. The random generation of this step requires special consideration. The type of step and its random distribution is described in section 5.2.1. Computers “draw” random numbers using a pseudo-random number generator that generates a series of seemingly random values on demand (Knuth, 2011a). A sufficiently “random” algorithm is required to ensure statistical independence between walkers (J. D. Cook, 2010). Furthermore, it is recommended to use a single random seed for a given experiment, with statistically independent streams for each realisation of a Monte Carlo simulation (Gentle, 2003). This can be achieved by series splitting or a leap-frog scheme: Either, each walker is assigned a certain section of the random number stream up-front by splitting, which requires knowledge of the number of random variables that will be consumed. The other option is to advance the random number stream by N_p every time (leap-frog).

Owing to the intrinsic parallelism of the random walk where each walker is considered fully independent, the algorithm is trivially parallelised. Different parallelisation options exist: The most trivial is to split off each walker separately at the beginning of the simulation and combine the results at the end. This is what is implemented in the code (appendix B.2.2). The work in the outer loop (algorithm 5.1) can be efficiently distributed among all available compute threads. The current implementation only supports CPU code. While GPUs offer superior parallel performance, this is limited to simple instructions. Rose (2015) found that GPUs are not particularly suited for handling complex walker-substrate interactions. Fortunately, different sub-sets of all N_p walkers can be scheduled separately, in parallel, and executed in a distributed system such as a high-performance compute cluster.

Another approach could have reversed the loop order in algorithm 5.1 and looped over all walkers at every time step. In fact this would lead to identical results[‡]. However, communication overhead associated with the parallel protocol then becomes significant as the number of time steps increases. If solutions at specific time points are required, it is recommended to break or pause the simulation sequence at times of interest. It is also possible to store a time history of positions (and other variables) during the whole simulation, however care must be taken that this does not exceed the available memory for large N_p and N_t.

5.4.3 Walking in a structured grid

Consider the domain in figure 5.9. The left image shows a pixelated 2D substrate composed of cardiomyocyte cross-sections. They are colour-coded to ensure that myocytes that are touching are identified as distinct objects. A simpler model is seen in the right image of figure 5.9. This chequerboard pattern has ECS (red) and ICS (white) in an alternating arrangement.

It should be clear that these domains are similar to what was described for the FDM/FVM methods in section 3.3.3. Instead of the continuum methods that consider the pixels/cells as part of the problem formulation and discretisation, walkers are now allowed to move arbitrarily in the domain. The approach described here is an efficient model for n-dimensional random walk simulations in voxelised domains. It is implemented in C++ using *linked lists* to handle the transit between neighbouring cells. For each of its faces, every voxel stores the pointer (memory address) to its neighbour and the

---

[‡] One needs to ensure that each walker draws the same sequence of pseudo-random numbers in both formats.

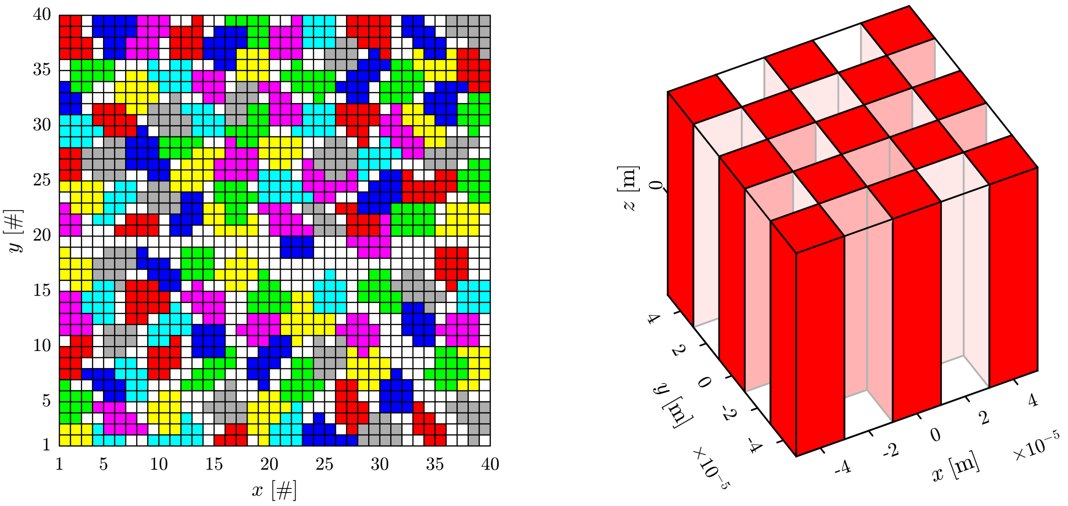

Figure 5.9: Possible voxelised domains for a grid-based random walk. **(Left)** 2D arrangement of individual, colour-coded cardiomyocytes. **(Right)** 3D chequerboard pattern with alternating ECS and ICS of equal size.

membrane permeability (if any). The implementation uses the efficient and parallel-compliant TRNG (Bauke, 2021, 2007) random number generator. The code is to be published at a later time.

The only concern regarding accuracy is the calculation of intersections of the step vector with the cell that the walker resides in. The implementation relies on *An Efficient and Robust Ray-Box Intersection Algorithm* by Williams et al. (2005).

An example of how a step vector interacts with the substrate is illustrated in figure 5.10. Initially, the walker is located inside the blue cell and attempts to move in the positive y and negative x direction. The first intersection test determines an intersection with the W-face of the current cell. The decision of the transit algorithm is to reflect the step, which happens elastically. Due to the remaining step length the next sub-step would put the walker outside the blue cell again, this time in the positive y direction through face N. The

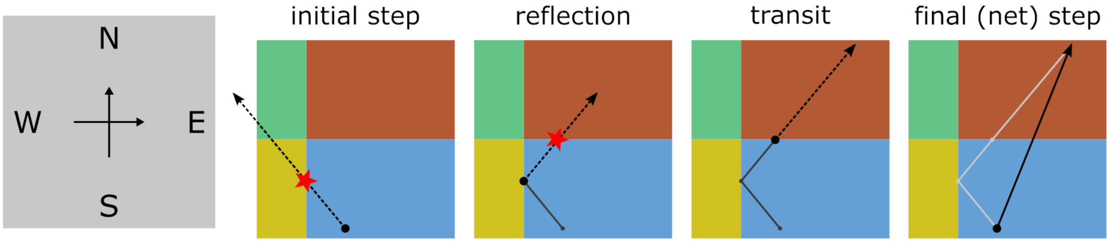

Figure 5.10: Random walk sub-stepping inside a 2D grid-based domain. From left to right: The grey cube on the left shows an individual voxel with its local xy coordinate frame and faces to neighbouring cells. The encounter of one selected step vector near a corner is described in the next four graphics.

transit decision allows the walker to transit and thus the compartment index is updated to place the walker in the orange cell. However, due to the higher diffusion coefficient inside the newly-entered cell the remaining step length is increased. The final sub-step encounters no further intersections and places the walker at its final position.

The grid implementation discussed above is an alternative to the 1D random walk code in appendix B.2.3. The ray-box algorithm is three-dimensional, and reduction of step dimension allows for 1D and 2D simulations using the same single codebase.

5.4.4 Walking in surface mesh geometries

Complex, arbitrary myocardial geometries cannot be efficiently represented by the methods described in section 5.4.3. Cardiomyocyte boundaries that are not aligned with the Cartesian frame are poorly resolved when voxelising the domain and require higher spatial resolution and thus increased computational effort. As an alternative, focus is now put on random walks in the presence of surface meshes.

Geometry data structures

Each modelled cardiomyocyte is tessellated and stored as a polyhedron. This is much less memory intensive, because only the representation needs to be stored instead of a grid of voxelised cells throughout the whole domain. The implementation is limited to polyhedra with triangular faces only. Triangles are the basic building blocks in computer graphics as they can efficiently represent arbitrary objects and because three points unambiguously define a plane. Many efficient algorithms exist to compute the intersection of lines with triangles in 3D. A triangulation consists of

- A list of `Vertices`, i.e. (x, y, z) coordinates; and
- A list of `Faces`, i.e. connectivities that determine which vertices correspond to which triangle. It is important to follow correct ordering to ensure the orientation of all normal vector is consistent (outward-pointing). That way, information about entering/exiting an object is encoded automatically.

Figure 5.11 illustrates the triangulation of a myocyte. For a detailed description of polygonal meshes, the reader is kindly directed to *Polygon Mesh Processing* (Botsch et al., 2010).

The simulation substrate is constructed from the tissue block that was segmented in section 2.3.4. To fill an entire imaging voxel, which is much larger than the block, a transform is used to map the global position of the walker inside the voxel to the local coordinate frame of the building block (Rose et al., 2019c). At the start of the simulation, given each walker's position, the compartment (polyhedron) that the walker is located

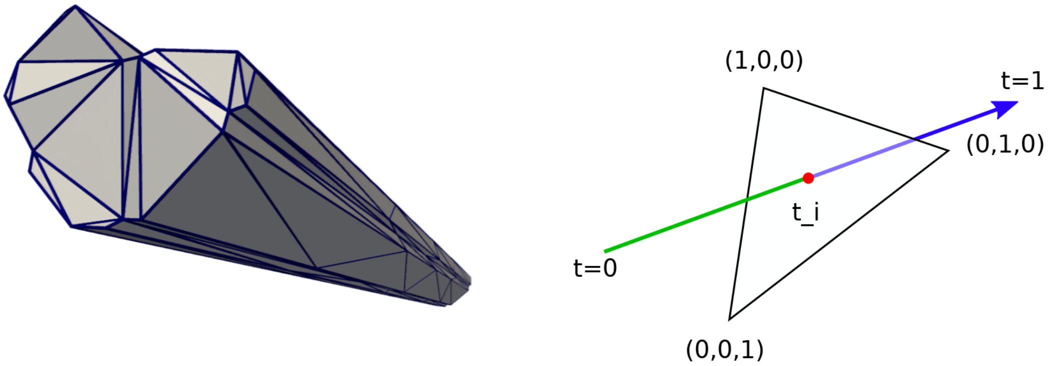

Figure 5.11: Triangulation and ray-triangle intersection explained. **(Left)** A single cardiomyocyte is represented as a polyhedron with triangular faces. The outline of a manually-segmented cell serves as the base polygon, which is triangulated using a Delaunay triangulation. The base is extruded by adding triangle strips to the sides of the cylinder. **(Right)** Barycentric coordinates are used to define the intersection location $\boldsymbol{x}_{\text{int}}$ on the triangle plane and subsequently at proportion $t_{\text{int}} \in [0, 1]$ along the step vector.

inside is identified and this compartment index is stored. Walkers in extra-cellular space are assigned a special value to identify this. For every time step, the walker uses its stored index to determine the step length based on the compartment's diffusion coefficient D_0. Interaction with the substrate barriers is described below.

Description of the software

The simulator described in this section was first presented by Rose et al. (2019c). It has now been made available, see appendix B.2.2. The code is written in MATLAB with performance-critical parts written in C and compiled with `mex`.

For each polyhedron, a *loose* bounding box is defined. It contains all vertices, with its size inflated by 1 % to prevent numerical inaccuracies around the extreme vertices. This accelerates the intersection search considerably, because it quickly eliminates bounding boxes from the more detailed and computationally involved intersection checking. Figure 5.12 explains how a single walker step is resolved in the presence of a mesh with bounding boxes. The actual ray-triangle intersections for polyhedra under consideration are then computed using the *Fast, Minimum Storage Ray-Triangle Intersection* (Möller–Trumbore) algorithm (Möller et al., 1997). A conservative approach is taken to ensure water-tightness of the geometry. The intersection point on the triangle is given in Barycentric coordinates as seen in figure 5.11. If one of these coordinates is deemed too close to an edge, this step is rejected and a new one is drawn. Without this, a walker might otherwise leave or enter a cell undetected. Also, walkers that have their initial position too close to the face are flagged due to possible ambiguity of compartment index. Investigations showed that these

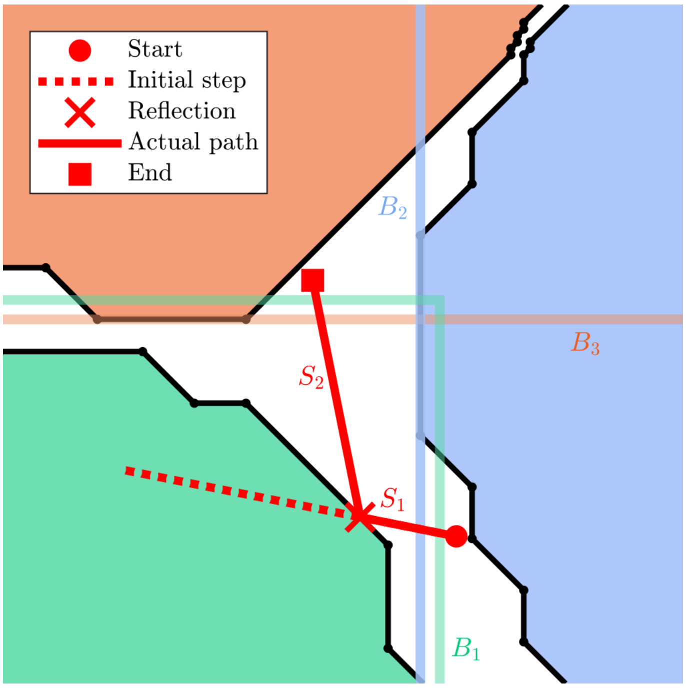

Figure 5.12: Resolving a random walk step inside a surface mesh–based domain. The bounding boxes B_i surround compartments Ω_i with barriers Γ_i. The steps of the algorithm are: **(1)** The walker is initially located at the circle in extra-cellular space inside B_2. The dotted line shows the initially-drawn random step vector. **(2)** Both Γ_2 (originating in B_2) and Γ_1 (entering B_1) need to be checked. An intersection point (cross) is found. The transit decision is to reflect the walker. **(3)** Sub-step S_1 is performed and now S_2 needs to be checked using the same procedure. Both Γ_1 and Γ_3 are checked this time but no intersection is found and the step terminates at the square. [*Reproduced with permission from (Rose et al., 2019c).*]

exceptions do not occur often and thus do not lead to substantial bias.

An improved version, written entirely in C++ and following the same approach as that in section 5.4.3, is currently being developed and requires future work. It takes advantage of advanced algorithms provided by the CGAL library (The CGAL Project, 2020) for accurate and efficient geometry handling. The primary performance gain originates from the use of an axis-aligned bounding box (AABB) tree (Alliez et al., 2020), illustrated in figure 5.13. For each triangular face, an AABB is constructed. These boxes are hierarchically grouped together to allow for efficient intersection queries.

Performance

Since it is trivial and efficient to parallelise the Monte Carlo random walk, parameters that determine the runtime of the simulation are: the number of walkers N_p, the computational cost per walker, and the available hardware like processor speed or number of available threads (Hall et al., 2009; Rafael-Patino et al., 2020). As shown in figure 5.14, the per-walker computational cost scales with both N_t and the number of faces (N_f) that are used

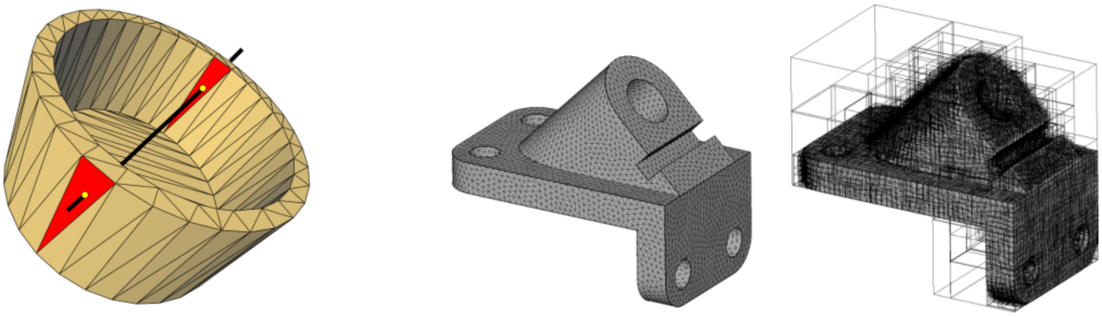

Figure 5.13: Triangulated surface mesh and corresponding axis-aligned bounding box (AABB) tree. The examples, extracted from the CGAL documentation (The CGAL Project, 2020), represent mechanical part but nonetheless serve to illustrate the capability of the library. **(Left)** CGAL supports efficient ray-triangle intersection. **(Right)** A hierarchical AABB tree accelerates queries. [*Reproduced with permission from (Alliez et al., 2020). The authors have dedicated this image to the public domain (CC0 1.0 license).*]

to represent the polyhedral cardiomyocyte geometries.

The impact of number of cardiomyocytes in the domain was not studied here. The current implementation does not use smart hierarchical structures to query only the local environment. As a result, increasing the size of the ROI is likely going to increase the runtime significantly.

5.5 Discussion

In this chapter, Monte Carlo random walk methods were discussed. This technique samples the underlying solution U with N_p walkers, and thus convergence is rapid and requires significantly less computational effort than traditional continuum-based methods such as those in chapter 3. Additionally, surface mesh–based implementations such as the one presented in section 5.4.4 allow for a more accurate and efficient representation of the substrate compared to a voxelised domain.

A significant portion of this chapter was spent analysing transit models. These models

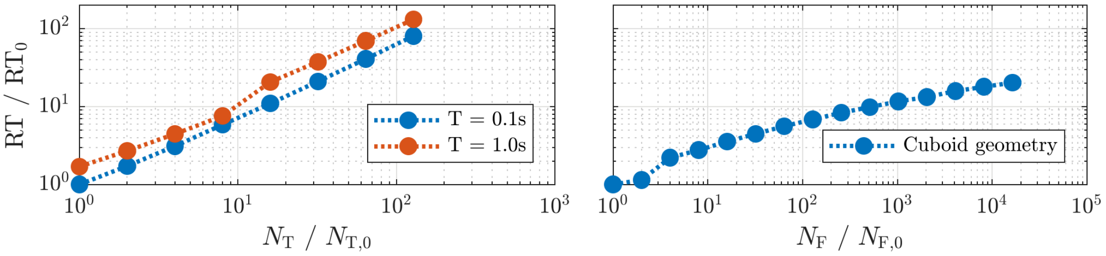

Figure 5.14: Scaling of simulation runtime of the mesh-based random walk simulator with number of time steps and faces. **(Left)** A realistic histology-based substrate is used for profiling. **(Right)** A simplified domain consisting of regular cuboids is progressively sub-divided to create an increasing number of triangular faces. [*Reproduced with permission from (Rose et al., 2019c).*]

are used to handle discontinuity in the random walk, for example when passing interfaces or membranes. It was determined that the model for interfaces by Maruyama (2017), given in equation (5.20), accurately captures a discontinuity in diffusion coefficient between two compartments. The commonly used model by Fieremans et al. (2010) in equation (5.21) is based on the membrane model by Powles et al. (1992), which handles a barrier with permeability κ. However, an investigation into the derivation of the model revealed error terms that cause a substantial bias beyond a certain critical time step in the case of different diffusion coefficients. Confirmed through flux analysis in section 5.3.3, an imbalance will develop that effectively traps walkers in regions of lower diffusion coefficient.

Note that due to the requirement that all geometric objects must be non-intersecting polyhedra, implementation of long fibres of cardiomyocytes is difficult. Two polyhedra can be made to *almost* touch at their end caps, however this would require the walker to pass through two permeable membranes with a κ that does not match that of intercalated discs (ICD). Additionally, the walker would briefly enter ECS which can be problematic. One solution is to represent ICDs as floating discs inside the ICS. These discs could be modelled similar to “force fields” at arbitrary planes, for which computational overhead would be low.

The MCRW simulator developed here will next be used to investigate realistic geometries in a parameter study.

Chapter 6

Simulations, Results, and Applications

Contents

6.1 Introduction

Chapters 3 to 5 described different numerical techniques for solving the diffusion equation and simulating DT-CMR. These methods are now applied to realistic myocardial tissue models developed in chapter 2.

First, this chapter presents results for impermeable membranes in section 6.2. Then, the suitability of the transit model that was analysed in section 5.3 is assessed numerically in section 6.3. Finally, a study of the effect of membrane permeability and its importance for realistic DT-CMR simulations is carried out in section 6.4.

6.2 Effect of microstructure on DT-CMR parameters

6.2.1 A histology-based microstructure with impermeable membranes

This section presents DT-CMR simulations in a realistic microstructure, based on previously published work (Rose et al., 2019c). For this initial study the cell membranes are considered impermeable. The purpose of these simulations is to obtain insights into the diffusion behaviour within a complex microstructure without the confounding effect of membrane permeability, which will be addressed later in section 6.4. Parameters intrinsic to the

Table 6.1: Sequence parameters for the three sequences shown in figure 3.1. The target gradient strength is 40 mT/m per axis with a b-value of 450 ms/µm^2. The individual parameters are defined in figure 3.2.

Sequence parameter	PGSE	M2-SE	STEAM
G_{max} (mT/m)	40.572	39.478	35.690
Δ (ms)	20.547	n/a[1]	1000
TE (ms)	39.332	70.757	23.824
TM (ms)	n/a	n/a	988.088
ϵ (ms)	0.676	0.661	0.595
δ (ms)	9.921	n/a	0.977
δ_1 (ms)	n/a	7.819	n/a
δ_2 (ms)	n/a	16.299	n/a

[1] The diffusion time Δ is not defined for the M2-SE sequence.

substrate tissue model (diffusion coefficient, ECV) as well as parameters external to the simulation (pulse sequence) are studied.

The substrate geometry is based on swine histology (Nielles-Vallespin et al., 2017). As described in section 2.3.4, it is constructed based on a ROI that fills the entire imaging voxel of size $2.8 \times 2.8 \times 8.0\,\text{mm}^3$. This model includes sheetlet structures and accounts for transmural rotation. The compartment-specific diffusion coefficients D_0 within the two compartments and the ECV of the substrate are varied in several experiments described below, where their choice is motivated further. The knowledge gained on the sensitivity of the diffusion signal with respect to these parameters will allow for more educated decisions on model parameter choices in future simulations.

The three typical DT-CMR sequences PGSE, M2-SE, and STEAM (recall these from section 3.2.2) are simulated. Their gradient waveforms are shown in figure 3.1 while the specific timing parameters are given in table 6.1. These parameters have a target gradient strength G_{max} of 40 mT/m and their b-value is 450 ms/µm^2, based on typical clinical MRI scanners and in-vivo studies.

As a result of the use of impermeable membranes, the random walk simulations can use Gaussian stepping to accelerate convergence. The normal distribution for the Cartesian step vector components is truncated to $\pm 5\sigma$ as permitted by section 5.2.1. Additionally, no restriction on the time step is necessary. Nonetheless, a maximum time step of 1 ms is imposed. During gradients, a lower maximum δt of 0.1 ms is enforced to increase accuracy. These time steps, respectively, correspond to (3D) step lengths of 3 and 0.95 µm for $D_0 = 1.5\,\text{µm}^2/\text{ms}$.

6.2.2 Convergence of simulations

Before carrying out meaningful simulations that study the effect of microstructural and imaging parameters, the choices of statistical (Monte Carlo) parameters must be verified first. The appropriate simulation parameters and the resulting convergence behaviour are dependent on the specific problem that is being considered, particularly the degree of geometric complexity at various scales and the imaging voxel size (which relates to the local walker density). It is thus wise to carry out such convergence checks whenever a significant change is made to the setup of the simulations (Hall et al., 2009). Particularly, the number of walkers N_p and time steps N_t required for *sufficiently* precise simulations of realistic histology are determined here. The choice of N_t is especially relevant because simulation runtime scales linearly with the number of time steps as demonstrated in figure 5.14. A trade-off is thus required to ensure the right balance is struck between computational effort and accuracy, with the ultimate goal of carrying out more simulations of different parameters within an acceptable time frame.

Random walk convergence study

Convergence with respect to N_p and N_t is studied similar to figure 5.3, where the optimal truncation point for the Gaussian step distribution was determined. A substrate from section 2.3.4 with a realistic ECV of 25 % is selected for the benchmark convergence study. Intra- and extra-cellular diffusion coefficients are set to $D_{\mathrm{ICS}} = 1.5\,\mu\mathrm{m}^2/\mathrm{ms}$ and $D_{\mathrm{ECS}} = 3\,\mu\mathrm{m}^2/\mathrm{ms}$ respectively.

Two values of N_t (10^3 and 10^4) and three values of N_p (10^3, 10^4, and 10^5) are considered. Each simulation is repeated 10 times per combination of parameters, each with different random seeds to allow an assessment of the inter-simulation variability. The diffusion tensor is then calculated for each data point and post-processed to obtain the mean diffusivity (MD) and fractional anisotropy (FA) as the integral quantities of interest. Figure 6.1 shows how both these variables converge with an increase in number of walkers. The highest resolution was $N_p = 10^6$ (combining all 10 runs with each $N_p = 10^5$) and $N_t = 10^4$, and its diffusion tensor is used as the fully-converged reference. In the figure, relative errors are reported with respect to this reference value.

As expected, the variance of tensor parameters for repeated experiments decreases with an increase in the number of walkers. While the spread of the 10 values is considerable at $N_p = 10^3$, their median value is already close to 0. The maximum absolute deviation of MD and FA is generally less than 5 % for $N_P = 10^4$ and $N_T = 10^3$. Similar values were observed for the individual eigenvalues (not shown here). The difference between using 10^3 and 10^4 time steps is negligible as a finer time step of $N_T = 10^4$ only slightly reduces the maximum error per N_p.

Similar behaviour is observed for all three sequences. However, at a low resolution ($N_p = 10^3$, $N_t = 10^3$) the STEAM sequence reports the highest variance in MD but smallest in FA. This may be explained by a constant absolute error that the insufficient sampling introduces and a relatively high FA and low MD as a result of the long diffusion time in

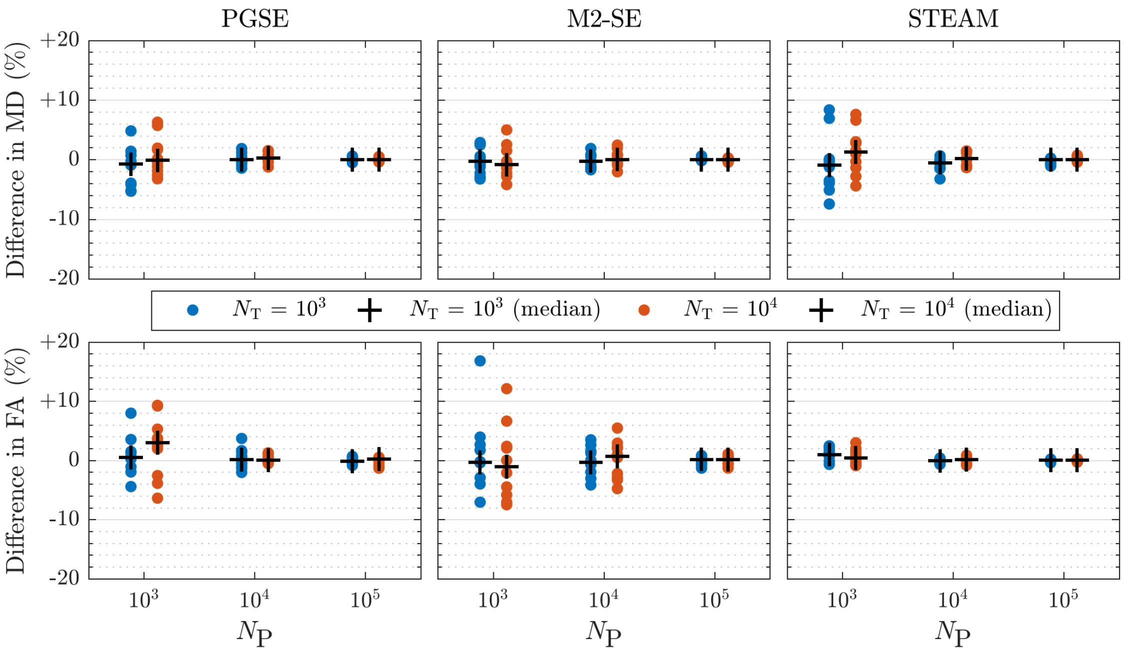

Figure 6.1: Convergence of mean diffusivity (MD) and fractional anisotropy (FA) with increasing number of walkers N_p and time steps N_t for all three pulse sequences, using $N_p = 10^6$ and $N_t = 10^4$ as a reference. Based on these results, $N_p = 10^4$ and $N_t = 10^3$ are considered sufficiently converged for use in the following studies. [*Reproduced with permission from (Rose et al., 2019c).*]

the STEAM sequence. Other factors may also play a role, such as the larger step length associated with STEAM for a constant N_t. In future work, setting a constant δt rather than constant N_t would allow for fairer comparison between sequences at the expense of longer simulation times for STEAM.

Assessing convergence by comparison with a continuum solution

The Monte Carlo random walk simulations are also compared with a reference solution, obtained from a finite volume method (FVM) in two dimensions (Rose et al., 2018e). The interested reader is directed back to section 3.3.3, where the techniques were described in detail. A description of the software and data is given in appendix B.2.1. At the time of these simulations, the GPU-based solver from section 3.3 had not been developed yet. The FVM code used here is thus based on the MATLAB project FVTool (Eftekhari, 2021) and uses implicit time stepping to ensure stability irrespective of time step. This allows synchronisation of the finite volume simulation with the random walk solution, which has no intrinsic time step limit, irrespective of image resolution.

An image-based (pixelised) domain is used where intra- and extra-cellular space corresponds directly to the manual segmentation mask from figure 2.9. Because the restricted intra-cellular diffusion is expected to converge quickly due to the limited geometric complexity of the random walk inside cells, diffusion is only modelled in extra-cellular space

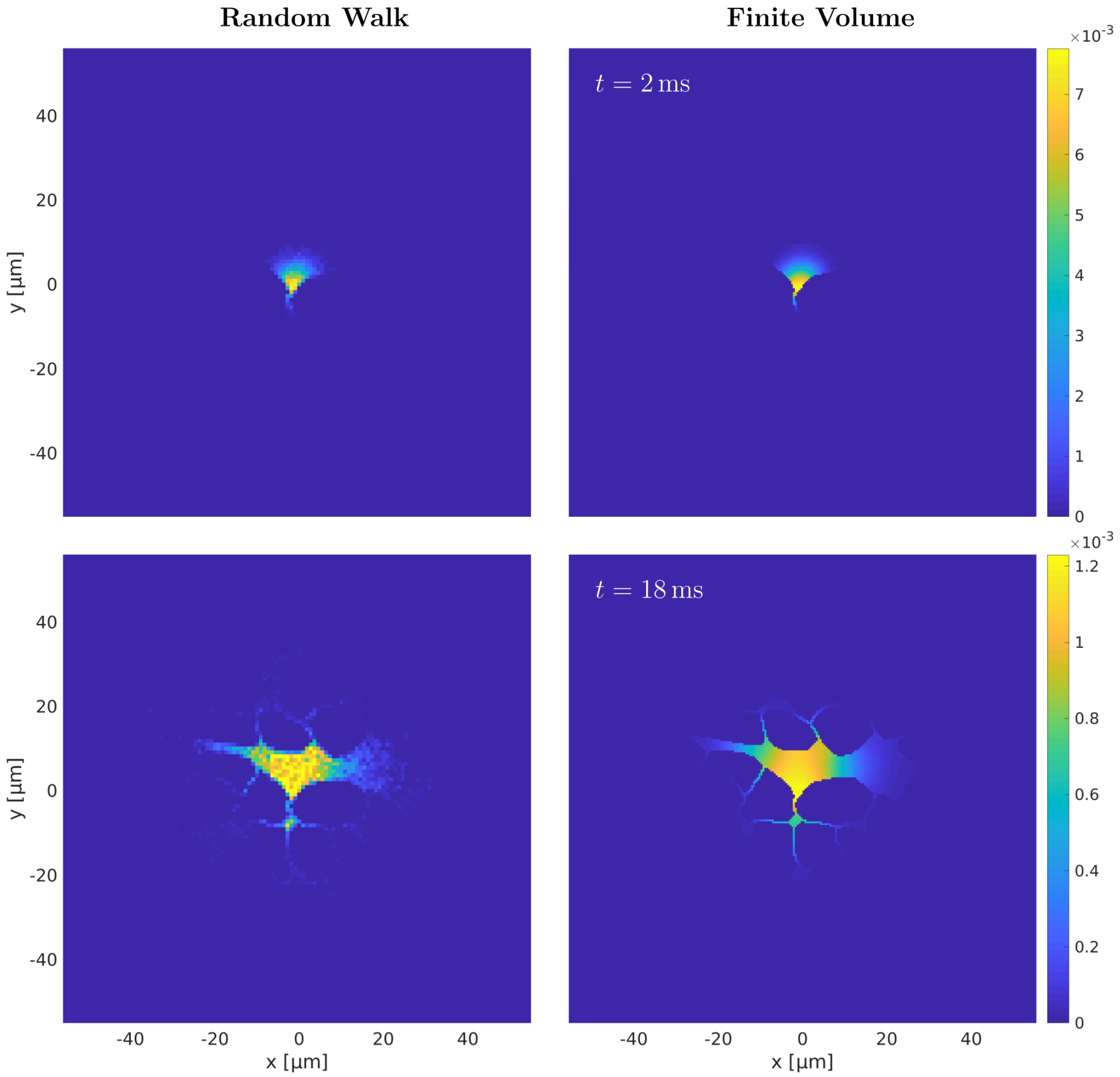

Figure 6.2: Qualitative comparison of random walk **(Left)** and finite volume **(Right)** simulations of diffusion in extra-cellular space. Walkers/concentration were initially located in ECS (with $D_{\mathrm{ECS}} = 3\,\mathrm{\mu m^2/ms}$) at the centre of a $100 \times 100\,\mathrm{\mu m^2}$ square containing impermeable cells. There is good visual agreement between the two methods.

at this stage. For a given initial condition $U(\boldsymbol{x}, 0) = \delta(\boldsymbol{x} - \boldsymbol{x}_0)$, a square sub-domain centred around $\boldsymbol{x}_0$ is extracted with sufficiently large side lengths such that (a significant amount of) concentration is not expected to reach the domain bounds and thus boundary effects (Hwang et al., 2003) are avoided. Figure 6.2 shows a qualitative comparison between the random walk and finite volume solutions for one of these sub-domains, simulated with $N_t = 10^4$ time steps and an extra-cellular diffusion coefficient of $D_{\mathrm{ECS}} = 3\,\mathrm{\mu m^2/ms}$. Two time points (2 and 18 ms) are chosen. Overall, there is good agreement between the two methods. The $N_p = 10^4$ random walkers are visualised by a 2D histogram calculated for bins corresponding to the individual pixels and normalised to match the FVM, which satisfies $\int_\Omega U \,\mathrm{d}x = 1$.

From figure 6.2 it is apparent that a large number of walkers would be needed to precisely recover the PDF (or distribution of concentration as provided by the FVM) at every pixel. This is especially true at higher times t where multiple peaks of maximum concentration appear in the MCRW results. Alternatively, larger histogram bins could help reduce the fluctuations intrinsic to the random walk. However, the primary focus of investigations in this chapter remains to simulate the integral diffusion quantities in a large DT-CMR voxel.

To quantify the amount of walkers needed to sufficiently sample restriction in the entire domain, 10^5 points in the ECS are randomly selected as individual seed points. For each point the MCRW simulation is run with a single walker. This returns one trajectory that samples the local PDF.

With the FVM, on the other hand, a single simulation returns the entire PDF. A large number of these local solutions are calculated to obtain the reference solution. In the limit of sampling the entire space, their convolution yields the underlying steady-state solution of constant concentration in the domain.

The apparent diffusion coefficients along the two Cartesian directions, D_x and D_y, as well as the mean (Euclidean) diffusivity MD $= \langle D \rangle$ are calculated from the mean squared displacement (MSD). For processing the random walk, equation (5.3) can be used. The continuum approach however does not contain a mechanism for tracking the migration of individual particles. Instead, the concentration at the discretised positions $\boldsymbol{x}$ is volume-averaged using

$$\langle \delta \boldsymbol{x} \rangle = \int_\Omega U(x)(\boldsymbol{x} - \boldsymbol{x}_0)^2 \,\mathrm{d}v \,. \tag{6.1}$$

The apparent diffusion coefficients after diffusion time Δ are then calculated via

$$D_x = |\langle \delta x \rangle_x^2|/(2\Delta) \tag{6.2a}$$

$$D_y = |\langle \delta x \rangle_y^2|/(2\Delta)\,, \tag{6.2b}$$

$$\langle D \rangle = \|\langle \delta x \rangle^2\|/(4\Delta)\,. \tag{6.2c}$$

These values are plotted in figure 6.3 for an increasing number of walkers, compared to the finite volume reference solution.

Similar to what was observed in figure 6.1, using $N_p = 10^4$ is sufficient for repeatable simulations, resulting in errors of <4 %. The mean value for ADC at the lower $N_p = 10^3$ is within the range of the maximum extent of values at $N_p = 10^4$ which suggests their deviation from the reference solution is due to random noise and not bias at low N_t. While the computational effort for computing *all* PDFs in the domain is large, especially with the finite volume method, it was shown here that sampling both the spatial component (which PDF to include, based on $\boldsymbol{x}_0$) and the PDFs themselves (as each walker only represents one

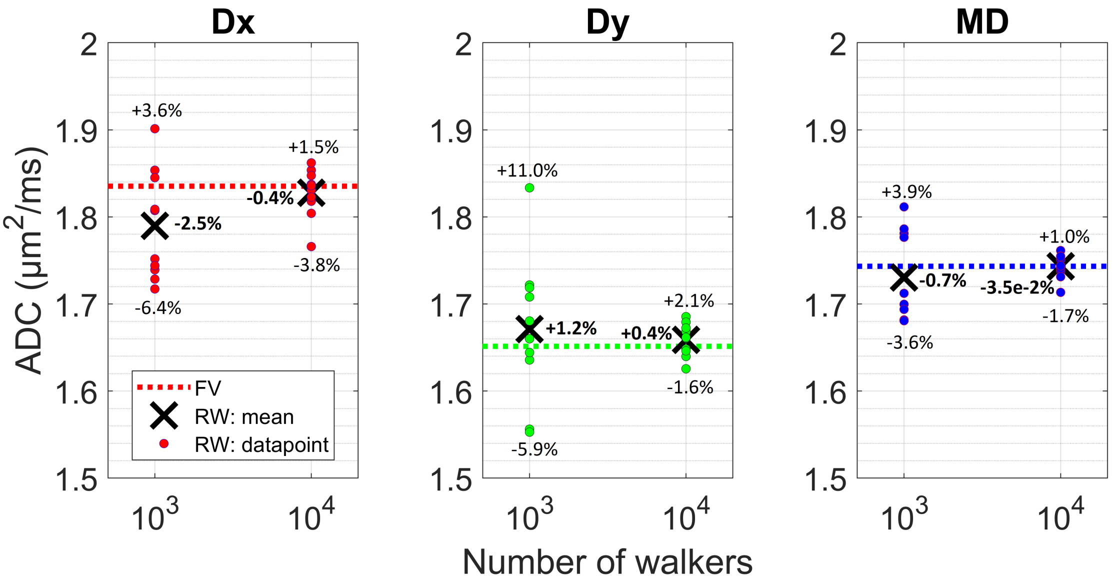

Figure 6.3: Apparent diffusivities calculated from the mean square displacement of walkers/concentration by random walk and finite volume method. D_x and D_y are only considering the component along the two respective Cartesian axes while MD is derived based on the Euclidean distance. FA is not calculated because no diffusion tensor is obtained from the data.

realisation) is an elegant and efficient way to obtain integral quantities such as apparent diffusion coefficients.

Conclusions about what constitutes a converged result

Due to the nature of Monte Carlo simulations, each data point is subject to random noise. Repeated simulations and in fact separate random walks of individual walkers in the same experiment differ only in and are fully determined by the initial random seed or (sub)sequence of the pseudo-random number generator (pRNG). In the limit of $N_p \to \infty$ the MCRW converges to the true analytical diffusion solution. For a finite number of walkers, a threshold needs to be determined where the difference from this true solution is minimal.

In this section, convergence of random walk simulations was studied by two means: First, random walk solutions of DT-CMR simulations were performed with increasingly more walkers and time steps. Second, a simulation of diffusion without diffusion-encoding gradients was verified by comparison to a continuum (FVM) solution in 2D.

Both methods independently suggest that using $N_p = 10^4$ walkers with $N_t = 10^3$ time steps per simulation provides sufficiently converged results. This recommendation is based on simulations of DT-CMR in histology-based domains and agrees with observations by Hall et al. (2009), who studied convergence for 3D simulations in domains of randomly packed circular cylinders. Further investigation is needed to make general statements

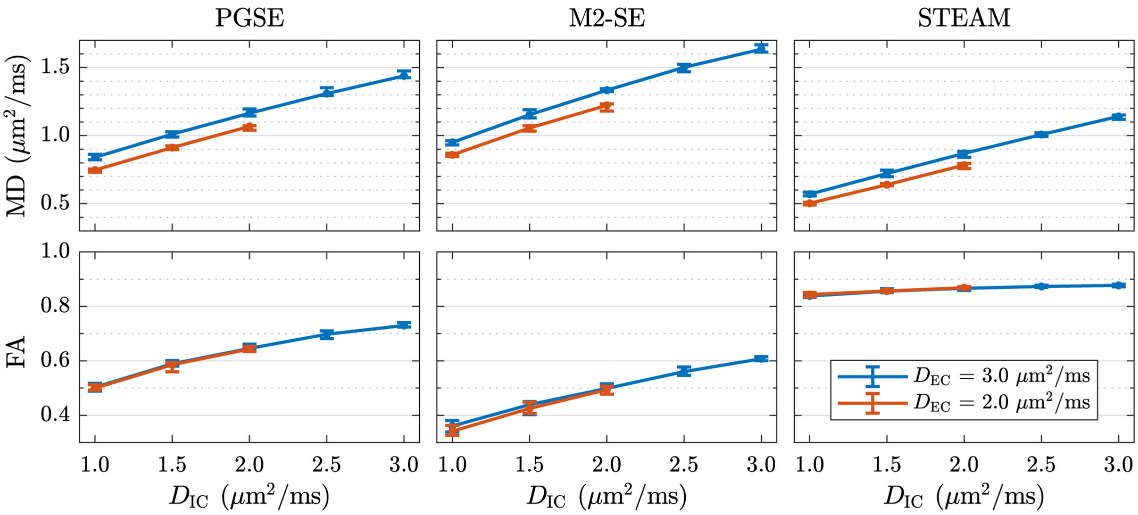

Figure 6.4: Sensitivity of DT-CMR parameters to compartment-specific diffusion coefficients. A histology-based simulation substrate with an ECV of 25 % is used. For each data point 10 random repetitions are performed and their median values are plotted with error bars to signal the two-sided 95 % confidence interval. [*Reproduced with permission from (Rose et al., 2019c).*]

about these numbers regarding geometric complexity; The number and size of features of interest, voxel size and particle density, and other factors are all expected to impact the rate of convergence.

Comparison with a continuum solution has demonstrated that integral quantities such as mean apparent diffusion coefficients are reliably calculated using few walkers, even though a considerably larger number may be necessary to accurately capture the probability density function $U(x, t; x_0)$ for certain points x_0. The use of Gaussian steps accelerates convergence as explained in section 5.2.1 but is permitted only for impermeable barriers (recall section 5.3), which are used in this section 6.2. Due to the relatively low number of random number draws ($N_p \cdot N_t = \mathcal{O}(10^7)$) it is nonetheless recommended to perform multiple repetitions of the experiment to obtain a distribution of values per set of input parameters. Reporting their median value alongside some measure of variance increases confidence in the results, especially if other parameters are varied and a priori knowledge is limited. In this work, 10 repetitions together with a 95 % two-sided confidence interval are used.

6.2.3 Model parameter study

A large-scale parameter study was carried out using a realistic 3D histology-based geometry (Rose et al., 2019c). The most relevant results from the study are shown here.

Diffusion coefficient

Figure 6.4 shows the sensitivity of DT-CMR parameters to D_{ICS} and D_{ECS}. The spin

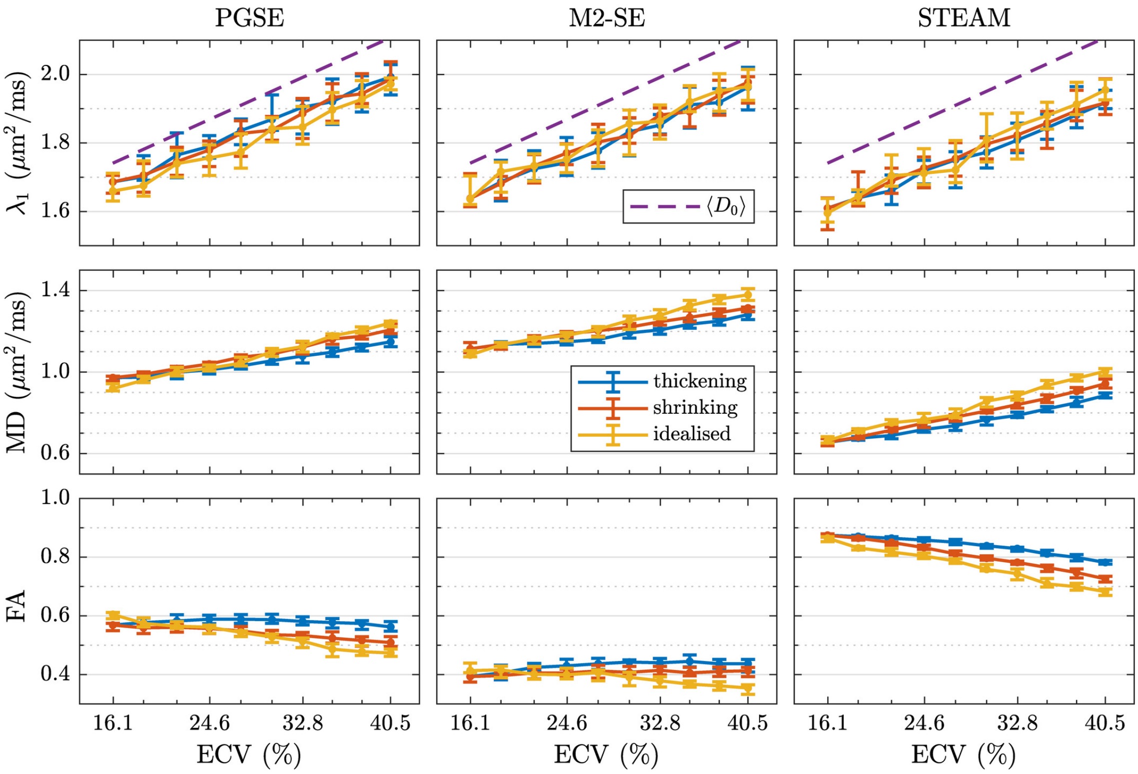

Figure 6.5: Sensitivity of DT-CMR parameters to extra-cellular volume fraction. Two histology-based substrates (thickening, shrinking) and one geometry based on regular cuboids (idealised) are simulated. For each data point 10 random repetitions are performed and their median values are plotted with error bars to signal the two-sided 95 % confidence interval. [*Reproduced with permission from (Rose et al., 2019c).*]

echo sequences show a strong dependence on intra-cellular diffusion coefficient. The MD is slightly reduced in the case of a lower D_{ECS} as expected due to slower diffusion overall. However, the FA is unaffected by this change in D_0.

The STEAM sequences shows an almost constant FA irrespective of D_0. This suggests that the shape of the restrictions is more important than the underlying diffusion coefficient, as the long mixing time of $\Delta = 1\,\mathrm{s}$ fully senses the boundaries. STEAM is, however, most sensitive to D_{ICS} when looking at the MD value.

Substrate type and ECV

Figure 6.5 plots the DT-CMR parameters as a function of ECV (modified via morphing, see section 2.3.5). Three different substrates are simulated: Thickening and shrinking were described and are plotted in figure 2.10. The idealised geometry consists of cuboidal cardiomyocytes in an arrangement that matches the ECV and average cell shape of the realistic histology-based domain, but lacks the sheetlet structure characteristic of the myocardium.

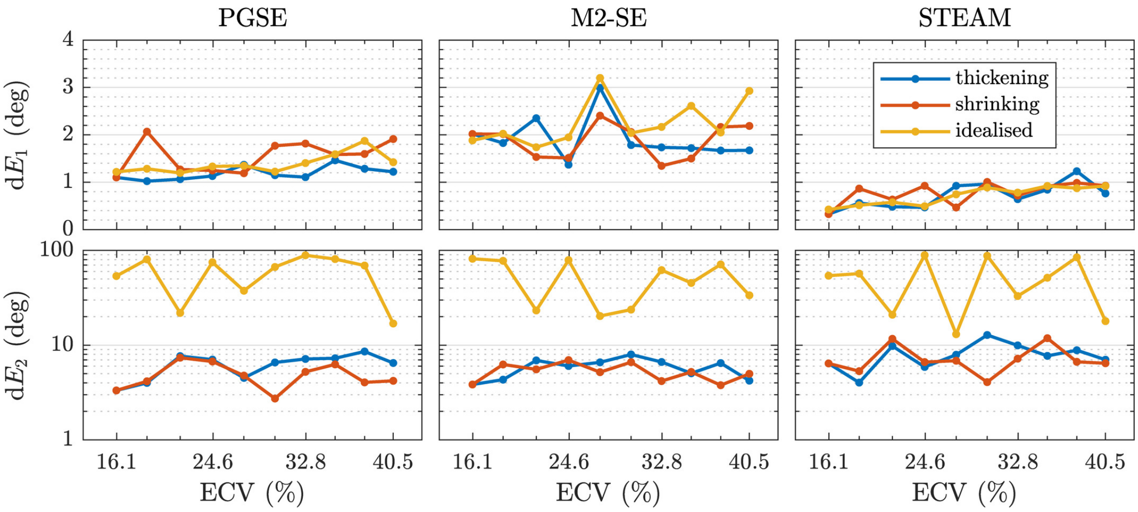

Figure 6.6: Cone of uncertainty analysis of DT-CMR parameters, sensitive to extra-cellular volume fraction. The same data points from figure 6.5 are processed to obtain the 95 % one-sided confidence interval of the error in the eigenvector orientations. [*Reproduced with permission from (Rose et al., 2019c).*]

Figure 6.5 shows that the spin echo sequences report an almost constant FA with change in ECV. The STEAM sequence shows much more sensitivity, with FA reducing for larger ECV. However, values of FA for STEAM are significantly larger than expected from in-vivo DT-CMR data. The almost pencil-like shape of the diffusion tensor is likely due to the lack of membrane permeability. Sensitivity of MD to ECV is similar for all three sequences.

Additionally, the cone of uncertainty (Jones, 2002) is calculated for all data points in figure 6.5. The uncertainty of the first and second eigenvector is plotted in figure 6.6. The STEAM sequences reports the lowest uncertainty of the first eigenvector, which makes sense given that its long Δ causes walkers to sense the pencil-like shape of the impermeable cardiomyocytes very well. More interesting is the uncertainty of the second eigenvector. Particularly, the difference between idealised and realistic geometry. The idealised cuboidal substrate lacks the preferred secondary direction of diffusion that real tissue shows as a result of the sheetlet structure. This shows that simplified geometries such as those used in literature (Bates et al., 2017; Wang et al., 2012) are insufficient in modelling realistic DT-CMR tensor shapes.

6.2.4 Discussion

The simulations of DT-CMR in a realistic, histology-based model of the myocardium have provided novel insights into the relationship between tissue model parameters and the diffusion tensor that characterises the diffusion within the substrate. Based on a convergence study, each simulation used $N_p = 10^4$ walkers and $N_t = 10^3$ time steps.

These Monte Carlo parameters result in accurate and reproducible DT-CMR measures while keeping the simulation time at an acceptable level. For example, simulations in section 6.2.3 required a total of 114 different combinations of input parameters. Simulations were run on the Imperial College High Performance Computing (HPC) cluster, where the computational effort of one data point using a modern CPU with 20 cores was recorded at $\approx$2000 s. Because each experiment was repeated 10 times, the total runtime was $\approx$650 h. Multiple compute nodes on the HPC system were used in parallel for a faster overall turnaround time.

Parameter studies varying model parameters like the diffusion coefficients and ECV were performed. In this initial investigation, membranes were considered impermeable in order to investigate the effects of intra- and extra-cellular compartments separately. Major findings include the different sensitivities of different pulse sequences to different tissue parameters and the need for accurate distribution of extra-cellular space to capture sheetlet objects.

The scale of the tissue model was limited to the ROI considered in section 2.3.4, chosen from histology images as being representative of the surrounding tissue in the mid-myocardium. This "building block" was replicated to fill a large imaging voxel, while applying the transmural rotation seen in the myocardium. The image region contains a predominant (horizontal) direction of extra-cellular space due to the shear layers between sheetlets, but a second population of vertically orientated sheetlets is present too. This is explained by the "two sheet" model (Kung et al., 2011). Additional processing and simulations would be necessary to compare and validate the findings by Kung et al. using a substrate with more well-defined sheetlet orientations and (initially) without the confounding effect of transmural rotation.

6.3 Incorporating the transit model for permeable membranes

Simulations in section 6.2 reported higher-than-expected values for the fractional anisotropy (FA), especially for the long diffusion times of the STEAM sequence. A hypothesis for explaining this observation is the assumption of impermeable membranes, which may not be appropriate for cardiomyocytes. Before repeating these previous simulations with permeable membranes later in section 6.4, the transit model that is to be used needs to be tested and verified.

Section 5.3 discussed in length the use of transit models for Monte Carlo random walk simulations as well as their mathematical underpinning. The popular model by Fieremans et al. (2010), given in equation (5.21), was found to contain an intrinsic error beyond a certain critical value of the time step. Here, this is evaluated numerically to assess the model's suitability for simulations with parameters typical for DT-CMR. The study is carried out in 1D, where the analytical solution from chapter 4 can serve as the ground truth and where visualisation and interpretation of results is most intuitive. The method can then be trivially extended to higher dimensions.

6.3.1 Analysis of the steady-state solution

The steady-state solution to permeable media with varying diffusion coefficients is a constant concentration throughout the domain, as supported by the analytical solution in chapter 4. Flux analysis in section 5.3.3 showed that the transit model in equation (5.21) does not have such a balanced steady-state solution. For membranes with a step change in diffusion coefficient across it, there is a net flux in the direction of lower D_0.

Model domain and parameter choice

Consider a domain with a single permeable barrier separating two compartments of different diffusion coefficients. This isolates a single interface and avoids confounding effects from other compartments. Diffusion coefficients are chosen to be $D_L = 0.5\,\mu\mathrm{m}^2/\mathrm{ms}$ and $D_R = 2.5\,\mu\mathrm{m}^2/\mathrm{ms}$, representing intra- and extra-cellular space respectively (section 2.3.1). The membrane permeability is set to $\kappa = 0.05\,\mu\mathrm{m}/\mathrm{ms}$, calculated using equation (2.4) based on an estimated $\tau_{\mathrm{ex}}^{-1} = 30\,\mathrm{Hz}$. For myocardial tissue this assumes an ECV of $\rho = 25\,\%$ based on Kellman et al. (2012). The claustrophobia ratio in equation (2.6) is calculated for cylindrical cardiomyocytes with radius $R = 15\,\mu\mathrm{m}$ and height $H = 110\,\mu\mathrm{m}$ based on Tracy et al. (2011).

To achieve an initially constant concentration density throughout the domain, walkers are seeded randomly inside the domain by drawing positions $x_p(0)$ from a uniform distribution. As shown in figure 6.7, using 10^6 walkers is sufficient for a smooth solution with an acceptable (random) error compared to the true steady-state. In the figure, histograms illustrate the random walk solution, density-normalised such that the bin density ρ_{bin} (which corresponds to a constant U in the bin) is $\rho_{\mathrm{bin}} = c_{\mathrm{bin}}/N_p/w_{\mathrm{bin}}$ where c_{bin} and w_{bin} are the bin count and width respectively.

Error at moderate time steps

The time step dependence of the membrane transit model is now investigated. Figure 6.8 shows histograms of the random walk solutions for different time steps δt (20, 4, 1, and 0.05 ms) and two solution times (20 and 1000 ms). The figure 6.8 also shows the results for the interface model in equation (5.20), which corresponds to a fully-permeable barrier. For the short-time solution at 20 ms, the membrane transit model fails to preserve the initial

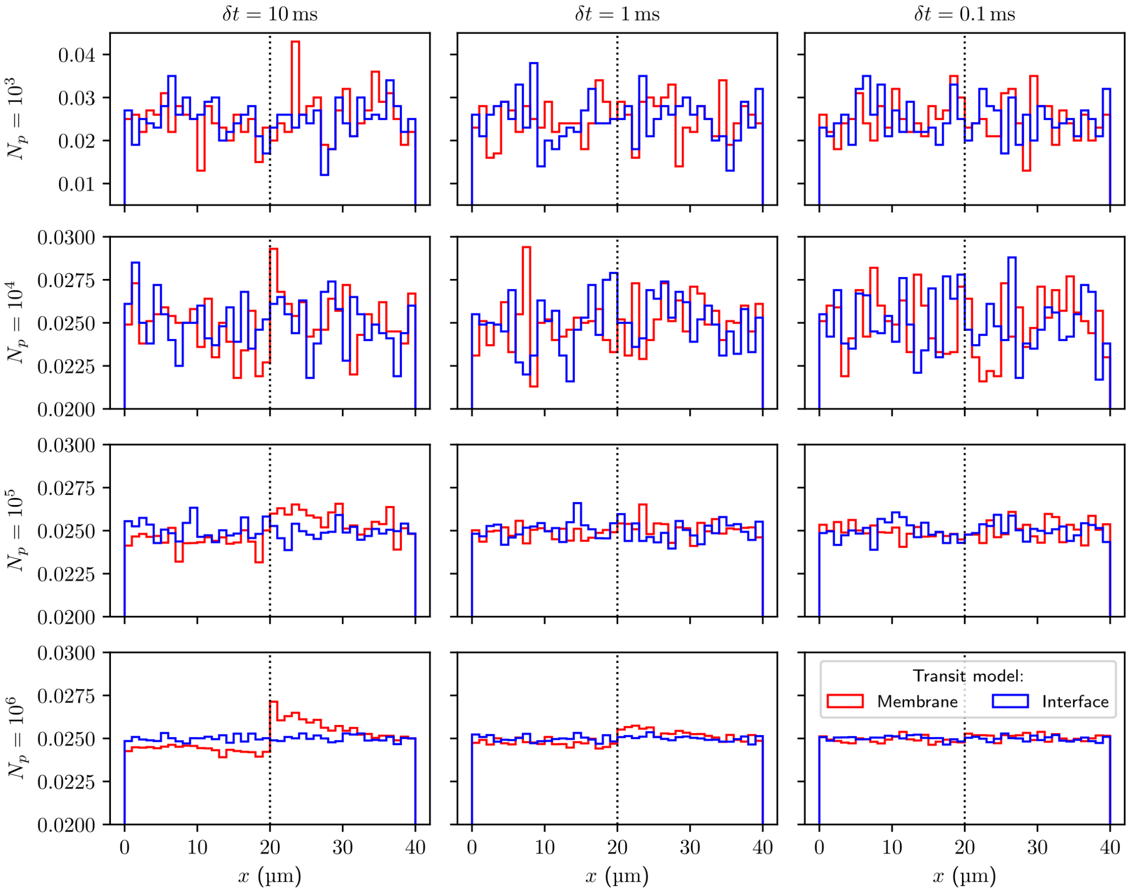

Figure 6.7: Convergence of random walk for membrane (red) and interface (blue) transit models. Using $N_p = 10^6$ random walkers is sufficient to reduce fluctuations due to randomness to an acceptable level for all time steps δt.

steady-state solution near the barrier at large time steps. As the time increases to 1000 ms, a visible concentration imbalance between the two compartments develops.

The difference in compartment density ΔU across the membrane increases with δt and appears to stabilise at some value as $t \to \infty$: For a solution time $t = 1000\,\mathrm{ms}$ and a time step $\delta t = 0.05\,\mathrm{ms}$, figure 6.8 shows an excess of concentration in the left compartment of 0.88 %, for $\delta t = 20\,\mathrm{ms}$ this increases to 10.2 %. The interface model on the other hand represents the expected solution with a constant U. A maximum of $\Delta U = 0.18\,\%$ is reported between all values of t and δt, suggesting that there is no accumulation of walkers for any time step when permeability is infinite. The variation in bin densities for the interface model can be attributed to randomness of the simulation. At $t = 1000\,\mathrm{ms}$ the difference between observed ρ_{bin} values relative to the expected $\rho^*_{\text{bin}} = 1/\sum L = 0.025$ has a median (among δt) standard deviation of 0.0013 (or 5 % relative to ρ^*_{bin}).

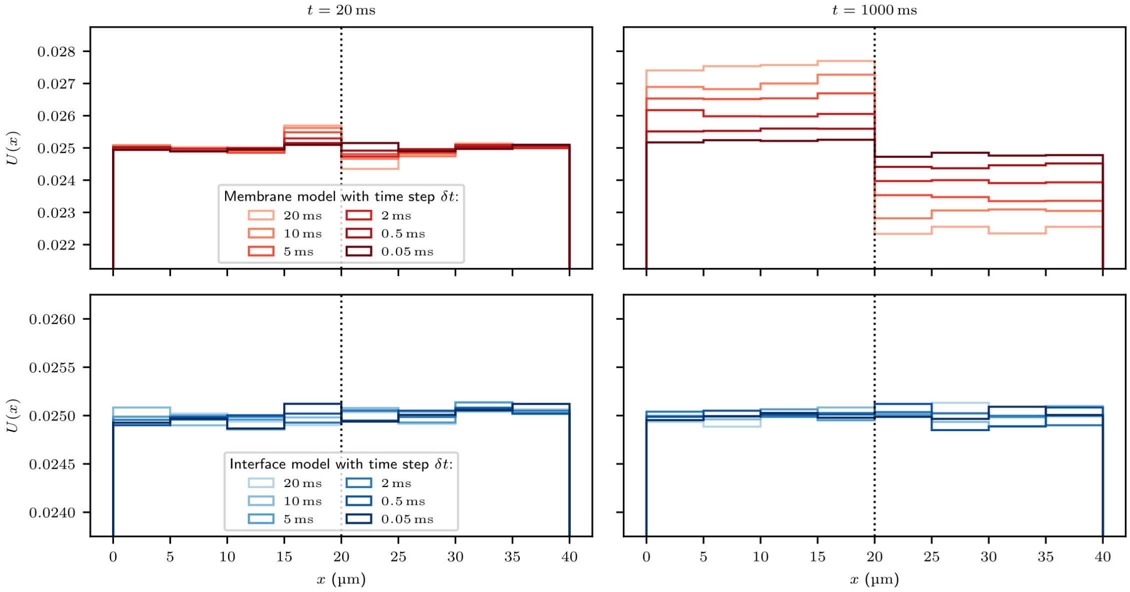

Figure 6.8: Histograms of walker positions after random walk simulations of the steady state for membrane **(Top)** and interface **(Bottom)** transit models. Initial positions were sampled from a uniform distribution to seed walkers with a constant density throughout the domain. Simulations were performed with varying step sizes δt for a short and a long simulation time t. The membrane model described in equation (5.21), with permeability $\kappa = 0.05\,\mu\mathrm{m/ms}$, shows a concentration imbalance develop with increased time step δt and duration t. The interface model **(Bottom)** from equation (5.20), which considers $\kappa \to \infty$, retains a constant concentration for all parameters. Noticing the difference between y-axis scales between the two rows of plots makes it clear that variations of histogram counts are the result of random fluctuations.

6.3.2 Analysis of the initial transient response

Histograms in figure 6.8 showed that the membrane transit model develops a concentration imbalance in the steady-state case for large time steps, which is consistent with the flux analysis in section 5.3.3. Here, the transient behaviour of $U(x, t; x_0)$ after an initial spike in concentration is investigated and the flux through the membrane is computed. Analysing the fluxes offers more insights into the exchange process, which is modelled as a random process, than looking at concentrations on either side of the interface. Additionally, the flux as an integral quantity can be compared easily with the analytical solution and does not rely on histogram binning, which is prone to noise.

Recall that equation (5.17) represents the flux boundary condition across the barrier(s) in the domain. Its left-hand side matches the definition of flux J in Fick's first law (recall equation (5.18)), while the right-hand side relates it to the permeability and difference in concentration across the barrier. The units of J are concentration (fraction of walkers) per unit time and unit area, but the latter is omitted such that $[J] = 1/\mathrm{ms}$. The flux in the analytical solution is calculated through the right-hand side of equation (5.17), evaluating U on either side of the discontinuity. In the case of the random walk, the net

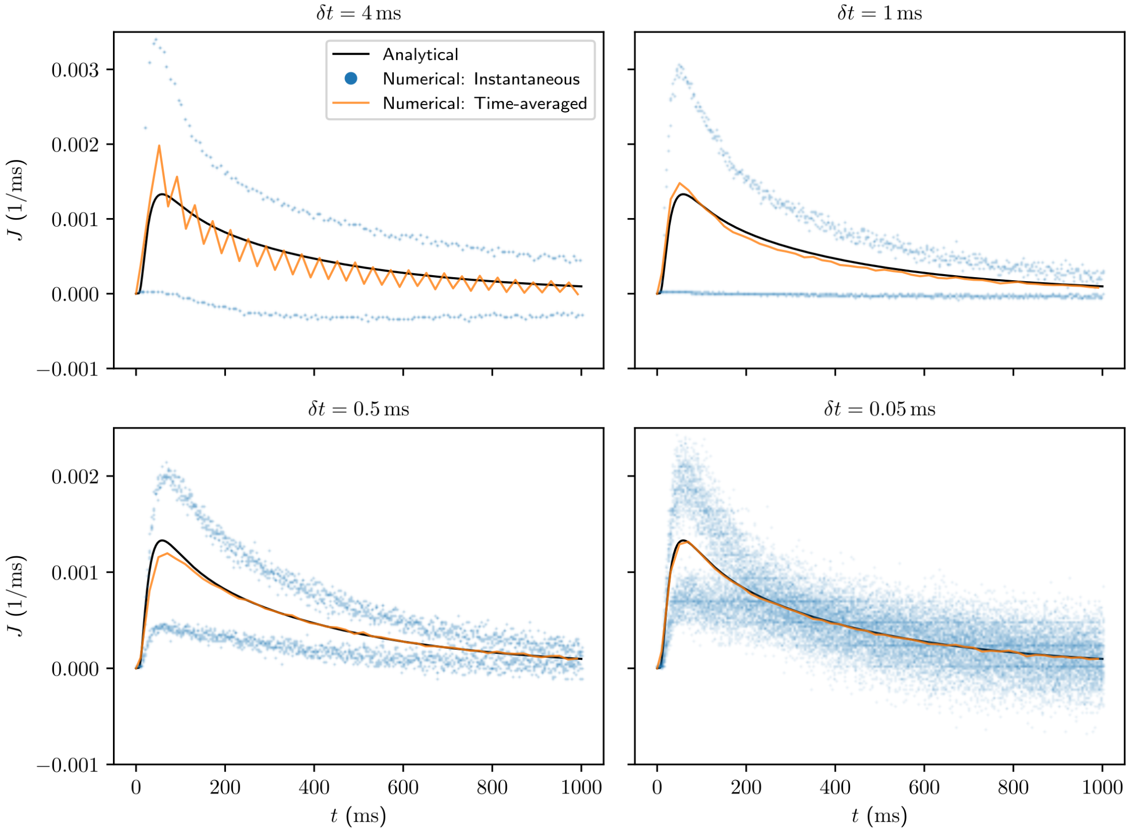

Figure 6.9: Instantaneous and time-averaged (plotted as the average of every interval with $\Delta t = 20\,\mathrm{ms}$) fluxes $J(t)$ through the membrane as a function of simulation time. Results are given for four different step sizes δt: 4, 1, 0.5, and 0.05 ms. Domain and simulation parameters: $D_L = 0.5\,\mathrm{\mu m^2/ms}$, $D_R = 2.5\,\mathrm{\mu m^2/ms}$, $\kappa = 0.05\,\mathrm{\mu m/ms}$, $L = 20\,\mathrm{\mu m}$, $x_0 = 10\,\mathrm{\mu m}$, $N_p = 10^6$.

fraction of walkers (normalised by $1/N_p$) crossing the barrier is counted every time step. This integral flux is divided by δt to obtain the instantaneous flux.

The influence of step size

The same domain as in section 6.3.1 is considered. All $N_p = 10^6$ walkers are seeded in the centre of the left compartment at $x_0 = 10\,\mathrm{\mu m}$. To prevent walker positions coinciding with the barrier location at $x_b = 20\,\mathrm{\mu m}$, the walkers are offset by $\epsilon = 10^{-10}$. As a result of integer step lengths for some δt, walker positions will otherwise have one of their steps land on the barrier resulting in $p_t = 0$ according to equation (5.21). Simulations are performed up to $t = 1000\,\mathrm{ms}$ using four different time steps δt: 4, 1, 0.5, and 0.05 ms. Figure 6.9 shows the instantaneous fluxes obtained from the random walk simulation at every time step alongside the analytical solution. For the random walk solution, a time-averaged flux is also plotted over fixed intervals of $\Delta t = 20\,\mathrm{ms}$ to allow for comparison between plots with different δt.

The (analytical) flux J rapidly increases early in the simulation and reaches a maximum

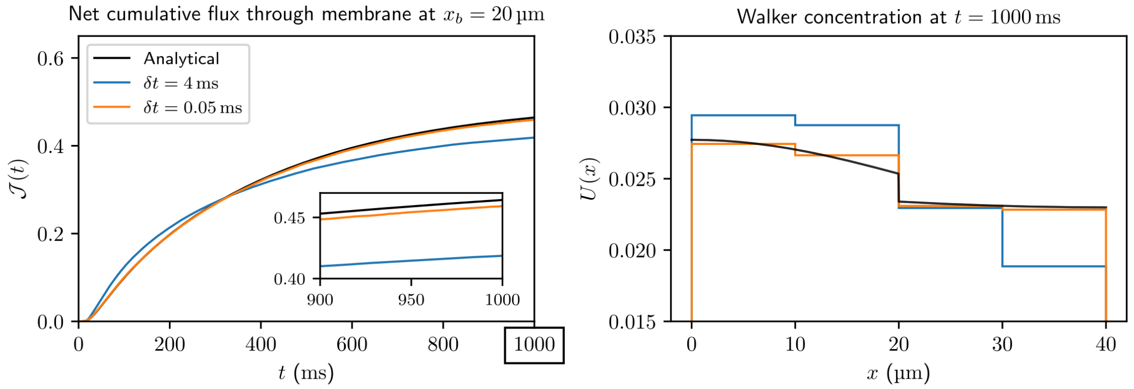

Figure 6.10: **(Left)** Net cumulative flux $\mathcal{J}(t) = \int_0^t J(\tau)\,\mathrm{d}\tau$, i.e. the net migration of concentration across the membrane at $x_b = 20\,\mu\text{m}$, plotted as a function of simulation time for both the analytical solution and numerical results using time steps 4 and 0.05 ms. Domain and simulation parameters: $D_L = 0.5\,\mu\text{m}^2/\text{ms}$, $D_R = 2.5\,\mu\text{m}^2/\text{ms}$, $\kappa = 0.05\,\mu\text{m}/\text{ms}$, $L = 20\,\mu\text{m}$, $x_0 = 10\,\mu\text{m}$, $N_p = 10^6$. **(Right)** Walker concentration at $t = 1000\,\text{ms}$ for the same simulations. The random walk results are shown as histograms.

at $t = 58.53\,\text{ms}$. As t increases, walkers continue to cross the membrane towards the initially empty compartment ($J > 0$ always). The numerical, time-averaged flux approximates the analytical solution well at the finest time step $\delta t = 0.05\,\text{ms}$. At $\delta t = 0.5\,\text{ms}$ the initial peak is underestimated but the tail of $J(t)$ is well represented. As the time step increases further, the time-averaged flux over-estimates the initial peak in magnitude and then underestimates the tail. At $t = 4\,\text{ms}$ oscillations can be observed. These may be attributed to poor sampling of the averaging window size $\Delta t = 20\,\text{ms}$. The instantaneous numerical flux J_{num}, i.e. the amount of concentration (walkers) crossing every time step, does not match the analytical solution. At $\delta t = 4\,\text{ms}$ the instantaneous values of J_{num} fluctuate around the analytical solution every time step, alternately over- and then underestimating the flux. As the time step is decreased, the amplitude of the fluctuation decreases. It may be possible to reduce this to near-zero with a *significantly* higher resolution, both through an increase in number of walkers and a decrease in time step.

In order to quantify the error between the numerical and analytical flux in figure 6.9, the cumulative flux $\mathcal{J}(t) = \int_0^t J(\tau)\,\mathrm{d}\tau$ is computed. Plotted in figure 6.10, this represents the net concentration that has crossed the membrane up until t and is required to approach 0.5 as $t \to \infty$ to match the steady-state solution in section 6.3.1. The two extreme δt values used in figure 6.9 are shown. The line for $\delta t = 0.05\,\text{ms}$ closely matches the analytical solution with only a small difference $\Delta\mathcal{J} = \mathcal{J}_{\text{num}} - \mathcal{J}_{\text{ana}}$ and a global error $\int |\,\Delta\mathcal{J}\,|\,\mathrm{d}t$ of 2.497 (0.8 % relative to $\int \mathcal{J}_{\text{ana}}\,\mathrm{d}t$). When increasing the time step to 4 ms, the cumulative flux of the random walk significantly deviates from the analytical solution. The flux is first overestimated (until $t = 321.57\,\text{ms}$) and then underestimated as $t \to \infty$, similar to what is observed in figure 6.9. The global error is 24.11 (7.56 %). At $t = 1000\,\text{ms}$ the difference between cumulative fluxes $\Delta\mathcal{J}$ suggests that insufficient concentration has crossed the

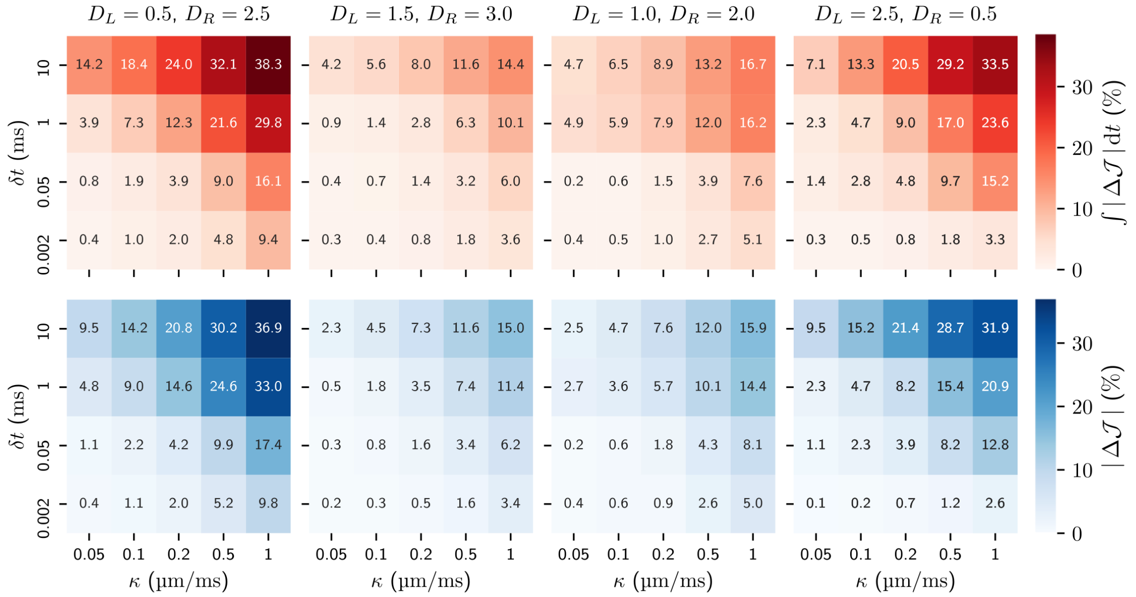

Figure 6.11: Errors in the random walk for different time steps δt and permeabilities κ in four different domains (the left-most domain is the model domain used in figures 6.8 and 6.9). Simulations were run until $t = 1000\,\mathrm{ms}$ with $N_p = 10^6$ walkers seeded at $x_0 = 10\,\mathrm{\mu m}$. **(Top)** The global error (relative to $\int \mathcal{J}_{\mathrm{ana}}\,\mathrm{d}t$) quantifies the degree to which the solution fluctuates around the analytical solution during the simulation. **(Bottom)** The cumulative error (relative to $\mathcal{J}_{\mathrm{ana}}$) represents the error in net flux at the end of the simulation.

membrane at the end the simulation. For $\delta t = 0.05\,\mathrm{ms}$ the error is $\Delta\mathcal{J} = -0.005$ ($-1.1\,\%$ with respect to $\mathcal{J}_{\mathrm{ana}}$), while for $\delta t = 4\,\mathrm{ms}$ it is -0.046 ($-9.82\,\%$). This is consistent with the observation in figure 6.8 where the transit model causes accumulation of walkers in compartments of lower diffusion coefficient. The histogram in figure 6.10 directly illustrates the distribution of concentration (analytical) and walkers (numerical) at $t = 1000\,\mathrm{ms}$. This supports the results shown in the cumulative flux plot in figure 6.10 and suggests the largest deficiency of walkers is at the far end of the right compartment.

The influence of diffusion coefficient and permeability

As shown in section 5.3.3, the membrane transit model from equation (5.21) has negligible error only for sufficiently small time steps. According to equation (5.45), the error depends on both the membrane permeability κ and the compartment diffusion coefficient D. In order to study the effects of these parameters numerically, four domains are used: the model domain used previously, as well as with the diffusion coefficients swapped such that $D_L > D_R$, and two additional domains with different magnitudes and intra-compartment ratios of diffusion coefficients. The domain parameters are indicated in figure 6.11. A range of permeabilities is considered: they increase from $0.05\,\mathrm{\mu m/ms}$ (cardiomyocytes) up to what may be expected in erythrocytes, where exchange times can be of the order of 50 to 100 Hz (Gianolio et al., 2016). Simulations are performed up to $t = 1000\,\mathrm{ms}$ for five different time steps δt: 10, 1, 0.5, 0.05, and 0.002 ms. Figure 6.11 reports the same error metrics considered in equation (5.45) in the form of heatmaps.

Both global and cumulative error have similar magnitude. The flux analysis in section 5.3.3 shows via equation (5.45) that for $D_L \neq D_R$ the transit model requires a time step that scales with $\delta t \sim \kappa^{-2}$. For a fixed δt an increase in error is observed as the permeability increases. At low δt this increase is almost linear with κ. This may be explained by the terms in equation (5.45). For a fixed κ there is a substantial increase in the error with increasing δt that appears most drastic between $\delta t = 0.05\,\text{ms}$ and $\delta t = 1\,\text{ms}$ but also depends on the domain. In general, small relative errors ($\leq 1\,\%$) are found for low permeabilities ($\kappa \leq 0.1\,\mu\text{m/ms}$) and small step sizes ($\delta t \leq 0.002\,\text{ms}$). This time step corresponds to $\max(p_t) \approx 0.01$ as suggested by Fieremans et al. (2010) for $\kappa = 0.05\,\mu\text{m/ms}$ only. As a result, higher values of κ do not satisfy the condition. Note that the required time step for $\kappa = 1\,\mu\text{m/ms}$ would be 6×10^{-6} ms.

6.3.3 Application to DWI and a histology-based domain

Now that the necessary parameter choices for the permeable membrane transit model have been established via 1D simulations, the model can be applied to more interesting higher-dimensional problems. As a precursor to full 3D simulations of DT-CMR in realistic domains (section 6.4), the findings above are now translated to a histology-based domain. A 1D domain is constructed where the 2D morphology is collapsed into an equivalent 1D geometry with a similar distribution of compartments. Additionally, through the narrow pulse approximation (NPA) the analytical solution can be applied to model a DWI signal.

Synthesised domain

The domain is based on a histology-image from swine myocardium (section 2.3.4). An example is shown in figure 6.12 (Top Left). Through the automatic segmentation method described in section 2.4 the distribution of cardiomyocyte sizes shown in figure 6.12 (Top Right) is obtained. From the data, a mean cell cross-sectional area of $\mu = 120\,\mu\text{m}^2$ and a standard deviation of $\sigma = 40\,\mu\text{m}^2$ are estimated. To create a synthesised histology-based domain, normally-distributed values in the range $\mu \pm 2\sigma$ are drawn. Assuming a circular cross-section for cardiomyocytes (Tracy et al., 2011), the cell areas are converted to diameters which are use as intra-cellular compartment length in the 1D domain. The extra-cellular space is drawn from a uniform distribution in the interval $[2, 4]$. This results in an extra-cellular volume fraction (ECV) of 20 %. The resulting domain can be seen in figure 6.12 (Bottom). Diffusion coefficients are set to $D_{\text{ICS}} = 0.5\,\mu\text{m}^2/\text{ms}$ and $D_{\text{ECS}} = 2.0\,\mu\text{m}^2/\text{ms}$. A permeability of $\kappa = 0.05\,\mu\text{m/ms}$ is used for all cell membranes.

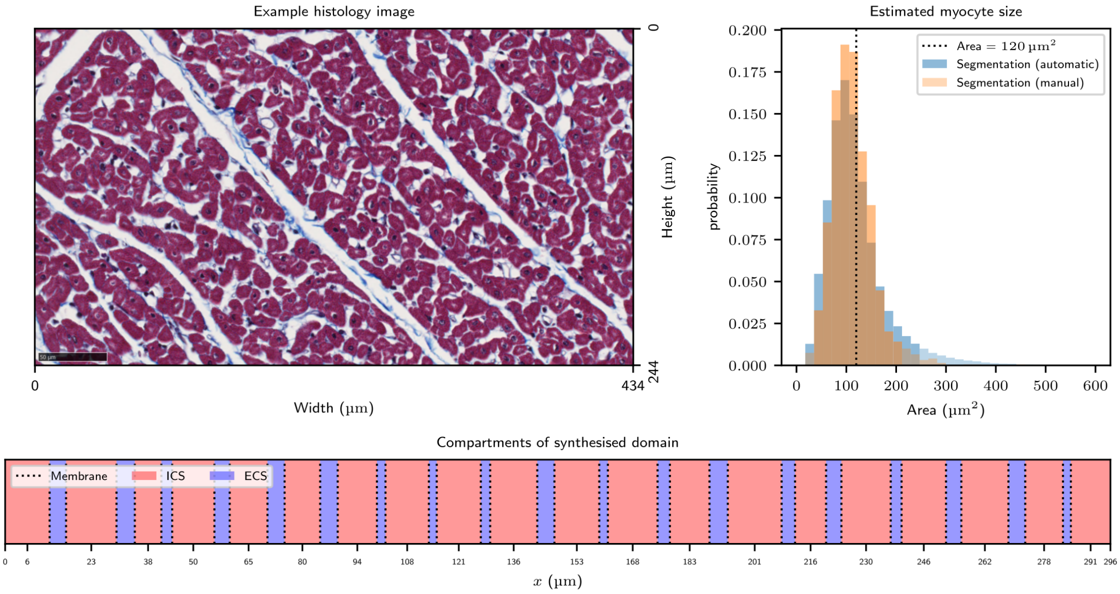

Figure 6.12: Illustration of the process of synthesising a 1D domain from histology data. **(Top Left)** An example of a region of histology from a wide-field microscopy image. This is part of a large vertical stack of histological slices obtained from the mesocardium of swine. Cardiomyocytes (red-purple) are cut perpendicular to the imaging plane. Extra-cellular space is white, while collagen is stained blue. **(Top Right)** Distribution of cell sizes from automatic segmentation for the entire stack of images as well as manual labelling of a small representative region. **(Bottom)** Intra-cellular compartment lengths are based on (circular) cell areas drawn from a distribution matching the histogram. The extra-cellular gaps are drawn from a uniform distribution and result in an extra-cellular volume fraction of 20 %.

Transient and steady-state solutions in the histology-based domain

Simulations use $N_p = 10^7$ walkers and a time step of $\delta t = 0.5\,\mathrm{ms}$. This intentionally exceeds the small time step required for accurate handling of transit using the model in equation (5.21), while still limiting walkers to a single barrier interaction per step (since $\min(L_{\mathrm{ECS}}) \geq 2\,\mathrm{\mu m}$ and $D_{\mathrm{ECS}} = 0.5\,\mathrm{\mu m^2/ms}$). The random walk is run for $t = 1000\,\mathrm{ms}$ and the analytical solution is evaluated for the same space and time parameters. The algorithm described in chapter 4 is used to obtain 2645 eigenvalues with $\lambda^\star \in [0, 500]$. From this, the analytical solution is calculated. The transient solution $U(x, t; x_0)$ of the random walk is obtained for x_0 located at the centre of the domain, while the steady-state solution is initialised by seeding the walkers uniformly in the domain. Results are plotted in figure 6.13. Overall a good agreement can be observed between the random walk solution and analytical solutions, despite the relatively large time step. In the steady-state there is an accumulation of walkers in ICS, which has a lower value for D than the ECS. This is consistent with findings in section 6.3.1.

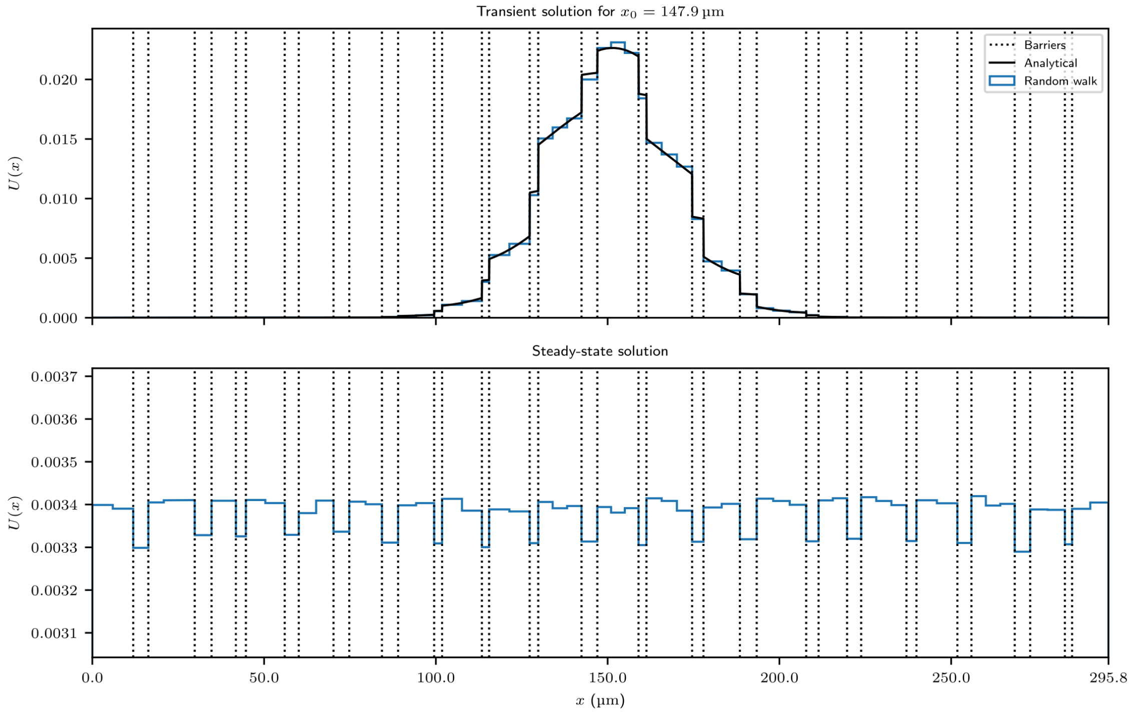

Figure 6.13: Analytical and random walk solutions (using $N_p = 10^7$ walkers and a time step of $\delta t = 0.5\,\mathrm{ms}$) at $t = 1000\,\mathrm{ms}$. **(Top)** Transient solution $U(x, t; x_0)$ for initial concentration at x_0 located in the centre of the domain (figure 6.12), showing good agreement between the two methods. **(Bottom)** Steady-state solution after uniform seeding of walkers in the domain. The random walk method results in accumulation of walkers in compartments with lower diffusion coefficient. Note that this effect is visually amplified by the choice of axis data range.

Narrow pulse approximation

Recall from section 5.2.2 that walkers acquire phase ϕ during DWI experiments. At readout/time of echo, the resulting signal S is the Fourier transform of the medium average diffusion propagator and is thus related to the distances that the spins have diffused during diffusion time Δ.

The methods presented in chapters 4 and 5 allow solving for the diffusion propagator $U(x, t; x_0)$. By means of the narrow pulse approximation (NPA) (P. T. Callaghan, 2010; Grebenkov et al., 2014) it is possible to estimate the DWI signal directly. This assumes that the gradients are applied instantaneously, i.e. $\delta \to 0$ as the wave number $q(t) = \gamma \int_0^t G(\tau)\,\mathrm{d}\tau$ remains finite ($= \gamma G \delta$).

Solutions are obtained for diffusion times Δ in the range 100 to 1000 ms and the walker positions $x_p(t)$ are stored for each of the time points $t = \Delta$ as well as at $t = 0$. Due to the NPA the effect of b-values can be evaluated, calculated as $b = q^2(\Delta - \delta/3)$, in the range 0.1

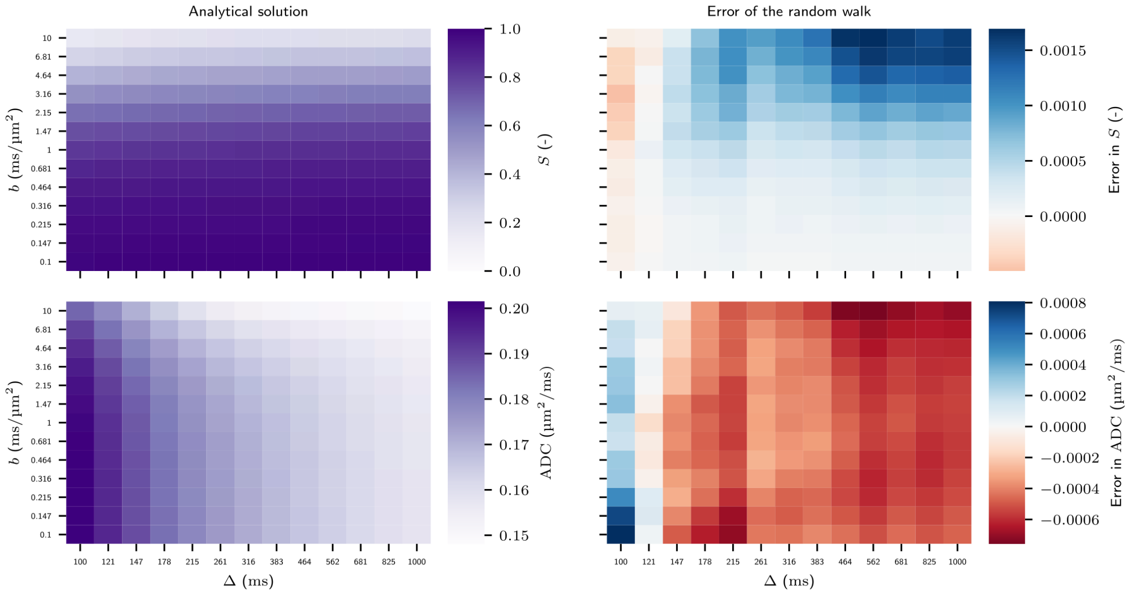

Figure 6.14: Diffusion signal S (Top) and apparent diffusion coefficient ADC (Bottom) computed based on a narrow pulse approximation with different b-values and diffusion times Δ. Plotted are the analytical solution **(Left)** and the error of the random walk solution with respect to the analytical **(Right)**. Simulations were performed in the domain from figure 6.12 with $\delta t = 0.5\,\mathrm{ms}$ and $N_p = 10^7$.

to $10\,\mathrm{ms/\mu m^2}$ without additional simulations. The signal magnitude S is computed as

$$S_{\mathrm{rw}}(\Delta, q) = \frac{1}{N_p}\left|\sum_{p}^{N_p} e^{-\mathrm{i}\,q\,(x_p(\Delta)-x_p(0))}\right|. \tag{6.3}$$

Here, i denotes the imaginary unit $\sqrt{-1}$. The analytical diffusion signal is calculated using an expression derived for uniform initial seeding (Moutal et al., 2019, SM. I.2):

$$S_{\mathrm{ana}}(\Delta, q) = \frac{1}{\sum_k L_k}\sum_n e^{-\lambda_n \Delta}\left|\int_\Omega \nu_n(x) e^{\mathrm{i}qx}\,\mathrm{d}x\right|^2. \tag{6.4}$$

The integral is approximated numerically using trapezoidal integration over the finely-discretised domain. Finally, the apparent diffusion coefficient (ADC) is derived from the signal attenuation through $\mathrm{ADC} = -\ln(S/S_0)/b$, assuming $S_0 = 1$.

Figure 6.14 shows the signal and ADC for the analytical solution for all combinations of b and Δ. As expected, S reduces (and ADC increases) with higher b-value and diffusion time. For S the effect of Δ is much smaller than that of b. The effect of increasing b is stronger for low diffusion times. The accuracy of the random walk solution is evaluated via the error/difference with respect to the analytical solution. Overall the error in ADC between the two solutions does not exceed $\pm 0.08\,\mathrm{\mu m^2/ms}$ and shows no distinct pattern with Δ or b. The relative error is largest for high b-values and high Δ, where ADC is lower. For the short diffusion time $\Delta = 100\,\mathrm{ms}$ the error is positive. As Δ increases and the accumulation of walkers in the "slower" intra-cellular compartments increases, the ADC becomes underestimated for all $\Delta > 121\,\mathrm{ms}$. While the error in signal S increases with both b and Δ, ADC shows an almost constant error at sufficiently large Δ.

Recall the mean squared displacement (MSD) from equation (5.3). It is interesting to consider q going to zero, as this corresponds to the case where S_{rw} approaches the bulk diffusion coefficient

$$\mathcal{D}(t) = \frac{1}{2t} \left\langle \delta x^2 \right\rangle \tag{6.5}$$

with MSD

$$\left\langle \delta x^2 \right\rangle = \int_{\Omega} \delta x^2 U(x,t) \,\mathrm{d}x\,. \tag{6.6}$$

Considering $b = 0.1\,\mathrm{ms/µm^2}$, the baseline error in ADC can be verified due to the errors in the random walk.

6.3.4 Discussion

The purpose of this section was to investigate the suitability of applying the transit model in equation (5.21) to simulations of DWI/DT-CMR in histology-like 1D domains. First, a model domain composed of two compartments separated by a barrier is used to study the intrinsic bias of the transit model. Accumulation of walkers in the compartment with lower diffusion coefficient is reported in the steady-state case, consistent with section 5.3.3. The transient evolution of membrane flux was then studied and the errors quantified.

Finally, a 1D domain is constructed based on histological data (figure 6.12). Using the narrow-pulse approximation, the DWI signal and resulting ADC are computed from the analytical and random walk solutions. The model error is acceptable if a moderate time step is used. The transit model is thus deemed suitable for DT-CMR simulations.

6.4 Effect of permeability on DT-CMR parameters

Simulations of impermeable cardiomyocyte membranes in section 6.2 resulted in an overestimation of the fractional anisotropy (FA) and underestimation of mean diffusivity (MD) compared to literature values for in-vivo DT-CMR. This was most noticeable for long diffusion times Δ in the STEAM sequence. While MD strongly correlates to the intrinsic diffusion coefficients and ECV used in the simulations and may thus be calibrated by careful choice of model parameter, FA is less sensitive to such changes. It was hypothesised that the lack of exchange in the model may be the reason for high FA reported in previous simulations.

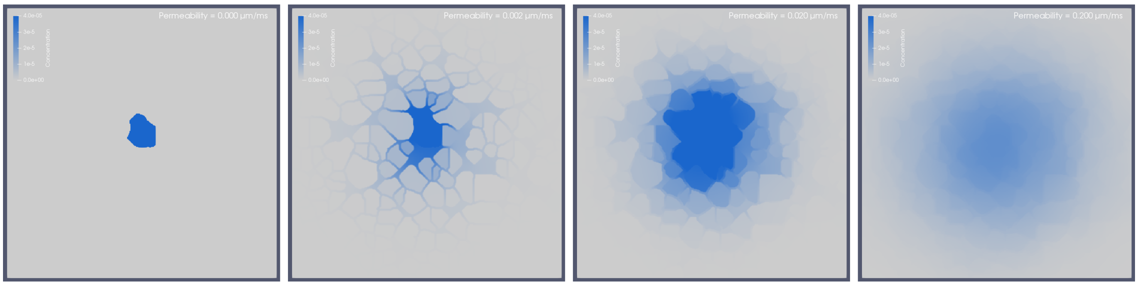

Figure 6.15: Simulation of the spread of concentration in a 2D histology-based domain using a finite difference method (FDM). A diffusion time of $\Delta = 1000\,\mathrm{ms}$ was used to model diffusion during a STEAM sequence. Membrane permeabilities κ were set to 0, 0.002, 0.02, and $0.2\,\mathrm{\mu m/ms}$ (from left to right), while the diffusion coefficients in ECS and ICS were 3 and $1\,\mathrm{\mu m^2/ms}$.

6.4.1 The need for permeability

Initially, the impact of membrane permeability on the diffusion propagator and DT-CMR results is assessed. The approach taken is based on previous work (Rose et al., 2019d) using the GPU-based Bloch–Torrey simulator described in section 3.3 and appendix B.2.4. The two-dimensional domain from figure 3.9 is used as input for simulations with the finite difference method (FDM). Extra- and intra-cellular diffusion coefficients D_{ECS} and D_{ICS} were set to 3 and $1\,\mathrm{\mu m^2/ms}$. The FDM treatment of membranes in equation (3.22) requires the outer-most pixels of any ICS region to take on a value for the diffusion coefficient of $D_m = \kappa \Delta x$, where the resolution is $\Delta x = 0.5\,\mathrm{\mu m}$. A STEAM sequence with parameters from table 6.1 is simulated, as this sequence type with the long diffusion time of $\Delta = 1000\,\mathrm{ms}$ is expected to be affected the most by permeability.

For initial, quantitative assessment of the impact of permeability the spread of concentration after an initial spike at $\boldsymbol{x}_0$ is simulated. A point inside a cardiomyocyte is chosen and the domain is limited to a length of $3\sqrt{2D_{\mathrm{ECS}}\Delta}$ in each direction to reduce the computational effort. The permeability is decreased from $0.2\,\mathrm{\mu m/ms}$ by one order of magnitude at a time until $\kappa = 0.002\,\mathrm{\mu m/ms}$. The impermeable case ($\kappa = 0$) is also simulated to demonstrate watertightness of the membrane boundary condition. The distribution of concentration $U(\boldsymbol{x}, \Delta)$ is shown in figure 6.15. It depicts the effect that permeability has on the diffusion of spins. At low κ significant anisotropy can be observed by imagining isocontours of constant concentration. The slow exchange between compartments together with a higher diffusion coefficient in the extra-cellular space causes the concentration to spread much farther in ECS than even in neighbouring cardiomyocytes. As κ increases, the distribution of concentration becomes more isotropic and the distinction between cell membranes becomes less observable leading to a coarse-graining of the microstructure (Novikov et al., 2019).

To quantify these observations, DT-CMR simulations of the magnetisation vector $\boldsymbol{M}$ are carried out as explained in section 3.3. Three different gradient directions are simulated

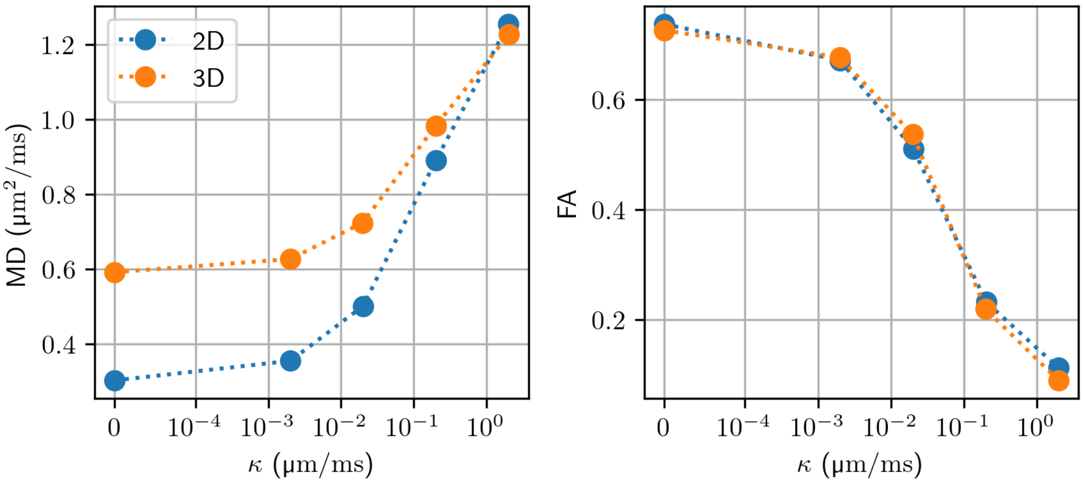

Figure 6.16: Change in DT-CMR parameters (FA and MD) as a function of membrane permeability. The plot uses a symmetric logarithmic scale (linear in the range 0 to 10^{-4}) to display the $\kappa = 0$ value. 2D values correspond directly to the simulation result, whereas the 3D values are based on an estimated primary eigenvalue $\lambda_1 = 1.2\,\mu\text{m}^2/\text{ms}$ (normal to the image).

and a 2×2 diffusion tensor is constructed that represents the apparent diffusion inside the domain. Five different permeabilities (2×10^{-3}, 2×10^{-2}, 2×10^{-1}, and $2\,\mu\text{m/ms}$ as well as the impermeable case) are applied. The resulting MD and FA are plotted in figure 6.16. The formula for FA_{2D} is the same as for FA_{3D} given in equation (3.9) with the exception of a different scaling factor, which becomes 2 instead of $\frac{3}{2}$.

FA strongly dependent on the permeability κ. It decreases from approximately 0.75 at $\kappa = 2 \times 10^{-3}\,\mu\text{m/ms}$ to almost 0.1 at $\kappa = 2\,\mu\text{m/ms}$. Similarly, MD increases from $0.35\,\mu\text{m}^2/\text{ms}$ to $1.2\,\mu\text{m}^2/\text{ms}$ over the same range. This is in line with qualitative observations from figure 6.15. The impermeable case only has a slightly higher/lower FA/MD than the case of $\kappa = 2 \times 10^{-3}\,\mu\text{m/ms}$.

Figure 6.16 also shows an estimation of MD and FA in 3D simulations. This FDM simulation is based on the fact that the 2D slice of histology was cut and imaged perpendicular to the cardiomyocyte longitudinal axis. It is well documented that the primary eigenvector $\boldsymbol{e}_1$ is aligned parallel to this axis. By definition of the diffusion tensor and its eigendecomposition, the second and third eigenvectors lie in the plane that these simulations are carried out in. Here, the assumption is made that diffusion along the first eigenvector is unrestricted. This serves as a good first approximation based on the findings in figure 6.5, where only a small reduction in λ_1 due to the cardiomyocyte end caps was observed. Consequently, $\lambda_{1,\text{3D}} = \langle D_0 \rangle$ where $\langle D_0 \rangle$ is the volume-averaged diffusion coefficient. Furthermore, $\lambda_{i+1,\text{3D}} = \lambda_{i,\text{2D}}$ for the remaining two eigenvalues. For each simulated 2D tensor, an equivalent 3D tensor is thus extrapolated and plotted in figure 6.16. The MD of the 3D tensor is higher as expected by virtue of eigenvalue ordering. The FA for both 2D and 3D tensors almost exactly matches. At present time, no explanation for this exists and it is likely due to a fortuitous combination of 2D tensor and $\langle D_0 \rangle$.

Overall, FDM simulations of DT-CMR in a realistic, histology-based domain have successfully reduced the FA of the observed diffusion tensor. For a physiological range of membrane permeabilities in the order of 10^{-2} to 10^{-3} µm/ms, the apparent diffusion over long times $\Delta = 1000\,\mathrm{ms}$ is significantly dependent on permeability. The resulting FA and MD values have changed in the direction towards what would be expected from in-vivo and ex-vivo studies (Deuster et al., 2016b; Kim et al., 2005; McGill et al., 2015a,b; Moulin et al., 2020a; Scott et al., 2018b; Stoeck et al., 2018).

6.4.2 Extending previous simulations by adding permeable membranes

The need for permeability was demonstrated above using a finite difference method. To build upon the MCRW simulations in section 6.2 and allow walkers to exchange between compartments, a transit model is required. The model by Fieremans et al. (2010) was previously studied numerically in section 6.3 and its limitations determined. Here, some of the work from section 6.2 is repeated for the same set of simulation inputs but with the addition of a realistic membrane permeability as opposed to impermeable barriers. The results of this come from recently published work (Rose et al., 2021a).

The simulation substrate from section 6.2 with ECV = 25 % is used. This is a realistic ECV and is located near the centre of the range of ECV values considered in section 6.2. Diffusion coefficients D_{ICS} and D_{ECS} are set to 1.5 and 3.0 µm^2/ms, which matches what was used in section 6.4.1.

The membrane permeability κ is varied from 0 µm/ms (impermeable, to compare with section 6.2) to 0.05 µm/ms (fast exchange, erythrocytes). Realistic values for myocardial tissue are most likely in the range 0.01 to 0.02 µm/ms (section 2.3.2). The PGSE and STEAM sequences from table 6.1 are simulated in a $2.8 \times 2.8 \times 8.0\,\mathrm{mm}^3$ voxel with $N_p = 10^4$ walkers. The transit probability p_t, calculated by equation (5.21), is required to be less than 0.01 which is enforced depending on κ. This greatly increases the number of time steps, but the number of walkers N_p cannot be reduced to compensate for this. As a result longer simulation runtimes are encountered, especially for the STEAM sequence.

The results are plotted in figure 6.17. Two clear trends are visible: FA decreases and MD increases with increasing κ for both sequences. For FA this appears to happen linearly, with a steeper slope for the STEAM sequence than PGSE. The longer diffusion time is thus more sensitive to permeability, as could be expected. The increase of MD with an increase in κ is again almost linear for PGSE, but the slope for STEAM appears to reduce with larger κ values.

Until this point, simulations were limited to realistic in-vivo DT-CMR sequences. Due to the nature of the beating heart, the diffusion time is therefore either kept as short as

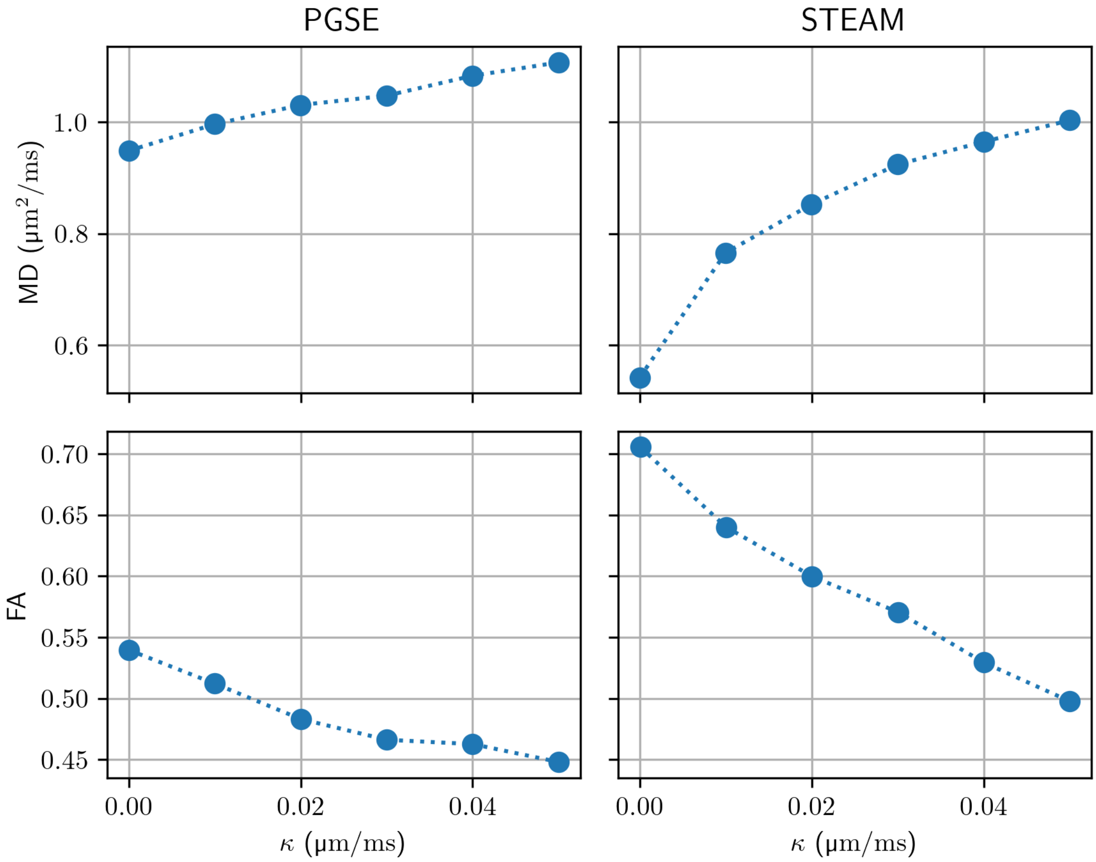

Figure 6.17: Effect of membrane permeability on DT-CMR parameters for a short (PGSE) and long (STEAM) pulse sequence. Plotted are median values obtained from 10 repetitions.

possible (PGSE and M2-SE) or synchronised to the ≈1 s long cardiac period (STEAM). This results in two distinct diffusion regimes that can be investigated with DT-CMR. To bridge the gap between these two extremes, simulations of varying Δ are performed. Using the sequence generation tool in section 3.2.3, STEAM sequence profiles are generated in the range of 100 to 2000 ms. Compare to this $\Delta = 20$ ms for PGSE. The resulting data may be compared to ex-vivo DT-CMR data, where no limitation on the diffusion time exists.

Figure 6.18 shows FA and MD as a function of Δ. For both values of permeability κ, 0 and 0.05 μm/ms, a similar behaviour of FA is observed. Until $\Delta = 300$ ms FA increases with Δ, but then approximately plateaus. The permeable simulations report a lower FA than the impermeable case, consistent with figure 6.17. The mean diffusivity continuously decreases with an increase in Δ for the impermeable case. This is an expected result for longer diffusion times in restricted and hindered environments. The difference between MD for permeable and impermeable simulations, however, is interesting. After $\Delta = 200$ ms, MD for $\kappa = 0.05$ μm/ms remains constant. A similar plateau in apparent diffusion coefficients

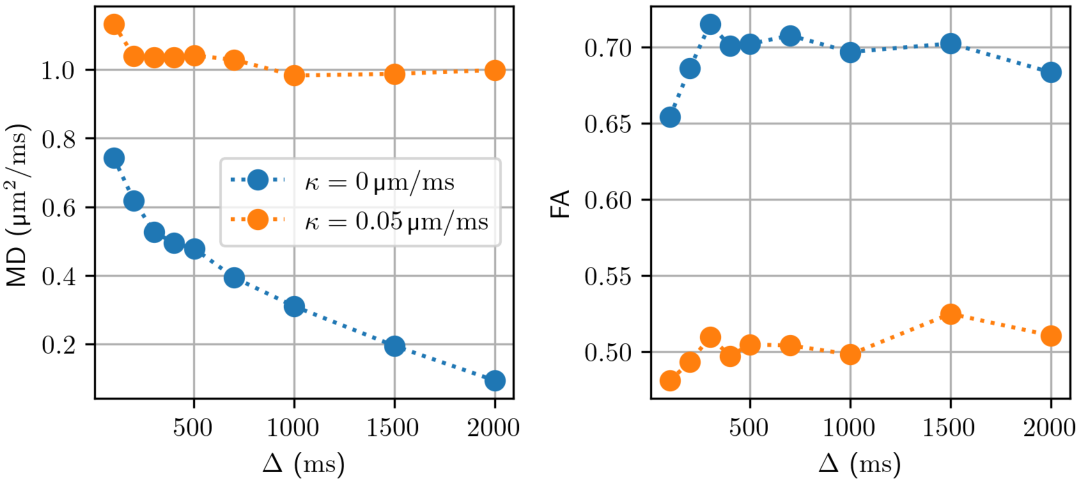

Figure 6.18: Effect of diffusion time on DT-CMR parameters for both impermeable and permeable membranes. All simulations were computed using a STEAM sequence with varying Δ.

with Δ increasing beyond 300 ms was reported by Kim et al. (2005).

6.4.3 Discussion

The inclusion of membrane permeability in the model of the myocardium has lead to a reduction in FA to levels closer to what is expected from DT-CMR acquisitions in vivo and ex vivo studies. Future simulation work will require the inclusion of membrane permeability in in-silico models of DT-CMR. Limitations of this work are that only the PGSE and STEAM sequences and not the M2-SE sequence were considered, and that the value of κ remains an unknown input parameter.

Chapter 7

Conclusions

Contents

7.1 Key findings

There is a need for accurate simulations of DT-CMR in realistic models of myocardial tissue to enable investigation of the effects that microstructural changes due to disease have on the DT-CMR results. In this project, a computational modelling framework for DT-CMR was developed that enables such simulations to be carried out effectively and reliably. The major findings, related to the research objectives (**RO**s) defined in section 1.2, are summarised below. Afterwards, the central hypothesis is revisited.

RO1: Realistic model of myocardial tissue

High-fidelity 3D numerical phantoms are necessary for DT-CMR simulations in order to accurately capture the microstructural features found in the myocardium.

The workflow proposed in this project considers large domains of realistic DT-CMR voxel size. Both transmural rotation of cardiomyocytes is considered as well as the sheetlet structure, which is of strong clinical interest (Nielles-Vallespin et al., 2017). Simulations in section 6.2 have shown that such realistic geometrical models are required to accurately capture DT-CMR parameters. In particular, measures relating to the second eigenvector of the diffusion tensor, like E2A or the eigenvector uncertainty, were shown. Using idealised cardiomyocyte shapes in regular arrangement as often found in literature result in DT-CMR measures that lack the prominent secondary eigenvector.

In order to assist with the generation of such complex substrate geometries, two sets of tools were developed: Image processing and deep learning–based methods for automatic segmentation of histology images, and a cell packing algorithm that can synthesise a substrate to match target statistics. Both sets of tools will be vital in future studies to increase the accuracy of the simulated microstructure over large voxel sizes.

RO2: Efficient and accurate numerical techniques

In order to efficiently simulate diffusion in large complex domains, Monte Carlo random walk (MCRW) simulations are preferred. A parallelised simulator was developed in this work that can operate on both voxelised and surface mesh–based domains.

While MCRW methods are superior to continuum solutions in terms of performance, a set of continuum solution–based techniques were also developed in this work. These methods directly solve the governing equations without need for statistical models and can thus be used to verify and assess accuracy of MCRW solutions. A GPU-based implementation of the finite difference and finite volume method provides a fast means to obtain such reference solutions. For example, 2D problems can be solved within minutes.

Additionally, an analytical solution in 1D was developed to better understand the effect that membrane permeability has on the diffusion process. It was also used to study the accuracy of transit models typically used in MCRW by comparing the membrane fluxes measured with the MCRW and ground truth analytical solutions. Using this approach, the critical maximum time step limit for the transit models was determined and the suitability for DT-CMR simulations was confirmed.

RO3: Sensitivity of pulse sequences to tissue parameters

To gain insights into the specific sensitivity of DT-CMR pulse sequences to pathological changes in the cardiac microstructure, parameter studies were performed. Both spin echo (PGSE, M2-SE) and stimulated echo (STEAM) sequences were simulated.

Initial simulations of impermeable membranes in a realistic microstructure demonstrated that spin echo sequences are more sensitive to changes in underlying compartment-specific diffusion coefficients than STEAM. The STEAM sequence on the other hands shows a stronger dependence on ECV.

Subsequent simulations addressed the effect of membrane permeability. The inclusion of transmembrane exchange via a transit model leads to walkers diffusing further, thus increasing MD and reducing FA. This effect is stronger for the long diffusion times associated with the STEAM sequence.

These findings have important clinical relevance: In future, modelling pathological changes like hypertrophy (increases in ECV, cardiomyocyte diameter, or cardiomyocyte length), disarray (disruption of normal cardiomyocyte orientation), and changes to diffusion and permeability coefficients, will allow the appropriate sequence to be selected or designed to provide maximum sensitivity to the desired changes based on findings from in-silico simulation studies.

Hypothesis

The central hypothesis (page 25) stated that *using a realistic virtual model as input for MCRW simulations allows for more realistic in-silico estimates of the DT-CMR measures typically found in vivo*. Simulations in section 6.2 confirmed that the use of histology-derived features like the organisation of cardiomyocytes into sheetlets is necessary to obtain realistic estimates of FA and a distinct second eigenvector. The addition of membrane permeability to these simulations brought the DT-CMR measures closer to what is typically observed in vivo.

Novelty

The validated simulations of DT-CMR presented in this work are unique in using a histology-based microstructure with permeable membranes, differences in diffusion coefficient between compartments, whilst allowing large voxel sizes and long diffusion times. A number of previous studies have included one or a subset of these features, but this is the first work to address all of these challenges, providing a framework suitable for simulation of DT-CMR data in the myocardium acquired with typical sequences used in in-vivo imaging.

7.2 Limitations and suggested future work

Geometric fidelity and scale

The histology-based substrate was constructed from a single ROI, a $400 \times 500\,\mu\text{m}^2$ block of tissue, which was replicated to fill a typical imaging voxel volume. Even though the ROI was taken from a representative region of the mid-myocardium, this is significantly smaller than the $3 \times 3 \times 8\,\text{mm}^3$ voxel size of DT-CMR. In the future, the techniques in sections 2.4 and 2.5 for automatically segmenting or synthesising substrate geometries should be explored further and applied to filling an entire voxel. Rule-based methods for cardiomyocyte fibre orientation (Doste et al., 2019) may be of assistance when attempting to expand the work beyond the mid-myocardium of the left ventricle.

Additionally, comparison with in-vivo or ex-vivo DT-CMR measurements such as from the recently performed Langendorff experiment by Scott et al. (2019) will require modelling of multiple voxels throughout the myocardium.

Bloch–Torrey equations and tissue properties

The Bloch–Torrey equations (3.2) were simplified to exclude relaxation effects and, instead, magnetisation was only considered in the transverse plane. In reality T1, T2, and T2* decay cause signal loss and this influences pulse sequence design. If included, the T_1 and T_2 relaxation time constants would need to be different for the two compartments ICS and ECS (Bruvold et al., 2007). This will lead to differently-weighted signal contributions from these compartments.

Regarding the diffusion term of the Bloch–Torrey equations, a scalar diffusion coefficient was used instead of a tensor. Studies of the internal micro- or nanostructure of cardiomyocytes in figure 2.4 revealed that cell features are primarily aligned with the longitudinal axis of the cardiomyocytes. As such, the assumption of isotropic free diffusion may need to be reconsidered. This has implications both for the continuum solutions whose numerical schemes would need to be reformulated, and for the random walk where a biased stepping protocol needs to be implemented. Note that this change in diffusion behaviour will most likely *increase* the FA in both spin echo and stimulated echo sequences.

Permeation and Perfusion

The transit model was shown to contain a fundamental bias that results in errors at moderate time steps in the case of a difference in diffusion coefficient across the membrane. The solution to this is a sufficiently small time step, which is computationally expensive and can become the prohibiting factor for large-scale simulations. To address this, it is recommended to investigate the membrane models proposed in section 5.3.4. Eliminating the time step restriction through a self-consistent model will be invaluable to accelerating Monte Carlo random walk simulations. The analytical methods developed in chapter 4 can be used for verification similar to how they were applied in section 5.3.

Furthermore, studies of permeability were done using a value of κ estimated based on τ_{ex} and equation (2.4). A logical next step is to carry out simulations where the mean residence time τ is measured in silico to allow comparison and validation with apparent exchange rates (AXR) measured in vivo (Coelho-Filho et al., 2013).

Only diffusive processes were modelled in this work, where transport of magnetisation is solely accomplished through the diffusion of water molecules. This includes modelling of exchange through membranes via diffusional permeability. In real biological tissue, however, other exchange processes like osmotic permeability need to be considered. In order to include this in a future model, these processes would need to be reviewed first. One way of implementing this in the random walk simulations is through asymmetric boundaries, where the probabilities of transit are asymmetric to account for a net flux in concentration as a result of osmotic pressure. The analytical framework developed in this work will be a crucial part in understanding and verifying such models. Methods like skew Brownian motion (SBM) may also be suited for this (Lejay, 2018, 2012).

Another limitation is that perfusion was not considered. There is a significant amount of (micro)vasculature in the extra-cellular space (Lapierre-Landry et al., 2020; Seidel et al., 2016). Perfusion is of interest to DT-CMR (Callot et al., 2003; Spinner et al., 2019). To build a perfusion model, a capillary network is needed. A multi-scale approach may be required (J. Lee et al., 2015). This could be constructed using recent work by R. Callaghan et al. (2020). Other approaches are capillary trees/networks (Palombo et al., 2019).

Other sources of motion

The motion of spins in the tissue was limited to diffusion in a static environment. However, the main challenge in DT-CMR is due to the beating of the heart muscle during the experiment. While imaging techniques like M2-SE and STEAM are designed to compensate for this, residual motion exists that can affect the signal (Stoeck et al., 2020). Modelling of bulk motion of the heart is straightforward from a walker perspective as it only requires an additional velocity term to be added at any given time step. What is more complicated is to develop a model for the motion of the cellular environment itself. Bulk motion of the heart during the cardiac cycle has been studied extensively and computational models for this exist (Young et al., 1994). However, this does not translate directly to the changes in cardiomyocyte shape. Additionally, strain-induced effects need to be considered as well, which will primarily affect intra-cellular water (Reese et al., 1995).

Computational considerations

Simulation methods are limited by their computational demand. Monte Carlo random walks require large numbers of walkers and, for permeable membranes, a small time step (section 6.3). The existing simulator code base does support parallelisation as stated in section 5.4.4, but performance is limited due to the use of MATLAB and lack of support for *distributed* computing on HPC systems.

Continuum methods do not scale well to 3D even for optimised algorithms on GPU hardware. One possible approach is to use an implicit time scheme, whose suitability would need to be investigated based on the provided accuracy. One promising use for FDM/FVM, besides verification of MCRW, is to generate a large number of local PDFs. An advantage is that these methods do not require an accurate geometry like MCRW does. By processing a large number of small sections of histology images, automatically segmented via the methods in section 2.4, a large library of high-quality training data may be built. This can be used for deep learning to directly analyse histology images and obtain the PDF or even integral quantities like ADC.

Verification and Validation

Verification of membrane exchange with analytical methods could only be performed in 1D due to the inherent limitation of the spectral analysis performed in chapter 4. While extension of random walk methods is trivial to higher dimensions, the resulting change in topology has implications for the error. For example, extra-cellular space is no longer confined to the gap between two intra-cellular spaces but extends much farther. Additionally, the ratio of membrane surface area to compartment volume and the anisotropy of the geometry in 3D are both not accurately represented in 1D. To address this limitation, higher-dimensional analytical solutions should be sought. For example, a 2D solution exists in radial coordinates (Singh et al., 2008). Highly resolved continuum solutions may also be used.

The parameter studies in chapter 6 are only qualitatively compared to in-vivo results. A future study should attempt to replicate specific data points through variation of model parameters. The most important of these were identified in this work. A recent experiment with a Langendorff-perfused porcine heart (Scott et al., 2019) obtained in-vivo and ex-vivo DT-CMR data. Tissue blocks were excised and imaged using confocal and wide-field microscopy. Using the techniques described in sections 2.4 and 2.5 it is possible to generate a subject-specific geometry. Through co-location of histology and DT-CMR images, quantitative comparison could be performed between the MCRW in the histology-based domain and the corresponding DT-CMR results from the in vivo and ex vivo acquisitions.

7.3 Concluding remarks

In this work, computational modelling was used to study the effects of changes to the myocardial microstructure on DT-CMR parameters. A realistic virtual model of the myocardium was constructed to serve as substrate for Monte Carlo random walk simulations of DT-CMR. A workflow was devised to generate such models directly from histology, which includes realistic geometric features not found in prior models. A parallelised simulator was developed to assess DT-CMR in high-fidelity mesh-based substrates, and results were verified using both analytical and reference solutions. The central hypothesis of the work, namely that the combination of a realistic virtual model and simulations using Monte Carlo random walk methods allows for more realistic in-silico estimates of DT-CMR parameters, was shown to hold. In the future, the simulation capabilities developed here will enable optimisation of DT-CMR acquisition methods for maximal sensitivity to the microstructural parameters of interest. The simulation results will also provide vital insights into the sensitivity of DT-CMR measures to pathological changes in the underlying microstructure.

Bibliography

Ackerman, Joseph J H and Jeffrey J Neil (Nov. 2010). 'Biophysics of Diffusion in Cells'. In: *Diffusion MRI: Theory, Methods, and Applications*. Ed. by Derek K Jones. Oxford University Press. Chap. 8. DOI: `10.1093/med/9780195369779.003.0008`.

ACM SIGGRAPH 2005 Courses (2005). SIGGRAPH (Los Angeles, CA, USA, 31st July–4th Aug. 2005). Association for Computing Machinery. DOI: `10.1145/1198555`.

Adair, Allan et al. (2021). *Shapely*. URL: `https://github.com/Toblerity/Shapely`. (Cited on page 46)

Aird, William C (2011). 'Discovery of the cardiovascular system: from Galen to William Harvey'. In: *Journal of Thrombosis and Haemostasis* 9 (s1), pp. 118–129. DOI: `10.1111/j.1538-7836.2011.04312.x`. (Cited on page 21)

Akenine-Möller, Tomas, Eric Haines and Naty Hoffman (2008). *Real Time Rendering*. 3rd ed. CRC Press. (Cited on page 109)

Alliez, Pierre, Stéphane Tayeb and Camille Wormser (2020). '3D Fast Intersection and Distance Computation'. In: *CGAL User and Reference Manual*. 5.2. CGAL Editorial Board. URL: `https://doc.cgal.org/5.2/Manual/packages.html#PkgAABBTree` (visited on 20/05/2021). (Cited on pages 115, 116)

Andrews, Steven S, Nathan J Addy, Roger Brent and Adam P Arkin (2010). 'Detailed Simulations of Cell Biology with Smoldyn 2.1'. In: *PLOS Computational Biology* 6 (3). DOI: `10.1371/journal.pcbi.1000705`. (Cited on pages 94, 109)

Ariga, Rina, Elizabeth M Tunnicliffe, Sanjay G Manohar, Masliza Mahmod, Betty Raman, Stefan K Piechnik, Jane M Francis, Matthew D Robson, Stefan Neubauer and Hugh Watkins (2019). 'Identification of Myocardial Disarray in Patients With Hypertrophic Cardiomyopathy and Ventricular Arrhythmias'. In: *Journal of the American College of Cardiology* 73 (20), pp. 2493–2502. DOI: `10.1016/j.jacc.2019.02.065`. (Cited on page 24)

Arts, T, P Bovendeerd, T Delhaas and F Prinzen (2003). 'Modeling the relation between cardiac pump function and myofiber mechanics'. In: *Journal of Biomechanics* 36 (5), pp. 731–736. DOI: `10.1016/S0021-9290(02)00451-7`. (Cited on page 21)

Aurentz, Jared L and Lloyd N Trefethen (2017). 'Chopping a Chebyshev Series'. In: *ACM Transactions on Mathematical Software* 43 (4). DOI: `10.1145/2998442`. (Cited on pages 80, 82)

Barnett, Vincent A (2009). 'Cellular Myocytes'. In: *Handbook of Cardiac Anatomy, Physiology, and Devices*. Ed. by Paul A Iaizzo. 2nd ed. Humana Press. Chap. 10. DOI: `10.1007/978-1-60327-372-5_10`. (Cited on page 29)

Basser, Peter J, Mattiello James and Denis Le Bihan (1994). 'Estimation of the Effective Self-Diffusion Tensor from the NMR Spin Echo'. In: *Journal of Magnetic Resonance, Series B* 103 (3), pp. 247–254. DOI: `10.1006/jmrb.1994.1037`. (Cited on pages 22, 54)

Basser, Peter J and Evren Özarslan (Nov. 2010). 'Anisotropic Diffusion: From the Apparent Diffusion Coefficient to the Apparent Diffusion Tensor'. In: *Diffusion MRI: Theory, Methods, and Applications*. Ed. by Derek K Jones. Oxford University Press. Chap. 6. DOI: `10.1093/med/9780195369779.003.0006`.

Bates, J, Irvin Teh, Darryl McClymont, Peter Kohl, Jürgen E Schneider and Vicente Grau (2017). 'Monte Carlo Simulations of Diffusion Weighted MRI in Myocardium: Validation and Sensitivity Analysis'. In: *IEEE Transactions on Medical Imaging* 36, pp. 1316–1325. DOI: `10.1109/TMI.2017.2679809`. (Cited on pages 25, 37, 109, 127)

Battles, Zachary and Lloyd N Trefethen (2004). 'An Extension of MATLAB to Continuous Functions and Operators'. In: *SIAM Journal on Scientific Computing* 25 (5), pp. 1743–1770. DOI: `10.1137/S1064827503430126`. (Cited on page 80)

Bauke, Heiko (2021). *Tina's Random Number Generator Library*. URL: `https://github.com/rabauke/trng4`. (Cited on page 112)

Bauke, Heiko and Stephan Mertens (2007). 'Random numbers for large-scale distributed Monte Carlo simulations'. In: *Physical Review E* 75 (6). DOI: `10.1103/PhysRevE.75.066701`. (Cited on page 112)

Bechtold, M, J Vanderborght, O Ippisch and H Vereecken (2011). 'Efficient random walk particle tracking algorithm for advective-dispersive transport in media with discontinuous dispersion coefficients and water contents'. In: *Water Resource Research* 47 (10). DOI: `10.1029/2010WR010267`. (Cited on page 98)

Behrens, T E J, M W Woolrich, M Jenkinson, Heidi Johansen-Berg, R G Nunes, S Clare, P M Matthews, J M Brady and S M Smith (2003). 'Characterization and propagation of uncertainty in diffusion-weighted MR imaging'. In: *Magnetic Resonance in Medicine* 50 (5), pp. 1077–1088. DOI: `10.1002/mrm.10609`. (Cited on page 37)

Bensley, Jonathan Guy, Robert De Matteo, Richard Harding and Mary Jane Black (2016). 'Three-dimensional direct measurement of cardiomyocyte volume, nuclearity, and ploidy in thick histological sections'. In: *Scientific Reports* 6 (1). DOI: `10.1038/srep23756`. (Cited on pages 29, 31)

Berestyki, Henry and Nancy Rodriguez (2016). 'Analysis of a heterogeneous model for riot dynamics: The effect of censorship of information'. In: *European Journal of Applied Mathematics* 27 (3), pp. 554–582. DOI: `10.1017/S0956792515000339`.

Berg, Howard C (1993). *Random Walks in Biology.* Princeton University Press. (Cited on page 89)

Berg, Stuart, Dominik Kutra, Thorben Kroeger, Christoph N Straehle, Bernhard X Kausler, Carsten Haubold, Martin Schiegg, Janez Ales, Thorsten Beier, Markus Rudy, Kemal Eren, Jaime I Cervantes, Buote Xu, Fynn Beuttenmueller, Adrian Wolny, Chong Zhang, Ullrich Koethe, Fred A Hamprecht and Anna Kreshuk (2019). 'ilastik: interactive machine learning for (bio)image analysis'. In: *Nature Methods* 16 (12), pp. 1226–1232. DOI: `10.1038/s41592-019-0582-9`. (Cited on page 51)

Berkowitz, Brian, Andrea Cortis, Marco Dentz and Harvey Scher (2006). 'Modeling non-Fickian transport in geological formations as a continuous time random walk'. In: *Reviews of Geophysics* 44 (2). DOI: `10.1029/2005RG000178`.

Bernstein, Matt A, Kevin F King and Xiaohong Joe Zhou (2004). *Handbook of MRI Pulse Sequences.* Elsevier Academic Press. DOI: `10.1016/B978-0-12-092861-3.X5000-6`. (Cited on page 54)

Berry, David B, Erin K Englund, Vitaly Galinsky, Lawrence R Frank and Samuel R Ward (2021). 'Varying diffusion time to discriminate between simulated skeletal muscle injury models using stimulated echo diffusion tensor imaging'. In: *Magnetic Resonance in Medicine* 85 (5), pp. 2524–2536. DOI: `10.1002/mrm.28598`. (Cited on page 37)

Berry, David B, Benjamin Regner, Vitaly Galinsky, Samuel R Ward and Lawrence R Frank (2018). 'Relationships between tissue microstructure and the diffusion tensor in simulated skeletal muscle'. In: *Magnetic Resonance in Medicine* 80 (1), pp. 317–329. DOI: `10.1002/mrm.26993`. (Cited on pages 25, 37, 109)

Bloch, Felix (1946). 'Nuclear Induction'. In: *Physical Review* 70 (7–8), pp. 460–474. DOI: `10.1103/PhysRev.70.460`. (Cited on page 53)

Botsch, Mario, Leif Kobbelt, Mark Pauly, Pierre Alliez and Bruno Levy (2010). *Polygon Mesh Processing.* 1st ed. CRC Press. DOI: `10.1201/b10688`. (Cited on page 113)

Braunwald, Eugene, John Ross and Edmund H Sonnenblick (1967). 'Mechanisms of Contraction of the Normal and Failing Heart'. In: *New England Journal of Medicine* 277 (15), pp. 794–800. DOI: `10.1056/NEJM196710122771505`. (Cited on pages 29, 30)

Brent, Richard P (1971). 'An algorithm with guaranteed convergence for finding a zero of a function'. In: *The Computer Journal* 14 (4), pp. 422–425. DOI: `10.1093/comjnl/14.4.422`. (Cited on page 83)

British Heart Foundation (May 2021). *Global Heart & Circulatory Diseases Factsheet.* Slide pack. URL: `https://www.bhf.org.uk/-/media/files/research/heart-`

`statistics/bhf-cvd-statistics-global-factsheet.pdf` (visited on 12/06/2021). (Cited on page 21)

Bruvold, Morten, John Georg Seland, Heidi Brurok and Per Jynge (2007). 'Dynamic water changes in excised rat myocardium assessed by continuous distribution of T1 and T2'. In: *Magnetic Resonance in Medicine* 58 (3), pp. 442–447. DOI: `10.1002/mrm.21340`. (Cited on pages 36, 148)

Burger, Doug, James R Goodman and Alain Kägi (1996). 'Memory bandwidth limitations of future microprocessors'. In: *Proceedings of the 23rd Annual International Symposium on Computer Architecture*. International Conference on Computer Architecture – ISCA '96 (Philadelphia, PA, USA, 22nd–24th May 1996). Association for Computing Machinery, pp. 78–89. DOI: `10.1145/232973.232983`. (Cited on page 61)

Callaghan, Paul T (1993). *Principles of Nuclear Magnetic Resonance Microscopy*. Clarendon Press. (Cited on page 52)

— (Nov. 2010). 'Physics of Diffusion'. In: *Diffusion MRI: Theory, Methods, and Applications*. Ed. by Derek K Jones. Oxford University Press. Chap. 4. DOI: `10.1093/med/9780195369779.003.0004`. (Cited on pages 95, 137)

Callaghan, Ross, Daniel C Alexander, Marco Palombo and Hui Zhang (2020). 'ConFiG: Contextual Fibre Growth to generate realistic axonal packing for diffusion MRI simulation'. In: *NeuroImage* 220. DOI: `10.1016/j.neuroimage.2020.117107`. (Cited on pages 45, 149)

Callaghan, Ross, Daniel C Alexander, Hui Zhang and Marco Palombo (2019). 'Contextual Fibre Growth to Generate Realistic Axonal Packing for Diffusion MRI Simulation'. In: *Information Processing in Medical Imaging*. 26th International Conference – IPMI 2019 (Hong Kong, China, 2nd–7th June 2019). Ed. by Albert C S Chung, James C Gee, Paul A Yushkevich and Siqi Bao. Vol. 11492. LNCS, pp. 429–440. DOI: `10.1007/978-3-030-20351-1_33`. (Cited on page 45)

Callot, Virginie, Eric Bennett, Ulrich K M Decking, Robert S Balaban and Han Wen (2003). 'In vivo study of microcirculation in canine myocardium using the IVIM method'. In: *Magnetic Resonance in Medicine* 50 (3), pp. 531–540. DOI: `10.1002/mrm.10568`. (Cited on page 149)

Campbell, Scott E, A Martin Gerdes and Teri D Smith (1987). 'Comparison of regional differences in cardiac myocyte dimensions in rats, hamsters, and guinea pigs'. In: *The Anatomical Record* 219 (1), pp. 53–59. DOI: `10.1002/ar.1092190110`. (Cited on page 51)

Campbell, Scott E, K Rakusan and A Martin Gerdes (1989). 'Change in cardiac myocyte size distribution in aortic-constricted neonatal rats'. In: *Basic Research in Cardiology* 84 (3), pp. 247–258. DOI: `10.1007/BF01907972`. (Cited on page 29)

Carslaw, H S and J C Jaeger (1986). *Conduction of Heat in Solids.* 2nd ed. Oxford University Press.

Cerqueira, Manuel D, Neil J Weissman, Vasken Dilsizian, Alice K Jacobs, Sanjiv Kaul, Warren K Laskey, Dudley J Pennell, John A Rumberger, Thomas Ryan and Mario S Verani (2002). 'Standardized Myocardial Segmentation and Nomenclature for Tomographic Imaging of the Heart'. In: *Circulation* 105 (4), pp. 539–542. DOI: `10.1161/hc0402.102975`. (Cited on page 27)

Chandrasekhar, Subrahmanyan (1943). 'Stochastic Problems in Physics and Astronomy'. In: *Reviews of Modern Physics* 15 (1), pp. 1–89. DOI: `10.1103/RevModPhys.15.1`. (Cited on page 89)

— (1949). 'Brownian Motion, Dynamical Friction, and Stellar Dynamics'. In: *Reviews of Modern Physics* 21 (3), pp. 383–388. DOI: `10.1103/RevModPhys.21.383`. (Cited on page 89)

Chung, Albert C S, James C Gee, Paul A Yushkevich and Siqi Bao, eds. (2019). *Information Processing in Medical Imaging.* 26th International Conference – IPMI 2019 (Hong Kong, China, 2nd–7th June 2019). Vol. 11492. LNCS. DOI: `10.1007/978-3-030-20351-1`.

Coelho-Filho, Otavio R, Ravi V Shah, Richard Mitchell, Tomas G Neilan, Heitor Moreno, Bridget Simonson, Raymond Kwong, Anthony Rosenzweig, Saumya Das and Michael Jerosch-Herold (2013). 'Quantification of Cardiomyocyte Hypertrophy by Cardiac Magnetic Resonance: Implications for Early Cardiac Remodeling'. In: *Circulation* 128 (11), pp. 1225–1233. DOI: `10.1161/CIRCULATIONAHA.112.000438`. (Cited on pages 36, 148)

Cook, John D (2010). 'Testing a Random Number Generator'. In: *Beautiful Testing: Leading Professionals Reveal How They Improve Software.* Ed. by Tim Riley and Adam Goucher. 2nd ed. O'Reilly. Chap. 10. (Cited on page 110)

Cook, P A, Y Bai, S Nedjati-Gilani, K K Seunarine, Matt G Hall, G J Parker and Daniel C Alexander (2006). 'Camino: Open-Source Diffusion-MRI Reconstruction and Processing'. In: *Proceedings of the ISMRM 14th Annual Meeting & Exhibition.* ISMRM 14th Scientific Meeting & Exhibition (Washington State Convention & Trade Center, Seattle, WA, USA, 6th–12th May 2006). International Society for Magnetic Resonance in Medicine, 2759. (Cited on page 109)

Crank, John (1975). *The Mathematics of Diffusion.* 2nd ed. Clarendon Press.

Davis, Martin et al. (2021). *GEOS – Geometry Engine, Open Source.* URL: `https://github.com/libgeos/geos`. (Cited on page 47)

De Schutter, Erik, ed. (2001). *Computational Neuroscience: Realistic Modeling for Experimentalists.* CRC Press. DOI: `10.1201/9781420039290`.

Decamps, Marc, Ann De Schepper and Marc Goovaerts (2004). 'Applications of δ-function perturbation to the pricing of derivative securities'. In: *Physica A: Statistical Mechanics and its Applications* 342 (3–4), pp. 677–692. DOI: `10.1016/j.physa.2004.05.035`.

Deussen, Oliver, Charles Hansen, Daniel Keim and Dietmar Saupe, eds. (2004). Joint Eurographics & IEEE VGTC Symposium on Visualization (Konstanz, Germany, 19th–21st May 2004). The Eurographics Association.

Deuster, Constantin von, Eva Sammut, Liya Asner, David Nordsletten, Pablo Lamata, Christian T Stoeck, Sebastian Kozerke and Reza Razavi (2016a). 'Studying Dynamic Myofiber Aggregate Reorientation in Dilated Cardiomyopathy Using In Vivo Magnetic Resonance Diffusion Tensor Imaging'. In: *Circulation: Cardiovascular Imaging* 9 (10). DOI: `10.1161/CIRCIMAGING.116.005018`. (Cited on pages 24, 33)

Deuster, Constantin von, Christian T Stoeck, Martin Genet, David Atkinson and Sebastian Kozerke (2016b). 'Spin echo versus stimulated echo diffusion tensor imaging of the in vivo human heart'. In: *Magnetic Resonance in Medicine* 76 (3), pp. 862–872. DOI: `10.1002/mrm.25998`. (Cited on page 142)

Donev, Aleksandar, Salvatore Torquato and Frank H Stillinger (2005). 'Neighbor list collision-driven molecular dynamics simulation for nonspherical hard particles. I. Algorithmic details'. In: *Journal of Computational Physics* 202 (2), pp. 737–764. DOI: `10.1016/j.jcp.2004.08.014`. (Cited on page 47)

Doste, Ruben, David Soto-Iglesias, Gabriel Bernardino, Alejandro Alcaine, Rafael Sebastian, Sophie Giffard-Roisin, Maxime Sermesant, Antonio Berruezo, Damian Sanchez-Quintana and Oscar Camara (2019). 'A rule-based method to model myocardial fiber orientation in cardiac biventricular geometries with outflow tracts'. In: *International Journal for Numerical Methods in Biomedical Engineering* 35 (4). DOI: `10.1002/cnm.3185`. (Cited on page 147)

Driscoll, Tobin A, Nicholas Hale and Lloyd N Trefethen, eds. (2014). *Chebfun Guide*. Pafnuty Publications. URL: `http://www.chebfun.org/docs/guide/` (visited on 10/03/2021). (Cited on pages 80, 82)

Dyckhoff, Harald (1990). 'A typology of cutting and packing problems'. In: *European Journal of Operational Research* 44 (2), pp. 145–159. DOI: `10.1016/0377-2217(90)90350-K`. (Cited on page 45)

Eftekhari, Ali Akbar (2021). *FVTool: Finite volume toolbox for MATLAB*. DOI: `10.5281/zenodo.593691`. URL: `https://github.com/simulkade/FVTool`. (Cited on pages 67, 121)

Ennis, Daniel B, Gordon Kindlmann, Ignacio Rodriguez, Patrick A Helm and Elliot R McVeigh (2005). 'Visualization of tensor fields using superquadric glyphs'. In: *Magnetic Resonance in Medicine* 53 (1), pp. 169–176. DOI: `10.1002/mrm.20318`. (Cited on pages 22, 55)

Fejér, Leopold (1903). ‘Untersuchungen über Fouriersche Reihen’. German. In: *Mathematische Annalen* 58 (1), pp. 51–69. DOI: `10.1007/BF01447779`. (Cited on page 86)

Ferreira, Pedro F, Philip J Kilner, Laura-Ann McGill, Sonia Nielles-Vallespin, Andrew D Scott, Siew Y Ho, Karen P McCarthy, Margarita M Haba, Tevfik F Ismail, Peter D Gatehouse, Ranil de Silva, Alexander R Lyon, Sanjay K Prasad, David N Firmin and Dudley J Pennell (2014). ‘In vivo cardiovascular magnetic resonance diffusion tensor imaging shows evidence of abnormal myocardial laminar orientations and mobility in hypertrophic cardiomyopathy’. In: *Journal of Cardiovascular Magnetic Resonance* 16 (1). DOI: `10.1186/s12968-014-0087-8`. (Cited on pages 24, 33)

Feynman, Richard, Robert Leighton and Matthew Sands (1964). *The Feynman Lectures on Physics: Mainly Mechanics, Radiation, and Heat.* Lecture notes. California Institute of Technology. URL: `https://www.feynmanlectures.caltech.edu/I_toc.html` (visited on 09/09/2021). (Cited on page 94)

Fick, Adolf (1855). ‘Ueber Diffusion’. German. In: *Annalen der Physik* 170 (1), pp. 59–86. DOI: `10.1002/andp.18551700105`. (Cited on page 97)

Fieremans, Els, Yves De Deene, Steven Delputte, Mahir S Özdemir, Yves D’Asseler, Jelle Vlassenbroeck, Karel Deblaere, Eric Achten and Ignace Lemahieu (2008). ‘Simulation and experimental verification of the diffusion in an anisotropic fiber phantom’. In: *Journal of Magnetic Resonance* 190 (2), pp. 189–199. DOI: `10.1016/j.jmr.2007.10.014`. (Cited on page 92)

Fieremans, Els and Hong-Hsi Lee (2018). ‘Physical and numerical phantoms for the validation of brain microstructural MRI: A cookbook’. In: *NeuroImage* 182, pp. 39–61. DOI: `10.1016/j.neuroimage.2018.06.046`. (Cited on page 25)

Fieremans, Els, Dmitry S Novikov, Jens H Jensen and Joseph A Helpern (2010). ‘Monte Carlo study of a two-compartment exchange model of diffusion’. In: *NMR in Biomedicine* 23 (7), pp. 711–724. DOI: `10.1002/nbm.1577`. (Cited on pages 34, 36, 98, 99, 102, 104, 117, 128, 135, 142)

Fujita, Seiya and Xian-Hua Han (2020). ‘Cell Detection and Segmentation in Microscopy Images with Improved Mask R-CNN’. In: *Computer Vision – ACCV 2020 Workshops.* 15th Asian Conference on Computer Vision (Virtual Kyoto, 30th Nov.–4th Dec. 2020). Ed. by Imari Sato and Bohyung Han. Vol. 12628. LNCS, pp. 58–70. DOI: `10.1007/978-3-030-69756-3_5`. (Cited on page 43)

Garrido, L, Van J Wedeen, K K Kwong, U M Spencer and H L Kantor (1994). ‘Anisotropy of water diffusion in the myocardium of the rat’. In: *Circulation Research* 74 (5), pp. 789–793. DOI: `10.1161/01.RES.74.5.789`. (Cited on page 35)

Gentle, James E (2003). *Random Number Generation and Monte Carlo Methods.* 2nd ed. Statistics and Computing. Springer. DOI: `10.1007/b97336`. (Cited on page 110)

Gerdes, A Martin, Jo A Moore, Joseph M Hines, P A Kirkland and Sanford P Bishop (1986). 'Regional differences in myocyte size in normal rat heart'. In: *The Anatomical Record* 215 (4), pp. 420–426. DOI: `10.1002/ar.1092150414`. (Cited on page 51)

Gianolio, E, G Ferrauto, E Di Gregorio and S Aime (2016). 'Re-evaluation of the water exchange lifetime value across red blood cell membrane'. In: *Biochimica et Biophysica Acta* 1858 (4), pp. 627–631. DOI: `10.1016/j.bbamem.2015.12.029`. (Cited on page 134)

Ginsburger, Kévin, Felix Matuschke, Fabrice Poupon, Jean-François Mangin, Markus Axer and Cyril Poupon (2019). 'MEDUSA: A GPU-based tool to create realistic phantoms of the brain microstructure using tiny spheres'. In: *NeuroImage* 193, pp. 10–24. DOI: `10.1016/j.neuroimage.2019.02.055`. (Cited on page 45)

Google Inc et al. (2021). *TensorFlow*. DOI: `10.5281/zenodo.4724125`. URL: `https://github.com/tensorflow/tensorflow`. (Cited on page 41)

Gorodezky, Margarita, Pedro F Ferreira, Sonia Nielles-Vallespin, Peter D Gatehouse, Dudley J Pennell, Andrew D Scott and David N Firmin (2019). 'High resolution in-vivo DT-CMR using an interleaved variable density spiral STEAM sequence'. In: *Magnetic Resonance in Medicine* 81 (3), pp. 1580–1594. DOI: `10.1002/mrm.27504`. (Cited on page 24)

Grebenkov, Denis S, Dang Van Nguyen and Jing-Rebecca Li (2014). 'Exploring diffusion across permeable barriers at high gradients. I. Narrow pulse approximation'. In: *Journal of Magnetic Resonance* 248, pp. 153–163. DOI: `10.1016/j.jmr.2014.07.013`. (Cited on page 137)

Hahn, David W and M Necati Özişik (2012). *Heat Conduction*. 3rd ed. DOI: `10.1002/9781118411285`. (Cited on page 75)

Hall, Matt G and Daniel C Alexander (2009). 'Convergence and Parameter Choice for Monte-Carlo Simulations of Diffusion MRI'. In: *IEEE Transactions on Medical Imaging* 28 (9), pp. 1354–1364. DOI: `10.1080/10867651.1997.10487468`. (Cited on pages 109, 115, 120, 124)

Hall, Matt G and Chris A Clark (2016). 'Diffusion in hierarchical systems: A simulation study in models of healthy and diseased muscle tissue'. In: *Magnetic Resonance in Medicine* 78 (3), pp. 1187–1198. DOI: `10.1002/mrm.26469`. (Cited on page 98)

Hanson, Lars G (2008). 'Is quantum mechanics necessary for understanding magnetic resonance?' In: *Concepts in Magnetic Resonance Part A* 32A (5), pp. 329–340. DOI: `10.1002/cmr.a.20123`. (Cited on page 53)

Harris, Charles R et al. (2020). 'Array programming with NumPy'. In: *Nature* 585 (7825), pp. 357–362. DOI: `10.1038/s41586-020-2649-2`.

Heckbert, Paul S, ed. (1994). *Graphics Gems IV*. The Graphics Gems Series. Academic Press. DOI: `10.1016/C2013-0-07360-4`. (Cited on page 109)

Herbst, M D and J H Goldstein (1989). 'A review of water diffusion measurement by NMR in human red blood cells'. In: *American Journal of Physiology-Cell Physiology* 256 (5), pp. C1097–C1104. DOI: `10.1152/ajpcell.1989.256.5.C1097`. (Cited on page 36)

Hickson, R I, S I Barry and G N Mercer (2009). 'Critical times in multilayer diffusion. Part 1: Exact solutions'. In: *International Journal of Heat and Mass Transfer* 52 (25-26), pp. 5776–5783. DOI: `10.1016/j.ijheatmasstransfer.2009.08.013`.

Hills, B P, P S Belton and G A Webb (1989). 'NMR Studies of Membrane Transport'. In: *Annual Reports on NMR Spectroscopy* 21, pp. 99–159. DOI: `10.1016/S0066-4103(08)60122-2`. (Cited on page 36)

Hooks, Darren A, Mark L Trew, Bryan J Caldwell, Gregory B Sands, Ian J LeGrice and Bruce H Smaill (2007). 'Laminar Arrangement of Ventricular Myocytes Influences Electrical Behavior of the Heart'. In: *Circulation Research* 101 (10), e103–e112. DOI: `10.1161/CIRCRESAHA.107.161075`. (Cited on page 32)

Hwang, Scott N, Chih-Liang Chin, Felix W Wehrli and David B Hackney (2003). 'An image-based finite difference model for simulating restricted diffusion'. In: *Magnetic Resonance in Medicine* 50 (2), pp. 373–382. DOI: `10.1002/mrm.10536`. (Cited on pages 68, 122)

Iaizzo, Paul A, ed. (2009). *Handbook of Cardiac Anatomy, Physiology, and Devices*. 2nd ed. Humana Press. DOI: `10.1007/978-1-60327-372-5`.

Jelescu, Ileana O, Marco Palombo, Francesca Bagnato and Kurt G Schilling (2020). 'Challenges for biophysical modeling of microstructure'. In: *Journal of Neuroscience Methods* 344. DOI: `10.1016/j.jneumeth.2020.108861`. (Cited on pages 25, 37)

Jiang, Tianzi, Nassir Navab, Josien P W Pluim and Max A Viergever, eds. (2010). *Medical Image Computing and Computer-Assisted Intervention*. 13th International Conference – MICCAI 2010 (Beijing, China, 20th–24th Sept. 2010). Vol. 6362.2. LNCS. DOI: `10.1007/978-3-642-15745-5`.

Jones, Derek K (2002). 'Determining and visualizing uncertainty in estimates of fiber orientation from diffusion tensor MRI'. In: *Magnetic Resonance in Medicine* 49 (1), pp. 7–12. DOI: `10.1002/mrm.10331`. (Cited on page 127)

— ed. (Nov. 2010). *Diffusion MRI: Theory, Methods, and Applications*. Oxford University Press. DOI: `10.1093/med/9780195369779.001.0001`. (Cited on page 55)

Kärger, Jörg (1985). 'NMR self-diffusion studies in heterogeneous systems'. In: *Advances in Colloid and Interface Science* 23, pp. 129–148. DOI: `10.1016/0001-8686(85)80018-X`. (Cited on pages 34, 88)

Kärger, Jörg, Douglas M Ruthven and Doros N Theodorou, eds. (2012). *Diffusion in Nanoporous Materials*. 1,2 vols. John Wiley & Sons. (Cited on pages 88, 89)

Kellman, Peter, Joel R Wilson, Hui Xue, Martin Ugander and Andrew E Arai (2012). 'Extracellular volume fraction mapping in the myocardium, Part 1: Evaluation of an automated method'. In: *Journal of Cardiovascular Magnetic Resonance* 14 (1). DOI: `10.1186/1532-429X-14-63`. (Cited on page 129)

Kerr, Rex A, Thomas M Bartol, Boris Kaminsky, Markus Dittrich, Jen-Chien Jack Chang, Scott B Baden, Terrence J Sejnowski and Joel R Stiles (2008). 'Fast Monte Carlo Simulation Methods for Biological Reaction-Diffusion Systems in Solution and on Surfaces'. In: *SIAM Journal on Scientific Computing* 30 (6), pp. 3126–3149. DOI: `10.1137/070692017`. (Cited on pages 94, 110)

Khalique, Zohya, Pedro F Ferreira, Andrew D Scott, Sonia Nielles-Vallespin, David N Firmin and Dudley J Pennell (2020a). 'Diffusion Tensor Cardiovascular Magnetic Resonance Imaging: A Clinical Perspective'. In: *JACC: Cardiovascular Imaging* 13 (5), pp. 1235–1255. DOI: `10.1016/j.jcmg.2019.07.016`. (Cited on page 28)

Khalique, Zohya, Pedro F Ferreira, Andrew D Scott, Sonia Nielles-Vallespin, Philip J Kilner, Robert Kutys, Maria Romero, Andrew E Arai, David N Firmin and Dudley J Pennell (2018). 'Deranged Myocyte Microstructure in Situs Inversus Totalis Demonstrated by Diffusion Tensor Cardiac Magnetic Resonance'. In: *JACC: Cardiovascular Imaging* 11 (9), pp. 1360–1362. DOI: `10.1016/j.jcmg.2017.11.014`. (Cited on pages 22, 24, 33, 186)

Khalique, Zohya, Pedro F Ferreira, Andrew D Scott, Sonia Nielles-Vallespin, Ana Martinez-Naharro, Marianna Fontana, Phillip Hawkins, David N Firmin and Dudley J Pennell (2020b). 'Diffusion Tensor Cardiovascular Magnetic Resonance in Cardiac Amyloidosis'. In: *Circulation: Cardiovascular Imaging* 13 (5). DOI: `10.1161/CIRCIMAGING.119.009901`. (Cited on page 24)

Khor, Jia Wei (2020). '3D Modelling of the Myocardium'. M.Eng. thesis. (Cited on page 44)

Kim, Sungheon, Alan S Chi-Fishman Gloria Barnett and Carlo Pierpaoli (2005). 'Dependence on diffusion time of apparent diffusion tensor of ex vivo calf tongue and heart'. In: *Magnetic Resonance in Medicine* 54 (6), pp. 1387–1396. DOI: `10.1002/mrm.20676`. (Cited on pages 142, 144)

Kindlmann, Gordon (2004). 'Superquadric Tensor Glyphs'. In: *VisSym*. Joint Eurographics & IEEE VGTC Symposium on Visualization (Konstanz, Germany, 19th–21st May 2004). Ed. by Oliver Deussen, Charles Hansen, Daniel Keim and Dietmar Saupe. The Eurographics Association, pp. 147–154. DOI: `10.2312/VisSym/VisSym04/147-154`. (Cited on page 55)

Kingsley, Peter B (2006a). 'Introduction to diffusion tensor imaging mathematics: Part I. Tensors, rotations, and eigenvectors'. In: *Concepts in Magnetic Resonance Part A* 28A (2), pp. 101–122. DOI: `10.1002/cmr.a.20048`. (Cited on page 55)

— (2006b). 'Introduction to diffusion tensor imaging mathematics: Part II. Anisotropy, diffusion-weighting factors, and gradient encoding schemes'. In: *Concepts in Magnetic*

Resonance Part A 28A (2), pp. 123–154. DOI: 10.1002/cmr.a.20049. (Cited on page 55)

Kingsley, Peter B (2006c). 'Introduction to diffusion tensor imaging mathematics: Part III. Tensor calculation, noise, simulations, and optimization'. In: *Concepts in Magnetic Resonance Part A* 28A (2), pp. 155–179. DOI: 10.1002/cmr.a.20050. (Cited on page 55)

Kiselev, Valerij G (Nov. 2010). 'The Cumulant Expansion: An Overarching Mathematical Framework For Understanding Diffusion NMR'. In: *Diffusion MRI: Theory, Methods, and Applications.* Ed. by Derek K Jones. Oxford University Press. Chap. 10. DOI: 10.1093/med/9780195369779.003.0010.

— (2017). 'Fundamentals of diffusion MRI physics'. In: *NMR in Biomedicine* 30 (3). DOI: 10.1002/nbm.3602. (Cited on page 54)

Knuth, Donald E (2011a). *The Art of Computer Programming. Seminumerical Algorithms.* 3rd ed. 1, 2, 3, 4A vols. Addison-Wesley. (Cited on page 110)

— (2011b). *The Art of Computer Programming.* 3rd ed. 1, 2, 3, 4A vols. Addison-Wesley.

Köthe, Ullrich (2003). 'Edge and Junction Detection with an Improved Structure Tensor'. In: *Pattern Recognition.* 25th DAGM Symposium (Magdeburg, Germany, 10th–13th Sept. 2003). Ed. by Bernd Michaelis and Gerald Krell. Vol. 2781. LNCS, pp. 25–32. DOI: 10.1007/978-3-540-45243-0_4. (Cited on page 44)

Kung, Geoffrey L, Tom C Nguyen, Aki Itoh, Stefan Skare, Neil B Ingels Jr, D Craig Miller and Daniel B Ennis (2011). 'The presence of two local myocardial sheet populations confirmed by diffusion tensor MRI and histological validation'. In: *Journal of Magnetic Resonance Imaging* 34 (5), pp. 1080–1091. DOI: 10.1002/jmri.22725. (Cited on pages 32, 128)

Landis, Charles S, Xin Li, Frank W Telang, Patricia E Molina, Ildiko Palyka, Gabor Vetek and Charles S Springer Jr (1999). 'Equilibrium transcytolemmal water-exchange kinetics in skeletal muscle in vivo'. In: *Magnetic Resonance in Medicine* 42 (3), pp. 467–478. DOI: 10.1002/(SICI)1522-2594(199909)42:3<467::AID-MRM9>3.0.CO;2-0. (Cited on page 36)

Lapierre-Landry, Maryse, Hana Kolesová, Yehe Liu, Michiko Watanabe and Michael W Jenkins (2020). 'Three-dimensional alignment of microvasculature and cardiomyocytes in the developing ventricle'. In: *Scientific Reports* 10 (1). DOI: 10.1038/s41598-020-71816-y. (Cited on page 149)

Lasič, Samo, Markus Nilsson, Jimmy Lätt, Freddy Ståhlberg and Daniel Topgaard (2011). 'Apparent exchange rate mapping with diffusion MRI'. In: *Magnetic Resonance in Medicine* 66 (2), pp. 356–365. DOI: 10.1002/mrm.22782. (Cited on page 36)

Lasič, Samo, Filip Szczepankiewicz, Erica Dall'Armellina, Arka Das, Christopher Kelly, Sven Plein, Jürgen E Schneider, Markus Nilsson and Irvin Teh (2020). 'Motion-compensated b-tensor encoding for in vivo cardiac diffusion-weighted imaging'. In: *NMR in Biomedicine* 33 (2). DOI: `10.1002/nbm.4213`. (Cited on page 24)

Le Bihan, Denis (2003). 'Looking into the functional architecture of the brain with diffusion MRI'. In: *Nature Reviews Neuroscience* 4 (6), pp. 469–480. DOI: `10.1038/nrn1119`.

— (Nov. 2010). 'Magnetic Resonance Diffusion Imaging: Introduction and Concepts'. In: *Diffusion MRI: Theory, Methods, and Applications*. Ed. by Derek K Jones. Oxford University Press. Chap. 5. DOI: `10.1093/med/9780195369779.003.0005`. (Cited on page 54)

Le Bihan, Denis and Heidi Johansen-Berg (2012). 'Diffusion MRI at 25: Exploring brain tissue structure and function'. In: *NeuroImage* 61 (2), pp. 324–341. DOI: `10.1016/j.neuroimage.2011.11.006`. (Cited on page 55)

Lee, Hong-Hsi, Els Fieremans and Dmitry S Novikov (2021). 'Realistic Microstructure Simulator (RMS): Monte Carlo simulations of diffusion in three-dimensional cell segmentations of microscopy images'. In: *Journal of Neuroscience Methods* 350. DOI: `10.1016/j.jneumeth.2020.109018`. (Cited on page 109)

Lee, Hong-Hsi, Antonios Papaioannou, Sung-Lyoung Kim, Dmitry S Novikov and Els Fieremans (2020a). 'A time-dependent diffusion MRI signature of axon caliber variations and beading'. In: *Communications Biology* 3 (1). DOI: `10.1038/s42003-020-1050-x`. (Cited on page 37)

Lee, Hong-Hsi, Antonios Papaioannou, Dmitry S Novikov and Els Fieremans (2020b). 'In vivo observation and biophysical interpretation of time-dependent diffusion in human cortical gray matter'. In: *NeuroImage* 222. DOI: `10.1016/j.neuroimage.2020.117054`.

Lee, Jack, Andrew Cookson, Radomir Chabiniok, Simone Rivolo, Eoin Hyde, Matthew Sinclair, Christian Michler, Taha Sochi and Nicolas Smith (2015). 'Multiscale Modelling of Cardiac Perfusion'. In: *Modeling the Heart and the Circulatory System*. Ed. by Alfio Quarteroni. Vol. 14. MS&A – Modeling, Simulation & Applications. Chap. 3. DOI: `10.1007/978-3-319-05230-4_3`. (Cited on page 149)

LeGrice, Ian J, Bruce H Smaill, L Z Chai, S G Edgar, J B Gavin and P J Hunter (1995a). 'Laminar structure of the heart: ventricular myocyte arrangement and connective tissue architecture in the dog'. In: *Am J Physiol* 269 (2), H571–H582. DOI: `10.1152/ajpheart.1995.269.2.H571`. (Cited on pages 32, 33, 186)

LeGrice, Ian J, Y Takayama and J W Covell (1995b). 'Transverse Shear Along Myocardial Cleavage Planes Provides a Mechanism for Normal Systolic Wall Thickening'. In: *Circulation Research* 77 (1), pp. 182–193. DOI: `10.1161/01.RES.77.1.182`. (Cited on page 32)

Lejay, Antoine (2018). 'A Monte Carlo estimation of the mean residence time in cells surrounded by thin layers'. In: *Mathematics and Computers in Simulation* 143, pp. 65–77. DOI: `10.1016/j.matcom.2017.05.008`. (Cited on page 149)

Lejay, Antoine and Géraldine Pichot (2012). 'Simulating diffusion processes in discontinuous media: A numerical scheme with constant time steps'. In: *Journal of Computational Physics* 231 (21), pp. 7299–7314. DOI: `10.1016/j.jcp.2012.07.011`. (Cited on page 149)

Li, Hua, Xiaoyu Jiang, Jingping Xie, J Oliver McIntyre, John C Gore and Junzhong Xu (2015). 'Time-Dependent Influence of Cell Membrane Permeability on MR Diffusion Measurements'. In: *Magnetic Resonance in Medicine* 75 (5), pp. 1927–1934. DOI: `10.1002/mrm.25724`.

Li, Jing-Rebecca, Donna Calhoun, Cyril Poupon and Denis Le Bihan (2014). 'Numerical simulation of diffusion MRI signals using an adaptive time-stepping method'. In: *Physics in Medicine & Biology* 59 (2), pp. 441–454. DOI: `10.1088/0031-9155/59/2/441`. (Cited on page 61)

Lipinski, Hans-Georg (1990). 'Monte Carlo simulation of extracellular diffusion in brain tissues'. In: *Physics in Medicine and Biology* 35 (3), pp. 441–447. DOI: `10.1088/0031-9155/35/3/012`. (Cited on page 25)

Lundell, Henrik and Samo Lasič (30th Apr. 2021). 'A minimal geometrical model for Monte Carlo simulations of time dependent diffusion in axons'. In: *Proceedings of the ISMRM 29th Annual Meeting & Exhibition.* 2021 ISMRM & SMRT Annual Meeting & Exhibition (Online, 15th–20th May 2021). International Society for Magnetic Resonance in Medicine, 3403. (Cited on page 37)

Maruyama, Yutaka (2017). 'Random walk to describe diffusion phenomena in three-dimensional discontinuous media: Step-balance and fictitious-velocity corrections'. In: *Physical Review E* 96 (3). DOI: `10.1103/PhysRevE.96.032135`. (Cited on pages 98, 103, 106–108, 117)

McClymont, Darryl, Irvin Teh, Eric Carruth, Jeffrey Omens, Andrew McCulloch, Hannah J Whittington, Peter Kohl, Vicente Grau and Jürgen E Schneider (2017). 'Evaluation of Non-Gaussian Diffusion in Cardiac MRI'. In: *Magnetic Resonance in Medicine* 78 (3), pp. 1174–1186. DOI: `10.1002/mrm.26466`. (Cited on page 24)

McGill, Laura-Ann, Pedro F Ferreira, Andrew D Scott, Sonia Nielles-Vallespin, Archontis Giannakidis, Philip J Kilner, Peter D Gatehouse, Ranil de Silva, David N Firmin and Dudley J Pennell (2015a). 'Relationship between cardiac diffusion tensor imaging parameters and anthropometrics in healthy volunteers'. In: *Journal of Cardiovascular Magnetic Resonance* 18. DOI: `10.1186/s12968-015-0215-0`. (Cited on page 142)

McGill, Laura-Ann, Andrew D Scott, Pedro F Ferreira, Sonia Nielles-Vallespin, Tevfik F Ismail, Philip J Kilner, Peter D Gatehouse, Ranil de Silva, Sanjay K Prasad, Archontis Giannakidis, David N Firmin and Dudley J Pennell (2015b). 'Heterogeneity of Fractional Anisotropy and Mean Diffusivity Measurements by In Vivo Diffusion Tensor Imaging in

Normal Human Hearts'. In: *PLOS ONE* 10 (7). DOI: `10.1371/journal.pone.0132360`. (Cited on page 142)

Medical Image Computing and Computer-Assisted Intervention (2015). 18th International Conference – MICCAI 2015 (Munich, Germany, 5th–9th Oct. 2015). Vol. 9351.3. LNCS. DOI: `10.1007/978-3-319-24574-4`.

Meier, Christian, Wolfgang Dreher and Dieter Leibfritz (2003). 'Diffusion in compartmental systems. I. A comparison of an analytical model with simulations'. In: *Magnetic Resonance in Medicine* 50 (3), pp. 500–509. DOI: `10.1002/mrm.10557`. (Cited on page 36)

Mekkaoui, Choukri, Marcel P Jackowski, William J Kostis, Christian T Stoeck, Aravinda Thiagalingam, Timothy G Reese, Vivek Y Reddy, Jeremy N Ruskin, Sebastian Kozerke and David E Sosnovik (2018). 'Myocardial Scar Delineation Using Diffusion Tensor Magnetic Resonance Tractography'. In: *Journal of the American Heart Association* 7 (3). DOI: `10.1161/JAHA.117.007834`. (Cited on page 24)

Metaxas, Dimitris N and Leon Axel, eds. (2011). *Functional Imaging and Modeling of the Heart*. 6th International Conference – FIMH 2011 (New York City, NY, USA, 25th–27th May 2011). Vol. 6666. LNCS. DOI: `10.1007/978-3-642-21028-0`.

Michaelis, Bernd and Gerald Krell, eds. (2003). *Pattern Recognition*. 25th DAGM Symposium (Magdeburg, Germany, 10th–13th Sept. 2003). Vol. 2781. LNCS. DOI: `10.1007/b12010`.

Mills, R (1973). 'Self-diffusion in normal and heavy water in the range 1-45°'. In: *The Journal of Physical Chemistry* 77 (5), pp. 685–688. DOI: `10.1021/j100624a025`. (Cited on page 35)

Mingasson, Tom, Tanguy Duval, Nikola Stikov and Julien Cohen-Adad (2017). 'AxonPacking: An Open-Source Software to Simulate Arrangements of Axons in White Matter'. In: *Frontiers in Neuroinformatics* 11. DOI: `10.3389/fninf.2017.00005`. (Cited on pages 45–47)

Möller, Tomas and Ben Trumbore (1997). 'Fast, Minimum Storage Ray-Triangle Intersection'. In: *Journal of Graphics Tools* 2 (1), pp. 21–28. DOI: `10.1109/TMI.2009.2015756`. (Cited on page 114)

Moulin, Kévin, Ilya A Verzhbinsky, Nyasha G Maforo, Luigi E Perotti and Daniel B Ennis (2020a). 'Probing cardiomyocyte mobility with multi-phase cardiac diffusion tensor MRI'. In: *PLOS ONE* 15 (11). DOI: `10.1371/journal.pone.0241996`. (Cited on page 142)

Moulin, Kévin, Magalie Viallon, Nyasha G Maforo, Valentina Mazzoli, Pierre Croisille and Daniel B Ennis (24th July 2020b). 'Sensitivity of Cardiac Diffusion Encoding Waveforms to Myocardial Extracellular Volume: A simulation study'. In: *Proceedings of the ISMRM 28th Annual Meeting & Exhibition*. 2020 ISMRM & SMRT Virtual

Conference & Exhibition (Online, 8th–14th Aug. 2020). International Society for Magnetic Resonance in Medicine, 2050. (Cited on page 37)

Moutal, Nicolas and Denis S Grebenkov (2019). 'Diffusion Across Semi-permeable Barriers: Spectral Properties, Efficient Computation, and Applications'. In: *Journal of Scientific Computing* 81 (3), pp. 1630–1654. DOI: `10.1007/s10915-019-01055-5`. (Cited on pages 76, 77, 79, 80, 82, 97, 138)

Moutal, Nicolas, Antoine Moutal and Denis S Grebenkov (2020). 'Diffusion NMR in periodic media: efficient computation and spectral properties'. In: *Journal of Physics A: Mathematical and Theoretical* 53 (32). DOI: `10.1088/1751-8121/ab977e`. (Cited on pages 58, 88)

Munafò, Marcus R, Brian A Nosek, Dorothy V M Bishop, Katherine S Button, Christopher D Chambers, Nathalie Percie du Sert, Uri Simonsohn, Eric-Jan Wagenmakers, Jennifer J Ware and John P A Ioannidis (2017). 'A manifesto for reproducible science'. In: *Nature Human Behaviour* 1 (1). DOI: `10.1038/s41562-016-0021`.

Nguyen, Christopher, Minjie Lu, Zhaoyang Fan, Xiaoming Bi, Peter Kellman, Shihua Zhao and Debiao Li (2015). 'Contrast-free detection of myocardial fibrosis in hypertrophic cardiomyopathy patients with diffusion-weighted cardiovascular magnetic resonance'. In: *Journal of Cardiovascular Magnetic Resonance* 17 (1). DOI: `10.1186/s12968-015-0214-1`. (Cited on page 34)

Nguyen, Khieu-Van, Edwin Hernández-Garzón and Julien Valette (2018). 'Efficient GPU-based Monte-Carlo simulation of diffusion in real astrocytes reconstructed from confocal microscopy'. In: *Journal of Magnetic Resonance* 296, pp. 188–199. DOI: `10.1016/j.jmr.2018.09.013`. (Cited on page 109)

Nielles-Vallespin, Sonia, Zohya Khalique, Pedro F Ferreira, Ranil de Silva, Andrew D Scott, Philip J Kilner, Laura-Ann McGill, Archontis Giannakidis, Peter D Gatehouse, Daniel B Ennis, Eric Aliotta, Majid Al-Khalil, Peter Kellman, Dumitru Mazilu, Robert S Balaban, David N Firmin, Andrew E Arai and Dudley J Pennell (2017). 'Assessment of Myocardial Microstructural Dynamics by In Vivo Diffusion Tensor Cardiac Magnetic Resonance'. In: *Journal of the American College of Cardiology* 69 (6), pp. 661–676. DOI: `10.1016/j.jacc.2016.11.051`. (Cited on pages 24, 28, 32, 37, 119, 145)

Nielles-Vallespin, Sonia, Andrew D Scott, Pedro F Ferreira, Zohya Khalique, Dudley J Pennell and David N Firmin (2020). 'Cardiac Diffusion: Technique and Practical Applications'. In: *Journal of Magnetic Resonance Imaging* 52 (2), pp. 348–368. DOI: `10.1002/jmri.26912`. (Cited on page 22)

Nirschl, Jeffrey J, Andrew Janowczyk, Eliot G Peyster, Renee Frank, Kenneth B Margulies, Michael D Feldman and Anant Madabhushi (2017). 'Deep Learning Tissue Segmentation in Cardiac Histopathology Images'. In: *Deep Learning for Medical Image Analysis*. Ed. by S Kevin Zhou, Hayit Greenspan and Dinggang Shen. 1st ed. The MICCAI Society book series. Academic Press. Chap. 8. DOI: `10.1016/B978-0-12-810408-8.00011-0`. (Cited on page 41)

Novikov, Dmitry S, Els Fieremans, Sune N Jespersen and Valerij G Kiselev (2019). ‘Quantifying brain microstructure with diffusion MRI: Theory and parameter estimation’. In: *NMR in Biomedicine* 32 (4). DOI: `10.1002/nbm.3998`. (Cited on pages 37, 140)

Novikov, Dmitry S, Jens H Jensen, Joseph A Helpern and Els Fieremans (2014). ‘Revealing mesoscopic structural universality with diffusion’. In: *Revealing mesoscopic structural universality with diffusion* 111 (14), pp. 5088–5093. DOI: `10.1073/pnas.1316944111`.

Novikov, Dmitry S and Valerij G Kiselev (2010). ‘Effective medium theory of a diffusion-weighted signal’. In: *NMR in Biomedicine* 23 (7), pp. 682–697. DOI: `10.1002/nbm.1584`.

Novikov, Dmitry S, Valerij G Kiselev and Sune N Jespersen (2018). ‘On modeling’. In: *Magnetic Resonance in Medicine* 79 (6), pp. 3172–3193. DOI: `10.1002/mrm.27101`.

Olivetti, Giorgio, Elena Cigola, Roberta Maestri, Domenico Corradi, Costanza Lagrasta, Steven R Gambert and Piero Anversa (1996). ‘Aging, Cardiac Hypertrophy and Ischemic Cardiomyopathy Do Not Affect the Proportion of Mononucleated and Multinucleated Myocytes in the Human Heart’. In: *Journal of Molecular and Cellular Cardiology* 28 (7), pp. 1463–1477. DOI: `10.1006/jmcc.1996.0137`. (Cited on page 29)

Özişik, M Necati, Helcio R B Orlande, Marcelo José Colaço and Renato Machado Cotta (2017). *Finite Difference Methods in Heat Transfer.* CRC Press. DOI: `10.1201/9781315121475`. (Cited on page 63)

Paddock, Stephen W, ed. (2014). *Confocal Microscopy: Methods and Protocols.* 2nd ed. Vol. 1075. Methods in Molecular Biology. DOI: `10.1007/978-1-60761-847-8`.

Palombo, Marco, Daniel C Alexander and Hui Zhang (2019). ‘A generative model of realistic brain cells with application to numerical simulation of the diffusion-weighted MR signal’. In: *NeuroImage* 188, pp. 391–402. DOI: `10.1016/j.neuroimage.2018.12.025`. (Cited on pages 37, 45, 149)

Panagiotaki, Eleftheria, Matt G Hall, Hui Zhang, Bernard Siow, Mark F Lythgoe and Daniel C Alexander (2010). ‘High-Fidelity Meshes from Tissue Samples for Diffusion MRI Simulations’. In: *Medical Image Computing and Computer-Assisted Intervention.* 13th International Conference – MICCAI 2010 (Beijing, China, 20th–24th Sept. 2010). Ed. by Tianzi Jiang, Nassir Navab, Josien P W Pluim and Max A Viergever. Vol. 6362.2. LNCS, pp. 404–411. DOI: `10.1007/978-3-642-15745-5_50`. (Cited on pages 45, 109)

Panagiotaki, Eleftheria, Torben Schneider, Bernard Siow, Matt G Hall, Mark F Lythgoe and Daniel C Alexander (2012). ‘Compartment models of the diffusion MR signal in brain white matter: A taxonomy and comparison’. In: *NeuroImage* 59 (3), pp. 2241–2254. DOI: `10.1016/j.neuroimage.2011.09.081`. (Cited on page 34)

Parks, David R, Mario Roederer and Wayne A Moore (2006). ‘A new “Logicle” display method avoids deceptive effects of logarithmic scaling for low signals and compensated data'. In: *Cytometry Part A* 69A (6), pp. 541–551. DOI: `10.1002/cyto.a.20258`. (Cited on page 79)

Pettigrew, James Bell (1864). 'XIV. On the arrangement of the muscular fibres in the ventricles of the vertebrate heart, with physiological remarks'. In: *Philosophical Transactions of the Royal Society of London* 154, pp. 445–500. DOI: `10.1098/rstl.1864.0014`. (Cited on page 28)

Phipps, Kellie, Maaike van de Boomen, Robert Eder, Sam Allen Michelhaugh, Aferdita Spahillari, Joan Kim, Shestruma Parajuli, Timothy G Reese, Choukri Mekkaoui, Saumya Das, Denise Gee, Ravi V Shah, David E Sosnovik and Christopher Nguyen (2021). 'Accelerated in Vivo Cardiac Diffusion-Tensor MRI Using Residual Deep Learning–based Denoising in Participants with Obesity'. In: *Radiology: Cardiothoracic Imaging* 3 (3). DOI: `10.1148/ryct.2021200580`. (Cited on page 24)

Powles, Jack G, M J D Mallett, Gerald Rickayzen and W A B Evans (1992). 'Exact analytic solutions for diffusion impeded by an infinite array of partially permeable barriers'. In: *Proceedings of the Royal Society of London. Series A: Mathematical and Physical Sciences* 436 (1897), pp. 391–403. DOI: `10.1098/rspa.1992.0025`. (Cited on pages 35, 92, 97–99, 102, 108, 117)

Price, Robert L, Stephen T Haley, Tara Bullard, Jeffrey Davis, Thomas K Borg and Louis Terracio (2014). 'Confocal Microscopy of Cardiac Myocytes'. In: *Confocal Microscopy: Methods and Protocols*. Ed. by Stephen W Paddock. 2nd ed. Vol. 1075. Methods in Molecular Biology. Chap. 8. DOI: `10.1007/978-1-60761-847-8_8`. (Cited on page 29)

Proceedings from the 22nd Annual SCMR Scientific Sessions (6th Feb. 2018). Global CMR: Innovation and Clinical Outcomes (Bellevue, WA, USA, 6th–9th Feb. 2019). Society for Cardiovascular Magnetic Resonance.

Proceedings of CMR 2018 (31st Jan. 2018). CMR 2018 – A Joint EuroCMR/SCMR Meeting (Barcelona, Spain, 31st Jan.–3rd Feb. 2018). Society for Cardiovascular Magnetic Resonance.

Proceedings of ISBI (2014). IEEE 11th International Symposium on Biomedical Imaging (Beijing, China, 29th Apr.–2nd May 2014). Institute of Electrical and Electronics Engineers. DOI: `10.1109/ISBI19594.2014`.

Proceedings of PD19 (2019). SIAM Conference on Analysis of Partial Differential Equations (PD19) (La Quinta Resort & Club, La Quinta, CA, USA, 11th–14th Dec. 2019). Society for Industrial and Applied Mathematics.

Proceedings of the 23rd Annual International Symposium on Computer Architecture (1996). International Conference on Computer Architecture – ISCA '96 (Philadelphia, PA, USA, 22nd–24th May 1996). Association for Computing Machinery. DOI: `10.1145/232973`.

Proceedings of the ISMRM 14th Annual Meeting & Exhibition (2006). ISMRM 14th Scientific Meeting & Exhibition (Washington State Convention & Trade Center, Seattle, WA, USA, 6th–12th May 2006). International Society for Magnetic Resonance in Medicine.

Proceedings of the ISMRM 26th Annual Meeting & Exhibition (1st June 2018). Joint Annual Meeting ISMRM-ESMRMB (Paris Expo Porte de Versailles, Paris, France, 16th–21st June 2018). International Society for Magnetic Resonance in Medicine.

Proceedings of the ISMRM 27th Annual Meeting & Exhibition (26th Apr. 2019). ISMRM 27th Annual Meeting & Exhibition (Palais des congrès de Montréal, Montréal, QC, Canada, 11th–16th May 2019). International Society for Magnetic Resonance in Medicine.

Proceedings of the ISMRM 28th Annual Meeting & Exhibition (24th July 2020). 2020 ISMRM & SMRT Virtual Conference & Exhibition (Online, 8th–14th Aug. 2020). International Society for Magnetic Resonance in Medicine.

Proceedings of the ISMRM 29th Annual Meeting & Exhibition (30th Apr. 2021). 2021 ISMRM & SMRT Annual Meeting & Exhibition (Online, 15th–20th May 2021). International Society for Magnetic Resonance in Medicine.

Proceedings of the ISMRM Workshop on Machine Learning (2018). ISMRM Workshop on Machine Learning (Asilomar Conference Grounds, Pacific Grove, CA, USA, 14th–17th Mar. 2018). International Society for Magnetic Resonance in Medicine.

Proceedings of WCB (2018). 8th World Congress of Biomechanics (Dublin, Ireland, 8th–12th July 2018).

Quarteroni, Alfio, ed. (2015). *Modeling the Heart and the Circulatory System*. Vol. 14. MS&A – Modeling, Simulation & Applications. DOI: `10.1007/978-3-319-05230-4`.

Rafael-Patino, Jonathan, David Romascano, Alonso Ramirez-Manzanares, Erick Jorge Canales-Rodríguez, Gabriel Girard and Jean-Philippe Thiran (2020). 'Robust Monte-Carlo Simulations in Diffusion-MRI: Effect of the Substrate Complexity and Parameter Choice on the Reproducibility of Results'. In: *Frontiers in Neuroinformatics* 14. DOI: `10.3389/fninf.2020.00008`. (Cited on pages 109, 115)

Reese, Timothy G, Robert M Weisskoff, R Neil Smith, Bruce R Rosen, Robert E Dinsmore and Van J Wedeen (1995). 'Imaging myocardial fiber architecture in vivo with magnetic resonance'. In: *Magnetic Resonance in Medicine* 34 (6), pp. 786–791. DOI: `10.1002/mrm.1910340603`. (Cited on pages 56, 149)

Reginald Waldeck, A, M Hossein Nouri-Sorkhabi, David R Sullivan and Philip W Kuchel (1995). 'Effects of cholesterol on transmembrane water diffusion in human erythrocytes measured using pulsed field gradient NMR'. In: *Biophysical Chemistry* 55 (3), pp. 197–208. DOI: `10.1016/0301-4622(95)00007-K`. (Cited on page 36)

Richardson, Mark et al. (2021). *ChebPy - A Python implementation of Chebfun*. URL: `https://github.com/chebpy/chebpy`. (Cited on page 80)

Riley, Tim and Adam Goucher, eds. (2010). *Beautiful Testing: Leading Professionals Reveal How They Improve Software*. 2nd ed. O'Reilly.

Röhrle, O, H Köstler and M Loch (2011). 'Segmentation of Skeletal Muscle Fibres for Applications in Computational Skeletal Muscle Mechanics'. In: *Computational Biomechanics for Medicine: Soft Tissues and the Musculoskeletal System*. 13th International Conference – MICCAI 2010 (Beijing, China, 20th–24th Sept. 2010). Ed. by Adam Wittek, Poul M F Nielsen and Karol Miller, pp. 107–117. DOI: `10.1007/978-1-4419-9619-0_12`.

Ronneberger, Olaf, Philipp Fischer and Thomas Brox (2015). 'U-Net: Convolutional Networks for Biomedical Image Segmentation'. In: *Medical Image Computing and Computer-Assisted Intervention*. 18th International Conference – MICCAI 2015 (Munich, Germany, 5th–9th Oct. 2015). Vol. 9351.3. LNCS. DOI: `10.1007/978-3-319-24574-4_28`. (Cited on pages 41, 43)

Rose, Jan N (2015). 'GPU-based Simulation to Improve Cardiac Diffusion Tensor Imaging'. M.Sc. thesis. (Cited on page 111)

— (12th July 2017). 'Modelling Restricted (Self-)Diffusion as a Monte Carlo Random Walk: A framework for synthesising realistic DTI data *in silico* based on microstructural imaging of histology'. Talk. CDT Fluids Student Symposium (Imperial College London, London, UK).

— (29th Nov. 2018a). 'Accelerating image-based finite difference methods using GPUs'. Seminar. RSE Lunchtime Seminar Series (Imperial College London, London, UK).

— (12th Dec. 2018b). 'Exploring the cardiac tissue microstructure: A random walk model of restricted diffusion'. Seminar. Aerodynamics Seminar Series (Imperial College London, London, UK).

— (7th Aug. 2019a). 'Histology based in-silico modelling of diffusion tensor imaging in myocardial tissue'. Invited lecture (Cincinnati Children's Hospital, Cincinnati, OH, USA).

Rose, Jan N, Ignasi Alemany, Jerome Garnier-Brun, Andrew D Scott and Denis J Doorly (n.d.). 'Accuracy of random walk diffusion simulations in permeable layered media evaluated through analytical methods'. In preparation. (Cited on page 185)

Rose, Jan N, Ignasi Alemany, Andrew D Scott and Denis J Doorly (30th Apr. 2021a). 'Realistic diffusion tensor cardiovascular magnetic resonance simulations in a histology-based substrate: The effect of membrane permeability'. In: *Proceedings of the ISMRM 29th Annual Meeting & Exhibition*. 2021 ISMRM & SMRT Annual Meeting & Exhibition (Online, 15th–20th May 2021). International Society for Magnetic Resonance in Medicine, 2853. (Cited on page 142)

Rose, Jan N, Wee Zhao Chua Khoo, Sonia Nielles-Vallespin, Pedro F Ferreira, David N Firmin, Andrew D Scott and Denis J Doorly (1st June 2018c). 'Deep learning based segmentation of cardiomyocytes to aid numerical simulations of diffusion cardiovascular magnetic resonance'. In: *Proceedings of the ISMRM 26th Annual Meeting & Exhibition.* Joint Annual Meeting ISMRM-ESMRMB (Paris Expo Porte de Versailles, Paris, France, 16th–21st June 2018). International Society for Magnetic Resonance in Medicine, 5238. (Cited on pages 42, 43, 184)

Rose, Jan N, Jerome Garnier-Brun, Andrew D Scott and Denis J Doorly (2019b). 'Mathematical Modelling and Computational Simulations of Diffusion in Cardiac Tissue'. In: *Proceedings of PD19.* SIAM Conference on Analysis of Partial Differential Equations (PD19) (La Quinta Resort & Club, La Quinta, CA, USA, 11th–14th Dec. 2019). Society for Industrial and Applied Mathematics, p. 19. (Cited on page 185)

Rose, Jan N, Sonia Nielles-Vallespin, Pedro F Ferreira, David N Firmin, Andrew D Scott and Denis J Doorly (31st Jan. 2018d). 'Simulating diffusion tensor cardiovascular magnetic resonance using a histology-based virtual microstructure'. In: *Proceedings of CMR 2018.* CMR 2018 – A Joint EuroCMR/SCMR Meeting (Barcelona, Spain, 31st Jan.–3rd Feb. 2018). Society for Cardiovascular Magnetic Resonance, 373719, pp. 1122–1123.

— (2019c). 'Novel insights into in-vivo diffusion tensor cardiovascular magnetic resonance using computational modelling and a histology-based virtual microstructure'. In: *Magnetic Resonance in Medicine* 81 (4), pp. 2759–2773. DOI: `10.1002/mrm.27561`. (Cited on pages 37, 38, 40, 56, 57, 93, 113–116, 118, 121, 125–127, 184)

— (2018e). 'Verifying Monte Carlo simulations of diffusion tensor cardiovascular magnetic resonance using a finite volume method'. In: *Proceedings of WCB.* 8th World Congress of Biomechanics (Dublin, Ireland, 8th–12th July 2018), O0874. (Cited on pages 67, 121)

Rose, Jan N, Andrew D Scott and Denis J Doorly (30th Apr. 2021b). 'Packing hierarchical structures in myocardial tissue to synthesise a realistic substrate'. In: *Proceedings of the ISMRM 29th Annual Meeting & Exhibition.* 2021 ISMRM & SMRT Annual Meeting & Exhibition (Online, 15th–20th May 2021). International Society for Magnetic Resonance in Medicine, 2854. (Cited on pages 46, 184)

— (2018f). 'Comparing Neural Network-Based Segmentation of Cardiomyocytes from Different Histology Data'. In: *Proceedings of the ISMRM Workshop on Machine Learning.* ISMRM Workshop on Machine Learning (Asilomar Conference Grounds, Pacific Grove, CA, USA, 14th–17th Mar. 2018). International Society for Magnetic Resonance in Medicine, 27. (Cited on pages 42, 43, 184)

Rose, Jan N, Lukasz Sliwinski, Sonia Nielles-Vallespin, Andrew D Scott and Denis J Doorly (26th Apr. 2019d). 'Studying the effect of membrane permeability with a GPU-based Bloch–Torrey simulator'. In: *Proceedings of the ISMRM 27th Annual Meeting & Exhibition.* ISMRM 27th Annual Meeting & Exhibition (Palais des congrès de Montréal,

Montréal, QC, Canada, 11th–16th May 2019). International Society for Magnetic Resonance in Medicine, 3644. (Cited on pages 45, 68, 69, 140, 185)

Rose, Jan N, Qiwei Xiao, Charlotte McIntyre, Neil S Tolley and Denis J Doorly (2018g). ‘Procedure for geometry regularisation to separate the effects of torsion and curvature on flow structure’. In: *Proceedings of WCB.* 8th World Congress of Biomechanics (Dublin, Ireland, 8th–12th July 2018), 1971. (Cited on page 184)

Rutkovskiy, Arkady, Guro Valen and Jarle Vaage (2013). ‘Cardiac aquaporins’. In: *Basic Research in Cardiology* 108 (6). DOI: `10.1007/s00395-013-0393-6`. (Cited on page 31)

Safford, R E, E A Bassingthwaighte and J B Bassingthwaighte (1978). ‘Diffusion of water in cat ventricular myocardium’. In: *Journal of General Physiology* 72 (4), pp. 513–538. DOI: `10.1085/jgp.72.4.513`. (Cited on page 35)

Sato, Imari and Bohyung Han, eds. (2020). *Computer Vision – ACCV 2020 Workshops.* 15th Asian Conference on Computer Vision (Virtual Kyoto, 30th Nov.–4th Dec. 2020). Vol. 12628. LNCS. DOI: `10.1007/978-3-030-69756-3`.

Satoh, H, L M Delbridge, L A Blatter and D M Bers (1996). ‘Surface:volume relationship in cardiac myocytes studied with confocal microscopy and membrane capacitance measurements: species-dependence and developmental effects’. In: *Biophysical Journal* 70 (3), pp. 1494–1505. DOI: `10.1016/S0006-3495(96)79711-4`. (Cited on page 29)

Scalas, Enrico (2006). ‘The application of continuous-time random walks in finance and economics’. In: *Physica A: Statistical Mechanics and its Applications* 362 (2), pp. 225–239. DOI: `10.1016/j.physa.2005.11.024`. (Cited on page 89)

Scollan, D F, A Holmes, J Zhang and R L Winslow (2000). ‘Reconstruction of Cardiac Ventricular Geometry and Fiber Orientation Using Magnetic Resonance Imaging’. In: *Annals of Biomedical Engineering* 28 (8), pp. 934–944. DOI: `10.1114/1.1312188`. (Cited on page 24)

Scott, Andrew D, Timothy Jackson, Zohya Khalique, Margarita Gorodezky, Ben Pardoe, Domenico Bruno, Rasheda A Chowdhury, Pedro F Ferreira, Sonia Nielles-Vallespin, Lale Begum, Malte Roehl, Padmini Sarathchandra, Jan N Rose, Denis J Doorly, Dudley J Pennell, Raimondo Ascione, Ranil de Silva and David N Firmin (6th Feb. 2018a). ‘Development of a large animal isolated perfused beating heart model for myocardial microstructure imaging’. In: *Proceedings from the 22nd Annual SCMR Scientific Sessions.* Global CMR: Innovation and Clinical Outcomes (Bellevue, WA, USA, 6th–9th Feb. 2019). Society for Cardiovascular Magnetic Resonance, 546390, pp. 303–306.

— (26th Apr. 2019). ‘Diffusion tensor cardiovascular magnetic resonance in a Langendorff perfused beating porcine heart’. In: *Proceedings of the ISMRM 27th Annual Meeting & Exhibition.* ISMRM 27th Annual Meeting & Exhibition (Palais des congrès de Montréal,

Montréal, QC, Canada, 11th–16th May 2019). International Society for Magnetic Resonance in Medicine, 0404. (Cited on pages 147, 150)

Scott, Andrew D, Timothy Jackson, Zohya Khalique, Margarita Gorodezky, Ben Pardoe, Domenico Bruno, Rasheda A Chowdhury, Pedro F Ferreira, Sonia Nielles-Vallespin, Malte Roehl, Padmini Sarathchandra, Jan N Rose, Denis J Doorly, Dudley J Pennell, Raimondo Ascione, Ranil de Silva and David N Firmin (n.d.). 'Development of a CMR compatible large animal isolated beating heart model for direct comparison of beating and arrested hearts'. Submitted.

Scott, Andrew D, Sonia Nielles-Vallespin, Pedro F Ferreira, Zohya Khalique, Peter D Gatehouse, Philip J Kilner, Dudley J Pennell and David N Firmin (2018b). 'An in-vivo comparison of stimulated-echo and motion compensated spin-echo sequences for 3 T diffusion tensor cardiovascular magnetic resonance at multiple cardiac phases'. In: *Journal of Cardiovascular Magnetic Resonance* 20 (1). DOI: `10.1186/s12968-017-0425-8`. (Cited on page 142)

Seidel, Thomas, J-C Edelmann and Frank B Sachse (2016). 'Analyzing Remodeling of Cardiac Tissue: A Comprehensive Approach Based on Confocal Microscopy and 3D Reconstructions'. In: *Annals of Biomedical Engineering* 44 (5), pp. 1436–1448. DOI: `10.1007/s10439-015-1465-6`. (Cited on pages 31, 66, 67, 149, 186)

Seland, John Georg, Morten Bruvold, Heidi Brurok, Per Jynge and Jostein Krane (2007). 'Analyzing equilibrium water exchange between myocardial tissue compartments using dynamical two-dimensional correlation experiments combined with manganese-enhanced relaxography'. In: *Magnetic Resonance in Medicine* 58 (4), pp. 674–686. DOI: `10.1002/mrm.21323`. (Cited on pages 35, 36)

Semmlow, John L (2004). *Biosignal and Medical Image Processing: MATLAB-Based Applications*. 2nd ed. Signal Processing and Communication Series. CRC Press. DOI: `10.1201/9780203024058`. (Cited on pages 43, 62)

Singh, Suneet, Prashant K Jain and Rizwan Uddin (2008). 'Analytical solution to transient heat conduction in polar coordinates with multiple layers in radial direction'. In: *International Journal of Thermal Sciences* 47 (3), pp. 261–273. DOI: `10.1016/j.ijthermalsci.2007.01.031`. (Cited on page 150)

Smerup, Morten, Eva Nielsen, Peter Agger, Jesper Frandsen, Peter Vestergaard-Poulsen, Johnnie Andersen, Jens Nyengaard, Michael Pedersen, Steffen Ringgaard, Vibeke Hjortdal, Paul P Lunkenheimer and Robert H Anderson (2009). 'The Three-Dimensional Arrangement of the Myocytes Aggregated Together Within the Mammalian Ventricular Myocardium'. In: *The Anatomical Record* 292 (1), pp. 1–11. DOI: `10.1002/ar.20798`. (Cited on pages 24, 31)

Snaar, J E M and H Van As (1992). ‘Probing water compartments and membrane permeability in plant cells by 1H NMR relaxation measurements’. In: *Biophysical Journal* 63 (6), pp. 1654–1658. DOI: `10.1016/S0006-3495(92)81741-1`. (Cited on page 34)

Sobol, W T, S C Jackels, R L Cothran and W H Hinson (1991). ‘NMR spin–lattice relaxation in tissues with high concentration of paramagnetic contrast media: Evaluation of water exchange rates in intact rat muscle’. In: *Medical Physics* 18 (2), pp. 243–250. DOI: `10.1118/1.596722`. (Cited on page 36)

Sosnovik, David E, Ruopeng Wang, Guangping Dai, Teresa Wang, Elena Aikawa, Mikhael Novikov, Anthony Rosenzweig, Richard J Gilbert and Van J Wedeen (2009). ‘Diffusion Spectrum MRI Tractography Reveals the Presence of a Complex Network of Residual Myofibers in Infarcted Myocardium’. In: *Circulation: Cardiovascular Imaging* 2 (3), pp. 206–212. DOI: `10.1161/CIRCIMAGING.108.815050`. (Cited on page 24)

Spinner, Georg R, Christian T Stoeck, Linda Mathez, Constantin von Deuster, Christian Federau and Sebastian Kozerke (2019). ‘On probing intravoxel incoherent motion in the heart-spin-echo versus stimulated-echo DWI’. In: *Magnetic Resonance in Medicine* 82 (3), pp. 1150–1163. DOI: `10.1002/mrm.27777`. (Cited on page 149)

Springer Jr, Charles S, Xin Li, Luminita A Tudorica, Karen Y Oh, Nicole Roy, Stephen Y-C Chui, Arpana M Naik, Megan L Holtorf, Aneela Afzal, William D Rooney and Wei Huang (2014). ‘Intratumor mapping of intracellular water lifetime: metabolic images of breast cancer?’ In: *NMR in Biomedicine* 27 (7), pp. 760–773. DOI: `10.1002/nbm.3111`. (Cited on page 36)

Stanisz, Greg J (2003). ‘Diffusion MR in Biological Systems: Tissue Compartments and Exchange’. In: *Israel Journal of Chemistry* 43 (1–2), pp. 33–44. DOI: `10.1560/E0WU-7FFH-31M6-VLYT`. (Cited on page 34)

Stejskal, Edward O and John E Tanner (1965). ‘Spin diffusion measurements: Spin echoes in the presence of a time-dependent field gradient’. In: *The Journal of Chemical Physics* 42 (1), pp. 288–292. DOI: `10.1063/1.1695690`. (Cited on pages 54, 55)

Stephenson, Robert S, Peter Agger, Paul P Lunkenheimer, Jichao Zhao, Morten Smerup, Peter Niederer, Robert H Anderson and Jonathan C Jarvis (2016). ‘The functional architecture of skeletal compared to cardiac musculature: Myocyte orientation, lamellar unit morphology, and the helical ventricular myocardial band’. In: *Clinical Anatomy* 29 (3), pp. 316–332. DOI: `10.1002/ca.22661`. (Cited on page 37)

Sterpetti, Antonio V (2019). ‘Cardiovascular Research by Leonardo da Vinci (1452–1519)’. In: *Circulation Research* 124 (2), pp. 189–191. DOI: `10.1161/CIRCRESAHA.118.314253`. (Cited on page 21)

Stiles, Joel R and Thomas M Bartol (2001). ‘Monte Carlo methods for simulating realistic synaptic microphysiology using MCell’. In: *Computational Neuroscience: Realistic*

Modeling for Experimentalists. Ed. by Erik De Schutter. CRC Press. Chap. 4. DOI: `10.1201/9781420039290`. (Cited on page 94)

Stoeck, Christian T, Constantin von Deuster, Thea Fleischmann, Miriam Lipiski, Nikola Cesarovic and Sebastian Kozerke (2018). 'Direct comparison of in vivo versus postmortem second-order motion-compensated cardiac diffusion tensor imaging'. In: *Magnetic Resonance in Medicine* 79 (4), pp. 2265–2276. DOI: `10.1002/mrm.26871`. (Cited on page 142)

Stoeck, Christian T, Constantin von Deuster, Robbert J H van Gorkum and Sebastian Kozerke (2020). 'Motion and eddy current–induced signal dephasing in in vivo cardiac DTI'. In: *Magnetic Resonance in Medicine* 84 (1), pp. 277–288. DOI: `10.1002/mrm.28132`. (Cited on page 149)

Streeter, Daniel D, Henry M Spotnitz, Dali P Patel, John Ross and Edmund H Sonnenblick (1969). 'Fiber Orientation in the Canine Left Ventricle during Diastole and Systole'. In: *Circulation Research* 24 (3), pp. 339–347. DOI: `10.1161/01.RES.24.3.339`. (Cited on pages 28, 39)

Strijkers, Gustav J, Sjoerd Hak, Maarten B Kok, Charles S Springer Jr and Klaas Nicolay (2009). 'Three-compartment T1 relaxation model for intracellular paramagnetic contrast agents'. In: *Magnetic Resonance in Medicine* 61 (5), pp. 1049–1058. DOI: `10.1002/mrm.21919`. (Cited on page 36)

Sukstanskii, Alexander L, Dmitriy A Yablonskiy and Joseph J H Ackerman (2004). 'Effects of permeable boundaries on the diffusion-attenuated MR signal: insights from a one-dimensional model'. In: *Journal of Magnetic Resonance* 170 (1), pp. 56–66. DOI: `10.1016/j.jmr.2004.05.020`.

Szafer, Aaron, Jianhui Zhong and John C Gore (1995). 'Theoretical Model for Water Diffusion in Tissues'. In: *Magnetic Resonance in Medicine* 33 (5), pp. 697–712. DOI: `10.1002/mrm.1910330516`. (Cited on pages 37, 96, 103, 106)

Tanner, John E (1978). 'Transient diffusion in a system partitioned by permeable barriers. Application to NMR measurements with a pulsed field gradient'. In: *The Journal of Chemical Physics* 69 (4), pp. 1748–1754. DOI: `10.1063/1.436751`. (Cited on pages 75, 97)

Tanner, John E and Edward O Stejskal (1968). 'Restricted Self-Diffusion of Protons in Colloidal Systems by the Pulsed-Gradient, Spin-Echo Method'. In: *The Journal of Chemical Physics* 49 (4). DOI: `10.1063/1.1670306`. (Cited on page 84)

Teh, Irvin, Darryl McClymont, Eric Carruth, Jeffrey Omens, Andrew McCulloch and Jürgen E Schneider (2020). 'Improved compressed sensing and super-resolution of cardiac diffusion MRI with structure-guided total variation'. In: *Magnetic Resonance in Medicine* 84 (4), pp. 1868–1880. DOI: `10.1002/mrm.28245`. (Cited on page 24)

The CGAL Project (2020). *CGAL User and Reference Manual.* 5.2. CGAL Editorial Board. URL: `https://doc.cgal.org/5.2/Manual/packages.html` (visited on 20/05/2021). (Cited on pages 115, 116)

Torrey, H C (1956). 'Bloch Equations with Diffusion Terms'. In: *Physical Review* 104 (3), pp. 563–565. DOI: `10.1103/PhysRev.104.563`. (Cited on page 53)

Tracy, Richard E and Gary E Sander (2011). 'Histologically Measured Cardiomyocyte Hypertrophy Correlates with Body Height as Strongly as with Body Mass Index'. In: *Cardiology Research and Practice* 2011. DOI: `10.4061/2011/658958`. (Cited on pages 129, 135)

Ureña, José R Solera, Salvador Olmos and Valerij G Kiselev (2011). 'Tissue–blood exchange of extravascular longitudinal magnetization with account of intracompartmental diffusion'. In: *Magnetic Resonance in Medicine* 66 (5), pp. 1445–1455. DOI: `10.1002/mrm.22919`.

Versteeg, Henk Kaarle and Weeratunge Malalasekera (2007). *An Introduction to Computational Fluid Dynamics: The Finite Volume Method.* 2nd ed. Pearson. (Cited on page 65)

Vignoles, Gerard L (2016). 'A hybrid random walk method for the simulation of coupled conduction and linearized radiation transfer at local scale in porous media with opaque solid phases'. In: *International Journal of Heat and Mass Transfer* 93, pp. 707–719. DOI: `10.1016/j.ijheatmasstransfer.2015.10.056`.

Virtanen, Pauli et al. (2020). 'SciPy 1.0: Fundamental Algorithms for Scientific Computing in Python'. In: *Nature Methods* 17 (3), pp. 261–272. DOI: `10.1038/s41592-019-0686-2`. (Cited on page 83)

Wang, Li-Hui (2013). 'Modeling and simulation of diffusion magnetic resonance imaging for cardiac fibers'. Ph.D. thesis.

Wang, Li-Hui, Yue-Min Zhu, Hongying Li, Wan-Yu Liu and Isabelle E Magnin (2012). 'Multiscale Modeling and Simulation of the Cardiac Fiber Architecture for DMRI'. In: *IEEE Transactions on Biomedical Engineering* 59 (1), pp. 16–19. DOI: `10.1109/TBME.2011.2166265`. (Cited on pages 37, 127)

— (2011). 'Simulation of Diffusion Anisotropy in DTI for Virtual Cardiac Fiber Structure'. In: *Functional Imaging and Modeling of the Heart.* 6th International Conference – FIMH 2011 (New York City, NY, USA, 25th–27th May 2011). Ed. by Dimitris N Metaxas and Leon Axel. Vol. 6666. LNCS, pp. 95–104. DOI: `10.1007/978-3-642-21028-0_12`. (Cited on page 37)

Wang, Li-Hui, Yue-Min Zhu, Feng Yang, Wan-Yu Liu and Isabelle E Magnin (2014). 'Simulation of dynamic DTI of 3D cardiac fiber structures'. In: *Proceedings of ISBI.* IEEE 11th International Symposium on Biomedical Imaging (Beijing, China, 29th Apr.–

2nd May 2014). Institute of Electrical and Electronics Engineers, pp. 714–717. DOI: `10.1109/ISBI.2014.6867970`. (Cited on pages 25, 37)

Welsh, C L, E V R DiBella and E W Hsu (2015). 'Higher-Order Motion-Compensation for In Vivo Cardiac Diffusion Tensor Imaging in Rats'. In: *IEEE Transactions on Medical Imaging* 34 (9), pp. 1843–1853. DOI: `10.1109/TMI.2015.2411571`. (Cited on pages 24, 55, 58)

Williams, Amy, Steve Barrus, R Keith Morley and Peter Shirley (2005). 'An Efficient and Robust Ray-Box Intersection Algorithm'. In: *ACM SIGGRAPH 2005 Courses*. SIGGRAPH (Los Angeles, CA, USA, 31st July–4th Aug. 2005). Association for Computing Machinery, 9–es. DOI: `10.1145/1198555.1198748`. (Cited on page 112)

Williamson, Nathan H, Rea Ravin, Dan Benjamini, Hellmut Merkle, Melanie Falgairolle, Michael James O'Donovan, Dvir Blivis, Dave Ide, Teddy X Cai, Nima S Ghorashi, Ruiliang Bai and Peter J Basser (2019). 'Magnetic resonance measurements of cellular and sub-cellular membrane structures in live and fixed neural tissue'. In: *eLife* 8. DOI: `10.7554/eLife.51101`.

Wilson, Alexander, Kévin Moulin, Gregory B Sands and Daniel B Ennis (30th Apr. 2021). 'Microstructure-Based Simulation of Myocardial Diffusion Using Extended Volume Confocal Microscopy'. In: *Proceedings of the ISMRM 29th Annual Meeting & Exhibition*. 2021 ISMRM & SMRT Annual Meeting & Exhibition (Online, 15th–20th May 2021). International Society for Magnetic Resonance in Medicine, 3621. (Cited on page 51)

Wilt, Nicholas (2013). *The CUDA Handbook: A Comprehensive Guide to GPU Programming*. Addison-Wesley Professional. (Cited on page 62)

Wittek, Adam, Poul M F Nielsen and Karol Miller, eds. (2011). *Computational Biomechanics for Medicine: Soft Tissues and the Musculoskeletal System*. 13th International Conference – MICCAI 2010 (Beijing, China, 20th–24th Sept. 2010). DOI: `10.1007/978-1-4419-9619-0`.

Wu, Rui, Dong-Aolei An, Jiani Hu, Meng Jiang, Qiang Guo, Jian-Rong Xu and Lian-Ming Wu (2018). 'The apparent diffusion coefficient is strongly correlated with extracellular volume, a measure of myocardial fibrosis, and subclinical cardiomyopathy in patients with systemic lupus erythematosus'. In: *Acta Radiologica* 59 (3), pp. 287–295. DOI: `10.1177/0284185117717763`. (Cited on page 34)

Xiao, Qiwei, Raul Cetto, Denis J Doorly, Alister J Bates, Jan N Rose, Charlotte McIntyre, Andrew Comerford, Gitta Madani, Neil S Tolley and Robert Schroter (2020). 'Assessing Changes in Airflow and Energy Loss in a Progressive Tracheal Compression Before and After Surgical Correction'. In: *Annals of Biomedical Engineering* 48 (2), pp. 822–833. DOI: `10.1007/s10439-019-02410-1`.

Yablonskiy, Dmitriy A and Alexander L Sukstanskii (2010). 'Theoretical models of the diffusion weighted MR signal'. In: *NMR in Biomedicine* 23 (7), pp. 661–681. DOI: `10.1002/nbm.1520`.

Yeh, Chun-Hung, Benoît Schmitt, Denis Le Bihan, Jing-Rebecca Li-Schlittgen, Ching-Po Lin and Cyril Poupon (2013). 'Diffusion Microscopist Simulator: A General Monte Carlo Simulation System for Diffusion Magnetic Resonance Imaging'. In: *PLOS ONE* 8 (10). DOI: `10.1371/journal.pone.0076626`. (Cited on page 109)

Young, Alistair A and Brett R Cowan (2012). 'Evaluation of left ventricular torsion by cardiovascular magnetic resonance'. In: *Journal of Cardiovascular Magnetic Resonance* 14 (1). DOI: `10.1186/1532-429X-14-49`. (Cited on page 28)

Young, Alistair A, Christopher M Kramer, Victor A Ferrari, Leon Axel and Nathaniel Reichek (1994). 'Three-dimensional left ventricular deformation in hypertrophic cardiomyopathy'. In: *Circulation* 90 (2), pp. 854–867. DOI: `10.1161/01.CIR.90.2.854`. (Cited on page 149)

Zhang, Hui, Torben Schneider, Claudia A Wheeler-Kingshott and Daniel C Alexander (2012). 'NODDI: Practical in vivo neurite orientation dispersion and density imaging of the human brain'. In: *NeuroImage* 61 (4), pp. 1000–1016. DOI: `10.1016/j.neuroimage.2012.03.072`. (Cited on page 37)

Zhang, Ming (2000). 'Calculation of Diffusive Shock Acceleration of Charged Particles by Skew Brownian Motion'. In: *The Astrophysical Journal* 541 (1), pp. 428–435. DOI: `10.1086/309429`.

Zhou, S Kevin, Hayit Greenspan and Dinggang Shen, eds. (2017). *Deep Learning for Medical Image Analysis*. 1st ed. The MICCAI Society book series. Academic Press. (Cited on page 41)

ZooFari (2010). *Heart diagram-en.svg*. Graphic. URL: `https://commons.wikimedia.org/wiki/File:Heart_diagram-en.svg` (visited on 11/06/2021). (Cited on page 28)

Appendices

Appendix A

Publications

This appendix contains a list of all publications and other contributions that resulted from this Ph.D.

Journal articles

Rose, **Jan N**, Ignasi Alemany, Jerome Garnier-Brun, Andrew D Scott and Denis J Doorly (n.d.). ‘Accuracy of random walk diffusion simulations in permeable layered media evaluated through analytical methods’. In preparation. (Cited on page 185)

Rose, **Jan N**, Sonia Nielles-Vallespin, Pedro F Ferreira, David N Firmin, Andrew D Scott and Denis J Doorly (2019c). ‘Novel insights into in-vivo diffusion tensor cardiovascular magnetic resonance using computational modelling and a histology-based virtual microstructure’. In: *Magnetic Resonance in Medicine* 81 (4), pp. 2759–2773. doi: `10.1002/mrm.27561`. (Cited on pages 37, 38, 40, 56, 57, 93, 113–116, 118, 121, 125–127, 184)

Scott, Andrew D, Timothy Jackson, Zohya Khalique, Margarita Gorodezky, Ben Pardoe, Domenico Bruno, Rasheda A Chowdhury, Pedro F Ferreira, Sonia Nielles-Vallespin, Malte Roehl, Padmini Sarathchandra, **Jan N Rose**, Denis J Doorly, Dudley J Pennell, Raimondo Ascione, Ranil de Silva and David N Firmin (n.d.). ‘Development of a CMR compatible large animal isolated beating heart model for direct comparison of beating and arrested hearts’. Submitted.

Xiao, Qiwei, Raul Cetto, Denis J Doorly, Alister J Bates, **Jan N Rose**, Charlotte McIntyre, Andrew Comerford, Gitta Madani, Neil S Tolley and Robert Schroter (2020). ‘Assessing Changes in Airflow and Energy Loss in a Progressive Tracheal Compression Before and After Surgical Correction’. In: *Annals of Biomedical Engineering* 48 (2), pp. 822–833. doi: `10.1007/s10439-019-02410-1`.

Conference proceedings

Rose, **Jan N**, Ignasi Alemany, Andrew D Scott and Denis J Doorly (30th Apr. 2021a). 'Realistic diffusion tensor cardiovascular magnetic resonance simulations in a histology-based substrate: The effect of membrane permeability'. In: *Proceedings of the ISMRM 29th Annual Meeting & Exhibition.* 2021 ISMRM & SMRT Annual Meeting & Exhibition (Online, 15th–20th May 2021). International Society for Magnetic Resonance in Medicine, 2853. (Cited on page 142)

Rose, **Jan N**, Wee Zhao Chua Khoo, Sonia Nielles-Vallespin, Pedro F Ferreira, David N Firmin, Andrew D Scott and Denis J Doorly (1st June 2018c). 'Deep learning based segmentation of cardiomyocytes to aid numerical simulations of diffusion cardiovascular magnetic resonance'. In: *Proceedings of the ISMRM 26th Annual Meeting & Exhibition.* Joint Annual Meeting ISMRM-ESMRMB (Paris Expo Porte de Versailles, Paris, France, 16th–21st June 2018). International Society for Magnetic Resonance in Medicine, 5238. (Cited on pages 42, 43, 184)

Rose, **Jan N**, Jerome Garnier-Brun, Andrew D Scott and Denis J Doorly (2019b). 'Mathematical Modelling and Computational Simulations of Diffusion in Cardiac Tissue'. In: *Proceedings of PD19.* SIAM Conference on Analysis of Partial Differential Equations (PD19) (La Quinta Resort & Club, La Quinta, CA, USA, 11th–14th Dec. 2019). Society for Industrial and Applied Mathematics, p. 19. (Cited on page 185)

Rose, **Jan N**, Sonia Nielles-Vallespin, Pedro F Ferreira, David N Firmin, Andrew D Scott and Denis J Doorly (31st Jan. 2018d). 'Simulating diffusion tensor cardiovascular magnetic resonance using a histology-based virtual microstructure'. In: *Proceedings of CMR 2018.* CMR 2018 – A Joint EuroCMR/SCMR Meeting (Barcelona, Spain, 31st Jan.–3rd Feb. 2018). Society for Cardiovascular Magnetic Resonance, 373719, pp. 1122–1123.

— (2018e). 'Verifying Monte Carlo simulations of diffusion tensor cardiovascular magnetic resonance using a finite volume method'. In: *Proceedings of WCB.* 8th World Congress of Biomechanics (Dublin, Ireland, 8th–12th July 2018), O0874. (Cited on pages 67, 121)

Rose, **Jan N**, Andrew D Scott and Denis J Doorly (30th Apr. 2021b). 'Packing hierarchical structures in myocardial tissue to synthesise a realistic substrate'. In: *Proceedings of the ISMRM 29th Annual Meeting & Exhibition.* 2021 ISMRM & SMRT Annual Meeting & Exhibition (Online, 15th–20th May 2021). International Society for Magnetic Resonance in Medicine, 2854. (Cited on pages 46, 184)

— (2018f). 'Comparing Neural Network-Based Segmentation of Cardiomyocytes from Different Histology Data'. In: *Proceedings of the ISMRM Workshop on Machine Learning.* ISMRM Workshop on Machine Learning (Asilomar Conference Grounds, Pacific Grove,

CA, USA, 14th–17th Mar. 2018). International Society for Magnetic Resonance in Medicine, 27. (Cited on pages 42, 43, 184)

Rose, **Jan N**, Lukasz Sliwinski, Sonia Nielles-Vallespin, Andrew D Scott and Denis J Doorly (26th Apr. 2019d). ‘Studying the effect of membrane permeability with a GPU-based Bloch–Torrey simulator’. In: *Proceedings of the ISMRM 27th Annual Meeting & Exhibition*. ISMRM 27th Annual Meeting & Exhibition (Palais des congrès de Montréal, Montréal, QC, Canada, 11th–16th May 2019). International Society for Magnetic Resonance in Medicine, 3644. (Cited on pages 45, 68, 69, 140, 185)

Rose, **Jan N**, Qiwei Xiao, Charlotte McIntyre, Neil S Tolley and Denis J Doorly (2018g). ‘Procedure for geometry regularisation to separate the effects of torsion and curvature on flow structure’. In: *Proceedings of WCB*. 8th World Congress of Biomechanics (Dublin, Ireland, 8th–12th July 2018), 1971. (Cited on page 184)

Scott, Andrew D, Timothy Jackson, Zohya Khalique, Margarita Gorodezky, Ben Pardoe, Domenico Bruno, Rasheda A Chowdhury, Pedro F Ferreira, Sonia Nielles-Vallespin, Lale Begum, Malte Roehl, Padmini Sarathchandra, **Jan N Rose**, Denis J Doorly, Dudley J Pennell, Raimondo Ascione, Ranil de Silva and David N Firmin (6th Feb. 2018a). ‘Development of a large animal isolated perfused beating heart model for myocardial microstructure imaging’. In: *Proceedings from the 22nd Annual SCMR Scientific Sessions*. Global CMR: Innovation and Clinical Outcomes (Bellevue, WA, USA, 6th–9th Feb. 2019). Society for Cardiovascular Magnetic Resonance, 546390, pp. 303–306.

— (26th Apr. 2019). ‘Diffusion tensor cardiovascular magnetic resonance in a Langendorff perfused beating porcine heart’. In: *Proceedings of the ISMRM 27th Annual Meeting & Exhibition*. ISMRM 27th Annual Meeting & Exhibition (Palais des congrès de Montréal, Montréal, QC, Canada, 11th–16th May 2019). International Society for Magnetic Resonance in Medicine, 0404. (Cited on pages 147, 150)

Talks & Seminars

Rose, **Jan N** (12th July 2017). ‘Modelling Restricted (Self-)Diffusion as a Monte Carlo Random Walk: A framework for synthesising realistic DTI data *in silico* based on microstructural imaging of histology’. Talk. CDT Fluids Student Symposium (Imperial College London, London, UK).

— (29th Nov. 2018a). ‘Accelerating image-based finite difference methods using GPUs’. Seminar. RSE Lunchtime Seminar Series (Imperial College London, London, UK).

— (12th Dec. 2018b). ‘Exploring the cardiac tissue microstructure: A random walk model of restricted diffusion’. Seminar. Aerodynamics Seminar Series (Imperial College London, London, UK).

Rose, **Jan N** (7th Aug. 2019a). 'Histology based in-silico modelling of diffusion tensor imaging in myocardial tissue'. Invited lecture (Cincinnati Children's Hospital, Cincinnati, OH, USA).

APPENDIX B

Software & Data

(Oh, ooh oh, ooh oh, oh)
I think there's a flaw in my **code**
(Oh, ooh oh, ooh oh, oh)
These voices won't leave me alone

Halsey (2015), *Gasoline*

This appendix contains a non-extensive list of all software tools developed in this project. For the full documentation (if available), please refer to source code in the individual software repositories. Some of these tools may not have been made public yet by the time this document is published.

B.1 Tissue modelling

B.1.1 `cell-morphing`

Source (repository)	`https://github.com/janniklasrose/cell-morphing`
Source (archived)	n/a
Data	doi:10.5281/zenodo.3925757
Published	Rose et al. (2019c)

B.1.2 `MyoSeg`

Source (repository)	n/a
Source (archived)	n/a
Data	doi:10.5281/zenodo.3925498
Published	Rose et al. (2018c,f)

B.1.3 `cell-packing`

Source (repository)	`https://github.com/janniklasrose/cell-packing`
Source (archived)	n/a
Data	doi:10.5281/zenodo.3925757
Published	Rose et al. (2021b)

B.2 Numerical simulations

B.2.1 `FV-RW-verification`

Source (repository)	`https://github.com/janniklasrose/FV-RW-verification`
Source (archived)	n/a
Data	doi:10.5281/zenodo.4495729
Published	Rose et al. (2018g)

B.2.2 `RWcDTI`

Source (repository)	`https://github.com/janniklasrose/RWcDTI`
Source (archived)	doi:10.5281/zenodo.4506756
Data	doi:10.5281/zenodo.3925757
Published	Rose et al. (2019c)

B.2.3 `diffusion-models`

Source (repository)	`https://github.com/janniklasrose/diffusion-models`
Source (archived)	doi:10.5281/zenodo.4447328
Data	n/a
Published	Rose et al. (n.d., 2019b)

B.2.4 `GPU-BT-sim`

Source (repository)	`https://github.com/janniklasrose/GPU-BT-sim`
Source (archived)	n/a
Data	doi:10.5281/zenodo.4309718
Published	Rose et al. (2019d)

Appendix C

Copyright Permissions

This appendix contains license agreements made with publishers of copyrighted materials used in this thesis, granting permission for their reproduction. They are summarised in table C.1.

Table C.1: Index of copyrighted material.

Location	Originally published	Attached
Figure 1.1	Khalique et al. (2018)	pages 187 to 190
Figure 2.7	LeGrice et al. (1995a)	pages 191 to 192
Figure 2.5	Seidel et al. (2016)	pages 193 to 196

ELSEVIER LICENSE
TERMS AND CONDITIONS

Sep 22, 2021

This Agreement between Jan Rose ("You") and Elsevier ("Elsevier") consists of your license details and the terms and conditions provided by Elsevier and Copyright Clearance Center.

License Number	5086040662920
License date	Jun 11, 2021
Licensed Content Publisher	Elsevier
Licensed Content Publication	JACC: Cardiovascular Imaging
Licensed Content Title	Deranged Myocyte Microstructure in Situs Inversus Totalis Demonstrated by Diffusion Tensor Cardiac Magnetic Resonance
Licensed Content Author	Zohya Khalique,Pedro F. Ferreira,Andrew D. Scott,Sonia Nielles-Vallespin,Philip J. Kilner,Robert Kutys,Maria Romero,Andrew E. Arai,David N. Firmin,Dudley J. Pennell
Licensed Content Date	Sep 1, 2018
Licensed Content Volume	11
Licensed Content Issue	9
Licensed Content Pages	3
Start Page	1360
End Page	1362
Type of Use	reuse in a thesis/dissertation
Portion	figures/tables/illustrations
Number of figures/tables/illustrations	1
Format	both print and electronic
Are you the author of this Elsevier article?	No
Will you be translating?	No
Title	Computational modelling of diffusion magnetic resonance imaging based on cardiac histology
Institution name	Imperial College London
Expected presentation date	Jun 2021
Portions	Figure 1
Requestor Location	Jan Rose Exhibition Road Department of Aeronautics Imperial College London London, SW72AZ United Kingdom Attn: Jan N Rose
Publisher Tax ID	GB 494 6272 12
Total	**0.00 GBP**
Terms and Conditions	

INTRODUCTION

1. The publisher for this copyrighted material is Elsevier. By clicking "accept" in connection with completing this licensing transaction, you agree that the following terms and conditions apply to this transaction (along with the Billing and Payment terms and conditions established by Copyright Clearance Center, Inc. ("CCC"), at the time that you opened your Rightslink account and that are available at any time at http://myaccount.copyright.com).

GENERAL TERMS

2. Elsevier hereby grants you permission to reproduce the aforementioned material subject to the terms and conditions indicated.

3. Acknowledgement: If any part of the material to be used (for example, figures) has appeared in our publication with credit or acknowledgement to another source, permission must also be sought from that source. If such permission is not obtained then that material may not be included in your publication/copies. Suitable acknowledgement to the source must be made, either as a footnote or in a reference list at the end of your publication, as follows:
"Reprinted from Publication title, Vol /edition number, Author(s), Title of article / title of chapter, Pages No., Copyright (Year), with permission from Elsevier [OR APPLICABLE SOCIETY COPYRIGHT OWNER]." Also Lancet special credit - "Reprinted from The Lancet, Vol. number, Author(s), Title of article, Pages No., Copyright (Year), with permission from Elsevier."
4. Reproduction of this material is confined to the purpose and/or media for which permission is hereby given.
5. Altering/Modifying Material: Not Permitted. However figures and illustrations may be altered/adapted minimally to serve your work. Any other abbreviations, additions, deletions and/or any other alterations shall be made only with prior written authorization of Elsevier Ltd. (Please contact Elsevier’s permissions helpdesk here). No modifications can be made to any Lancet figures/tables and they must be reproduced in full.
6. If the permission fee for the requested use of our material is waived in this instance, please be advised that your future requests for Elsevier materials may attract a fee.
7. Reservation of Rights: Publisher reserves all rights not specifically granted in the combination of (i) the license details provided by you and accepted in the course of this licensing transaction, (ii) these terms and conditions and (iii) CCC's Billing and Payment terms and conditions.
8. License Contingent Upon Payment: While you may exercise the rights licensed immediately upon issuance of the license at the end of the licensing process for the transaction, provided that you have disclosed complete and accurate details of your proposed use, no license is finally effective unless and until full payment is received from you (either by publisher or by CCC) as provided in CCC's Billing and Payment terms and conditions. If full payment is not received on a timely basis, then any license preliminarily granted shall be deemed automatically revoked and shall be void as if never granted. Further, in the event that you breach any of these terms and conditions or any of CCC's Billing and Payment terms and conditions, the license is automatically revoked and shall be void as if never granted. Use of materials as described in a revoked license, as well as any use of the materials beyond the scope of an unrevoked license, may constitute copyright infringement and publisher reserves the right to take any and all action to protect its copyright in the materials.
9. Warranties: Publisher makes no representations or warranties with respect to the licensed material.
10. Indemnity: You hereby indemnify and agree to hold harmless publisher and CCC, and their respective officers, directors, employees and agents, from and against any and all claims arising out of your use of the licensed material other than as specifically authorized pursuant to this license.
11. No Transfer of License: This license is personal to you and may not be sublicensed, assigned, or transferred by you to any other person without publisher's written permission.
12. No Amendment Except in Writing: This license may not be amended except in a writing signed by both parties (or, in the case of publisher, by CCC on publisher's behalf).
13. Objection to Contrary Terms: Publisher hereby objects to any terms contained in any purchase order, acknowledgment, check endorsement or other writing prepared by you, which terms are inconsistent with these terms and conditions or CCC's Billing and Payment terms and conditions. These terms and conditions, together with CCC's Billing and Payment terms and conditions (which are incorporated herein), comprise the entire agreement between you and publisher (and CCC) concerning this licensing transaction. In the event of any conflict between your obligations established by these terms and conditions and those established by CCC's Billing and Payment terms and conditions, these terms and conditions shall control.
14. Revocation: Elsevier or Copyright Clearance Center may deny the permissions described in this License at their sole discretion, for any reason or no reason, with a full refund payable to you. Notice of such denial will be made using the contact information provided by you. Failure to receive such notice will not alter or invalidate the denial. In no event will Elsevier or Copyright Clearance Center be responsible or liable for any costs, expenses or damage incurred by you as a result of a denial of your permission request, other than a refund of the amount(s) paid by you to Elsevier and/or Copyright Clearance Center for denied permissions.

LIMITED LICENSE

The following terms and conditions apply only to specific license types:
15. **Translation**: This permission is granted for non-exclusive world **English** rights only unless your license was granted for translation rights. If you licensed translation rights you may only translate this content into the languages you requested. A professional translator must perform all translations and reproduce the content word for word preserving the integrity of the article.
16. **Posting licensed content on any Website**: The following terms and conditions apply as follows: Licensing material from an Elsevier journal: All content posted to the web site must maintain the copyright information line on the bottom of each image; A hyper-text must be included to the Homepage of the journal from which you are licensing at http://www.sciencedirect.com/science/journal/xxxxx or the Elsevier homepage for books at http://www.elsevier.com; Central Storage: This license does not include permission for a scanned version of the material to be stored in a central repository such as that provided by Heron/XanEdu.
Licensing material from an Elsevier book: A hyper-text link must be included to the Elsevier homepage at http://www.elsevier.com . All content posted to the web site must maintain the copyright information line on the bottom of each image.

Posting licensed content on Electronic reserve: In addition to the above the following clauses are applicable: The web site must be password-protected and made available only to bona fide students registered on a relevant course. This permission is granted for 1 year only. You may obtain a new license for future website posting.

17. **For journal authors:** the following clauses are applicable in addition to the above:
Preprints:
A preprint is an author's own write-up of research results and analysis, it has not been peer-reviewed, nor has it had any other value added to it by a publisher (such as formatting, copyright, technical enhancement etc.).
Authors can share their preprints anywhere at any time. Preprints should not be added to or enhanced in any way in order to appear more like, or to substitute for, the final versions of articles however authors can update their preprints on arXiv or RePEc with their Accepted Author Manuscript (see below).
If accepted for publication, we encourage authors to link from the preprint to their formal publication via its DOI. Millions of researchers have access to the formal publications on ScienceDirect, and so links will help users to find, access, cite and use the best available version. Please note that Cell Press, The Lancet and some society-owned have different preprint policies. Information on these policies is available on the journal homepage.
Accepted Author Manuscripts: An accepted author manuscript is the manuscript of an article that has been accepted for publication and which typically includes author-incorporated changes suggested during submission, peer review and editor-author communications.
Authors can share their accepted author manuscript:

- immediately
    - via their non-commercial person homepage or blog
    - by updating a preprint in arXiv or RePEc with the accepted manuscript
    - via their research institute or institutional repository for internal institutional uses or as part of an invitation-only research collaboration work-group
    - directly by providing copies to their students or to research collaborators for their personal use
    - for private scholarly sharing as part of an invitation-only work group on commercial sites with which Elsevier has an agreement
- After the embargo period
    - via non-commercial hosting platforms such as their institutional repository
    - via commercial sites with which Elsevier has an agreement

In all cases accepted manuscripts should:

- link to the formal publication via its DOI
- bear a CC-BY-NC-ND license - this is easy to do
- if aggregated with other manuscripts, for example in a repository or other site, be shared in alignment with our hosting policy not be added to or enhanced in any way to appear more like, or to substitute for, the published journal article.

Published journal article (JPA): A published journal article (PJA) is the definitive final record of published research that appears or will appear in the journal and embodies all value-adding publishing activities including peer review co-ordination, copy-editing, formatting, (if relevant) pagination and online enrichment.
Policies for sharing publishing journal articles differ for subscription and gold open access articles:
Subscription Articles: If you are an author, please share a link to your article rather than the full-text. Millions of researchers have access to the formal publications on ScienceDirect, and so links will help your users to find, access, cite, and use the best available version.
Theses and dissertations which contain embedded PJAs as part of the formal submission can be posted publicly by the awarding institution with DOI links back to the formal publications on ScienceDirect.
If you are affiliated with a library that subscribes to ScienceDirect you have additional private sharing rights for others' research accessed under that agreement. This includes use for classroom teaching and internal training at the institution (including use in course packs and courseware programs), and inclusion of the article for grant funding purposes.
Gold Open Access Articles: May be shared according to the author-selected end-user license and should contain a CrossMark logo, the end user license, and a DOI link to the formal publication on ScienceDirect.
Please refer to Elsevier's posting policy for further information.
18. **For book authors** the following clauses are applicable in addition to the above: Authors are permitted to place a brief summary of their work online only. You are not allowed to download and post the published electronic version of your chapter, nor may you scan the printed edition to create an electronic version. **Posting to a repository:** Authors are permitted to post a summary of their chapter only in their institution's repository.
19. **Thesis/Dissertation**: If your license is for use in a thesis/dissertation your thesis may be submitted to your institution in either print or electronic form. Should your thesis be published commercially, please reapply for permission. These requirements include permission for the Library and Archives of Canada to supply single copies, on demand, of the complete thesis and include permission for Proquest/UMI to supply single copies, on demand, of the complete thesis. Should your thesis be published commercially, please reapply for permission. Theses and dissertations which contain embedded PJAs as part of the formal submission can be posted publicly by the awarding institution with DOI links back to the formal publications on ScienceDirect.

Elsevier Open Access Terms and Conditions
You can publish open access with Elsevier in hundreds of open access journals or in nearly 2000 established subscription journals that support open access publishing. Permitted third party re-use of these open access articles is defined by the author's choice of Creative Commons user license. See our open access license policy for more information.

Terms & Conditions applicable to all Open Access articles published with Elsevier:
Any reuse of the article must not represent the author as endorsing the adaptation of the article nor should the article be modified in such a way as to damage the author's honour or reputation. If any changes have been made, such changes must be clearly indicated.
The author(s) must be appropriately credited and we ask that you include the end user license and a DOI link to the formal publication on ScienceDirect.
If any part of the material to be used (for example, figures) has appeared in our publication with credit or acknowledgement to another source it is the responsibility of the user to ensure their reuse complies with the terms and conditions determined by the rights holder.
Additional Terms & Conditions applicable to each Creative Commons user license:
CC BY: The CC-BY license allows users to copy, to create extracts, abstracts and new works from the Article, to alter and revise the Article and to make commercial use of the Article (including reuse and/or resale of the Article by commercial entities), provided the user gives appropriate credit (with a link to the formal publication through the relevant DOI), provides a link to the license, indicates if changes were made and the licensor is not represented as endorsing the use made of the work. The full details of the license are available at http://creativecommons.org/licenses/by/4.0.
CC BY NC SA: The CC BY-NC-SA license allows users to copy, to create extracts, abstracts and new works from the Article, to alter and revise the Article, provided this is not done for commercial purposes, and that the user gives appropriate credit (with a link to the formal publication through the relevant DOI), provides a link to the license, indicates if changes were made and the licensor is not represented as endorsing the use made of the work. Further, any new works must be made available on the same conditions. The full details of the license are available at http://creativecommons.org/licenses/by-nc-sa/4.0.
CC BY NC ND: The CC BY-NC-ND license allows users to copy and distribute the Article, provided this is not done for commercial purposes and further does not permit distribution of the Article if it is changed or edited in any way, and provided the user gives appropriate credit (with a link to the formal publication through the relevant DOI), provides a link to the license, and that the licensor is not represented as endorsing the use made of the work. The full details of the license are available at http://creativecommons.org/licenses/by-nc-nd/4.0. Any commercial reuse of Open Access articles published with a CC BY NC SA or CC BY NC ND license requires permission from Elsevier and will be subject to a fee.
Commercial reuse includes:

- Associating advertising with the full text of the Article
- Charging fees for document delivery or access
- Article aggregation
- Systematic distribution via e-mail lists or share buttons

Posting or linking by commercial companies for use by customers of those companies.

20. **Other Conditions**:

v1.10

Questions? customercare@copyright.com or +1-855-239-3415 (toll free in the US) or +1-978-646-2777.

THE AMERICAN PHYSIOLOGICAL SOCIETY LICENSE TERMS AND CONDITIONS

Sep 22, 2021

This Agreement between Jan Rose ("You") and The American Physiological Society ("The American Physiological Society") consists of your license details and the terms and conditions provided by The American Physiological Society and Copyright Clearance Center.

The publisher has provided special terms related to this request that can be found at the end of the Publisher's Terms and Conditions.

License Number	5022361356197
License date	Mar 05, 2021
Licensed Content Publisher	The American Physiological Society
Licensed Content Publication	Am J Physiol- Heart and Circulatory Physiology
Licensed Content Title	Laminar structure of the heart: ventricular myocyte arrangement and connective tissue architecture in the dog
Licensed Content Author	I. J. LeGrice, B. H. Smaill, L. Z. Chai, et al
Licensed Content Date	Aug 1, 1995
Licensed Content Volume	269
Licensed Content Issue	2
Type of Use	Thesis/Dissertation
Requestor type	author of original work
Format	print and electronic
Portion	figures/tables/images
Number of figures/tables/images	2
Will you be translating?	no
World Rights	English plus translations
Title	Computational modelling of diffusion magnetic resonance imaging based on cardiac histology
Institution name	Imperial College London
Expected presentation date	May 2021
Portions	Figure 6, Figure 8
Requestor Location	Jan Rose Exhibition Road Department of Aeronautics Imperial College London London, SW72AZ United Kingdom Attn: Jan N Rose
Billing Type	Invoice
Billing Address	Jan N Rose Exhibition Road Department of Aeronautics Imperial College London London, United Kingdom SW72AZ Attn: Jan N Rose
Total	**0.00 GBP**
Terms and Conditions	

Terms and Conditions:

©The American Physiological Society (APS). All rights reserved. The publisher for this requested copyrighted material is APS. By clicking “accept” in connection with completing this license transaction, you agree to the following terms and conditions that apply to this transaction. At the time you opened your Rightslink account you had agreed to the billing and payment terms and conditions established by Copyright Clearance Center (CCC) available at http://myaccount.copyright.com
The APS hereby grants to you a nonexclusive limited license to reuse published material as requested by you, provided you have disclosed complete and accurate details of your proposed reuse of articles, figures, tables, images, and /or data in new or derivative works. Licenses are for a one-time English language use with a maximum distribution equal to the number of copies identified by you in the licensing process, unless additional options for translations or World Rights were included in your request. Any form of print or electronic republication must be completed within three years from the date hereof. Copies prepared before then may be distributed thereafter
The following conditions are required for a License of Reuse:
Attribution: You must publish in your new or derivative work a citation to the original source of the material(s) being licensed herein, including publication name, author(s), volume, year, and page number prominently displayed in the article or within the figure/image legend.
Abstracts: APS Journal article abstracts may be reproduced or translated for noncommercial purposes without requesting permission, provided the citation to the original source of the materials is included as noted above (“Attribution”). Abstracts or portions of abstracts may not be used in advertisements or commercial promotions.
Non-profit/noncommercial reuse: APS grants permission for the free reuse of APS published material in new works published for educational purposes, provided there is no charge or fee for the new work and/or the work is not directly or indirectly commercially supported or sponsored. Neither original authors nor non-authors may reuse published material in new works that are commercially supported or sponsored including reuse in a work produced by a commercial publisher without seeking permission.
Video and photographs: Some material published in APS publications may belong to other copyright holders and cannot be republished without their permission. The copyright holder of photographs must be ascertained from the original source by the permission requestor. Videos and podcasts may not be rebroadcast without proper attribution and permission as requested here. For further inquiries on reuse of these types of materials, please contact cvillemez@the-aps.org
Figures/Tables/Images are available to the requestor from the APS journals website at http://www.the-aps.org/publications/journals/. The obtaining of content is a separate transaction and does not involve Rightslink or CCC, and is the responsibility of the permission seeker. Higher resolution images are available at additional charge from APS; please contact cvillemez@the-aps.org
Original Authors of Published Works: To see a full list of original authors rights concerning their own published work http://www.the-aps.org/publications/authorinfo/copyright.htm
Content reuse rights awarded by the APS may be exercised immediately upon issuance of this license, provided full disclosure and complete and accurate details of the proposed reuse have been made; no license is finally granted unless and until full payment is received either by the publisher or by CCC as provided in CCC’s Billing and Payment Terms and Conditions. If full payment is not received on a timely basis, then any license preliminarily granted shall be deemed automatically revoked and shall be void as if never granted. Further, in the event that you breach any of these Terms and Conditions or any of CCC’s Billing and Payment Terms and Conditions, the license is automatically revoked and shall be void as if never granted. Use of materials as described in a revoked license, as well as any use of the materials beyond the scope of the license, may constitute copyright infringement and the Publisher reserves the right to take action to protect its copyright of its materials.
The APS makes no representations or warranties with respect to the licensed material. You hereby indemnify and agree to hold harmless the publisher and CCC, and their respective officers, directors, employees and agents, from and against any and all claims arising out of your use of the licensed material other than as specifically authorized pursuant to this license.
This license is personal to you /your organization and may not be sublicensed, assigned, or transferred by you /your organization to another person /organization without the publisher’s permission.This license may not be amended except in writing signed by both parties, or in the case of the publisher, by CCC on the publisher’s behalf.
The APS reserves all rights not specifically granted in the combination of (i) the license details provided by you and accepted in the course of this licensing transaction, (ii) these Terms and Conditions and (iii) CCC’s Billing and Payment Terms and Conditions.
v1.0

Questions? customercare@copyright.com or +1-855-239-3415 (toll free in the US) or +1-978-646-2777.

SPRINGER NATURE LICENSE TERMS AND CONDITIONS

Sep 22, 2021

This Agreement between Jan Rose ("You") and Springer Nature ("Springer Nature") consists of your license details and the terms and conditions provided by Springer Nature and Copyright Clearance Center.

License Number	5024790037546
License date	Mar 09, 2021
Licensed Content Publisher	Springer Nature
Licensed Content Publication	Annals of Biomedical Engineering
Licensed Content Title	Analyzing Remodeling of Cardiac Tissue: A Comprehensive Approach Based on Confocal Microscopy and 3D Reconstructions
Licensed Content Author	Thomas Seidel et al
Licensed Content Date	Sep 23, 2015
Type of Use	Thesis/Dissertation
Requestor type	academic/university or research institute
Format	print and electronic
Portion	figures/tables/illustrations
Number of figures/tables/illustrations	1
Will you be translating?	no
Circulation/distribution	1 - 29
Author of this Springer Nature content	no
Title	Computational modelling of diffusion magnetic resonance imaging based on cardiac histology
Institution name	Imperial College London
Expected presentation date	May 2021
Portions	Figure 5
Requestor Location	Jan Rose Exhibition Road Department of Aeronautics Imperial College London London, SW72AZ United Kingdom Attn: Jan N Rose
Total	**0.00 GBP**
Terms and Conditions	

Springer Nature Customer Service Centre GmbH
Terms and Conditions

This agreement sets out the terms and conditions of the licence (the **Licence**) between you and **Springer Nature Customer Service Centre GmbH** (the **Licensor**). By clicking 'accept' and completing the transaction for the material (**Licensed Material**), you also confirm your acceptance of these terms and conditions.

1. Grant of License

1. 1. The Licensor grants you a personal, non-exclusive, non-transferable, world-wide licence to reproduce the Licensed Material for the purpose specified in your order only. Licences are granted for the specific use requested in the order and for no other use, subject to the conditions below.

1. 2. The Licensor warrants that it has, to the best of its knowledge, the rights to license reuse of the Licensed Material. However, you should ensure that the material you are requesting is original to the Licensor and does not carry the copyright of another entity (as credited in the published version).

1. 3. If the credit line on any part of the material you have requested indicates that it was reprinted or adapted with permission from another source, then you should also seek permission from that source to reuse the material.

2. Scope of Licence

2. 1. You may only use the Licensed Content in the manner and to the extent permitted by these Ts&Cs and any applicable laws.

2. 2. A separate licence may be required for any additional use of the Licensed Material, e.g. where a licence has been purchased for print only use, separate permission must be obtained for electronic re-use. Similarly, a licence is only valid in the language selected and does not apply for editions in other languages unless additional translation rights have been granted separately in the licence. Any content owned by third parties are expressly excluded from the licence.

2. 3. Similarly, rights for additional components such as custom editions and derivatives require additional permission and may be subject to an additional fee. Please apply to Journalpermissions@springernature.com/bookpermissions@springernature.com for these rights.

2. 4. Where permission has been granted **free of charge** for material in print, permission may also be granted for any electronic version of that work, provided that the material is incidental to your work as a whole and that the electronic version is essentially equivalent to, or substitutes for, the print version.

2. 5. An alternative scope of licence may apply to signatories of the STM Permissions Guidelines, as amended from time to time.

3. Duration of Licence

3. 1. A licence for is valid from the date of purchase ('Licence Date') at the end of the relevant period in the below table:

Scope of Licence	Duration of Licence
Post on a website	12 months
Presentations	12 months
Books and journals	Lifetime of the edition in the language purchased

4. Acknowledgement

4. 1. The Licensor's permission must be acknowledged next to the Licenced Material in print. In electronic form, this acknowledgement must be visible at the same time as the figures/tables/illustrations or abstract, and must be hyperlinked to the journal/book's homepage. Our required acknowledgement format is in the Appendix below.

5. Restrictions on use

5. 1. Use of the Licensed Material may be permitted for incidental promotional use and minor editing privileges e.g. minor adaptations of single figures, changes of format, colour and/or style where the adaptation is credited as set out in Appendix 1 below. Any other changes including but not limited to, cropping, adapting, omitting material that affect the meaning, intention or moral rights of the author are strictly prohibited.

5. 2. You must not use any Licensed Material as part of any design or trademark.

5. 3. Licensed Material may be used in Open Access Publications (OAP) before publication by Springer Nature, but any Licensed Material must be removed from OAP sites prior to final publication.

6. Ownership of Rights

6. 1. Licensed Material remains the property of either Licensor or the relevant third party and any rights not explicitly granted herein are expressly reserved.

7. Warranty

IN NO EVENT SHALL LICENSOR BE LIABLE TO YOU OR ANY OTHER PARTY OR ANY OTHER PERSON OR FOR ANY SPECIAL, CONSEQUENTIAL, INCIDENTAL OR INDIRECT DAMAGES, HOWEVER CAUSED, ARISING OUT OF OR IN CONNECTION WITH THE DOWNLOADING, VIEWING OR USE OF THE MATERIALS REGARDLESS OF THE FORM OF ACTION, WHETHER FOR BREACH OF CONTRACT, BREACH OF WARRANTY, TORT, NEGLIGENCE, INFRINGEMENT OR OTHERWISE (INCLUDING, WITHOUT LIMITATION, DAMAGES BASED ON LOSS OF PROFITS, DATA, FILES, USE, BUSINESS OPPORTUNITY OR CLAIMS OF THIRD PARTIES), AND
WHETHER OR NOT THE PARTY HAS BEEN ADVISED OF THE POSSIBILITY OF SUCH DAMAGES. THIS LIMITATION SHALL APPLY NOTWITHSTANDING ANY FAILURE OF ESSENTIAL PURPOSE OF ANY LIMITED REMEDY PROVIDED HEREIN.

8. Limitations

8. 1. ***BOOKS ONLY:***Where **'reuse in a dissertation/thesis'** has been selected the following terms apply: Print rights of the final author's accepted manuscript (for clarity, NOT the published version) for up to 100 copies, electronic rights for use only on a personal website or institutional repository as defined by the Sherpa guideline (www.sherpa.ac.uk/romeo/).

8. 2. For content reuse requests that qualify for permission under the STM Permissions Guidelines, which may be updated from time to time, the STM Permissions Guidelines supersede the terms and conditions contained in this licence.

9. Termination and Cancellation

9. 1. Licences will expire after the period shown in Clause 3 (above).

9. 2. Licensee reserves the right to terminate the Licence in the event that payment is not received in full or if there has been a breach of this agreement by you.

Appendix 1 — Acknowledgements:

For Journal Content:
Reprinted by permission from [**the Licensor**]: [**Journal Publisher** (e.g. Nature/Springer/Palgrave)] [**JOURNAL NAME**] [**REFERENCE CITATION** (Article name, Author(s) Name), [**COPYRIGHT**] (year of publication)

For **Advance Online Publication papers:**
Reprinted by permission from [**the Licensor**]: [**Journal Publisher** (e.g. Nature/Springer/Palgrave)] [**JOURNAL NAME**] [**REFERENCE CITATION** (Article name, Author(s) Name), [**COPYRIGHT**] (year of publication), advance online publication, day month year (doi: 10.1038/sj.[JOURNAL ACRONYM].)

For Adaptations/Translations:
Adapted/Translated by permission from [**the Licensor**]: [**Journal Publisher** (e.g. Nature/Springer/Palgrave)] [**JOURNAL NAME**] [**REFERENCE CITATION** (Article name, Author(s) Name), [**COPYRIGHT**] (year of publication)

Note: For any republication from the British Journal of Cancer, the following credit line style applies:

Reprinted/adapted/translated by permission from [**the Licensor**]: on behalf of Cancer Research UK: : [**Journal Publisher** (e.g. Nature/Springer/Palgrave)] [**JOURNAL NAME**] [**REFERENCE CITATION** (Article name, Author(s) Name), [**COPYRIGHT]** (year of publication)

For **Advance Online Publication** papers:
Reprinted by permission from The [**the Licensor**]: on behalf of Cancer Research UK: [**Journal Publisher** (e.g. Nature/Springer/Palgrave)] [**JOURNAL NAME**] [**REFERENCE CITATION** (Article name, Author(s) Name), [**COPYRIGHT**] (year of publication), advance online publication, day month year (doi: 10.1038/sj.[JOURNAL ACRONYM])

For Book content:
Reprinted/adapted by permission from [**the Licensor**]: [**Book Publisher** (e.g. Palgrave Macmillan, Springer etc) [**Book Title**] by [**Book author**(s)] [**COPYRIGHT**] (year of publication)

Other Conditions:

Version 1.3

Questions? customercare@copyright.com or +1-855-239-3415 (toll free in the US) or +1-978-646-2777.